ESCUELA TÉCNICA SUPERIOR DE INGENIERÍA DE TELECOMUNICACIÓN
UNIVERSIDAD POLITÉCNICA DE CARTAGENA

Proyecto Fin de Carrera

Aportación al Estudio de Antenas de Lentes Dieléctricas Milimétricas

AUTOR: Carlos Alberto Tourné Sánchez
DIRECTORES: José María Molina García-Pardo
Ronan Saleau

Cartagena, Octubre 2006

Autor	Carlos Alberto Tourné Sánchez
E-mail del Autor	ctournes@hotmail.com
Director(es)	Jose María Molina García-Pardo, Ronan Saleau
E-mail del Director	josemaria.molina@upct.es, ronan.sauleau@univ-rennes1.fr
Codirector(es)	
Título del PFC	Aportación al Estudio de antenas de lentes dieléctricas milimétricas
Descriptores	IMELSI, MATLAB

Resúmen

Al crecer la demanda de sistema de comunicación *wireless* de banda-ancha, la banda de frecuencias de microondas se va congestionando, y no puede soportar las cada vez más elevadas velocidades de transmisión requeridas. Por esto, gradualmente se van usando más las ondas milimétricas. Esto ha hecho que en los últimos años haya aumentado el interés en desarrollar antenas milimétricas en circuitos integrados para comunicaciones exteriores e interiores

Una técnica muy usada de implementar estos sistemas es la integración de antenas planares y su correspondiente circuitería en la base de una lente dieléctrica. Este proyecto pretende estudiar estas implementaciones, especialmente todo lo referido al diseño de las lentes dieléctricas, analizando sus características radiativas. También se pretende estudiar sus posibles aplicaciones como sistema multi-rayo.

Titulación	Ingeniero de Telecomunicación
Intensificación	Redes y Servicios de Telecomunicación
Departamento	Tecnologías de la Información y las Comunicaciones
Fecha de Presentación	Octubre - 2006

Table of Contents

Chapter 1: Introduction

As the need for broad-band wireless communication systems is growing, the microwave frequency band either becomes too congested or simply cannot support the ever-increasing data-rate requirements. Therefore, the corresponding operating frequency is gradually shifting toward millimeter-wave (mm-wave) frequencies. In recent years, this has generated an increased interest in developing mm-wave integrated circuit (IC) antennas for indoor and outdoor wireless communications.

A successful technique for implementing mm-wave subsystems has been the integration of planar antennas and electronics at the back of substrate lenses. The main advantages of this approach include highly directive antenna patterns, compatibility with IC techniques, mechanical rigidity, and thermal stability, as well as the capability of multiple-beam formation in a simple way. In addition, this approach is capable of suppressing surface-wave losses, which become an important consideration at mm-wave frequencies.

1.1 Objectives

This project has several purposes. One of them is to make an accurate study of the millimetric lens antennas, of the hyper-hemispherical type, stressing on the influence of each design parameter in the behaviour of radiating configurations. The conclusion we obtain will be useful for other researchers who want to use this structure in their projects, they will be able to choose a design according with their specifications with a lesser work in optimization, since the analysis of these structures requires simulations with a hard expense in computer resources.

The behaviour we can obtain with this structure alone is limited. Once we have learned its possibilities we will study variations in the typical design in order to obtain different radiation patterns. This will allow a wider range of suitable applications. We will be centred in the patches array, the lenses fed by patches network has some of the most interesting applications (see chapter 2). We will settle the bases of its behaviour with a concrete lens design.

1.2 Contents

The work was developed during nine months, in my Erasmus period in Rennes. This is actually a compilation of the work I made under the tutorial of Ronan Saleau, doctor in the IETR, in the workgroup of antennas and hyper-frequencies.

The second chapter is a literature review of the researches where we base this work, and a small study of the evolution in this area, introduced by a brief explanation of the basic concepts used in this project.

In the third chapter we describe theoretically the methods for the analysis we are carrying out. We also present the software used to make the designs and the simulations and how we treat the results.

The fourth chapter is the first one where we show our results. We start with a general analysis of the lens antenna and its parameter, using several dielectrics and dimensions, and feeding it with a wave-guide.

When we have a general view of this structure, in the fifth chapter we carry out a deeper analysis with a configuration which had good practical results with other work-team.

Now that we have a deep knowledge of how the lens parameters affect the radiation, we choose a design in the sixth chapter in order to use it for the application we have in mind, the patches array. We need to find out how the design behaves when we change the patch position from the centre, and which the limits of this decentring are.

Finally, taking in account the effects of the decentring studied in the previous chapter, we design some patches network and study its behaviour in the seventh chapter.

In the appendix we will find the Imelsi implementation and general design of the lenses used in each chapter and the printed sources of the last ones.

Chapter 2: State of the Art.

2.1 Introduction

Some hyper-frequencies applications, like high-speed local communications, security of cars or satellite communications, need radiating structures with a gain between 40~50 dB. The antennas with reflectors and the printed antenna networks cover partially these values. However, the classic reflectors are voluminous (especially for the built-in configurations), and the printed technology give us millimetric antenna networks with low efficiency, because of the losses in the arborescence feed and the ones caused by surface waves. A third solution can be found in the association of a primary excitation source (printed or guided) with a focalisation system, like a lens. Our work is inscribed in this area.

The bibliographic synthesis carried out is about the two main systems of homogeneous dielectric lens antennas: the lens antennas and the substrate lenses. In the first one, the lens is fed by a main source (usually a horn) placed in the far field zone. In the second one, the printed source is in direct contact with the lens.

Lots of other focalisation techniques have been put forward; they will not be described here. We can quote for example : (1) Shells in the Fresnez zones [1-3], (2) reflecting planes [4,5], (3) antennas with gaussian beams with Fabry-Pérot resonators [6-8], (4) constrained propagation lenses made with guiding structures (for example : lenses with metallic wave guides [9-11], multifocal lenses [12], Rotman lenses [13-15], ferroelectric layers lenses [16,17]), (5) non-homogeneous dielectric lenses [18-20] or also (6) artificial dielectric lenses [21-23].

2.2 Previous concepts

We will define some basic concepts theoretically before entering in the explanation of the ideas developed in this project.

An antenna is an electronic component designed to transceive radio signals (and, more generally, other electromagnetic waves). Antennas are for transmission of radio wave energy through the natural media (i.e., air, earth, water, etc.) for point-to-point communication or for the reception of such transmitted radio wave energy. Antennas are primarily designed for transmission of radio wave energy through free space or any space where the movement of energy in any direction is substantially unimpeded, such as interplanetary space (such as the interplanetary medium or interstellar medium), the atmosphere, the ocean (and other large bodies of water), or the Earth. Antennas are used for communicating and conveying information specifically in larger systems, such as the radio, telephone, and the telegraph.

Physically, an antenna is an arrangement of conductors designed to radiate (transmit) an electromagnetic field in response to an applied alternating voltage and the associated

alternating electric current, or to be placed into an electromagnetic field so that the field will induce an alternating current in the antenna and a voltage between its terminals.

There are two fundamental types of antennas, which, with reference to a specific three dimensional (usually horizontal or vertical) plane are:

- either omni-directional (radiate equally in the plane)
- directional (radiates more in one direction than in the other).
-

All antennas radiate (or emanate) some energy in all directions in free space but careful construction results in large directivity in certain directions and negligible energy radiated in other directions.

There are several critical parameters that affect an antenna's performance and can be adjusted during the design process. These are resonant frequency, impedance, gain, aperture or radiation pattern, polarization, efficiency and bandwidth. Transmit antennas may also have a maximum power rating, and receive antennas differ in their noise rejection properties.

The "*resonant frequency*" and "*electrical resonance*" is related to the electrical length of the antenna. The electrical length is usually the physical length of the wire multiplied by the ratio of the speed of wave propagation in the wire. Typically an antenna is tuned for a specific frequency, and it is effective for a range of frequencies usually centred on that resonant frequency. However, the other properties of the antenna (especially radiation pattern and impedance) change with frequency, so the antenna's resonant frequency may merely be close to the central frequency of these other more important properties.

Antennas can be made resonant on harmonic frequencies with lengths that are fractions of the target wavelength. Some antenna designs have multiple resonant frequencies, and some are relatively effective over a very broad range of frequencies. The most commonly known type of wide band aerial is the logarithmic or log periodic, but its gain is usually much lower than that of a specific or narrower band aerial.

In antenna design, "*gain*" is the logarithm of the ratio of the intensity of an antenna's radiation pattern in the direction of strongest radiation to that of a reference antenna. If the reference antenna is an isotropic antenna, the gain is often expressed in units of dBi (decibels over isotropic). For example, a dipole antenna has a gain of 2.14 dBi. Often, the dipole antenna is used as the reference (since a perfect isotropic reference is impossible to build), in which case the gain of the antenna in question is measured in dBd (decibels over dipole).

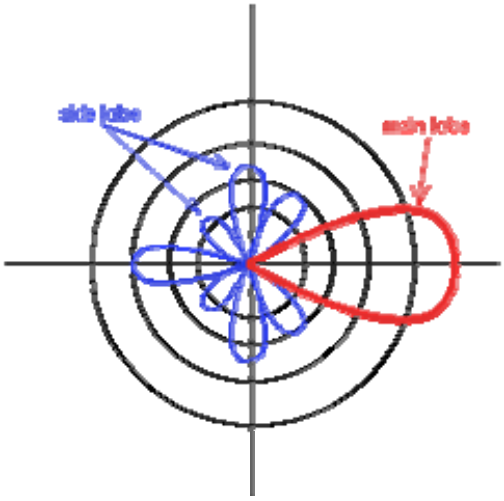

figure 2.1. Radiation Pattern. Main and Side lobes.

The gain of an antenna is a passive phenomena - power is not added by the antenna, but simply redistributed to provide more radiated power in a certain direction than would be transmitted by an isotropic antenna. If an antenna has a positive gain in some directions, it must have a negative gain in other directions as energy is conserved by the antenna. The gain that can be achieved by an Antenna is therefore trade-off between the range of directions that must be covered by an Antenna and the gain of the antenna.

"*Aperture*" (or "*opening*", as we will refer it after), and "*radiation pattern*" are closely related to gain. *Aperture* is the shape of the "beam" cross section in the direction of highest gain, and is two-dimensional. (Sometimes aperture is expressed as the radius of the circle that approximates this cross section or the angle of the cone.) *Radiation pattern* is the three-dimensional plot of the gain, but usually only the two-dimensional horizontal and vertical cross sections of the radiation pattern are considered. Antennas with high gain typically show side lobes in the radiation pattern. Side lobes are peaks in gain other than the main lobe (the "beam"). Side lobes detract from the antenna quality whenever the system is being used to determine the direction of a signal, as in radar systems and reduce gain in the main lobe by distributing the power. Usually, in this work, we will measure the secondary lobe level, which is the level of the higher side lobe referred to the radiation maximum.

The "*bandwidth*" of an antenna is the range of frequencies over which it is effective, usually centred around the resonant frequency. The bandwidth of an antenna may be increased by several techniques, including using thicker wires, replacing wires with *cages* to simulate a thicker wire, tapering antenna components (like in a feed horn), and combining multiple antennas into a single assembly and allowing the natural impedance to select the correct antenna. Small antennas are usually preferred for convenience, but there is a fundamental limit relating bandwidth, size and efficiency.

"*Impedance*" is analogous to refractive index in optics. As the electric wave travels through the different parts of the antenna system (radio, feed line, antenna, free space) it may encounter differences in impedance. At each interface, depending on the impedance match, some fraction of the wave's energy will reflect back to the source, forming a standing wave in the feed line.

The "*polarization*" of an antenna is the orientation of the electric field (E-plane) of the radio wave with respect to the Earth's surface and is determined by the physical structure of the antenna and by its orientation. It has nothing in common with antenna directionality terms: "horizontal", "vertical" and "circular". Thus, a simple straight wire antenna will have one polarization when mounted vertically, and a different polarization when mounted horizontally.

Polarization is the sum of the E-plane orientations over time projected onto an imaginary plane perpendicular to the direction of motion of the radio wave. For a linearly polarized antenna, the E-plane is the one containing the electric field vector and the direction of maximum radiation. The electric field or "E" plane determines the polarization or orientation of the radio wave. In the case of the same linearly polarized antenna, the H-plane contains the magnetic field vector and the direction of maximum radiation. The magnetic field or "H" plane lies at a right angle to the "E" plane.

In practice it is important that linearly polarized antennas be matched, lest the received signal strength be greatly reduced. So horizontal should be used with horizontal and vertical with vertical. Intermediate matchings will lose some signal strength, but not as much as a complete mismatch. Transmitters mounted on vehicles with large motional freedom commonly use circularly polarized antennas so that there will never be a complete mismatch with signals from other sources. In the case of radar, this is often reflections from rain drops.

In this study, when we measure the radiation patterns we will usually do it in both planes and we will consider the Co-polarization and the Cross-polarization. The first is the field that would receive an antenna with the same polarization as the emitter, and the second is the one received by an antenna with the opposite polarization.

"*Efficiency*" is the ratio of power actually radiated to the power put into the antenna terminals. A dummy load may have a SWR of 1:1 but an efficiency of 0, as it absorbs all power and radiates heat but not RF energy, showing that SWR alone is not an effective measure of an antenna's efficiency. Radiation in an antenna is caused by radiation resistance which can only be measured as part of total resistance including loss resistance. Loss resistance usually results in heat generation rather than radiation, and therefore, reduces efficiency.

We can distinguish between far field and near field measures. The near field is that part of the radiated field nearest to the antenna, where the radiation pattern depends on the distance from the antenna. Beyond the near field is the far field, where the angular field distribution is essentially independent of distance from the source. If the source has a maximum overall dimension D that is large compared to the wavelength, the far-field region is commonly taken to exist at distances greater than $2D^2/\lambda$ from the source, λ being the wavelength.

2.3 Lens Antennas

The conception principles of the lens antennas are based on the optics geometric (Snell-Descartes laws, power conservation inside a beam tube, optic way length). They have been enunciated since the 1950's-1960's. That's why we find the most detailed

descriptions of these devices in old references (ex. [24-28]), though a thesis was written by Lee [29] in 1989.

The most elemental device is the lens with revolution symmetry and *a bending surface*, the other side behaves like a constant phase surface, face to face with the incoming wave (which can be either plane or spherical). If we have a punctual source and a lens with a relative permittivity over 1, we can check easily that this lens is a revolution hyperboloid [28]. The plan-spherical lenses are also used often with optical and infra-red wavelengths. However, they do not satisfy the Fermat principle for the off-axis beams and have a worse performance in these directions than in the hyperbolic ones [30].

Adding a *second bending surface* give us an additional freedom degree. With this we can, for example, improve the lens performance with off-axis sources [31], or changing the characteristics of the quasi-optic gaussian beams ([31bis], ***figure 2.2***).

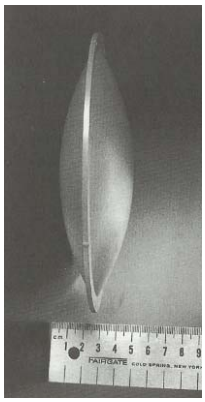

figure 2.2. Rexolite bihyperbolic Lens

Otherwise, the lens profiles can be defined in order to get (in the output) a certain field distribution in amplitude and phase. We can either work with a classic formalism as optic-geometric and beam tracing [32,33], or work with the complex beam notion [34].

For instance, two millimetric lenses with great performances were proposed by Lee [32,33] (***figure 2.3-a***) and by Rotman [35] (***figure 2.3-b***) for multi-beam application at 44 GHz (military communications by satellite). This lenses are made of Rexolite ($\varepsilon_r = 2{,}54$).

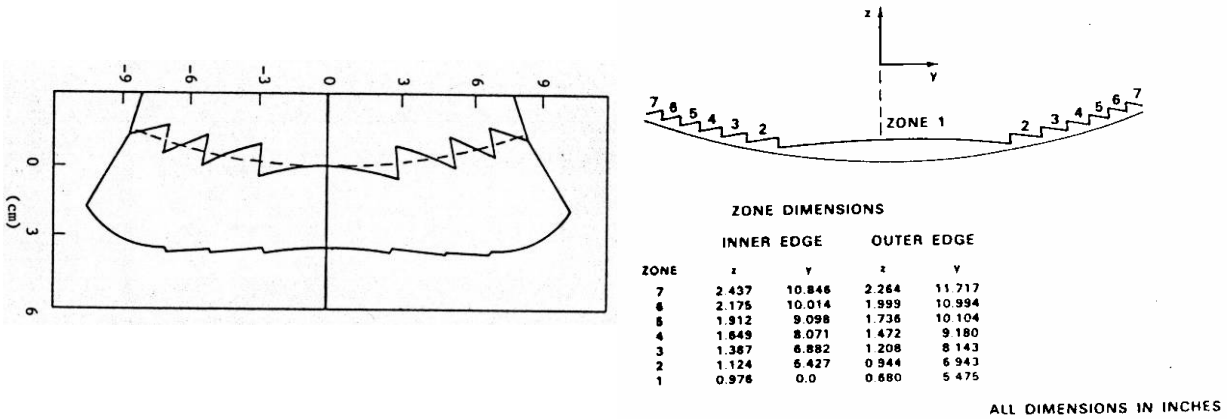

(a) [32-33] *(b) [35]*

figure 2.3. Multi-beam Lens at 44 GHz

In the first case (***figure 2.3-a***), the lens has a diameter of 20.7 cm (30 λ_0) and 24.5 cm of focal distance. Its gain is 33 dB and the opening is of 3.3º. The secondary lobes are under -30dB across the axis. The two surfaces zoning allows us to reduce the lens weight. The mean profile placed next to the source is spherical in order to satisfy the Abbe sine condition and then reduce the cubic phase aberrations (coma). This technique allow us to depoint the beam about ± 12° (***figure 2.4***), without an important degradation in the radiation diagram.

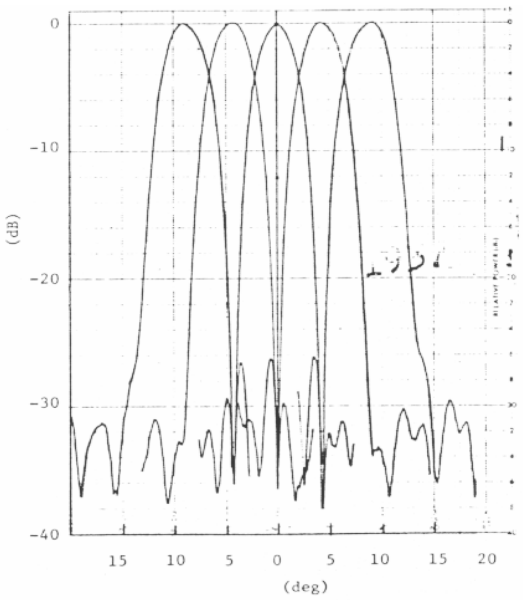

figure 2.4. Radiation Diagram of the lens represented in **figure 1.2a** [33]

In the second case (***figure 2.3-b***), the lens gain is far higher (48dB) with an opening of 0.73º and secondary lobes under –20dB. It has a diameter of 60cm (88 λ_0) and a focal distance of 90 cm. Its minimum thickness is 0.6 cm. We can scan the beam ± 8.6° because the zoned lens is too thin and its profile is almost spherical.

The dielectric bifocal lenses [36] or the planar-convex lenses with its refraction index as close as possible to *n=1.62* [37] also show good performances when the source is decentred.

Save for the quasi-optical systems and the employment of lenses in the mouth of horn antennas (for example in order to improve the Cassegrain antennas efficiency [37bis] or for the conception of antennas with gaussian beam [37ter]), the lens antennas can be used in many applications, for example:

❶ The wireless broad-band communication systems at 25 GHz [38], at 30 GHz [39-41], and around 44 GHz [42-44] and 60 GHz [41-43,45-47].

On the reference [38], the small size lenses (diameter between 2.5×λ_0 and 3.5×λ_0, ***figure 2.5a***) in melted quartz are excited in near field by a coplanar multi-source antenna (***figure 2.5b***) printed over an aluminium subtract with a thickness of 254 µm. The antenna's measured gain is 16.2 dB at 25 GHz (***figure 2.5c***), which means a surface performance of 40%.

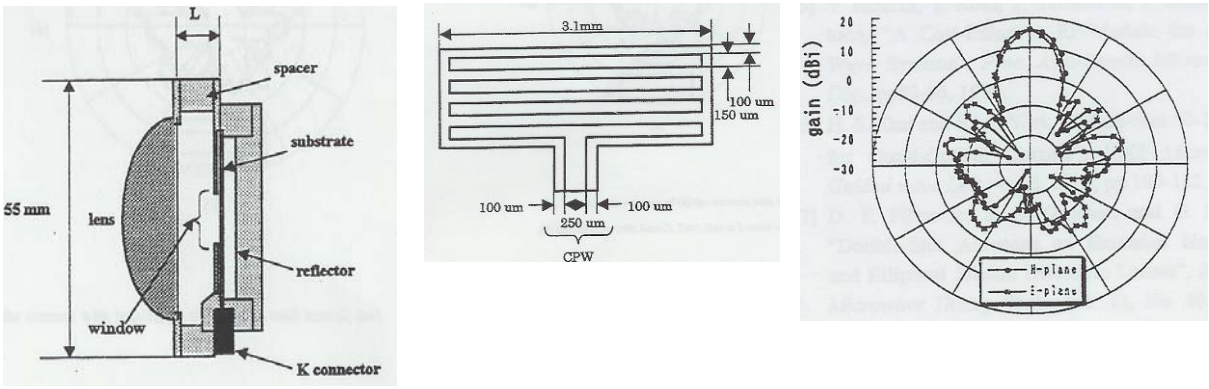

(a) *(b)* *(c)*

figure 2.5. (a) Planar-convex lens antenna (diameter=40mm, thickness=12.6mm, radius of curvature=23.0mm) in melted quartz excited by a main source of the multi-source coplanar antenna kind (b). (c) Radiation diagram measured at 25 GHz (L=12mm≅ λ_0) [38].

At LMDS frequencies (28 GHz in North America, 42 GHz in Europe), the gains are usually required between 25 dB and 35 dB [40]. In order to reduce the size of the focal devices, we can use, for example, two lenses systems [39, ***figure 2.6***]. Compared to an one subtract lens, this solution allow us to reduce the total weight in 75% and a scan angle (by commuting sources within a hexagonal planar network [48]) in a sector around ±6° for H=10.54cm or ±9.6° for H=7.73cm (not-centred system).

Finally, we can optimise the quality of the radio-electric links in the buildings shaping the radiation diagram of the base stations. The ***figure 2.7*** shows an example of lens antenna in polyethylene fed by an helix (circular polarization) excited by a metallic rectangular wave-guide. This antenna radiates a cosecant pattern; it has a pass band of 10% and an expected performance of 90%. Using an anti-reflection layer allow us to reduce the undulations of the diagram in a significative way.

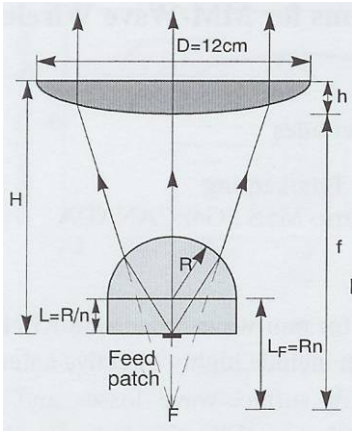

figure 2.6. Rexolite bi-lens system ($\varepsilon_r=n^2=2.54$) which consists of an hyper-hemispheric subtract lens (R=1.5cm, f/D=0.80) and an hyperbolic thin lens [39].

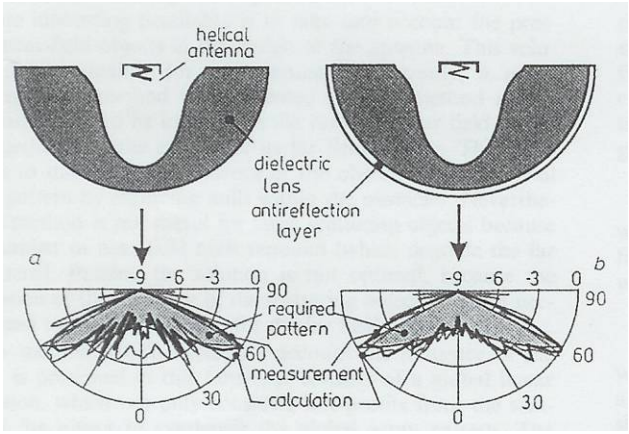

figure 2.7. Lens illuminated by an helix in circular polarization for communications in buildings at 30 GHz [41].

In this domain, bigger works have been made by the C. Fernandes' team (IST, Lisbonne), in the frame of two European projects ACTS AC204 SAMBA (System for Advanced Mobile Broadband Applications, band 42.5-46.5 GHz) and RACE II 2067 MBS (Mobile Broadband Systems, band 62-66 GHz). The ***figure 2.8*** shows two examples of developed prototypes. The lenses developed by IST are fed either by wave-guides [42,43,45-47], or by a printed antenna with longitudinal radiation [44]. Their profiles are defined within the Optic Geometric [49,50] : The objective lies in generating a radiation pattern from some given specifications (hemispheric sectorial diagram or cosecant). They can be either of revolution [45,49] or quasi-revolution [46]. For example, the ***figure 2.9b*** shows a cosecant radiation pattern obtained at 62.5GHz with a Plexiglas lens (ε_r=2.53, tanδ=0.012) a diagonal of 84mm and 32mm of thickness (***figure 2.9a***). Finally, we can widen the pass band of these structures using two-layers lenses [47] (***figure 2.10***) or broad-band primary sources (***figure 2.11*** shows an example of subtract lens sort of structure [51]).

(a) (b)

figure 2.8. Lenses with its profile designed for broad-band communications systems

(a) Project SAMBA, (b) Project MBS.

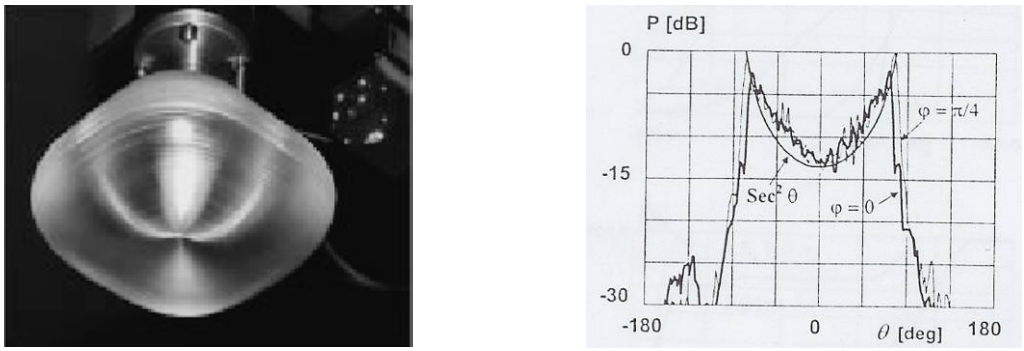

(a) (b)

figure 2.9. (a) Lens antenna for base stations (square piece).
(b) Theoretical radiation patterns and measures at 62.5 GHz.

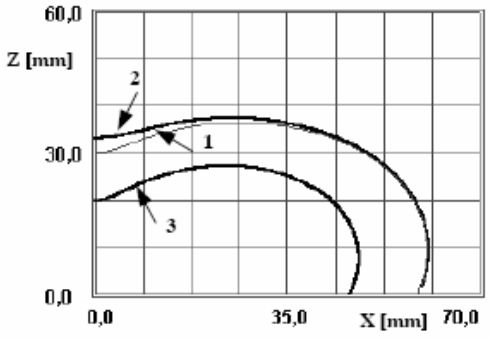

figure 2.10. Double layer lens: profiles 1 (ε_r =2.53) and 2 (ε_r=1.59) at 62.5 GHz. Cosecant diagram, fed by circular guide [47].

figure 2.11. Plexiglas lens fed by log-periodic planar antenna [51].

❷ The car driving assistance radars on the 76-77 GHz band [52,53]. The ***figure 2.12a*** represents the emitter (TX) and reception (RX) antennas of a mono-pulse radar [54] using linear bi-polarization patches fed by source and printed on Duroïd 5880 (127µm). In emission, we get a beam with an opening of 10º thanks to a Teflon lens (ε_r=2.2) with a diameter of 2.5 cm placed 1 cm next to the primary source (***figure 2.12b***). In reception, three directive beams (3º of opening, ***figure 2.12c***) are generated thanks to a Teflon zoned lens if Friedlander's kind (the profile placed next to the patches is spherical).

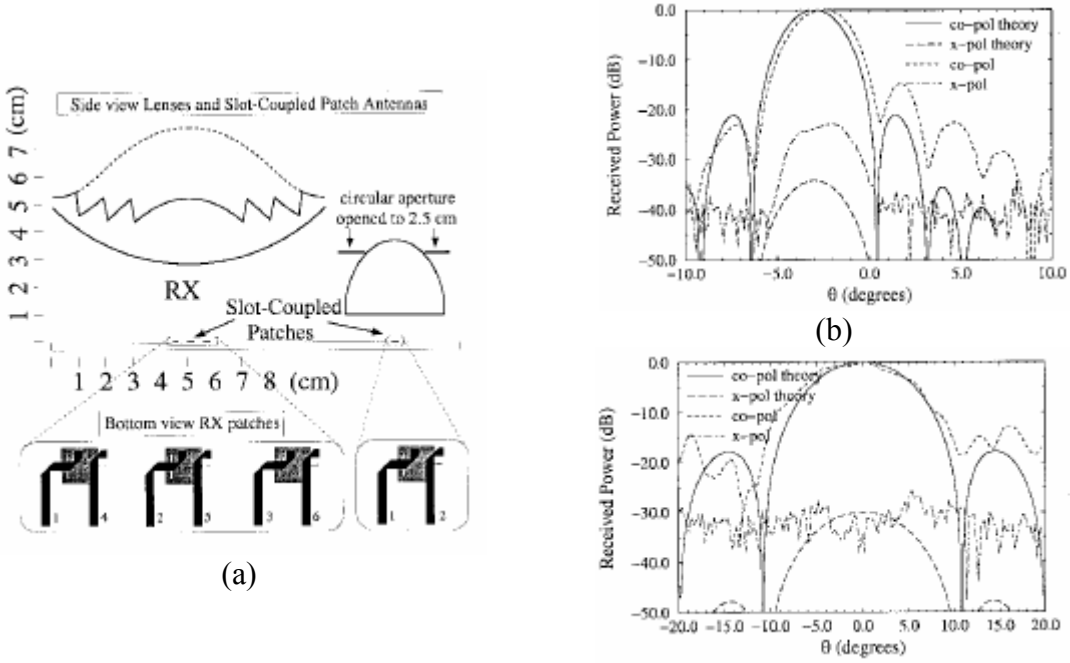

figure 2.12. (a) Emitter and reception antenna. Radiation patterns on H plane at 76.5 GHz : (b) RX, not-zoned lens, (c) TX [54].

Two other lens antennas geometries for ACC radar (« Automotive Cruise Control ») have been proposed by the Michigan University [55,56]. In the first case ([55], ***figure 2.13***), 33 beams with 5'5º of opening are got illuminating a Teflon lens (diameter 5 cm) with the help of the TSA antennas (« Tapered Slot Antenna ») printed on Duroïd 127µm and spread over a half-circle placed 13mm from the lens surface. This antenna assures a beam scan angle over an angular sector of ±90°. A more compact structure has also been proposed [56]: It uses now a hemispherical lens and a planar reflector. The principle scheme is represented in ***figure 2.14a,*** the prototype in ***figure 2.14b*** and the measured diagrams in ***figure 2.14c***. Compared with ***figure 2.13b***, the quality of the diagrams (secondary lobes < -18 dB) is only kept over an angular sector of 35º.

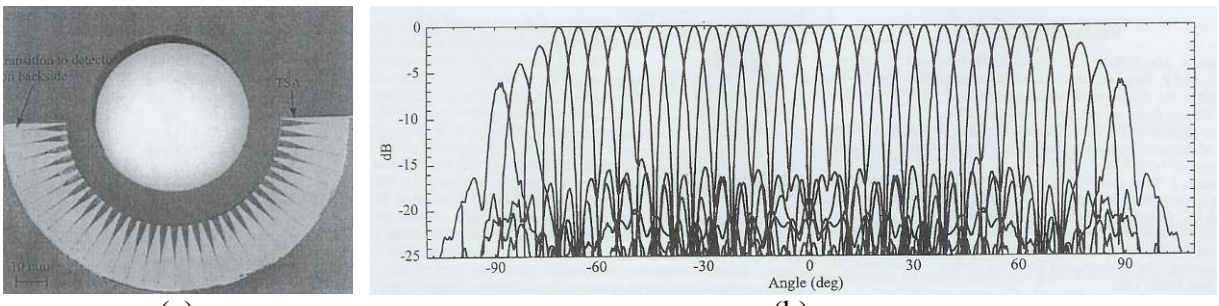

figure 2.13. (a) Multi-beam lens antenna.
(b)Radiation diagrams measured at 77 GHz [55]

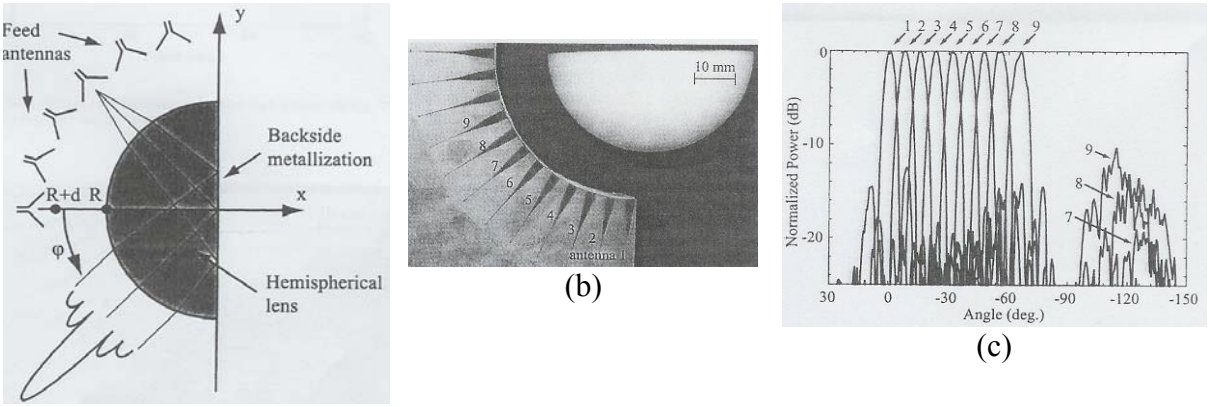

(a) (b) (c)

figure 2.14. Multi-beam lens antenna of small size [55].
(a) Principle, (b) Prototype, (c) Radiation patterns at 77 GHz.

Finally, a strong angular resolution can be obtained with a mechanical sweep of the primary source. Such solution has been proposed in [57]: a plan-convex lens (ε_r=6.6, tanδ=10^{-3}, diameter D = 88mm, f/D = 0.3) excited by a circular horn which position is adjusted by a NRD 0dB connector. The antenna gain is 34.1 dB, its performance is 52% and the secondary lobe level remains under –15dB for a scan angle of ±10°.

❸ Tracking satellites in low orbit. Knowing their spherical symmetry and their excellent focalisation properties, the Luneburg lenses [58] have a great adaptation with these applications. However, the fabrication costs of lenses with gradient index (overlapped shells, artificial dielectrics) are prohibitive. A lower cost solution (homogeneous spherical lens in foam technology, ***figure 2.15a***) has been proposed lately [59,60]. The newness of this approximation is in the correction of the lens aberrations with the help of a primary source « compensator » (horn with floating dielectric inserted) (***figure 2.15b***)).

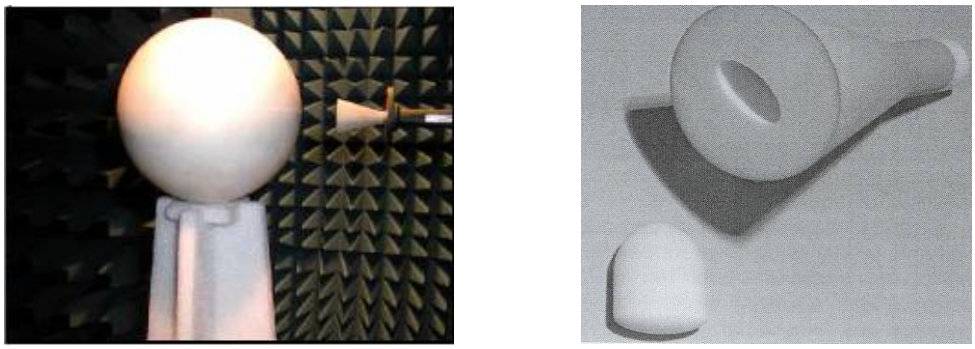

(a) (b)

figure 2.15. (a) Lens antenna with foam technology (ε_r=1.8). (b) Primary source : horn with floating dielectric inserted (ε_r=1.7, tanδ=0.004)) [60].

❹ Communication systems via high platforms on the 28 GHz and 47/48 GHz band. These stratospherical platforms (17km) could assure a cellular coverture of some land regions. Within each cell, the constant power sections must be circular (that means the generation of an asymmetrical beam with 5º of opening on a plane and 9.4º on the other for an elevation of 32º and a cell of 6km of diameter). Besides, the secondary lobe level must be very low (<-40 dB). The geometry of a suitable lens

antenna is shown in ***figure 2.16a*** [61]. The side source profile is defined in order to obtain a revolution beam with 5º of opening ; the conformation (along a plane) of the second lens side allow us to control the phase distribution in the opening and then make the beam asymmetrical ***(figure 2.16b***).

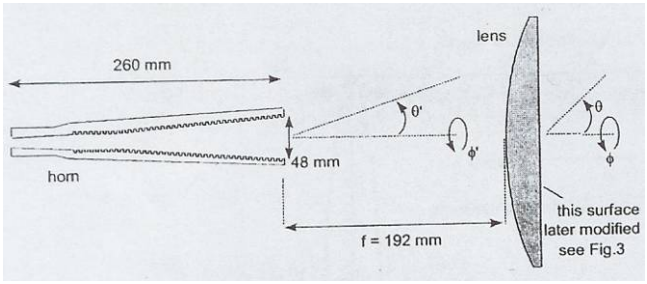

(a)

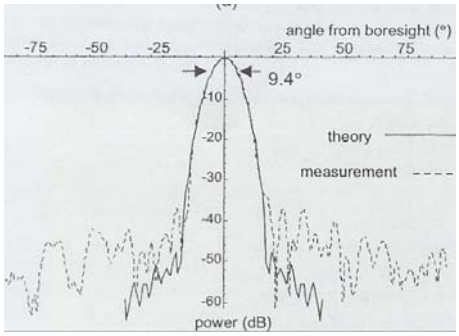

(b)

figure 2.16. (a) Polyethylene lens antenna ($\varepsilon_r \approx 2.25$, diameter=160mm) excited by a rough horn. (b) Radiation patterns measured and calculated at 28 GHz in the plane where the beam is large [61].

2.4 Subtract Lenses

The millimetrical (and beyond) subtracts become guiding. The surface waves generated cause a performance reduction [62] and increase the coupling between elements, which is specially harmful in multi-caption systems in focal imaging, for example [63]. In order to reduce this phenomenon, several approximations have been proposed, like the subtract / supertract configuration [64], the physique alteration of the subtract (volume micro-fabrication [65], materials with photonic forbidden band [66]) or also high impedance surfaces [66b].

The interest here is in the solution based on subtract lenses. In fact, the subtract modes are no longer excited if the sources are printed on an infinite thickness subtract. They radiate by a majority inside the dielectric [67,68] in a ratio $\varepsilon_r^{3/2} : 1$ (compared with air). Their radiation is unidirectional "per se" for high permittivity subtract (aluminium), Si, GaAs), which avoids the use of reflectors (hard to integrate).

An infinite thickness subtract can be simulated making the antennas over the flat side of a dielectrical hemisphere (***figure 2.17-a***). That's the reason of the name, subtract lens. Since all the beams reach with normal incidence the spherical side of the lens, they can't be trapped, avoiding the apparition of surface waves.

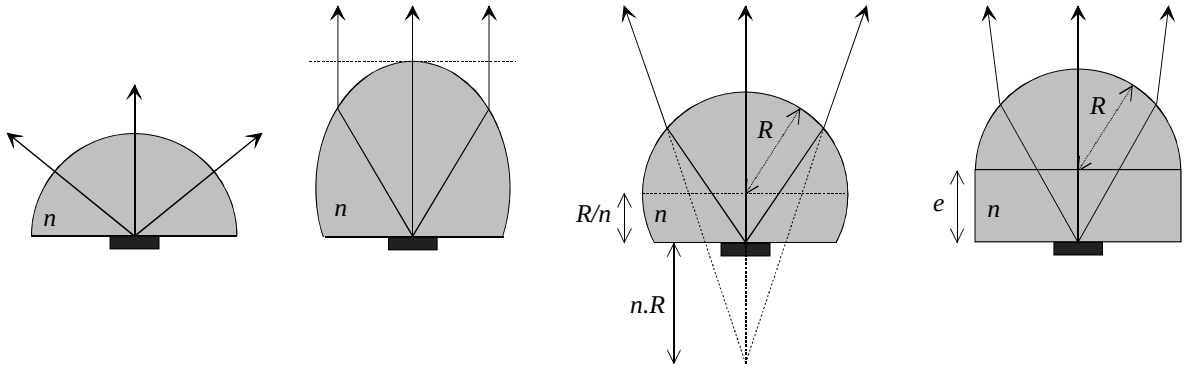

(a) *- Hemisphere* ***(b)*** *- Ellipse* ***(c)*** *– Hyper-hemisphere* ***(d)*** *– Extended Hemisphere*

figure 2.17. Usual configuration of subtract lenses (index $n = \sqrt{\varepsilon_r}$)

In practice, it's preferable to use other configurations in order to improve the antenna's directivity.

- *Elliptical Lens* (***figure 2.17-b***) : The primary source is placed in the second focus of the ellipse : The emitted rays form a beam of parallel rays in the output. The system works in the diffraction limit [70]. These lenses are excited by log-periodical antennas [69], dipole [70], double dipole [71] or double source [72]. The difference between these configurations concerns the secondary lobe level and the cross polarization. The gaussian coupling performance is about 80% [73].
- *Hyper-hemispherical Lens* (***figure 2.17-c***): It's a dielectrical sphere with radius *R* and index *n* cut along a plane placed from its centre a distance *e = R/n* [73]. This lens satisfies the Abbe's sinus condition, so the coma aberrations are annulated. These structures have lower directivity than the elliptical ones. It can be increased adding a thin lens [73-75] (***figures 2.6*** and ***2.18***). For the lenses antennas whose patterns are fine (double dipole, double slit, ringed slit, or butterfly antenna), the gaussicity is excellent – over 90% [72,76].

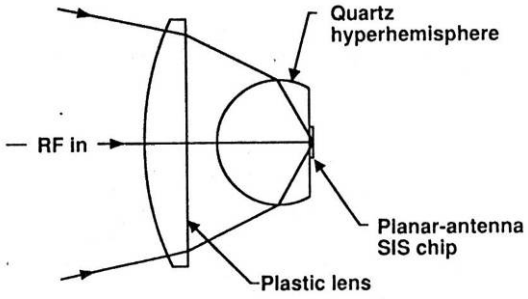

figure 2.18. Hyper-hemispherical subtract lens and planar-convex lens associated to a double slit mixer.

- *Extended Hemispheric Lens* (***figure 2.17-d***): It consists of a dielectric hemisphere (radius *R* and index *n*) connected with a cylindrical section with the same index and with a height *e*. For *e = R/n*, it's similar to the hyper-hemispherical lens (provided

that the lens diameter is bigger than $3\times\lambda_0$ [77]; besides, this approximation is more accurate the higher the material permittivity is [72]). The assembly and fabrication are simplified. This is the most usual configuration, since it allows us to control easily the directivity and the gaussian coupling performance modifying the extension *e* (***figure 2.19***).

The extension *e* varies between *R/n* (cut plane of the hyper-hemispherical lens) and a value that makes the phase front in the output almost flat. We call it synthesized elliptical lens.

There are several applications , for example : multifunction antennas built on automobile vehicles [77a] ; terminals for maritime communications with bipolarisation by *Ku* band satellite [77b] ; LMDS systems around 30 GHz (linear polarization [75] or circular polarisation [77c]) or 40 GHz [77d,77d-bis], even over the whole *Ka* band [77e, 77f] ; obstacle detector radars [77g, 85] ; millimetrical instrumentation [78] and terahertz [77h, 77i] ; millimetrical and submillimetrical receptors [63,67-74,76,77j,77k,77l,77m,77n].

Several kind of primary sources have been used : coplanar double slit [72,76,78-80] ; rectangular slit [81] ; ringed slit [77j,77k,82] ; log-periodical antenna [77m,77n] ; logarithmical spire [77l] ; butterfly antenna[77j,77k,82] ; printed patch (or network) with excitation : (*i*) coaxial probe [83,84], (*ii*) electromagnetic coupling [77b,77d] or (*iii*) fed by linear slit (two layers version [85,86] or three layers version [77f]) or cross slit [77c] ; planar antennas with longitudinal radiation [87].

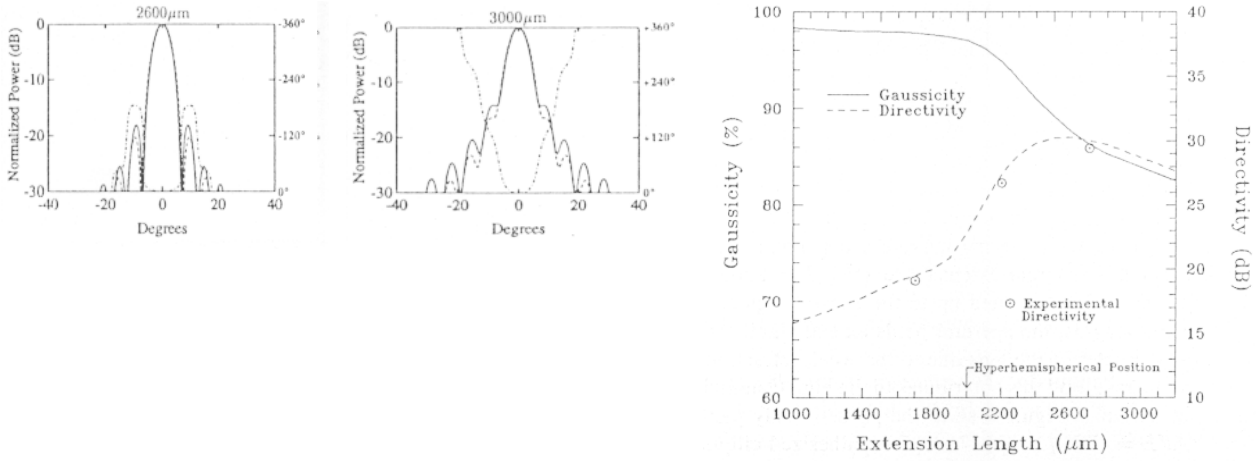

figure 2.19. (1) Radiation patterns for four e values (1600 µm, 2200 µm, 2600 µm et 3000 µm). (2) Directivity and gaussicity depending on the extension e [72] (extended hyper-hemispherical lens in silicon(R = 6,85 mm ; n = 3,42) – double slit antenna)

Depending on the considered applications, the subtract lenses gain varies between 10 dB and 35 dB. It mainly depends on the lens diameter and its extension. Usually, when the diameter is over $5\times\lambda_0$, the most directive configuration is the synthesized ellipse [72]. For smaller diameters, the maximum directivity is obtained with specific extensions whose value depends on the diameter and the permittivity [77, 77-gael]. Super-directive configurations have also been described [77-gael].

The bandwidth of these antennas have not been studied thoroughly since it's not a strong constrain beyond 100 GHz. For frequencies between 15 GHz and 60 GHz the values found in the literature are usually within the interval 3%~10% [77a, 77-gael, 77d] and 40% [77f]. The rise of band is obtained using a broadband primary source.

In order to support the subtract lenses radiation, we can use high permittivity materials (Si, aluminium, MgO). Besides the reduction of the radiating elements size, this solution has other drawback, which is the losses increase caused by the reflection in the interface lens/air. The multiple reflections modify meaningfully the radiation performance: it rises the secondary lobe level, the cross component [77c,88,89] the rear radiation level, and there is a reduction in the pass band. In the same way, the primary source's input impedance can be relatively perturbed, specially in hyper-hemispherical or elliptical configurations [89,90,91]. Similar phenomenon have been observed in small size lenses [77,77-gael]. In addition, usually an additional anti-reflection treatment is considered to be necessary when $\varepsilon_r > 4$.

For smaller permittivity (Teflon, Rexolite, quartz, polymehyl-pentene, polystyrene, polyethylene), the rear radiation rises. It can be strongly reduced using a simple reflector plane, a cavity [77j,77k], or a ground plane which separates the radiating elements and the circuits, as most of the printed primary sources (***figures 2.20*** et ***2.21***).

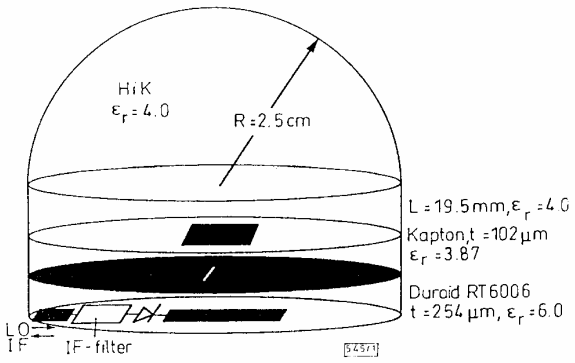

figure 2.20. Extended hyper-hemispherical lens excited by a patch fed by slit [85] (30,4 dB at 70 GHz - Cross component = -26 dB - Ratio F/B = 50 dB)

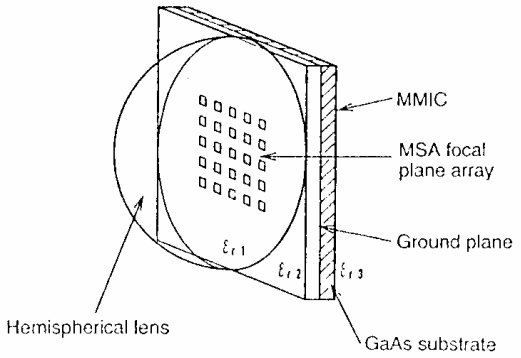

figure 2.21. Patch network fed by slit coupled to an hemispherical lens [93] (9.8 dB at 52 GHz – Cross component = -20 dB)

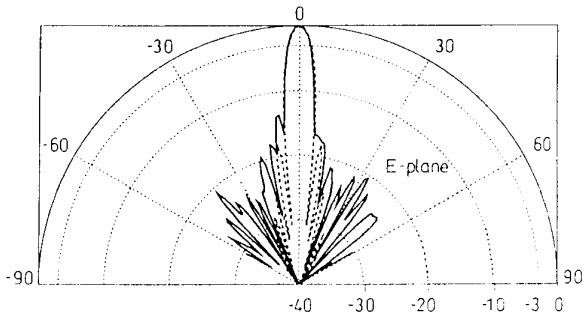

figure 2.22. Radiation pattern (E plane) of the antenna in **figure 2.20**

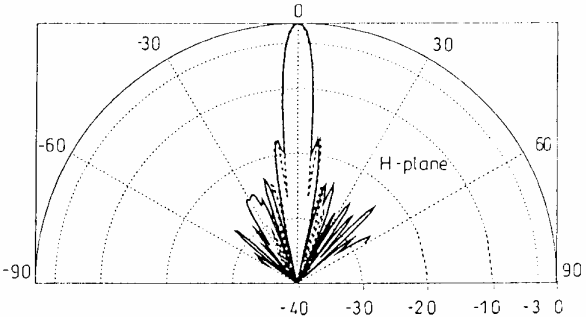

figure 2.23. Radiation pattern (H plane) of the antenna in **figure 2.20**

We can design multi-beam antennas (commuting the decentred sources [94]) feeding the subtract lens with a network (with hexagonal meshing) of printed patches network with circular polarization [77c]. ***figure 2.24*** shows the working principle. The experimental results obtained are represented in ***figure 2.25*** for a sweeping of ±20°.

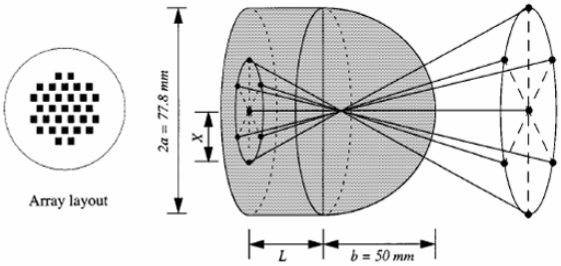

figure 2.24. Lens antenna excited by printed patches network at 30 GHz [77c]

The authors state that the directivity reduction due to multiple reflections is lower than 1.8 dB. The measured isolation between sources and the gain fall are respectively under –26 dB and –1.5 dB on the whole frequency band (28-32 GHz). The axial ratio does not overrun 2 dB at 30.4 GHz, regardless of the chosen patch in the hexagonal network.

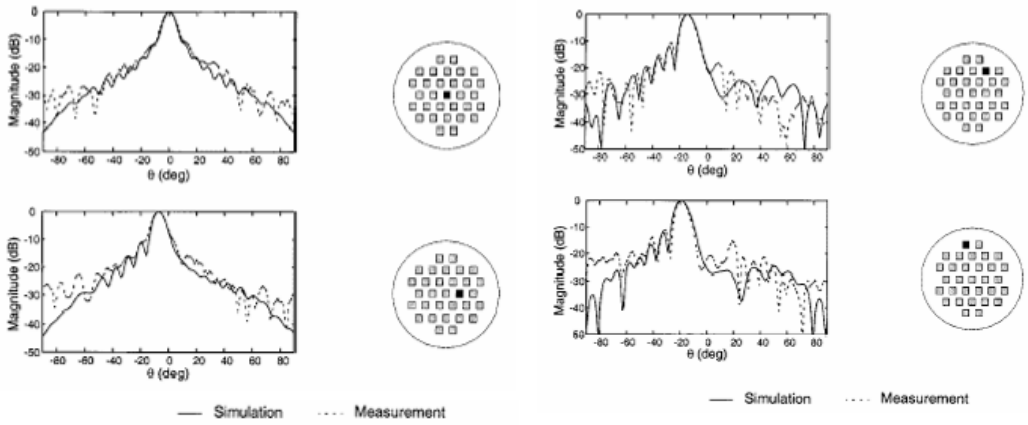

figure 2.25. Theoretical and experimental radiation patterns and for different positions of the fed source [77c]. The antenna geometry is represented in **figure 2.23**.

Finally, most of the subtract lenses we have described have a diameter D relatively big compared to the working wave-guide ($D >> 5\times\lambda_0$). However, some authors have studied the theoretical characteristics of the small size devices ($0.5\times\lambda_0 < D < 5\times\lambda_0$) by asymptotical [95,96], analytic [97] or purely numeric methods [77-gael]. Some realizations have also been proposed in *Ka* band ($D\approx4.5\times\lambda_0$ in [97b]) and *Q* band ($D\approx4.6\times\lambda_0$ in [86]).

Chapter 3: Methodology

In this study, a deep analysis of the radiation in the subtract lens is being carried out. In order to make it, a simulation environment is necessary. There is a flow in the work: first, the design of the structure and the definition of its parameters (permittivity, losses) as well as the simulation parameters; second, the numeric calculations involved in the simulation, which will be run by a super-computer; and third, the interpretation of the results obtained.

This chapter contains an overview of the different steps involved in this process, and the description of its concepts.

3.1 Extended Hemispherical Lens

This is the mains structure used in the project, its fundaments have been previously explained in section **2.3**, here we will state the way we are going to implement it in the simulations and the general nomenclature. The following figure is a view of an extended hemispherical lens fed by a waveguide:

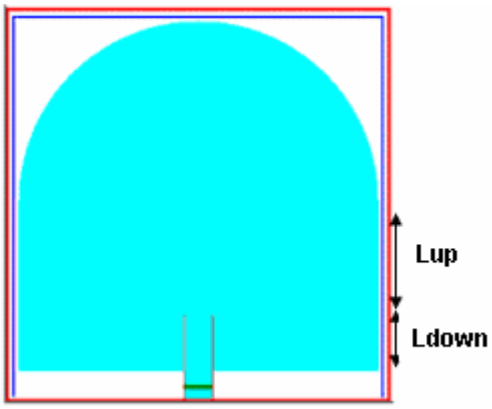

figure 3.1. Extended Hemispherical Lens with Waveguide Source

The radius of the lens will always be referred to the working wavelength (for example, $D=6\cdot\lambda_0$). When we use a waveguide, the central frequency used will be 60GHz (that means a λ_0=5mm). If we use a printed patch, this wavelength may change depending on the dielectric of the source.

The extension is represented by two variables, *Lup* and *Ldown*, as we can see in ***figure 3.1***. *Lup* is the extension above the mouth of the waveguide, theoretically it would be the real extension of the lens, while *Ldown* is the one left under it, and it can be necessary in the fabrication to plug properly the lens to the waveguide; it's up to us to find if it has influence on the diagrams. When we have a ground plane, or when we work with a printed source, *Ldown* will always be null.

The extension size is represented with the percentage of the synthesized elliptical lens extension. This lens is a synthesis of the ellipse lens, which has the property of focalising the radiation to the infinite according to the geometrical-optics theory. However, this lens

is not suitable because it does not respect always the geometrical-optics hypothesis. So this ellipse is only a reference, the height of the synthesized ellipse lens have to be the same of the ellipse lens. We can see in the figure how we can measure its dimensions.

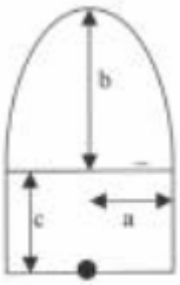

figure 3.2. Ellipse Lens

The variables are:

$$b = \frac{a}{\sqrt{1 - \frac{1}{\varepsilon_r}}} \tag{1}$$

$$c = \frac{b}{\sqrt{\varepsilon_r}} \tag{2}$$

To obtain the extension of the synthesized ellipse, we just consider the total height (c+b) and we subtract the Radius a:

$$L_{100\%} = b + c - a \tag{3}$$

3.2 FDTD

3.2.1 Definition

The FDTD (Finite Difference Time Domain) is a finite differences method in the temporal domain. The electromagnetic fields analysis by FDTD was introduced by Kane Yee in 1966. Yee chose a geometrical relation for the spatial sampling of the vectorial components of the electric and magnetic fields which are represented in the integral and differential form from the Maxwell's equations.

The continuous rising evolution of the computers capacity made FDTD one of the most used methods during the last years, not only for the antennas study but also for the SER problems or the biomedical studies on the cancer treatments. More recently, this numeric

method have been used in the study of the effects of the electromagnetic waves generated by the cellular phones on the human body, and more specifically, on the zone near the antenna: the brain.

This method has important highlights:

- The FDTD is accurate. It describes correctly the physical world.

- The FDTD is supple and easy. It can model antennas with complex geometry or alimentation. It can work along with the SPICE software.

- The FDTD is robust. It can model any kind of material for the electromagnetic technology: conductors, dielectrics, anisotropic medium and non-linear and dispersive materials.

- The FDTD give us the details of the near field around the antenna.

- The FDTD is broad-band. An impulse excitation in the time domain gives a response in frequency, after Fourier transform, over a large spectrum (for an only run FDTD).

3.2.2 Yee Algorithm

In 1966, Kane Yee wrote the curve Maxwell equations as differential equations in time domain. The medium where the electric and magnetic fields lie is decomposed in elemental cells (***figure 3.3***) with a different dimension in each axis: Δx, Δy and Δz.

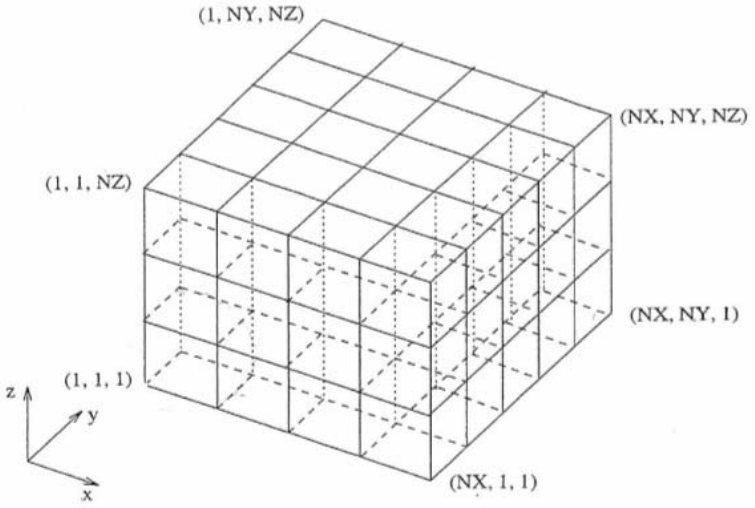

figure 3.3. Elemental cell decomposition

Each of these cells is indexed following the three axes (from 1 to NX along the *x* axis, from 1 to NY along the *y* axis, from 1 to NZ along the *z* axis). So the total calculation volume has NX x NY x NZ cells.

The E_x component of the electric field inside the cell (i,j,k) in the discrete instant t_n (that is, $t_n=n\cdot\Delta t$) is expressed as:

$$E_x(i\Delta x, j\Delta y, k\Delta z, n\Delta t) = E_x^n(i, j, k)\ b = \frac{a}{\sqrt{1-\frac{1}{\varepsilon_r}}} \tag{4}$$

As we can see in ***figure 3.4*** the Yee algorithm centre the components of the E and H fields in the three dimensional space so that each E component is surrounded by 4 circulating components of H, and each H component is surrounded by four circulating components of E.

- This algorithm calculates simultaneously the integral and differential form of the Maxwell equations. It's very useful for specifying the conditions in the field limits and the singularities.

- The differential expressions for the spatial derivatives of the curve operators are centred by default and have a second order accuracy.

- The E and H tangent fields' continuity through the interface is easily carried out because that interface is parallel to one of the axis.

- The E and H components position in the Yee cell and the operations of centred differences force that the Gauss laws are always verified and impose the absence of electric and magnetic charges.

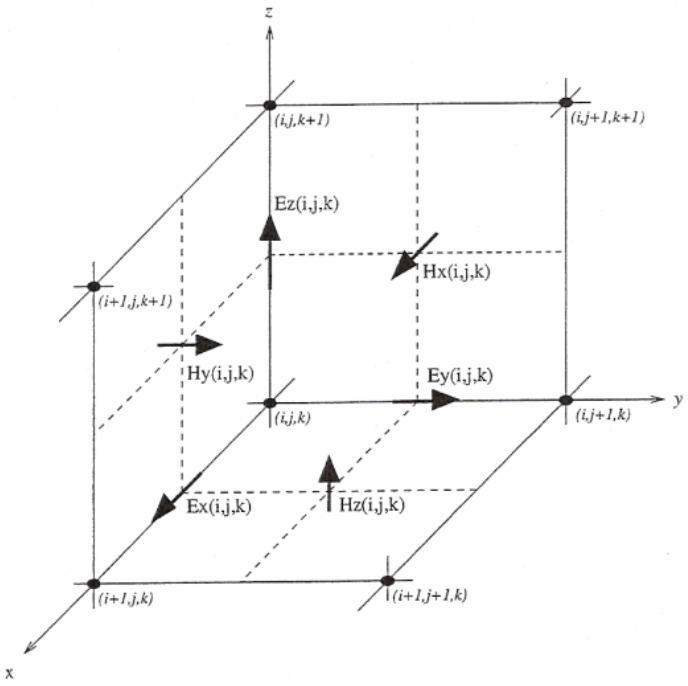

figure 3.4. Yee Cell

The Yee Algorithm also centres the E and H components in time domain: The E components are calculated at the instant $t_n = n\Delta t$, and the H components are calculated at the instant $t_{n+\frac{1}{2}} = \left(n + \frac{1}{2}\right) \cdot \Delta t$.

3.3 The FDTD software

3.3.1 Imelsi

Imelsi (Impulse electromagnetic simulator) is an electromagnetic FDTD simulator developed by the IETR. This simulator allows us to carry out electromagnetic simulations on finite or infinite structures, taking in account (if necessary) the losses and the dispersion in the dielectrics and the metals. The designer contains also the formalisms about localized elements, thin slits and thin threads. We can choose the conditions in the limits (general PML, Floquet conditions, electric or magnetic walls). It's a very versatile simulator that allows us to obtain the adaptation results, the radiation characteristics, the field cartographies in time and frequency domain.

With this software we have optimised the primary sources and we have simulated the associations source – lens. For big electric designs there is an important need of computational resources. The calculations can't be done in PC or work stations. In order to run the simulations, we have used the resources of the calculation centre IDRIS, which lends operational processors with a huge computational capacity and hard-drives and memories in the same scale. The programs can be run on machines NEX-SX5, for example, with performances about 8 GHz for each processor (we can use up to 16 processors, but usually our simulations are made with 8) and a memory of 60 Gbytes. With these processors we can simulate big FDTD volumes and get the results back in some hours.

3.3.2 Lens meshing

Imelsi has a graphic interface that allows us to draw 3D structures quite easily. However, there isn't any function yet to mesh lenses, so software for lens meshing has been developed (in C language), that generates files importable in Imelsi.

This software has been programmed to create elliptical lenses, with a hemispheric extension. We just have to insert the essential data, like the lens centre, the radius, the extension length, and the half-ellipse axis length to obtain the lens files. Once we do this, we can import it in Imelsi and integrate it within the calculation volume.

3.3.3 Far Field

There are two approximations to calculate the far field, the first is temporal, that is, the far field is obtained in the time domain. With the Fourier transform we get the frequencial response in broadband. However, this approximation consumes a lot of memory and computing resources.

This version is not efficient when our analysis is run on a limited number of frequencies. The frequencial approximation is an efficient method in computer time and memory to calculate the radiation patterns when the number of frequencies is limited (up to 10 or 20 frequencies). In our simulations we will use this approximation.

Three stages are obligatory in the far field definition:

1.- Huygens surface definition

2.- Stockage: frequencial in our case, we have to choose the studied frequencies.

3.- Definition of the planes where the far field is calculated.

The user has to specify the number, shape, size and position of the Huygens surfaces. The Huygens surfaces have to surround completely the radiating structure. If this is not possible because there is an infinite ground plane or subtract we will have to set the surfaces so that they can receive the maximum of radiation without traversing the structure. Besides, the Huygens surfaces have to be the nearest as possible to the structure in order to minimize the computing time, and they can't be in the PML cells.

Normally we will use one only surface when we want to measure the far field of a plane structure (like a subtract patch antenna without lens), and five for a different structure. We will not use 6 surfaces because our designs have always an infinite component (either a ground plane, or a subtract, or a waveguide, etc).

The calculation planes are defined in spherical coordinates. Two kinds of diagrams are available, in 2D and in 3D. We will use the 3D diagrams, so we will have to define the minimum and maximum azimuth and the step of its variation, and the same for the elevation. In our studies we will always define only the superior plane, that is, we will not calculate the rear radiation.

3.3.4 Image

Each time we have a ground plane in the design we will have to apply the image principle. The presence of a ground plane makes necessary the application of the near field transform – far field of the half space. It requires the introduction of a fictitious Huygens surface symmetric to the real one with the ground plane. On this unreal surface there are current sources flowing which generate an electro-magnetic field equivalent to the one reflected by the ground plane. The image principle describes the way of the electric and magnetic currents over the fictitious Huygens surface like in ***Figure 3.5***.

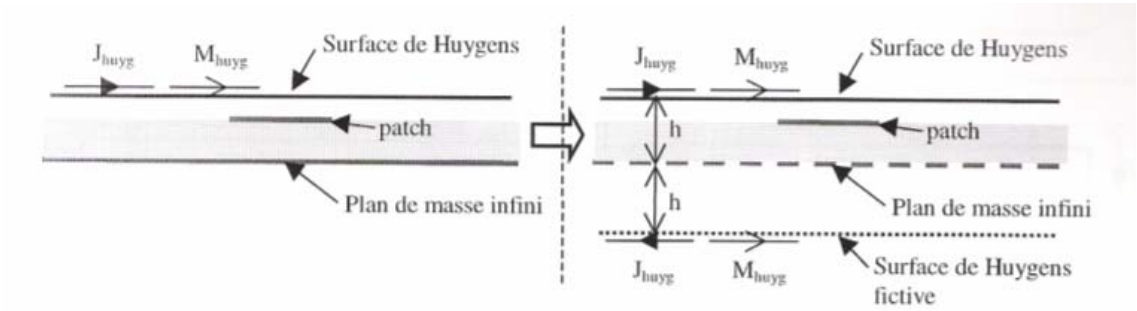

figure 3.5. Image Principle

There are two possible cases:

If the distance h between the Huygens surface and the ground plane is much smaller than the wave length ($h<<\lambda$) the sum of the electric currents in the real Huygens surface and the unreal one is null. We only keep the magnetic current sources of the Huygens surface, which will be doubled (the contribution of the unreal Huygens surface is identical to the real one for the magnetic current). So we don't need the fictitious Huygens surface to calculate the far field.

If h is non negligible compared to the wavelength, then we have to apply rigorously the image principle.

In our study, we will use the fist approximation when we want to measure the far field of source with a ground plane (i.e. a waveguide with a ground plane or a patch source). In this case, we will place an only Huygens surface near to the radiating surface. For other more complex configurations, like a lens, we will have to use five Huygens surfaces, and the rigorous method.

3.3.5 Excitation

All the designs, either fed by a waveguide or a printed patch, are excited with a sine-gaussian signal. The mathematic expression of this signal is the following one:

$$e(t) = A_0 \cdot \sin(2\pi f_0 t + \varphi_0) e^{\frac{(t-t_0)^2}{T^2}} \tag{5}$$

This impulse is a gaussian centred at the frequency f_0. The parameters t_0 and T are determined by following formulas:

$$T = \sqrt{\ln(Att_{f\max})} / \pi \cdot \Delta f \tag{6}$$

$$t_0 = \ln(Att_0) T \tag{7}$$

$2 \cdot \Delta f$ is the used spectral bandwidth (interval [f0 - Δf, f0 + Δf]), Att_0 is the initial attenuation (at t=0), and Att_{fmax} is the attenuation at the maximum frequency. The following graphs represent a certain sine-gaussian impulse:

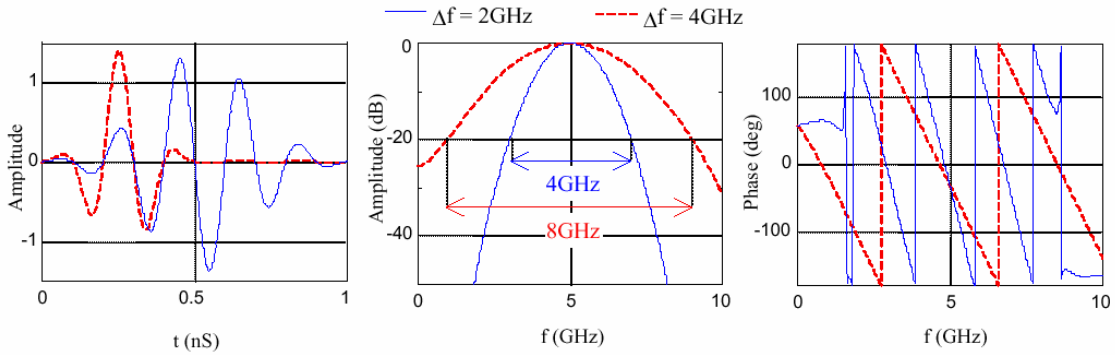

figure 3.6. Temporal and frequencial response of two sine-gaussian impulses, Δt=1.83pS; F_0=5GHz; Att_0=0.01;Att_{fmax}=20dB.

With this kind of excitation, we have a clean impulsion in frequency, its parameters are easy to describe. The frequencial perturbations in the region close to 0 and the maximal one are caused by the almost null level of the signal.

Depending on its parameters, the impulse has a length in iterations. The number of iterations considered in the designs is over 100 times the length of the impulse, so all the reflections can be considered properly.

Chapter 4: Dielectric Lenses Parameter Study

4.1 Introduction

This is the first chapter of the study where we will use the results obtained in the simulations. Within my whole work, this can be considered mainly a first contact with the lens design and simulation.

We are going to work with extended hemispherical lenses (see section **2.3** and ***figure 2.16d***) fed by a waveguide (described in **4.2**), the objective of this section is to have a general scope of the behaviour of this radiating structure and the influence of the most important design patterns in radiation characteristics. The description of these parameters is in section **4.3.**

We are working with FDTD cells sized 0.1mm, and our excitation is a sine-gaussian signal. The excitation parameters are showed here:

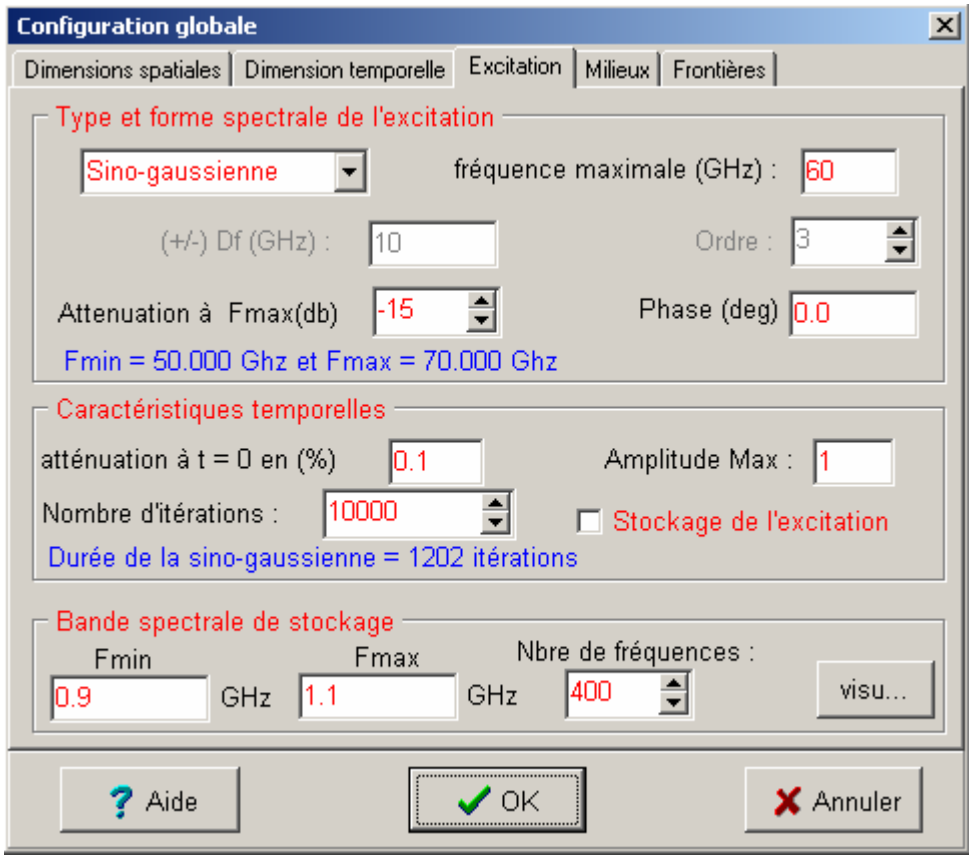

figure 4.1. Excitation configuration in Imelsi

To obtain the far field measures, we place five Huygens surfaces enclosing the design (these are the blue lines in ***figure 4.2***). We will simulate three frequencies, 55, 60 and 65 GHz.

4.2 Waveguide behaviour

The dimension of the waveguide will be of 2.0x2.0mm for all the simulations. The length of the waveguide is 71 cells (that is, 7.1mm), and the current sources are placed in the beginning Z=10, pointing at +X.

The first measurement will be taken only with the waveguide, that is, the source. The waveguide is filled with Teflon:

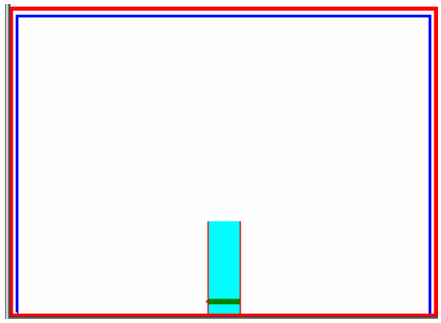

figure 4.2. Waveguide filled with Teflon, dimensions: 2.0x2.0mm

FDTD Dimensions:

Nº x cells	Nº y cells	Nº z cells
314	**314**	**226**

Directivity:

Frequency	55 GHz	60 GHz	65 GHz
Do (dB)	6.87	6.95	7.29

table 4.1: Directivity and FDTD Dimensions of a Waveguide filled with Teflón

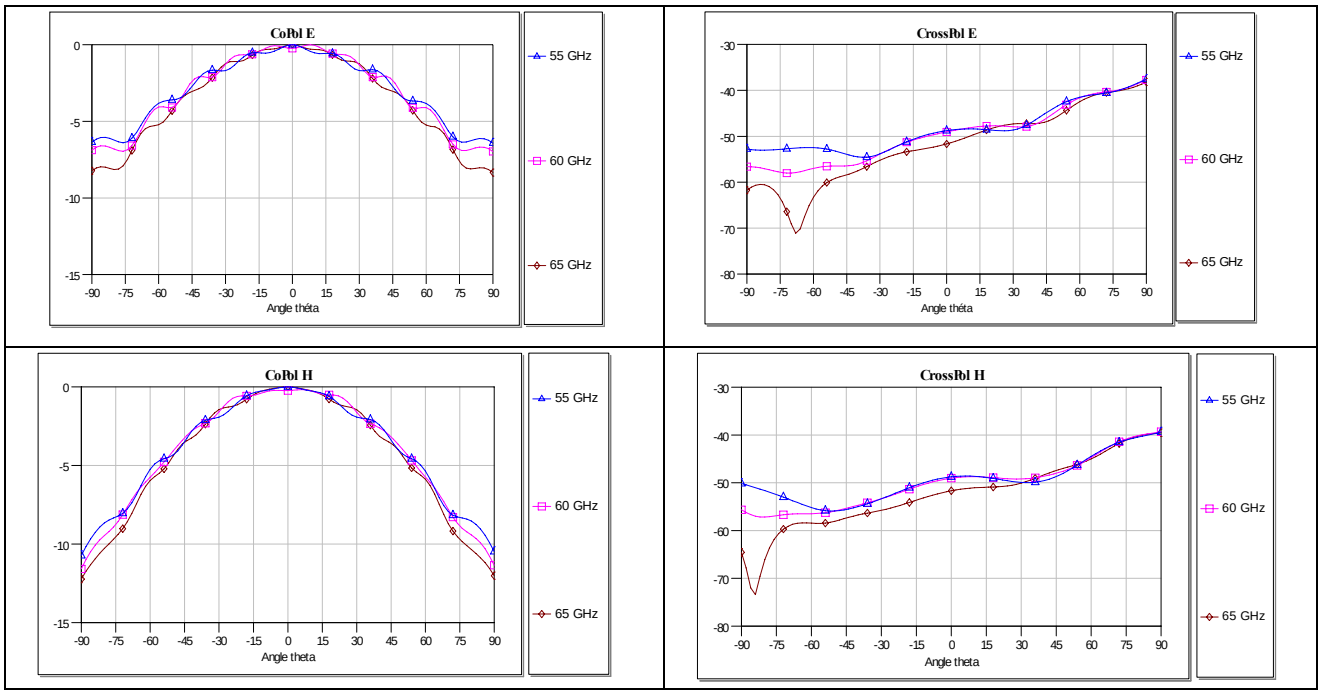

figure 4.3. Waveguide filled with Teflon – Diagrams (Co-Polarization and Cross-Polarization in both E and H plane)

The radiation of the waveguide is, as expected, conformed by a very wide lobe with some perturbations caused by the reflections in the interface Teflon-air. It has a very low directivity, as well as a barely null cross-polarization. Adding a subtract lens we basically try to get a radiation pattern much more directive.

4.3 Lenses Design

Now we will put the lens on the source. An extended hemispherical lens fed by the previous waveguide will be used. The configuration is showed here:

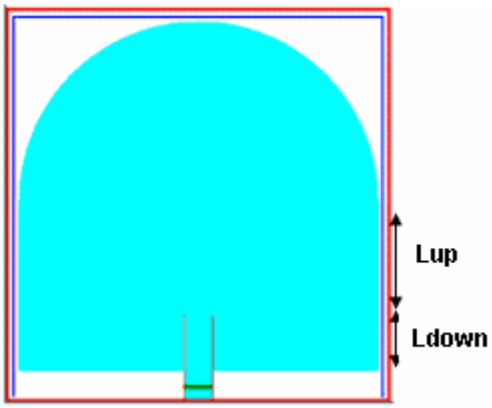

figure 4.4. Lens Antenna with Waveguide Source

In order to check the influence of each parameter in the radiation patterns of these sets, we are going to make several sweeps, involving the extensions, the diameter, and the electrical permittivity.

a. Extensión: This parameter involves two variables, *Lup* and *Ldown*, which are represented in ***figure 4.4***. *Lup* is the extension above the mouth of the waveguide, theoretically it would be the real extension of the lens, while *Ldown* is the one left under it, and it can be necessary in the fabrication; it's up to us to find if it has influence on the diagrams. We will make a sweep of *Lup* (0%-150%), for several values of *Ldown* (0%-100%). We will start with a diameter of $6\lambda_0$ and a relative permittivity of 2.2.

b. Diameter: We will sweep the diameter of the lenses. We will make simulations with values of $6\lambda_0$, $3\lambda_0$ and λ_0.

c. Electrical Permittivity: We will make simulations with:
Teflon: ε_r=2.2; tgδ=0
Quartz: ε_r=3.8; tgδ=0

With the software Imelsi we have run lots of simulations sweeping the specified parameters. The simulations have been configured as in section **4.1**. In the following sections we are going to show a comparative of the radiation patterns and performance parameters we want to measure.

4.4 Extension Influence

First we are going to check the results for the extension sweep with a diameter of $6\lambda_0$ and made of Teflon. We can compare the maximum directivities of each lens with the following graphics. We will draw a different line for each *Ldown*, with *Lup* as abscises:

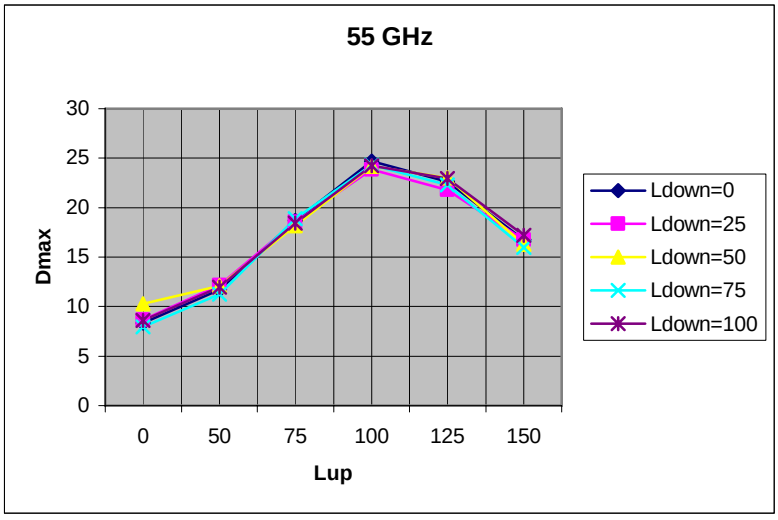

figure 4.5. Maximum Directivities in dB. Lens diameter $6\lambda_0$, Teflon, 55GHz

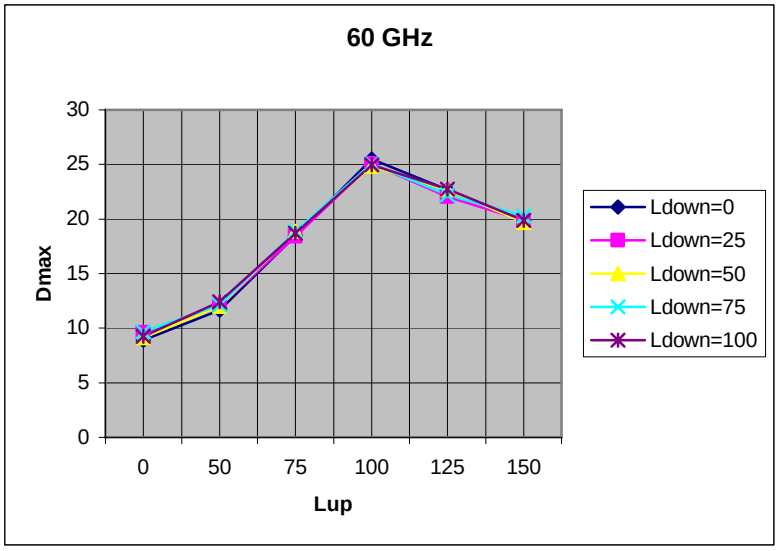

figure 4.6. Maximum Directivities in dB. Lens diameter $6\lambda_0$, Teflon, 60GHz

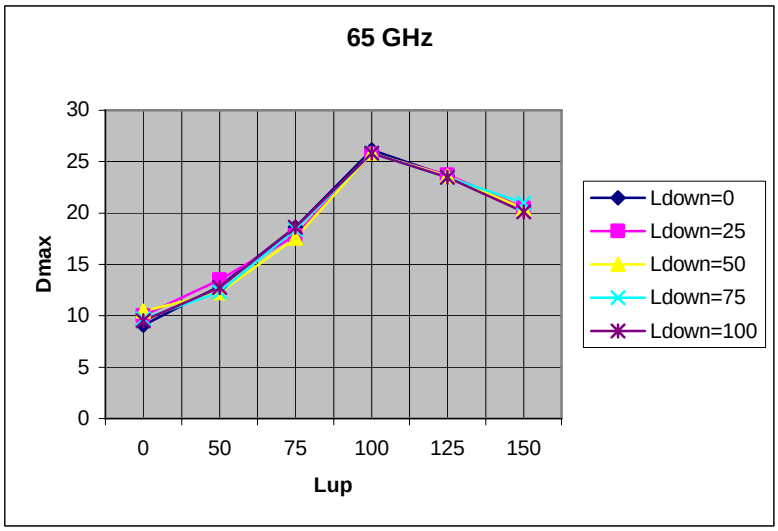

figure 4.7. Maximum Directivities in dB. Lens diameter $6\lambda_0$, Teflon, 65GHz

With these results we can notice that the configuration with the best directivity is always the one with *Lup*=100% (that is, the synthesized ellipse). It rises from 0% to 100% in a convex line, from the hemispherical configuration it start's falling softly. We can study further the influence of *Lup* in the next graph:

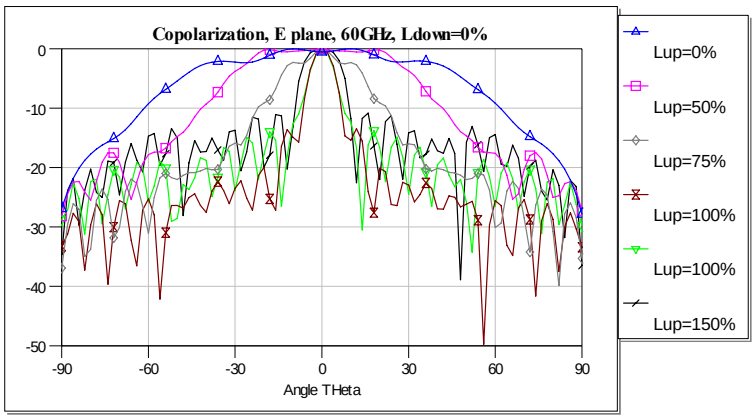

figure 4.8. Copolarization E plane, Ldown=0%, diameter $6\lambda_0$, teflon,, 60 GHz

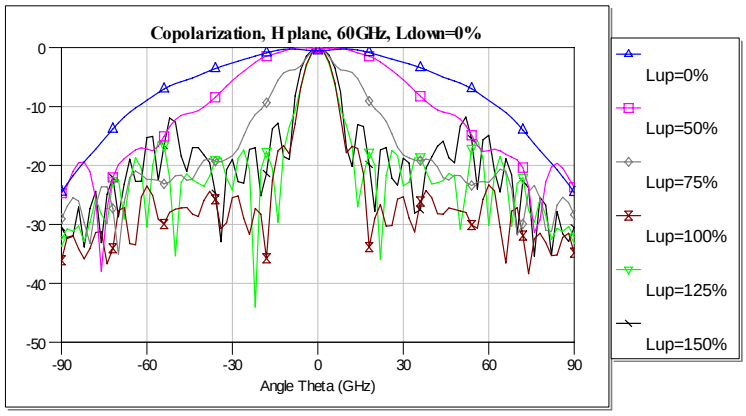

figure 4.9. Copolarization H plane, Ldown=0%, diameter $6\lambda_0$, teflon,, 60 GHz

We can see that with higher than *Lup*=100% values, though not having a big directivity reduction, the secondary lobe level rises around 5dB with *Lup*=125%, and 10dB with *Lup*=150%. With lower values the main lobe is wider but the radiation pattern is hardly directive. So, the synthesized hemispherical lens is the configuration with the better performance in Teflon.

The *Ldown* parameter in this configuration is far from being a critic factor; the variation of the directivity is very low for any frequency (as we can check in **figures 4.10** and **4.11**), we can't find any useful pattern for further design.

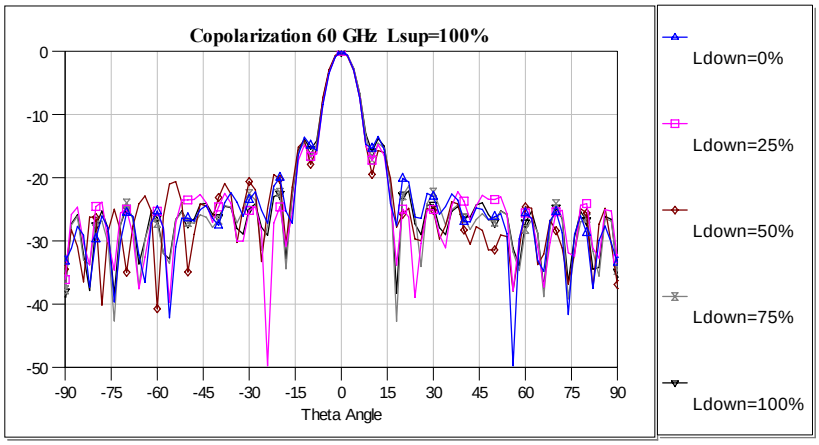

figure 4.10. Copolarization E plane, Lup=100%, diameter $6\lambda_0$, teflon,, 60 GHz

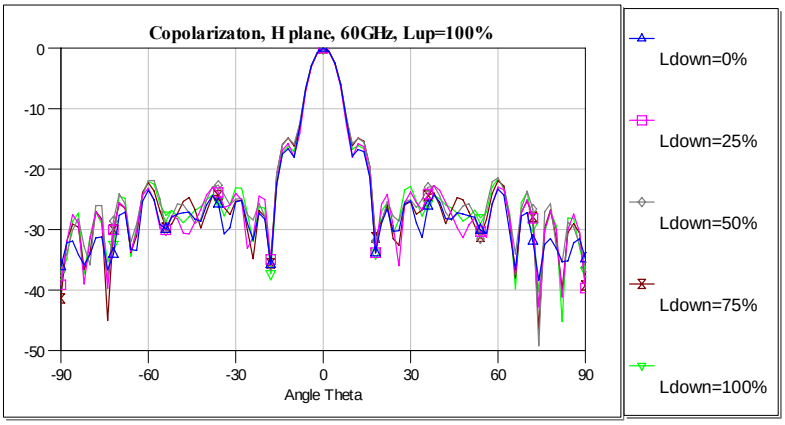

figure 4.11. Copolarization H plane, Lup=100%, diameter $6\lambda_0$, teflon,, 60 GHz

Here, we can see that the main lobe is almost the same with all the values of *Ldown*. Out of the main lobe, the graphs are more homogenic with high values of *Ldown*, but being 20 dB under the main lobe directivity makes that difference worthless.

Making the *Ldown* sweep with all the diameters and permittivity will raise dramatically the number of simulations. We will check the influence of this parameter just in one diameter on each permittivity. Now we repeat the experience with the quartz lens, for computation reasons, the simulations for all the *Ldown* values are only made with the $3\lambda_0$ diameter. We will draw the same graphs we did for the first configuration:

For Quartz:

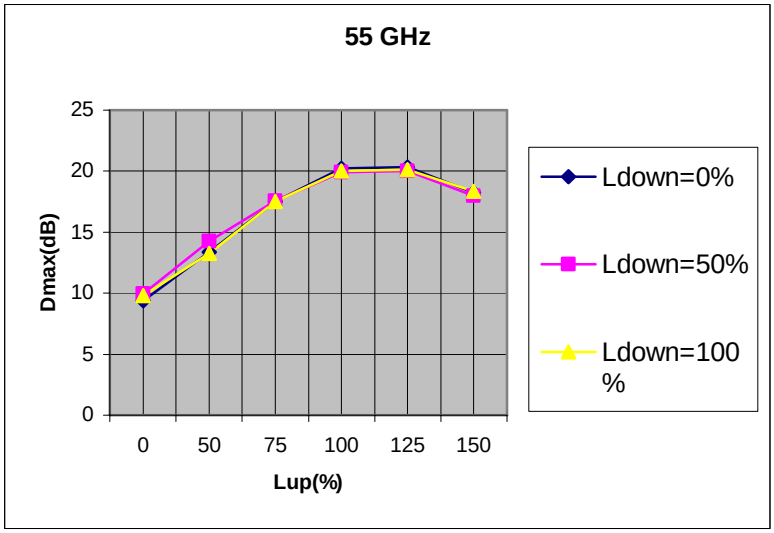

figure 4.12. Maximum Directivities. Lens diameter $3\lambda_0$, quartz, 55GHz

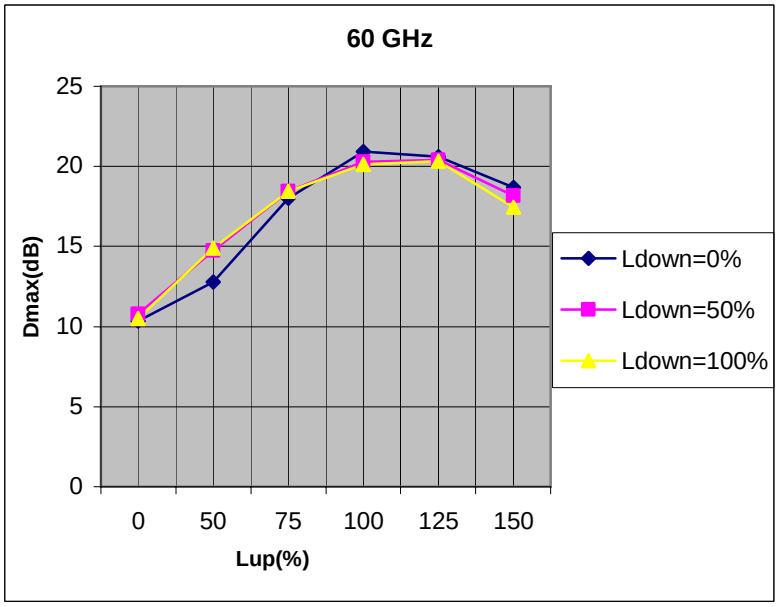

figure 4.13. Maximum Directivities. Lens diameter $3\lambda_0$, quartz, 60GHz

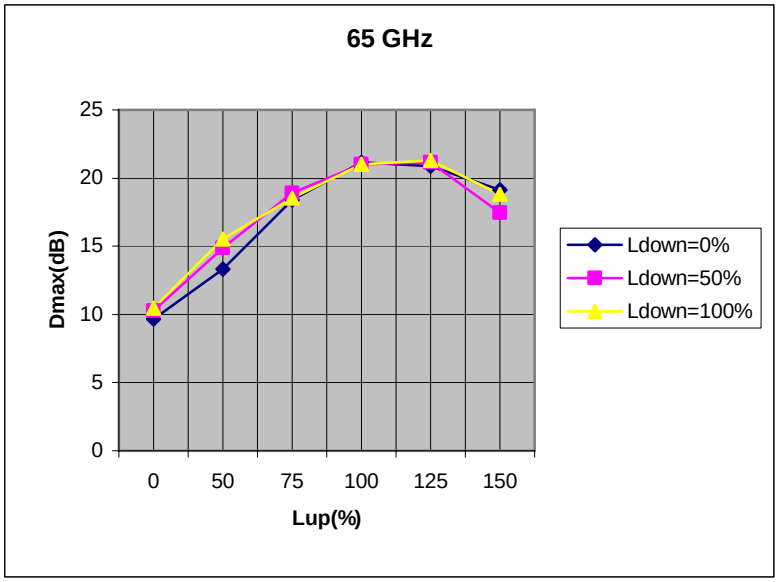

figure 4.14. Maximum Directivities. Lens diameter $3\lambda_0$, quartz, 65GHz

Here we get the maximum directivity for values of *Lup* between 100% and 125%, so we will have to check the radiation pattern to choose one of these extensions. The rise from the lower extension is not as fast as in Teflon, and the maximum directivity is around 21dB, being in the previous configurations around 25dB. This parameter suffers little changes with *Ldown*, depending on the frequency, though these variations are not really important.

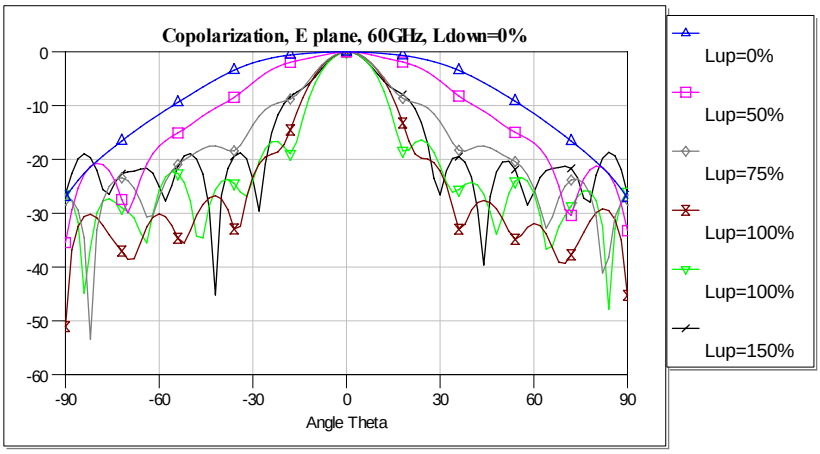

figure 4.15. Copolarization E plane, Ldown=0%, diameter $3\lambda_0$, quartz,, 60 GHz

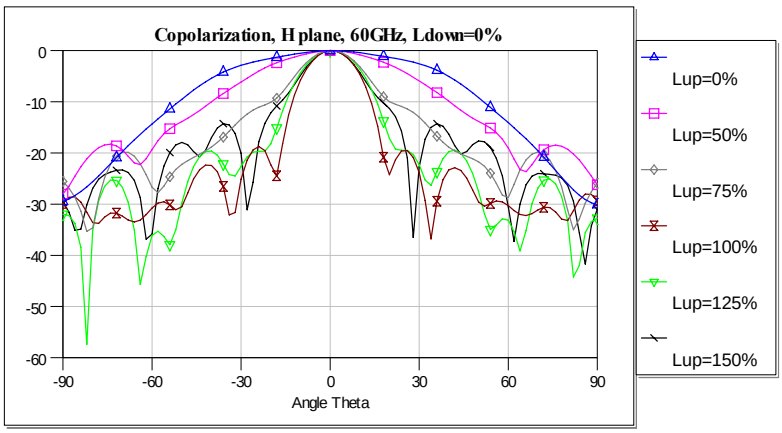

figure 4.16. Copolarization H plane, Ldown=0%, diameter $3\lambda_0$, quartz,, 60 GHz

Watching the radiating patterns more carefully, we find that the behaviour is better with an upper extension of 100%. Though with 125% we get the same directivity, it has a wider lobe and the side radiation is slightly worse. So the synthesized hemispherical lens is also the configuration with a better performance in quartz.

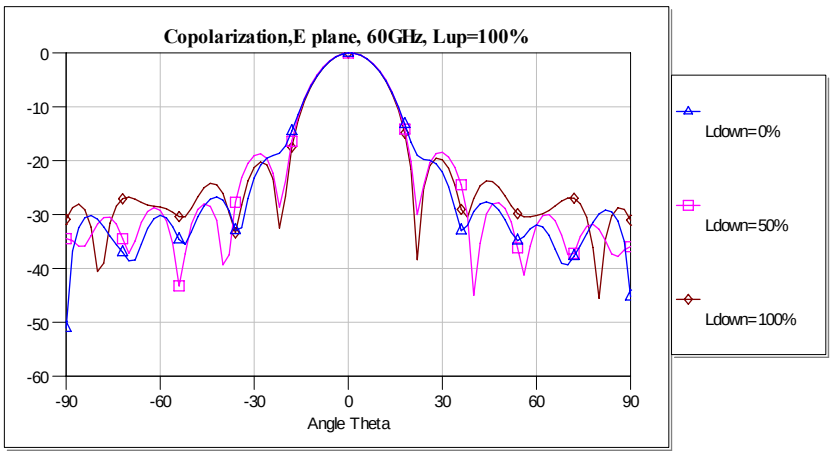

figure 4.17. Copolarization E plane, Lup=100%, diameter $3\lambda_0$, quartz,, 60 GHz

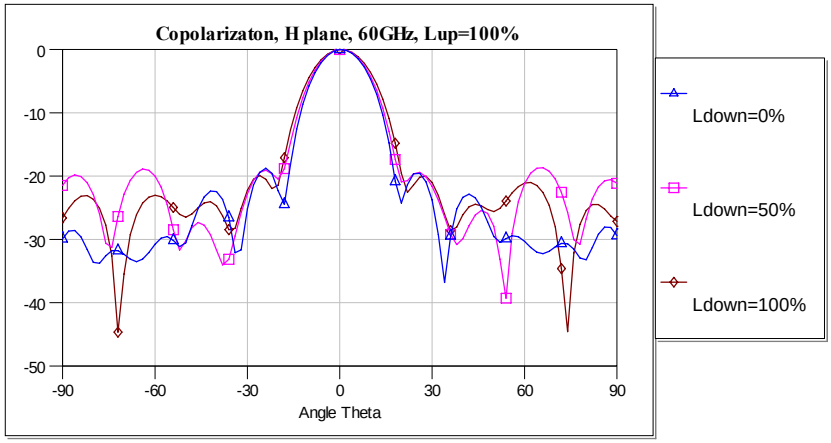

figure 4.18. Copolarization H plane, Lup=100%, diameter $3\lambda_0$, quartz,, 60 GHz

In general, the *Ldown* parameter doesn't make a big difference with quartz, but its influence is not as low as in Teflon lenses, and may be taken into account. We check that in silicon lenses, it has a strong dependence on the frequency, and it doesn't follow any pattern we can detect clearly.

4.5 Diameter and Permittivity influence

Now we will check the influence of the lens diameter, comparing the evolution of the directivity in every medium:

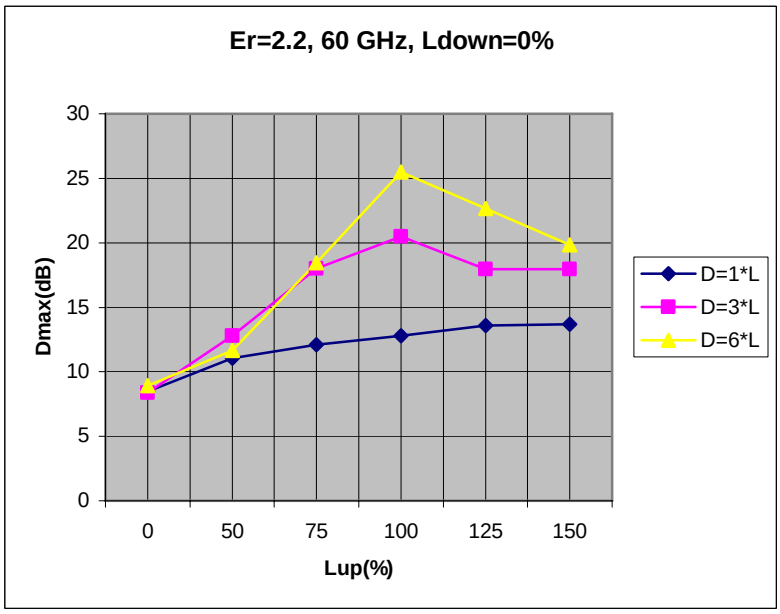

figure 4.19. Maximum Directivities. Ldown=0%, teffon, 60GHz

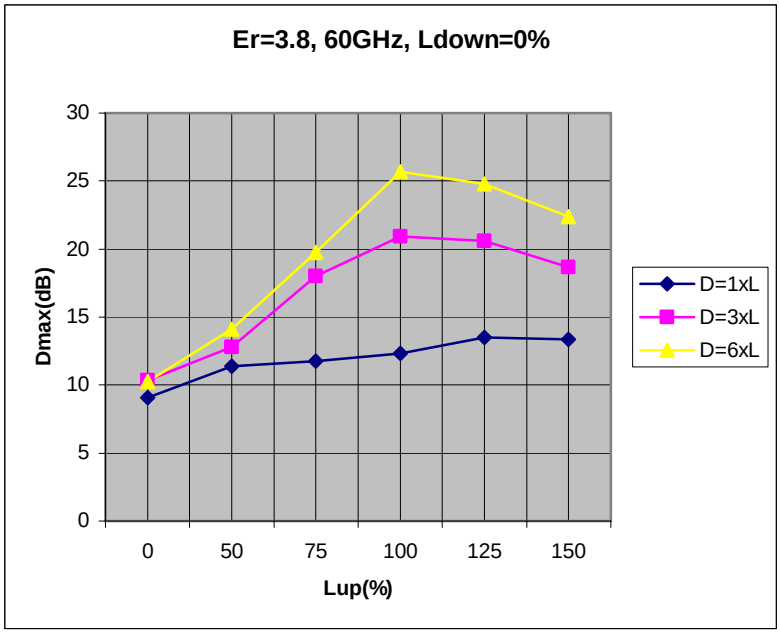

figure 4.20. Maximum Directivities. Ldown=0%, quartz, 60GHz

As expected, the biggest the diameter is, the highest will be the directivity. The variation with the upper extension of this parameter is similar for $3 \cdot \lambda_0$ and $6 \cdot \lambda_0$, as we saw in the previous section, it increases until it arrives at 100%, when it starts falling. With $6 \cdot \lambda_0$, this change is more abrupt than with the intermediate diameter. With a diamteter of λ_0 the directivity is much lower, and it has a very little rise, reaching the maximum in 125%. So the λ_0 diameter is not suitable for high directive specifications with these dielectrics.

Now we will do the same with the medium permittivity:

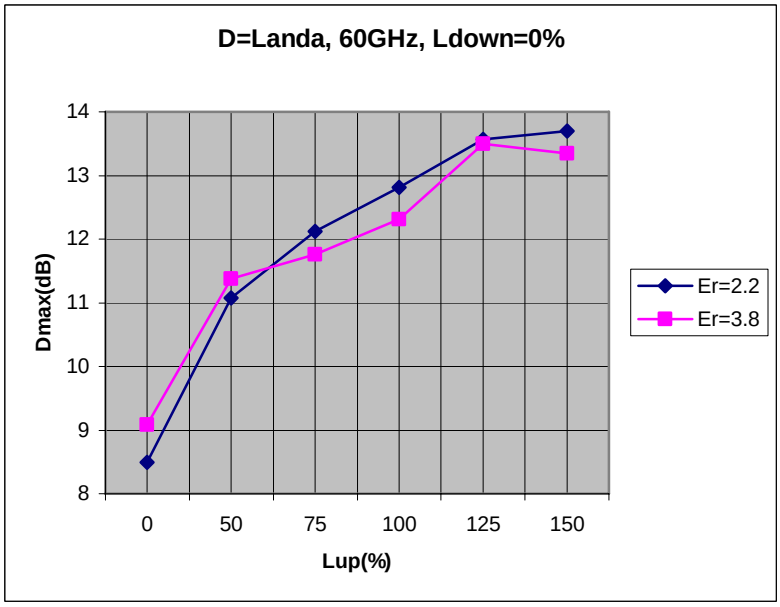

figure 4.21. Maximum Directivities. Ldown=0%, Lens diameter λ_0, 60GHz

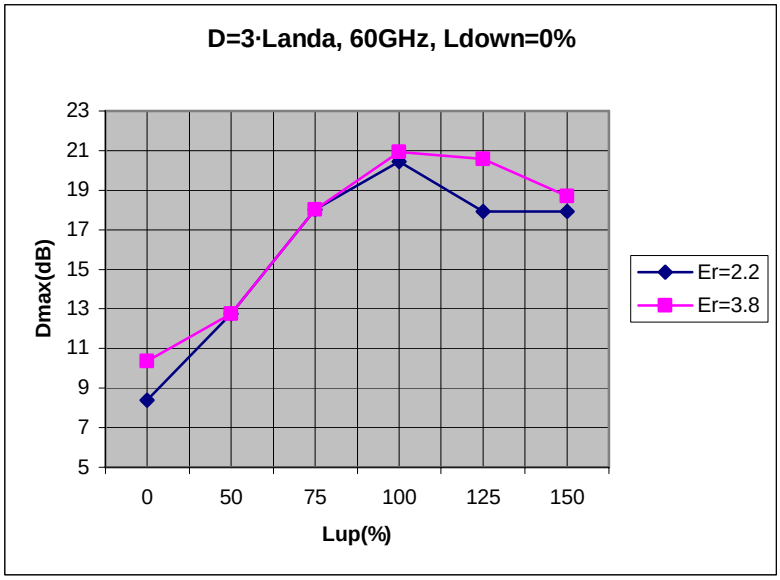

figure 4.22. Maximum Directivities. Ldown=0%, Lens diameter $3\lambda_0$, 60GHz

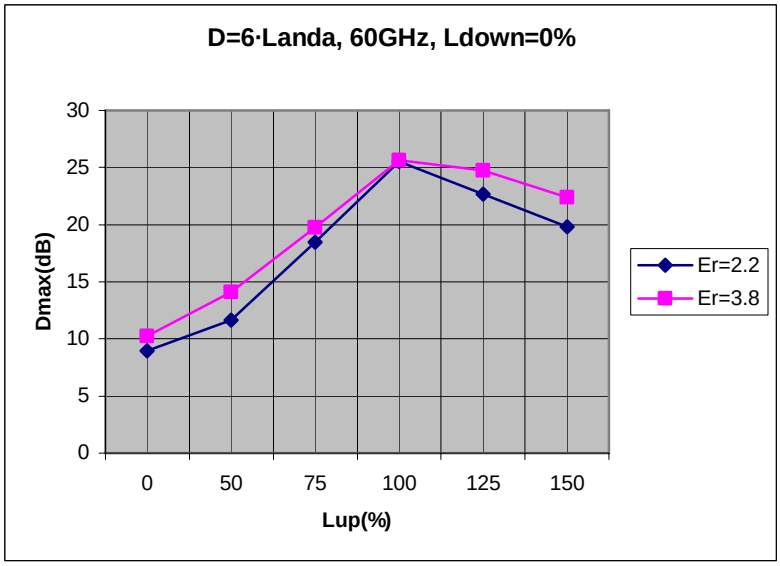

figure 4.23. Maximum Directivities. Ldown=0%, Lens diameter $6\lambda_0$, 60GHz

The behaviour of the lenses directivity is quite similar for both mediums. For upper extensions higher than 100%, the quartz has a better behaviour than Teflon, where the fall is bigger.

For other considerations, we have to compare the radiation diagrams. The most significant results are the ones got with *Lup*=100%, so we will compare these.

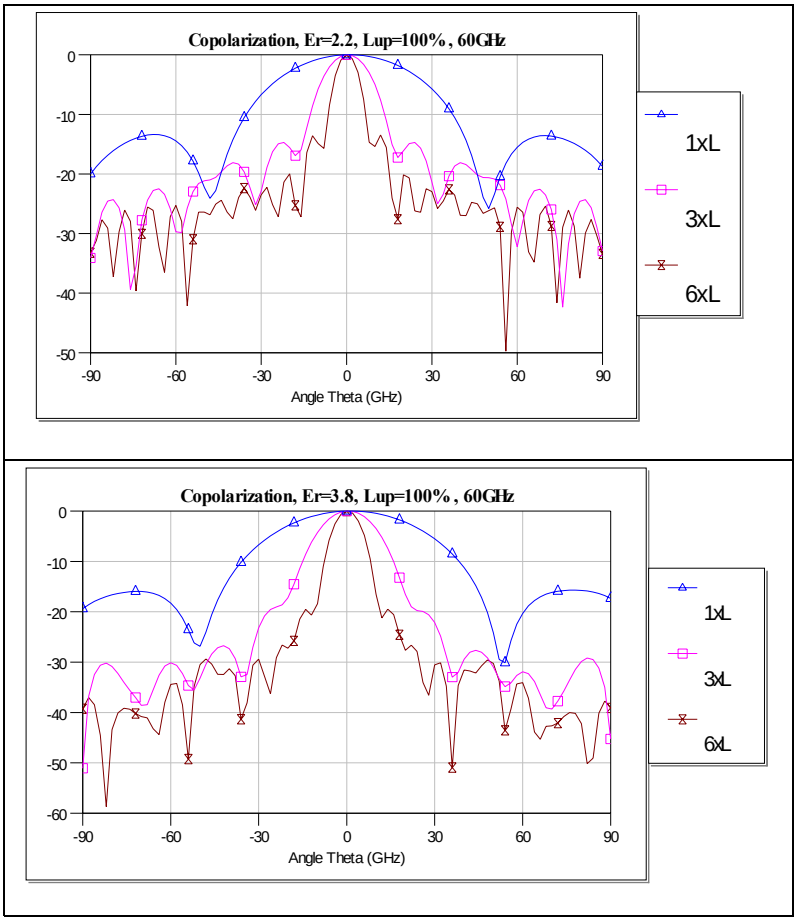

figure 4.24. Copolarization E Field, comparison, Lup=100%, 60GHz

The first thing we notice is the strong dependence of the main lobe width with the diameter of the lens. The bigger the diameter is, the narrowest the lobe is, which implies a directivity rise (as we can see in the previous graphics). Though with $3\lambda_0$ and $6\lambda_0$ the variation is important, with λ_0 it becomes completely different, we get a very simple diagram, just with a big main lobe and two side ones, and we checked in **figure 4.20** that it always has a very low directivity, so we can conclude that with this diameter the desired focalisation is not obtained, at least for the studied permittivities.

About the permittivity we check that with quartz the directivity is bigger than with Teflon. The width of its main lobe is very similar, but the secondary lobes level is higher with Teflon. The most directive design is the quartz one with a diameter of $6\lambda_0$.

4.6 S11

We will also calculate S11 parameter, to measure the reflections caused by the differences of the permittivity between the free space and the lenses.

We will make several parameter sweeps:

Teflon	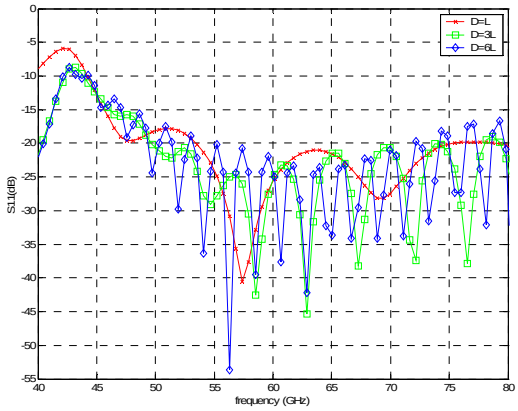
Quartz	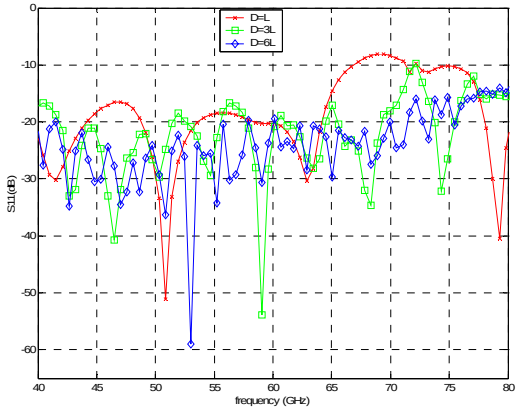

figure 4.25. S11(dB), Lup=100%, Ldown=0%, Diameter Sweep for Teflon and quartz

D= λ_0	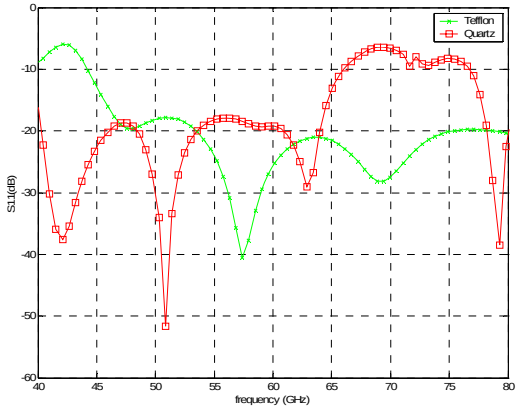
D= 3·λ_0	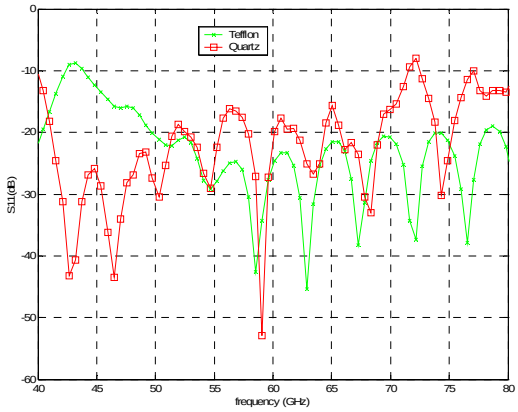
D= 6·λ_0	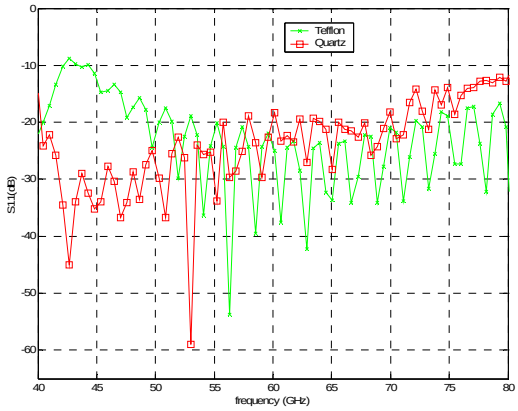

figure 4.26. S11(dB), Lup=100%, Ldown=0%, Permittivity sweep for different diameters

The most evident difference is the periodicity of S11. The bigger the lenses are, the more apart will be the reflections, cause of the physical distance that has to cover the incident and reflected waves, so the period of the reflections will be bigger. In frequency, this means that the period will be smaller. More importantly, the diameter doesn't have an important influence on the S11 level.

With the permittivity the difference is not also very violent, since its values are not so different actually. For diameters of λ_0 and $3\lambda_0$, quartz lenses show a noticeable worse S11 around the central frequency, but for $6\lambda_0$ this difference disappears. In general the

behaviour has similar characteristics with Teflon and quartz lenses, oscillating between -20dB and -10dB.

The lower extension doesn't have an important influence over the S11 parameter, as we can check in the following figures:

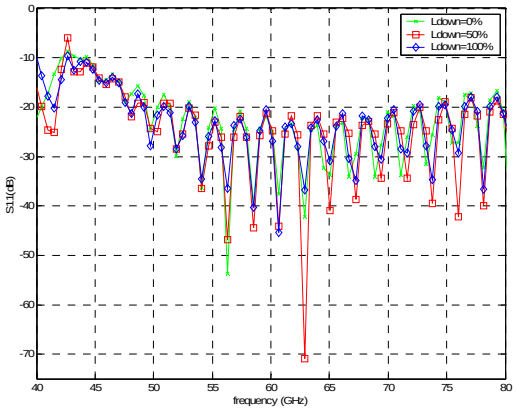

figure 4.27. S11(dB), Teflon, D=6λ_0, Lup=100%

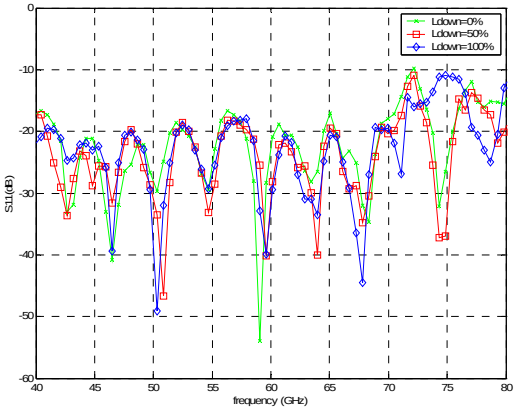

figure 4.28. S11(dB), Quartz, D=3λ_0, Lup=100%

4.7 Conclusions

- In the design of the lens, the upper extension is the most decisive pattern, since is the one that has the biggest influence in the focalisation of the radiated wave. The synthesized ellipse is the configuration that focalise the wave to the infinite, and it is the one with whom we obtain the best results in terms of directivity and secondary lobe level. However, the lower extension, which actually may be more a fabrication necessity than a parameter of design, has proven to have no importance.

- The size of the lens also has influence on the focalisation. With bigger diameters, better directivities can be obtained, despite of the increase in the size and the weight. If we want to reduce its size to permit its use in very exigent application, we have to be careful because with small diameters the lens may not focalise properly. From a diameter of $3 \cdot \lambda_0$ we have always obtained suitable results.

- The permittivity does not have a big influence on the radiation performance compared with the other parameters.

- The S11 keeps its level bellow -10dB with the $3 \cdot \lambda_0$ and $5 \cdot \lambda_0$ diameters. Permittivity and lower extension does not have an important influence on this parameter.

Chapter 5: Extended hemispherical lenses (Eccostock) fed by waveguides

5.1 Introduction

In this chapter we are going to analyse a subtract lens with a higher permittivity. We have chosen the lens used in the IST study [98], the lens diameter will be $6 \cdot \lambda_0$, since we have checked that has a better directivity (section **4.5**). Our objective is to make a deeper study on subtract lenses, since we have a smaller range of parameters to measure and we know that the already chosen are suitable for our .We want to simulate that structure with our methodology, making a similar study as we made in the previous chapter, but adding some deepness now that we are more centred in a particular configuration.

We are going to make a study of the radiation of lenses with some particular parameters already tested in previous studies. The dielectric material we are using is Eccostock, considering it with no losses. To prevent higher modes propagation, we are using a smaller waveguide than in the previous simulations. We will use the same excitation as in previous chapters; we are considering now eleven frequencies in the band between 55 and 65 GHZ.

Eccostock: ε_r=8.8; tgδ=0
Waveguide dimensions: 1.4x1.4mm

The measures we are taking are:

- Maximum Directivities: For each of the eleven frequencies we are considering. It's also calculated the surface efficiency ($\boldsymbol{\eta_s}$) and the direction of maximum directivity in spherical coordinates.

- Radiation Patterns: Co-polarization and cross-polarization of E and H fields, just with the extremes and central frequencies.

- Radiated Power: We will surround the radiating structures with surfaces which will measure the power that is going through them for each frequency. If a surface contains a section of the waveguide, we have to subtract the influence of that section.

Note: $\eta_s = \dfrac{D_0(lin)}{\dfrac{4 \cdot \Pi \cdot S}{\lambda_0^{\,2}}}$

With :

D_0(lin)=Maximum Directivity. Linear (not in dB)

S=Surface=$\dfrac{\Pi \phi^2}{4}$

λ_0=wavelength at working frequency

For the study of the radiated power, it's interesting to obtain the power injected by the waveguide. With this, we can compare the power that has been finally radiated with the power that was available.

To calculate this, we need a waveguide configuration without any loss or reflection. This one will work:

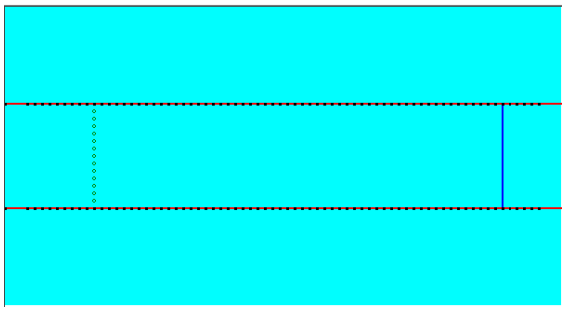

figure 5.1. Waveguide terminated with PML

The green line represents the current sources that feed the waveguide. The blue line represents a surface we will use to measure the power the power that goes through the waveguide. Each of the extremes is terminated with a PML, and we know that the dielectric (Eccostock) has no losses. The obtained power is:

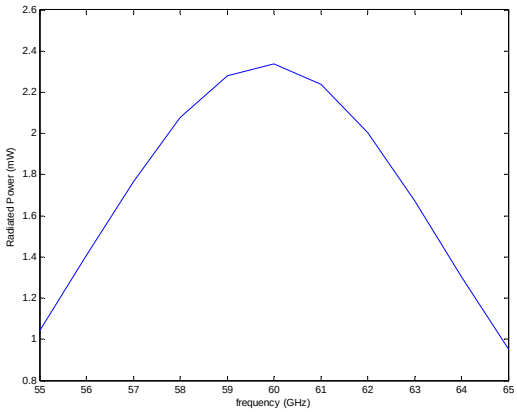

figure 5.2. Power injected by the waveguide in our simulations

The radiated power in frequency has the same shape that the frequential representation of the impulse signal (see *figure **3.6***)

To calculate the power injected in the waveguide we have to make a frequential cartography in the plane represented by the blue line. All the power generated by the waveguide goes through that surface. Once we have measured the electric and magnetic fields, we calculate the vector of Poynting with the vectorial product of the fields. Finally,

to obtain the power that goes through the surface we have to integrate over that surface. The final formula would be the following:

$$P = \int \vec{E} x \vec{H} \cdot d\vec{S} \tag{8}$$

Notice that this operation must be done for each frequency whose power we want to calculate. The result is a scalar for each frequency.

In the *Appendix V* it's the Matlab program that makes this operation.

5.2 Waveguide

First, we study only the waveguide, radiating to the free space. We consider five Huygens surfaces around the guide. These surfaces will be also used to measure the radiated power. The description method of the Huygens surfaces is explained in **section 3.3.3.**

In order to calculate the radiated power, now we need several surfaces to wrap completely the radiating system, and make the cartographies. If we don't have a ground plane in the design, we need six surfaces to do it. The bottom surface will contain also the power inside the guide; we have to erase this when we make the operations. With this we will have the power that goes through each surface. To calculate the total radiated power by the waveguide we just have to sum the power of the six surfaces (obviously a different sum for each frequency).

We want to check also the influence of the position of these surfaces when we measure the radiated power, so we are making also a simulation with the surfaces of the frequential cartography more separated from the waveguide. We should get in both cases the same results. In both **figure 5.3** and **figure 5.7** we can see the disposition of the surfaces we use to calculate the radiated power:

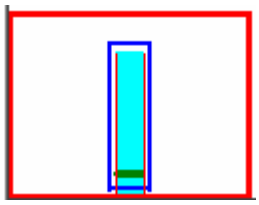

figure 5.3. Waveguide in free space with Huygens surfaces near the guide

Directivity:

Frequency	Dmax (dB)
55 GHz	9.05
56 GHz	9.13
57 GHz	9.22
58 GHz	9.31
59 GHz	9.40
60 GHz	9.49
61 GHz	9.57
62 GHz	9.65
63 GHz	9.73
64 GHz	9.81
65 GHz	9.89

table 5.1: Directivity of a waveguide filled with Eccostock radiating in free space

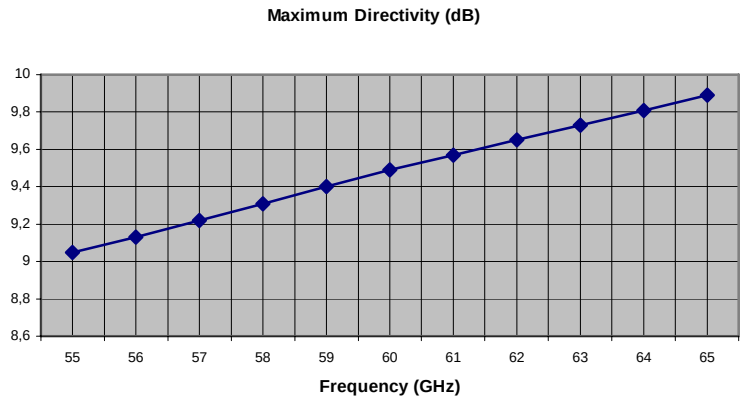

figure 5.4. Maximum directivity in dB for each frequency for Waveguide in free space

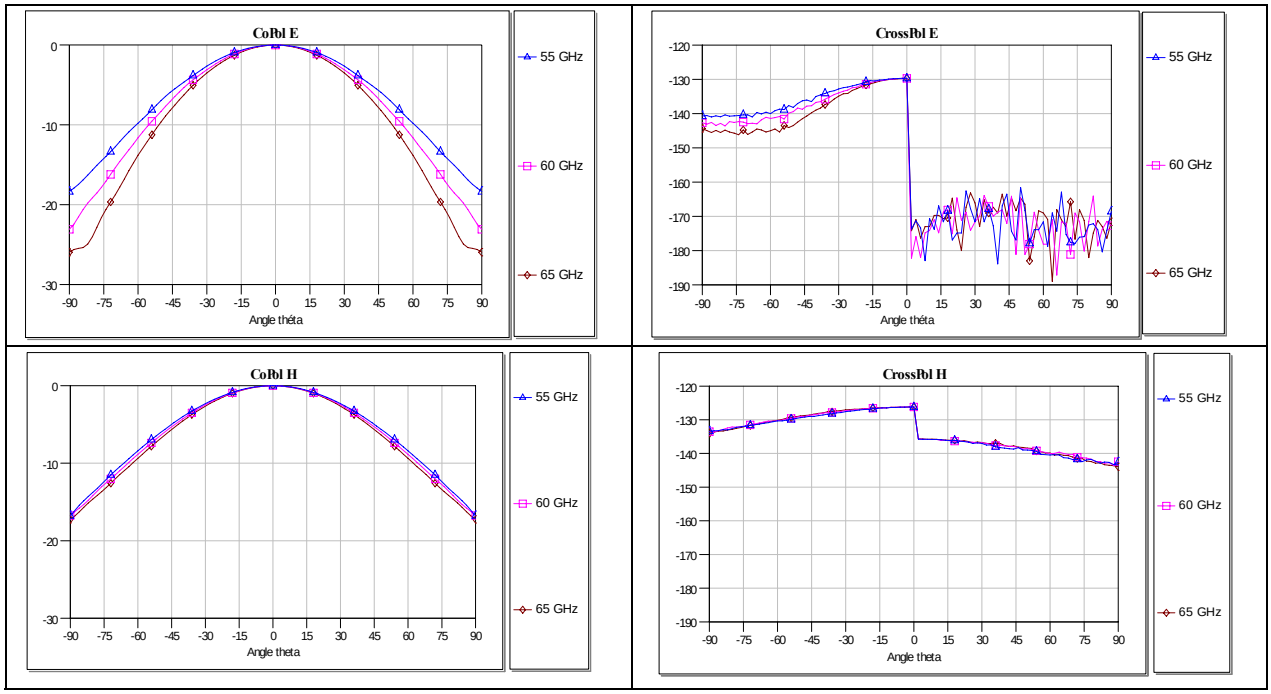

figure 5.5. Radiation Patterns for Waveguide in free space.

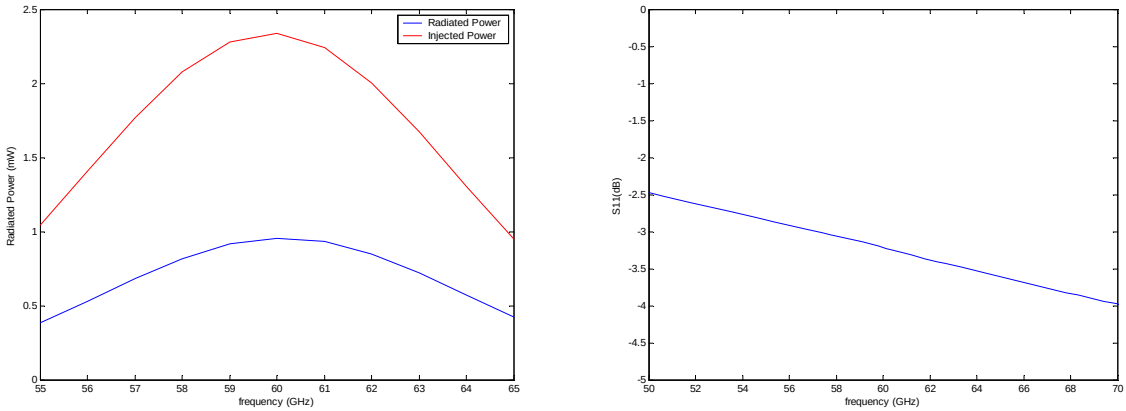

figure 5.6. Radiated power in mW and S11 in dB.

These simulations are repeated placing the Huygens surfaces near of the design. The results obtained are exactly the same, so they will not be represented again. In the following graph is possible to check the position of the Huygens surfaces in the design:

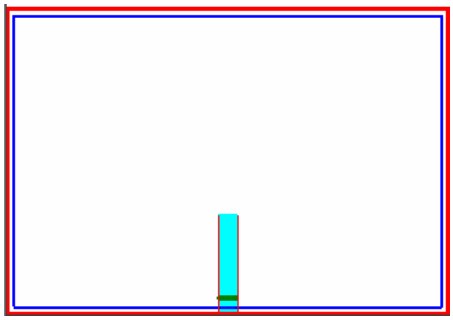

figure 5.7. Waveguide in free space with Huygens surfaces far from the guide.

With these results we check that our method to obtain the radiated power does not depend on the distance of the surfaces we use to measure it. In this configuration, the waveguide is not matched to the free space, so we have a very high S11, around -3dB. Most of the power is reflected and returns through the waveguide. We can watch better this loss in the following graph:

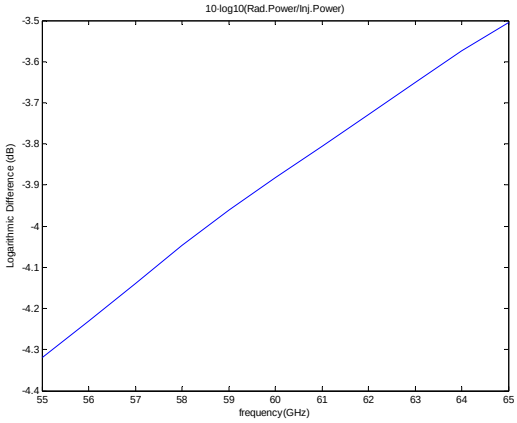

figure 5.8. Logarithmic Difference between Radiated Power and Injected Power.

We are also going to study the same configuration with an infinite ground plane placed on the top of the guide. We only need a Huygens surface to measure the far field. To calculate the radiated power we need five surfaces, because the ground plane reflects the power. In the figure 5 we can see the placement of these five surfaces; the upper one is the same as the Huygens one.

Because of this infinite ground plane, we have to use the image principle. With one Huygens surface we will use **J=0, 2M**.

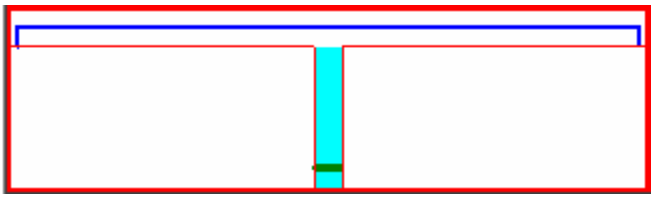

figure 5.9. Waveguide with ground-plane

Directivity:

Frequency	Dmax (dB)
55 GHz	8.82
56 GHz	8.96
57 GHz	9.10
58 GHz	9.19
59 GHz	9.26
60 GHz	9.37
61 GHz	9.47
62 GHz	9.56
63 GHz	9.69
64 GHz	9.82
65 GHz	9.91

table 5.2: Directivity of a waveguide with ground plane filled with Eccostock radiating in free space.

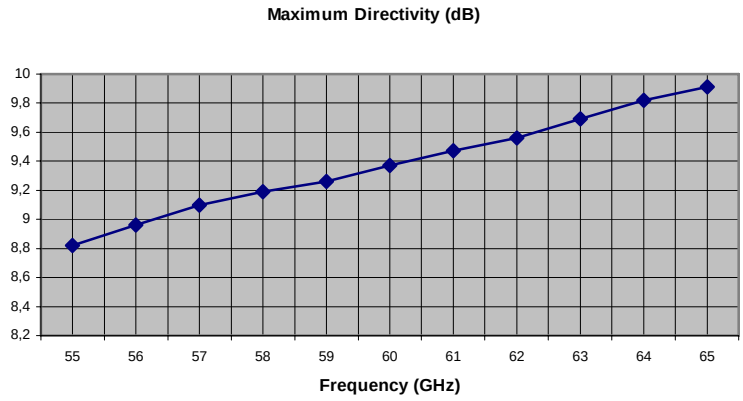

figure 5.10. Maximum directivity in dB for each frequency for Waveguide with ground plane in free space

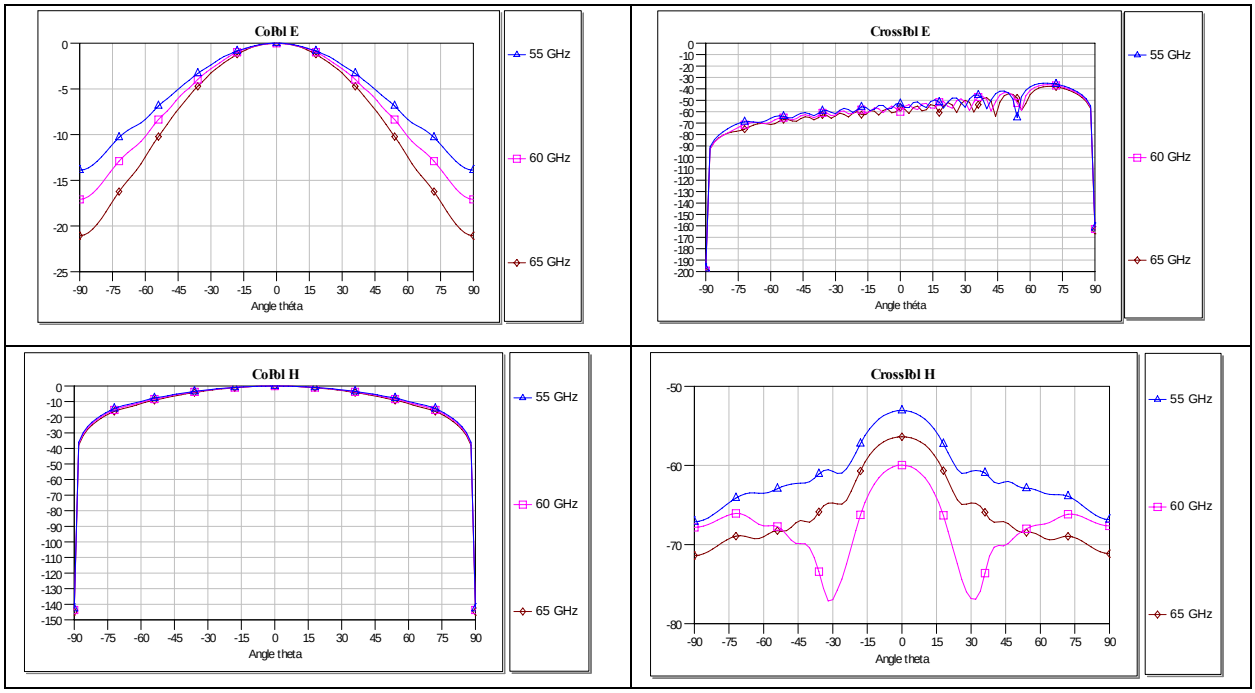

figure 5.11. Radiation Patterns for Waveguide with ground plane in free space.

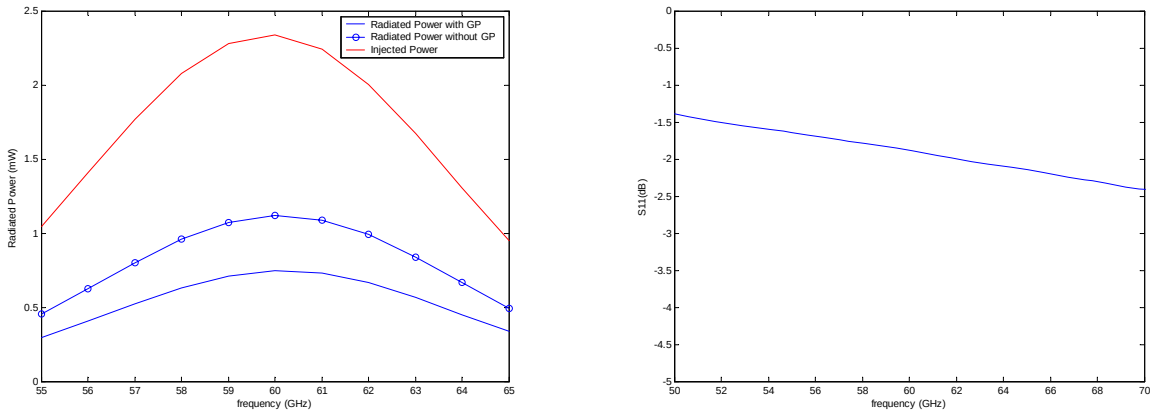

figure 5.12. Radiated power and S11 of a waveguide with a ground plane in free space.

We notice that, in both cases, the directivity has a nearly linear dependence with the frequency in the graph, but being this directivity expressed in dB, it means that the dependence is actually exponential. It's easy to check the correspondence of these results with the E field co-polarization graph, where the higher the frequency is, the lower gets the level of the side areas of the lobe.

The main difference between using or not the ground plane is in the cross-polarization. Without ground plane it's extremely low (under -120dB), but with it, we can get a level higher than -40dB. That's because the polarization change made by the ground plane.

The radiated power is even lower than without a ground plane. That is, the mismatching is higher. In the next sections we will see how the lenses have influence on the adaptation.

5.3 Lenses with metallic plane

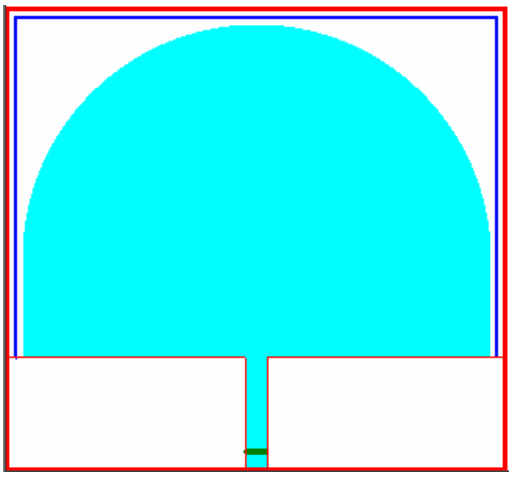

figure 5.13. Waveguide with ground plane and lens.

First, we are going to study the fields radiated by a lens with a ground metallic plane by the mouth of the guide. Here we don't have a lower extension, so we are just studying the influence of the upper one. We will sweep this parameter from 0% to 150%, like in the previous studies.

In **figure 5.13** can be seen the Huygens surfaces distribution around the lenses, which will be also used to measure the radiated power.

Because of this infinite ground plane, we have to use the image principle. With five Huygens surfaces we will use strict image.

The following graph shows the dependence of the maximum directivity with the frequency for each *Lup* value, which will provide us some useful information about the lenses behaviour.

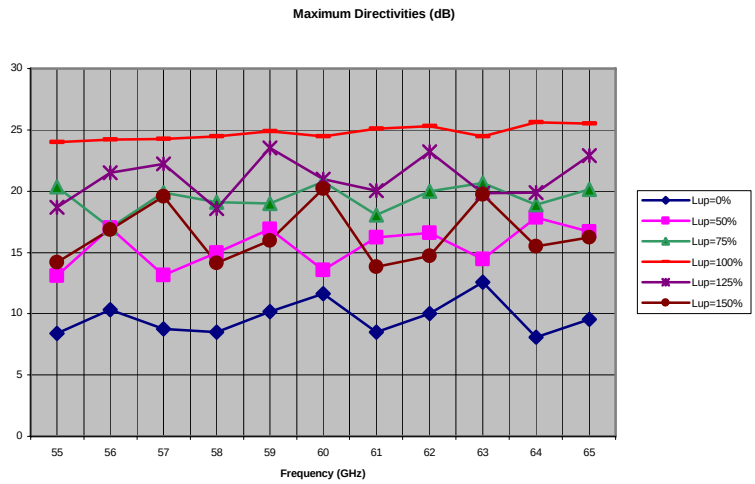

figure 5.14. Maximum Directivities comparison, lenses with a metallic plane. Lup Sweep, Diameter=6λ_0, Eccostock

It's easy to notice that the maximum directivity is reached when *Lup*=100% for all the frequencies. When we increase the extension from 0%, the directivity grows until 100%, from here it decreases. We also check that with the synthesised ellipse the directivity is less sensitive with the frequency, and the shape is more similar to the one we obtained in the simulation without lens (like a straight line with a little slope). For the other extensions there are strong directivity variations with the frequency, with a saw shape, especially in the ones with *Lup* higher than 100%.

Now we will compare the radiation patterns for the central frequency, sweeping the extension:

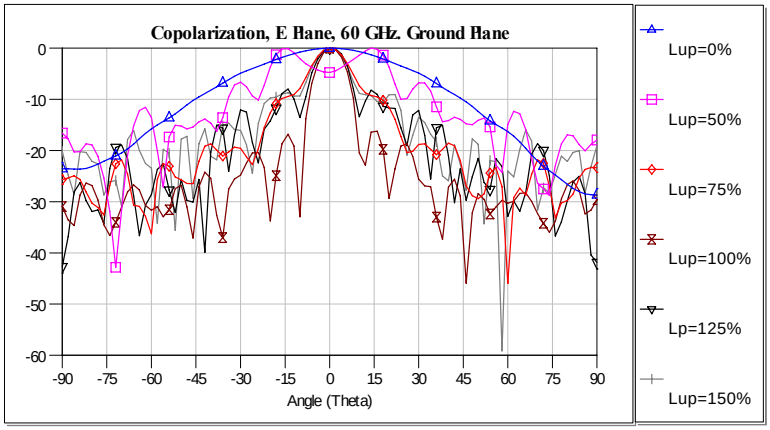

figure 5.15. Copolarization E Field,60 GHz, diameter 6λ_0, Eccostock, with ground plane

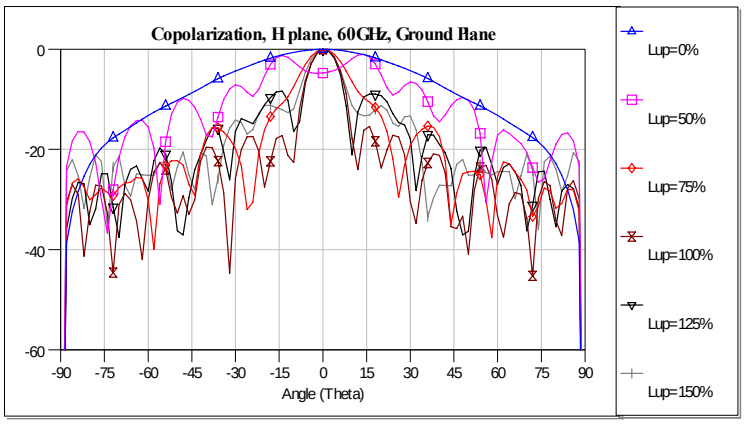

figure 5.16. Copolarization H Field, 60 GHz, diameter $6\lambda_0$, Eccostock, with ground plane

These comparisons are coherent with the directivities we obtained before. The more directive pattern is obtained with *Lup*=100%, having the rest a similar shape, save *Lup*=0% and Lup=50%, the first one is a simple lobe, and the second one doesn't even have a proper central lobe. The electric field in H plane at the ground plane direction is always null.

Now, we will compare the radiated power for each *Lup* value:

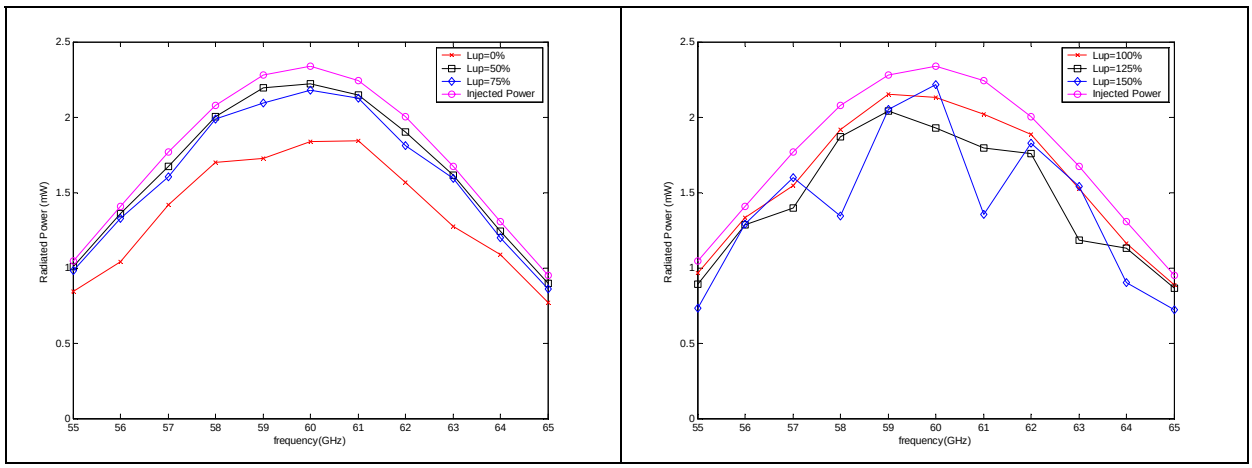

figure 5.17. Radiated Power comparison. diameter $6\lambda_0$, Eccostock, with ground plane

The S11 of each extension, measured in dB, is represented in the following graphs:

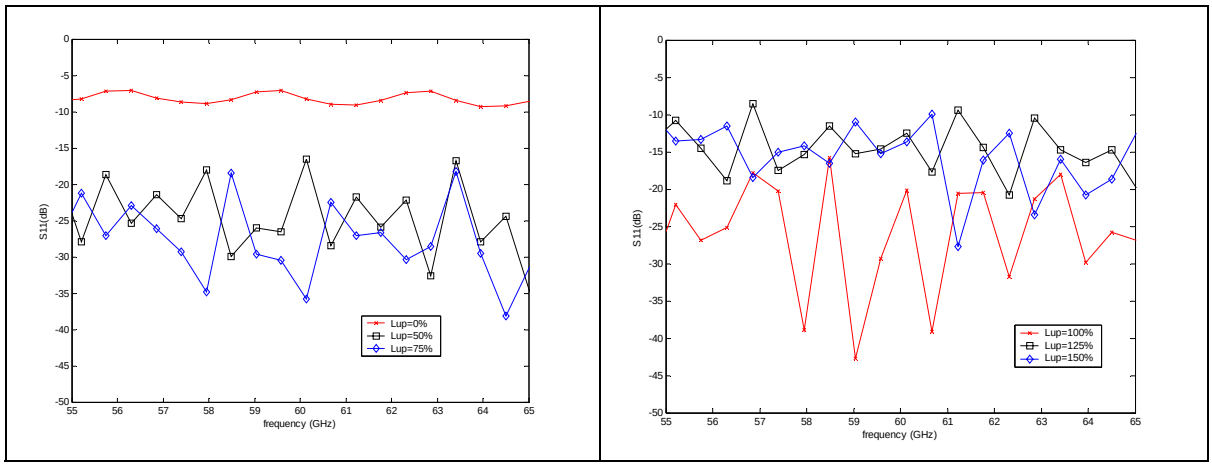

figure 5.18. S11 comparison. diameter $6\lambda_0$, Eccostock, with ground plane

The relationship between S11 and the radiated power is clear, the configuration with more reflections radiates the less. We see that the extensions between 50% and 100% are the ones that have less reflections and its radiated power is more similar to the injected one.

With the hemispherical lens (*Lup*=0%) we know that there are problems with the reflections, cause the rays rebound in the surface of the lens with the same direction they had, going inside the waveguide again. It seems that with the synthesized ellipse the response is very erratic with the frequency, but anyway it's always under –15 dB, so we can consider its behaviour correct.

5.4 Lenses without a metallic plane.

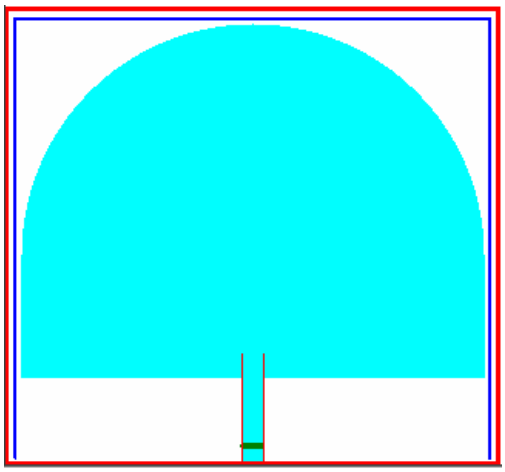

figure 5.19. Waveguide with ground plane and lens

Now we will make the same study but in the classical configuration of the lenses without the metallic ground plane. We have two extension parameters to sweep: *Lup* and

Ldown, so we draw the same graphs, but with both parameters. Here, the surfaces used to measure the radiated power are not the same as the Huygens ones. We will use a cube which contains the lens, like in the **figure 5.19**. In the post-treatments the influence of the feeding waveguide will be erased.

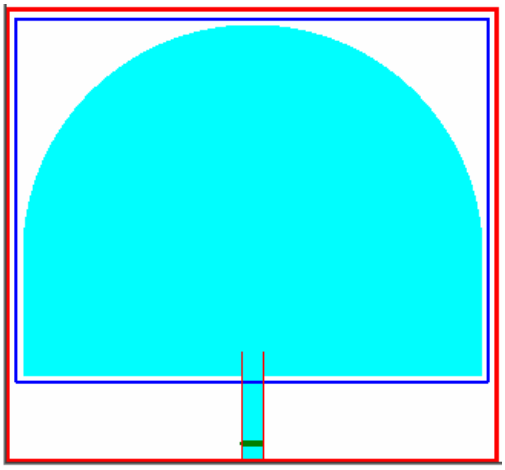

figure 5.20. Cube around the lenses for measuring the radiated power

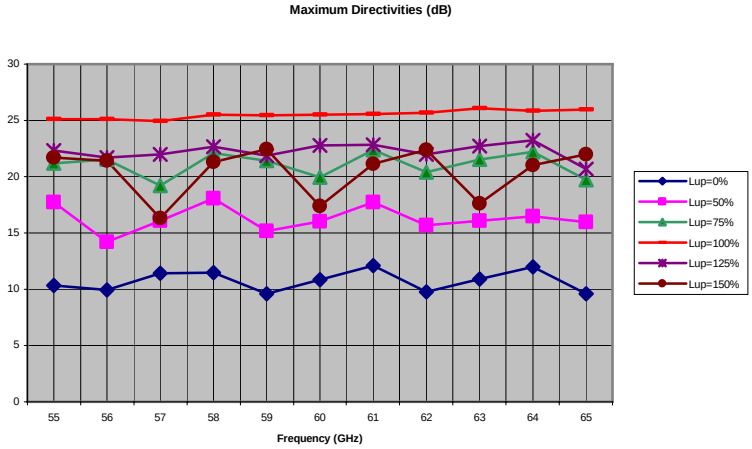

figure 5.21. Maximum Directivities comparison, lenses without a metallic plane. Lup Sweep, Ldown=0%, Diameter=6λ_0, Eccostock

We check that the results are similar to the configuration with ground plane, the synthesized ellipse is clearly the most directive configuration with an almost linear behaviour. The differences are not really big:

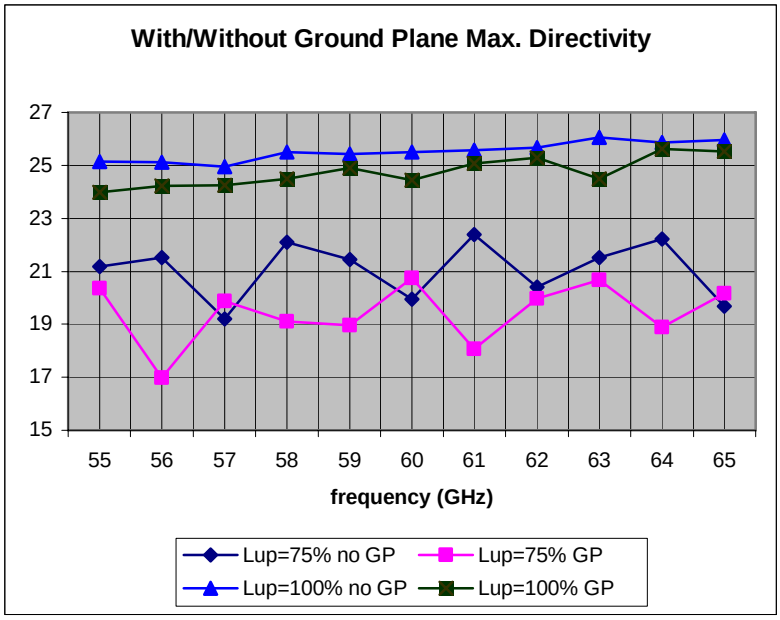

figure 5.22. Maximum Directivities comparison, lenses with and without a metallic plane. *Lup* Sweep, *Ldown*=0%, Diameter=6λ_0, Eccostock

In general, without a ground plane we obtain higher directivities, but this difference is not very important in the *Lup*=100% case, where there is only 1dB between them.

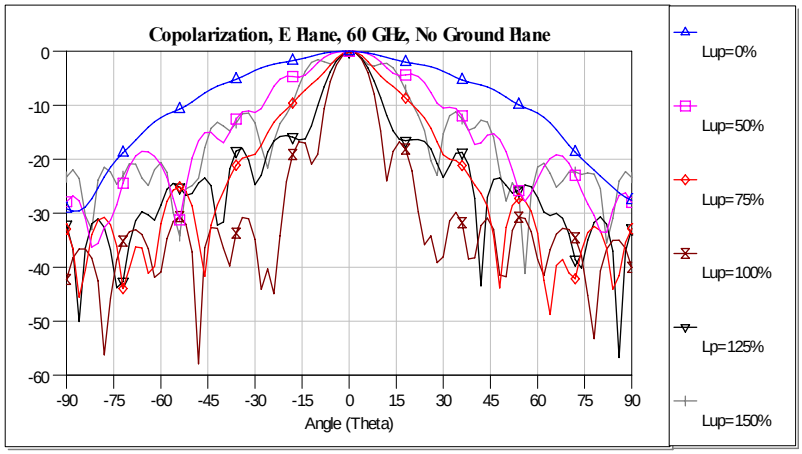

figure 5.23. Copolarization E Field,60GHz, Ldown =0%, diameter 6λ_0, Eccostock, without ground plane

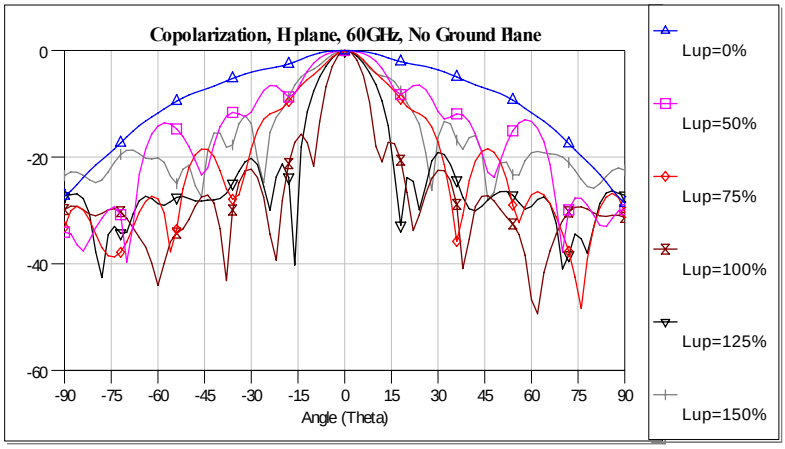

figure 5.24. Copolarization H Field,60 GHz, Ldown=0%, diameter $6\lambda_0$, Eccostock, without ground plane

As we could guess from **figure 5.22**, with the upper extension of 100% we have the most directive and narrowest lobe, and also the smallest side lobe level. For 125% we also have a defined (though wider) lobe with good characteristics.

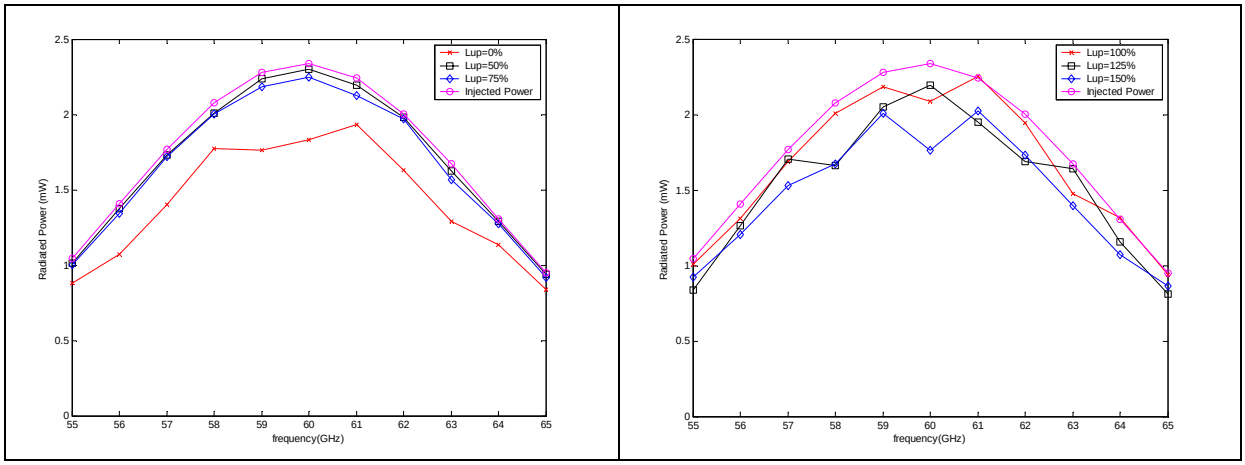

figure 5.25. Radiated Power comparison. diameter $6\lambda_0$, Eccostock, Ldown=0%, without ground plane

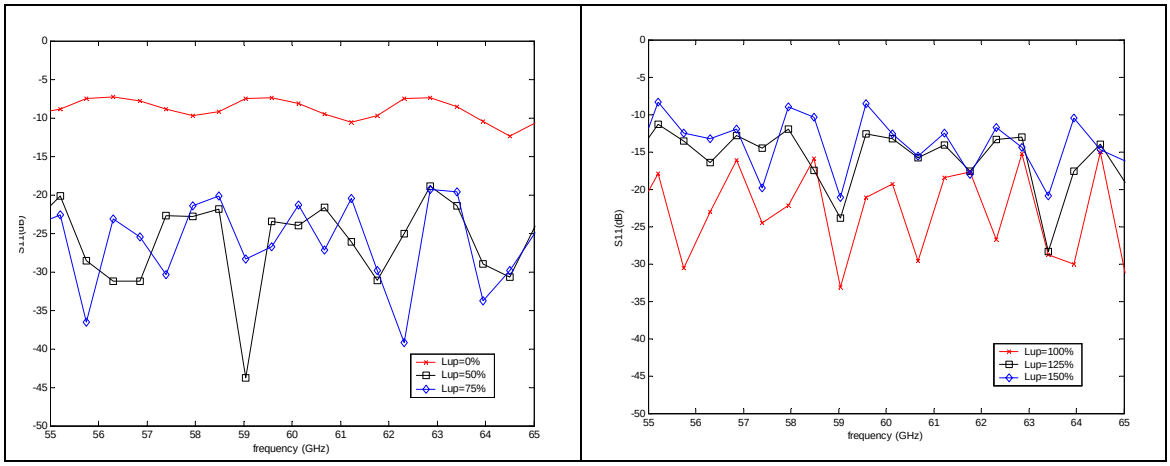

figure 5.26. S11 comparison. diameter $6\lambda_0$, Eccostock, Ldown=0%, without ground plane

As in the previous study, small reflections permits more radiated power. These results don't differ very much with the ones obtained with the metallic ground plane configuration. The best return loss is obtained with the extensions between 50% and 100%, it rises with higher extensions.

Now we check the influence of *Ldown*:

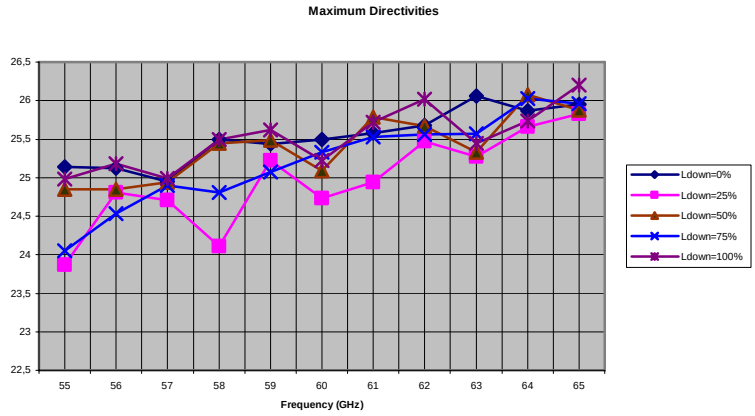

figure 5.27. Maximum Directivities comparison, lenses without a metallic plane. *Ldown* Sweep, *Lup*=100%, Diameter=$6\lambda_0$, Eccostock

The directivity behaviour has a similar shape with all these extensions. With a *Ldown*=25% we have a distribution somehow more chaotic, it doesn't follows the imaginary line as good as the rest and has more extreme values. It's difficult to obtain a clear pattern from this graph, but the directivity value hardly ever differs more than 1dB for each frequency, so its importance is very weak.

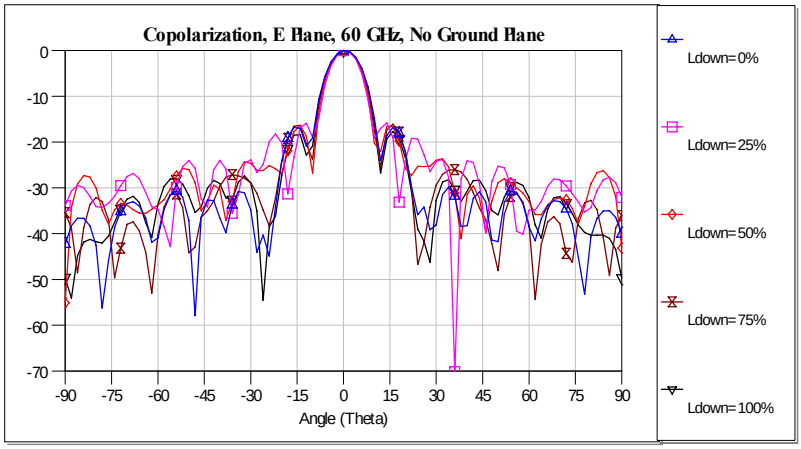

figure 5.28. Co polarization E Field, 60 GHz, Lup =100%, diameter $6\lambda_0$, Eccostock, without ground plane

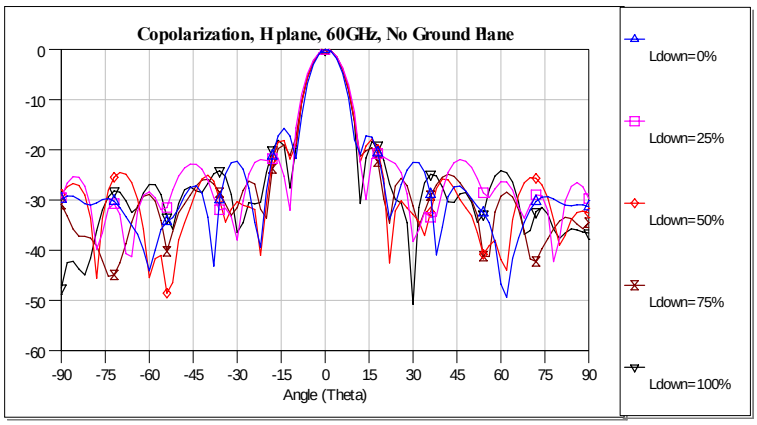

figure 5.29. Co polarization H Field, 60 GHz, Lup =100%, diameter $6\lambda_0$, Eccostock, without ground plane

The radiation pattern is quite similar in all the extensions, specially the main lobe. The rest of undulations have a different phase, but don't make a slightly difference in the secondary lobe level.

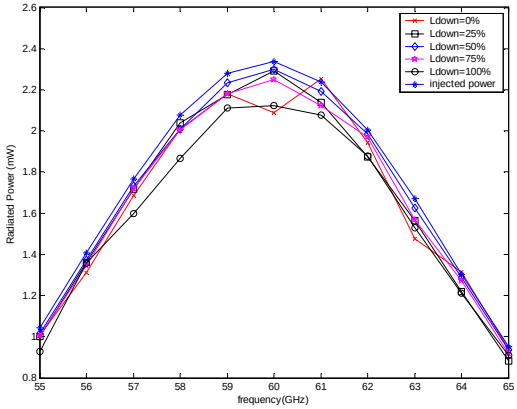

figure 5.30. Radiated Power comparison. Diameter $6\lambda_0$, Eccostock, Lup=100%, without ground plane

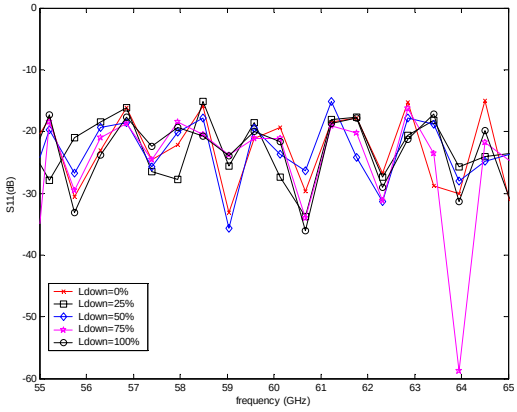

figure 5.31. S11 comparison. Diameter $6\lambda_0$, Eccostock, Lup=100%, without ground plane

Studying the reflections, the lower extension is not as important as the upper one. Except with the 100% extension, the power level is quite the same, being the optimum one the 50% extension.

5.5 Dielectric with losses

Now we will consider that the lenses are made with the same dielectric, but this has losses. We will to check the influence of this new parameter in several configurations with the synthesised ellipse (*Lup*=100%): with no lower extension, a 50% lower extension, and with a metallic ground plane. We will try with a loss tangent of 10^{-4}, 10^{-3}, $5\cdot10^{-3}$ and 10^{-2}.

We are taking three different measures. First the radiated power in frequency for each of the loss tangent values, then the loss of power in dB in frequency for each of the dielectrics (see formula 9); finally, the logarithmic difference has the expression 10:

$$Loss(dB) = 10\cdot\log_{10}(Power_{NoLosses} - Power_{\tan\delta\neq 0})) \tag{9}$$

$$LD(dB) = 10\cdot\log_{10}\left(\frac{\left|E_{\max}{}^{2}{}_{tg\delta=0}\right|}{\left|E_{\max}{}^{2}{}_{tg\delta\neq 0}\right|}\right) \tag{10}$$

The obtained results are in the following figures (**5.32, 5.33** and **5.34**).

We can check that in both configurations the losses in the dielectrics have similar effects. Very low losses dielectrics (tgδ~10^{-4}) will not have a sensitive influence on the radiated power. But we can check in the graphs that, as the loss tangent increases, the difference in the radiated power rises exponentially (linearly in dB). The frequency has also some importance, since in each one we have a difference slope in the logarithmic difference, though the behaviour is still exponential.

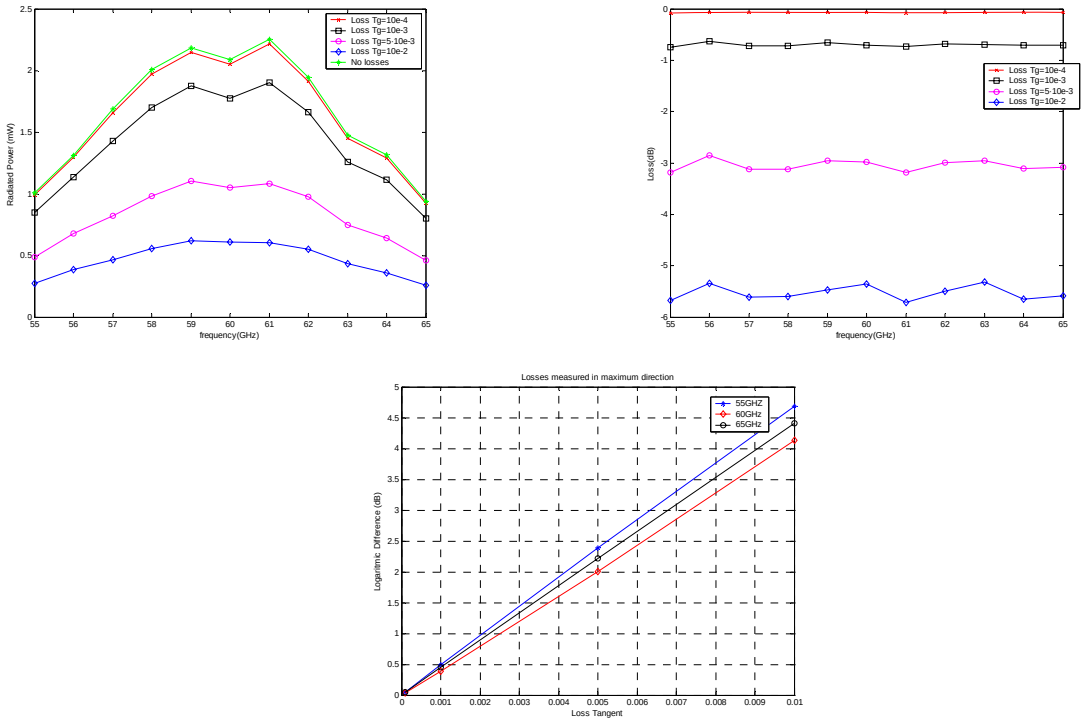

figure 5.32. Losses comparison, Eccostock, Lup=100%, Ldown=0%, without ground plane

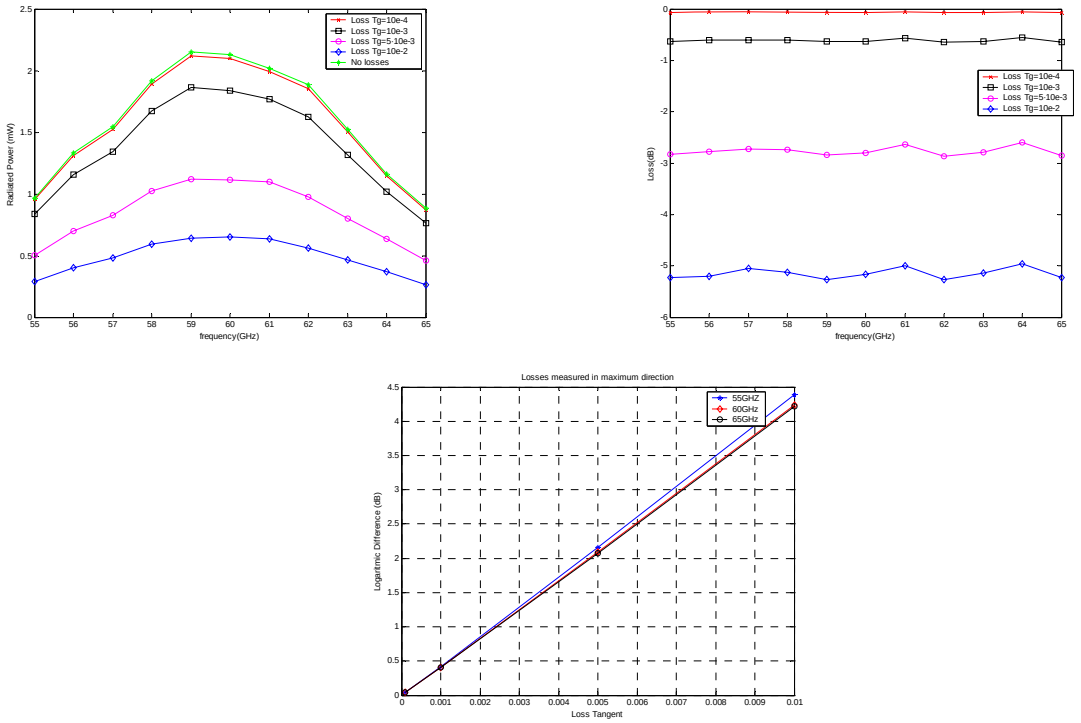

figure 5.33. Losses comparison, Eccostock, Lup=100%, with ground plane

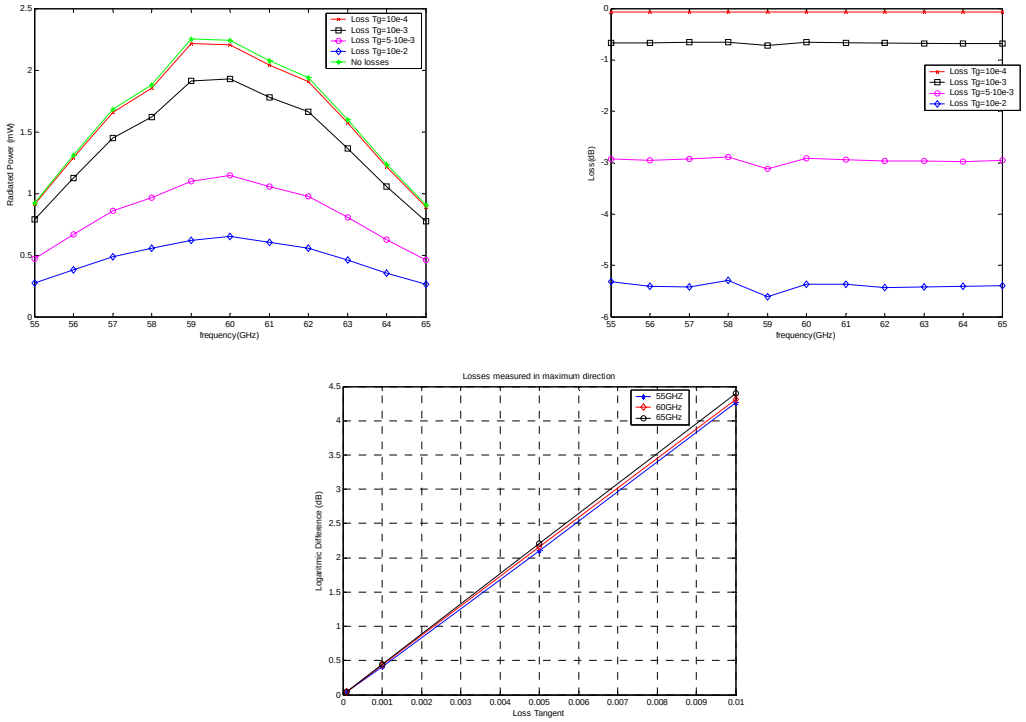

figure 5.34. Losses comparison, Eccostock, Lup=100%, Ldown=50%

5.6 Reflections Influence:

Finally, we will study how the reflections in the dielectric lenses have influence in the radiated power. We are going to compare the results we obtain when we run the simulation until the incident wave reaches the Huygens surfaces, not considering the effects of the reflections, with the whole simulation, when the reflections have been measured.

First we have to find the iteration when we have to stop the simulation. We will use the scope we placed for calculating S11, in the 40th cell of the waveguide (in all the simulations the waveguide is the same), and we will check when the signal arrives:

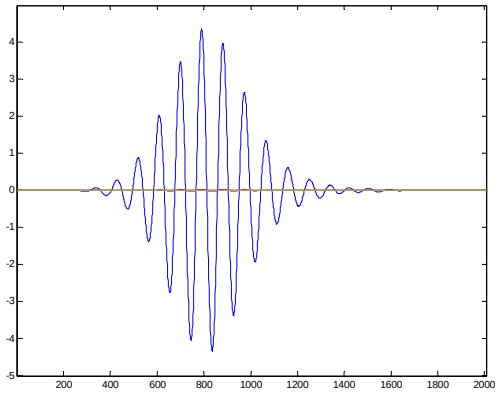

figure 5.35. Excitation inside the waveguide.

The signal finishes going through the scope near the 1600th iteration. But we have to consider also all the trip the wave makes until finally reaching the Huygens surface. We are going to make this study only with upper extensions of 100%, so we will only have to calculate it once.

From the scope to the end of the guide there are 30 cells, from the guide to the end of the lens in the axial direction there are 213 cells, and 3 more to the Huygens surface. To calculate the number of iterations we have to do the following operations:

```
va=3e8;              %Propagation speed in air
vd=3e8/sqrt(8.8);    %propagation speed inside lens
tceld=1e-4/vd;       %time needed to go through a cell in dielectric
tcela=1e-4/va;       %time needed to go through a cell in air
Td=tceld*(213+30);  %Total time in the dielectric
Ta=tcela*3;        %Total time in air
Ti=0.18294e-12;    %Iteration duration
Ni=(Td+Ta)/Ti      %Number of Iterations needed in the axial direction
Tseg=tcela*48;%Security range
Nseg=(Td+Ta+Tseg)/Ti
```

Code 1. Approximation to the number of iterations without reflections

The longest way is the diagonal one, that has 295 cells (48 more than the axial way). The time needed to go through lens cell is longer than the air cell one, so the difference is not going to be much bigger. However, we are going to consider that in the worst case the signal goes through 48 air cells more (actually is less), to have a security range.

Doing this, we obtain 1406 iterations. So, adding this to the 1600 iterations considered before, and giving some time to let the wave get measured, we find that to obtain a good measure of the incident wave without having reflections we need around 3500 iterations.

The following graphs are comparisons between the first reflection and the whole simulation:

ε_r	Diameter	Lsup	Ldown
8.8	$6\lambda_0$	100%	0%

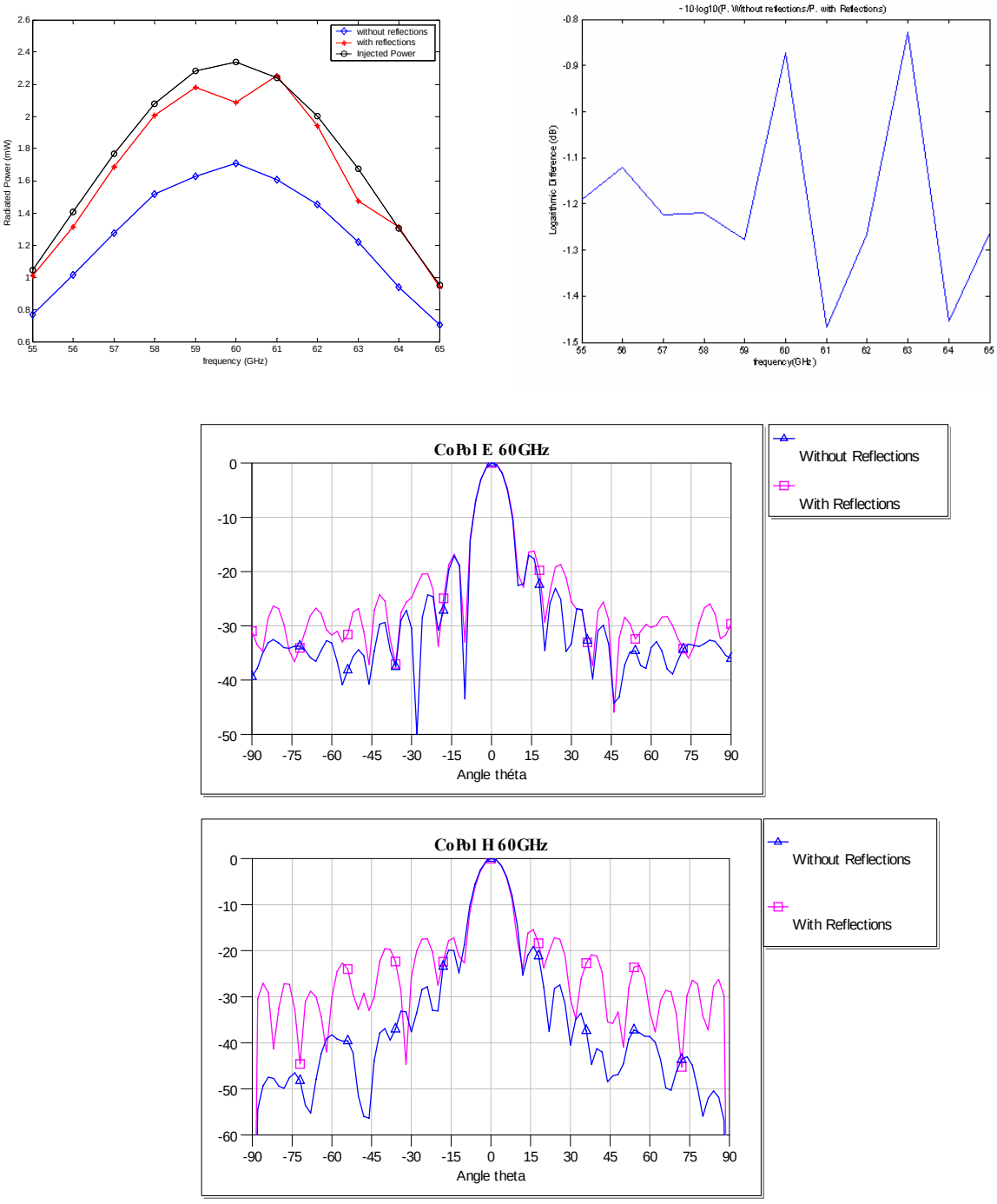

figure 5.36. Radiated Power and Radiation Pattern Comparison. 'without reflections' simulation runs till 3500 iterations.

ε_r	Diameter	Lsup	Ldown
8.8	$6\lambda_0$	100%	50%

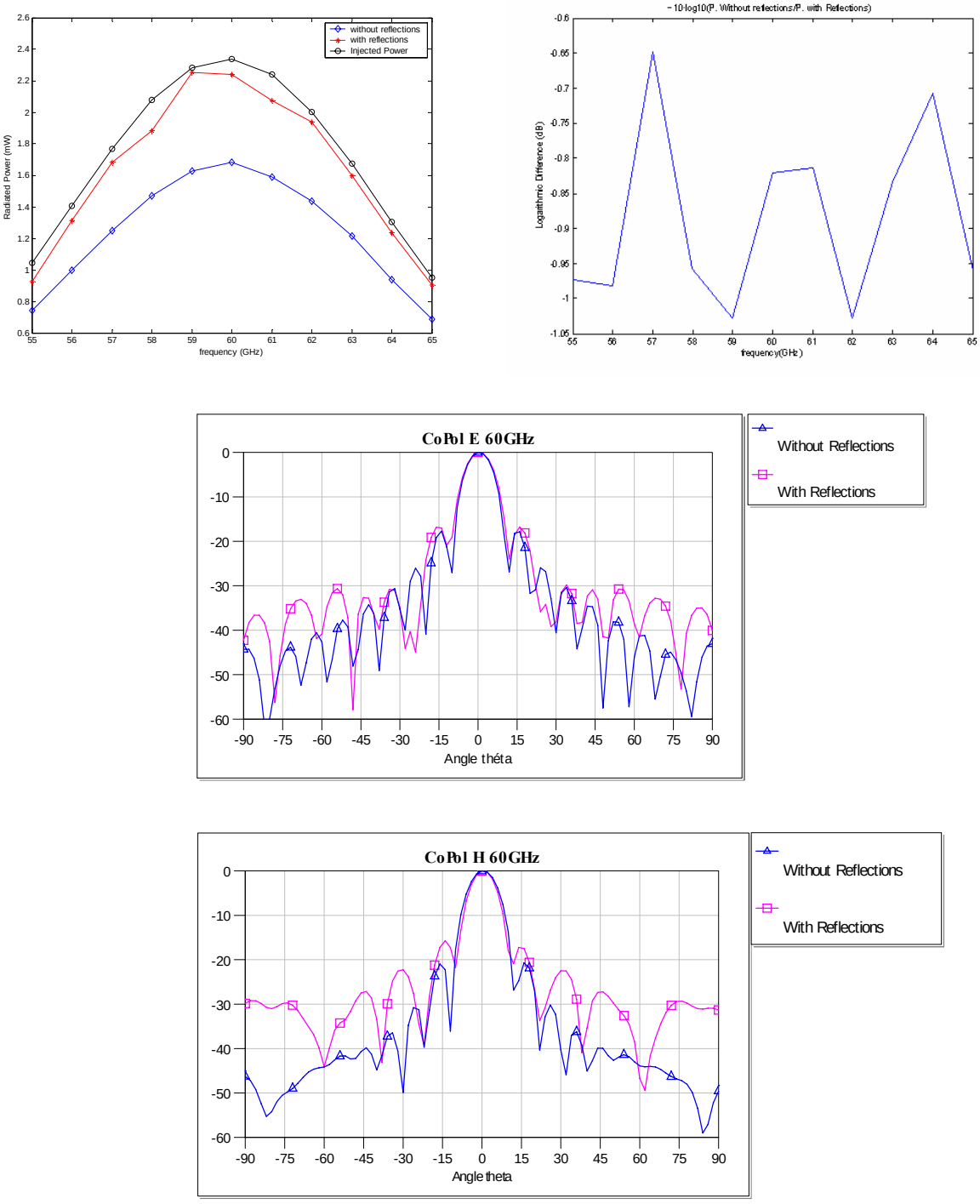

figure 5.37. Radiated Power and Radiation Pattern Comparison. 'without reflections' simulation runs till 3500 iterations.

ε_r	tgδ	Diameter	Lsup	Ldown
8.8	10^{-2}	$6\lambda_0$	100%	Ground Plane

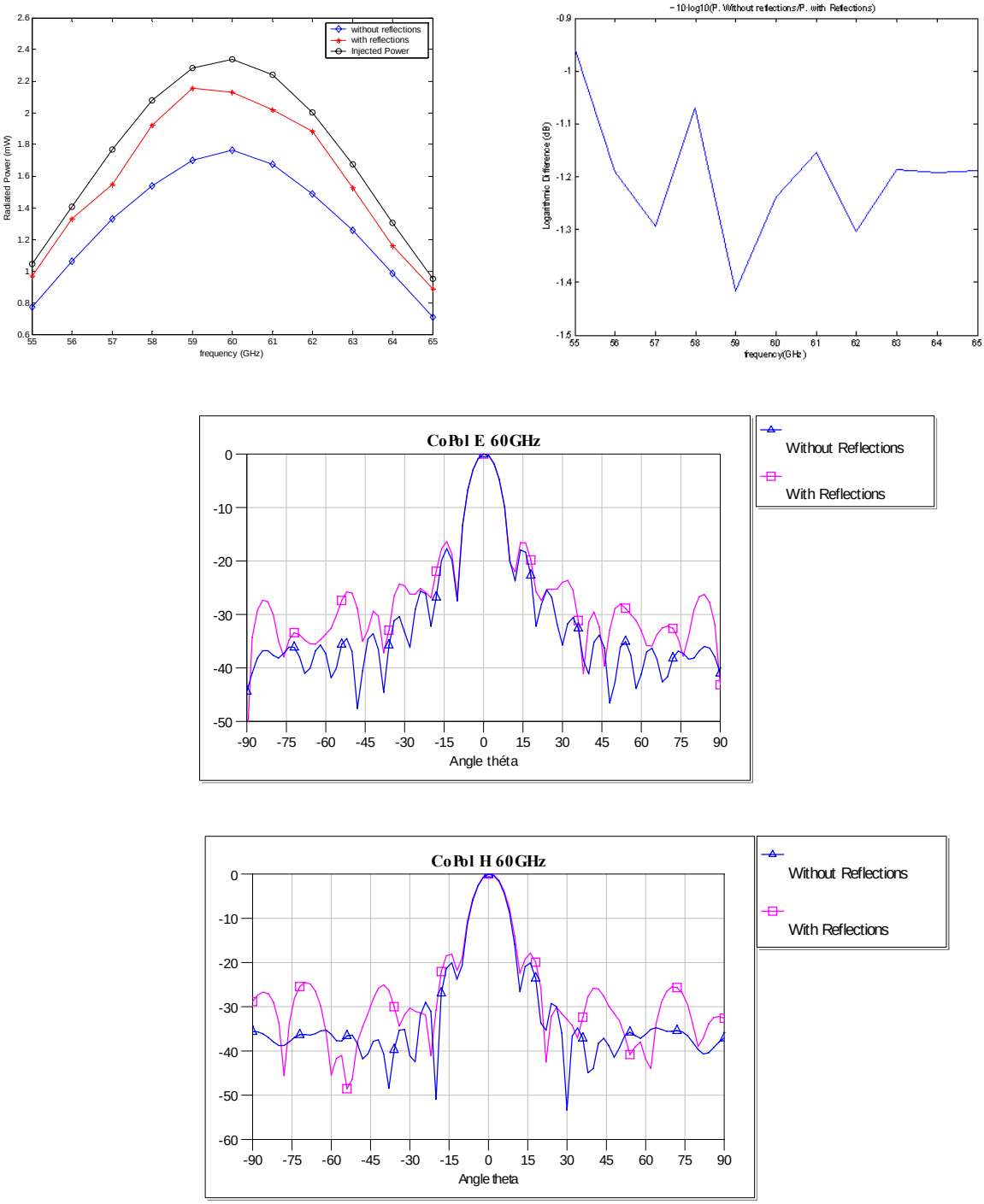

figure 5.38. Radiated Power and Radiation Pattern Comparison. 'without reflections' simulation runs till 3500 iterations.

We can see that, though the first incident wave carries most of the radiated power by the lens, there is still a very important amount of power that will be radiated with the reflections. The first incident wave has a slightly gaussian shape in the three configurations, while after the reflections it turns more irregular because of the influence of the frequency in the internal reflections behaviour.

In the radiation patterns we check that the shape of the main lobe hardly suffers any change. The main differences are in the side radiation, the reflections make it raise quite a lot, which also makes the performance get worse, especially the secondary lobe level. So we can conclude that the first incident wave conforms a clean main lobe and the reflections make the secondary lobe level rise.

5.7 Conclusions

- Adding a ground plane to the lens is only suitable when we work with a synthesized ellipse one, otherwise the side lobe level increases a lot. However, it does not have an important influence on the directivity.

- The directivity of the waveguide without lenses has an exponential increase with the frequency. The only configuration that respects this relationship is the synthesized ellipse lens, others have a chaotic behavior.

- The configurations that radiates more power, that is, they have fewer reflections, are the ones with its extension between 50% and 100%. The ground plane does not have an important influence on the radiated power.

- When the lens dielectric has losses, the difference of radiated power increases exponentially with the losses tangent. The rate of the exponential is minimal at the central frequency, while with a different one it has a little increase.

- A big amount of the radiated power is in the reflections. The first incident wave conforms a radiation pattern with a clean main lobe and its maximum directivity, while the next ones increase the secondary lobe level.

Chapter 6: Synthesized elliptical Macor lenses (L=100%; 3λ and 5λ) with offset feeds

6.1 Introduction

After the complete study of lens antennas we have carried out in the previous chapter, we are going to make an approach in these two last chapters to one of the most interesting applications of the substrate lenses nowadays, the pointing applications. This implies moving the centre of the lens feed, so the maximum radiation will be pointing in a direction different to 0º form the top. We want to study the effects of this decentring, the scan angle we can radiate with an acceptable loss of performance.

In these studies we will not use waveguide sources, but a printed one, which is the source used within the researches in this area. We will work with the synthesized ellipse because it has the better performance, though we don't know if it's also the better one for decentring configurations, further studies would be interesting.

We will simulate two lens diameter, 3·λ and 5·λ. Though we know that the second one will be more directive, we want to study also the influence of the diameter in the performance loss with the scan angle. Also, some of these applications may require a very little lens, so we can't just suppose that we will be always able to use the bigger one.

We are going to study the effect of changing the position of the patch antennas when we couple it to a lens. These changes don't emulate any error, like in the previous studies, with this we are supposed to obtain a configuration that radiates in a certain angle, not always in the perpendicular direction. Then, we will be able to use an array of antennas as source, but we will work with it in the next part.

We are going to move the centre of the patch some certain fractions of the radius depending on the design.

The results of this study depend also on the meshing size we choose. We will work with two different ones:

Big Meshing:	Small Meshing:
Δx=0.280mm	Δx=0.113mm
Δy=0.280mm	Δy=0.113mm
Δz=0.254mm	Δz=0.127mm

table 6.1: Definition of big and small meshing

We are going to use the big meshing for all the configurations, and then we will check the differences with the results obtained with the small meshing. We have check if the big meshing is enough to model these lenses or the small one is needed for an accurate study.

Finally, the influence of the reflections also has to be studied; it can explain the different results obtained with the different configurations and models.

The offsets of the metallic patch are going to be made in both axes, like in the following designs:

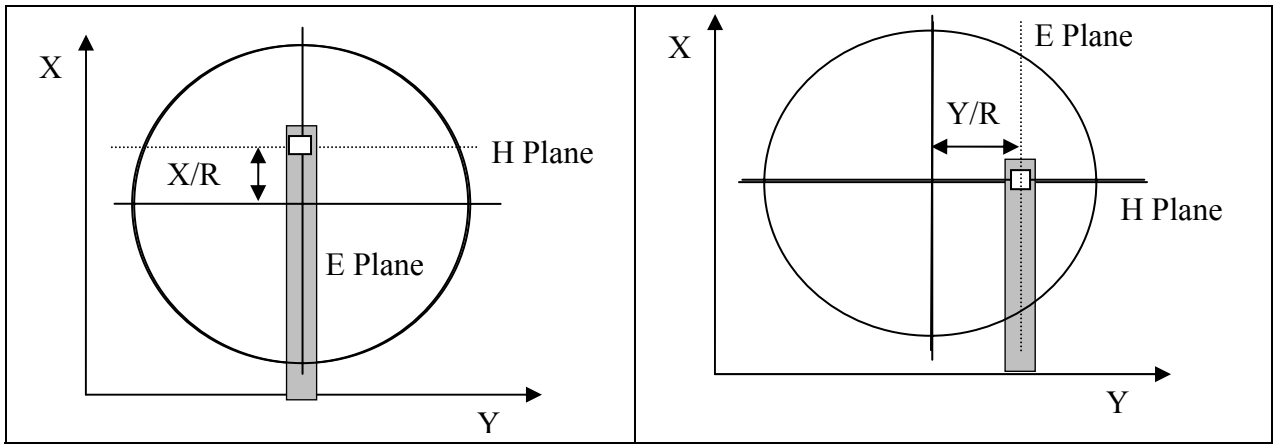

figure 6.1. Patch decentring directions

So, when we move across the X axis we will be moving the centre in the E Plane, and when we move across the Y axis we move the centre in the H Plane, as we will check in the result graphs. We will decentre the patches a radius fraction that will be expressed as X/R and Y/R. Its typical values will be 0 (patch centred), 0.2, 0.32, 0.4 and 0.64.

In the **Appendix B** is described the design of the printed sources in Imelsi for both the big and small Meshing, and its radiation patterns.

6.2 Number of Iterations

The difference of permittivity in the dielectric makes this design have a lot of reflections, so we have to take care with the time we leave the simulation running, it must be enough to consider an important number of reflection orders for an accurate calculation. So, first of all, we want to be sure that in each configuration the number of iterations we have chosen.

We will start with the big meshing. We take the worst case related to reflections and delay of the wave, which is the bigger lens (Diameter of 5·λ) and the patch placed in $\frac{X}{R} = 0.64$.

Big Meshing – Simulations at 26GHz:

Nº of Iterations	Directivity	Co-Polarization	Cross-Polarization
8000	15.9dB	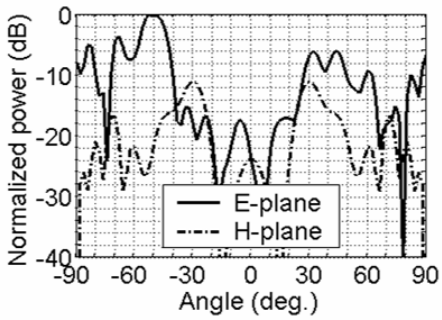	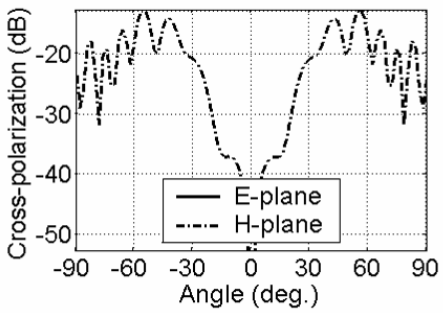
12000	15.7dB	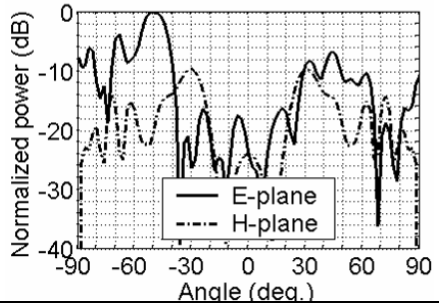	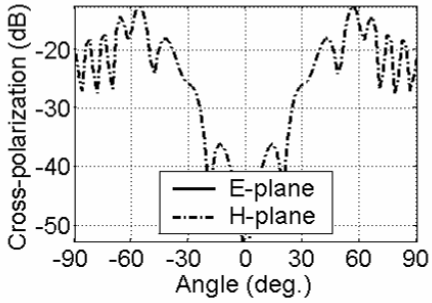
15000	15.7dB	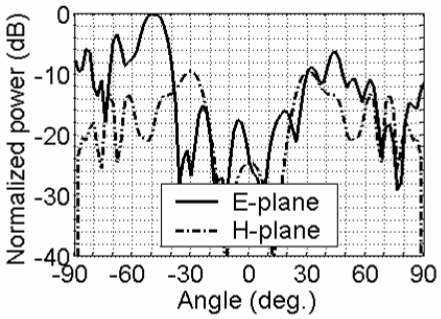	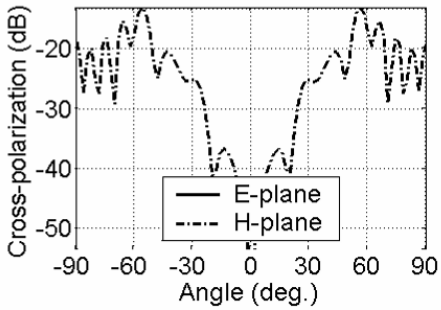
20000	15.7dB	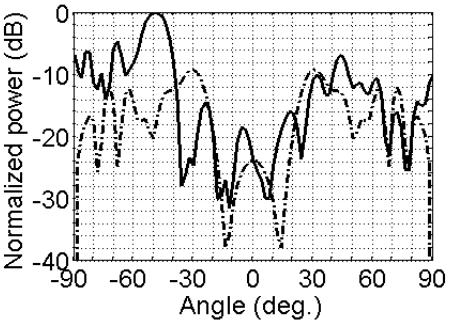	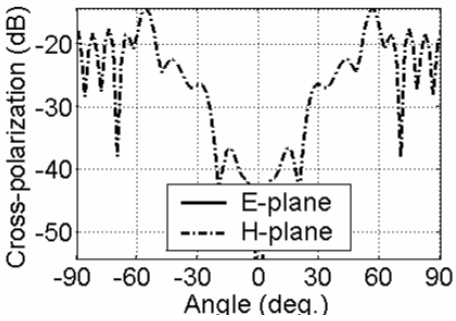

figure 6.2. Radiation Patterns and Directivity for different number of Iterations. Macor lens, D=5·λ, with patch source decentred X/R=0.64. Big Meshing.

Small Meshing – Simulations at 26GHz:

Nº of Iterations	Directivity	Radiation pattern	Cross Polarization
15000	16.1dB	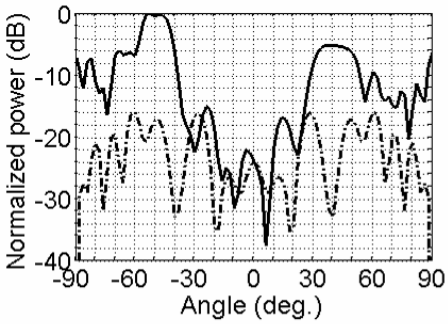	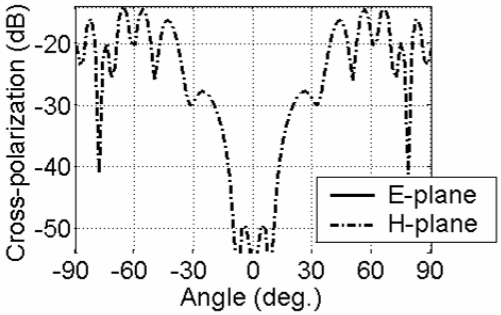
20000	15.4dB	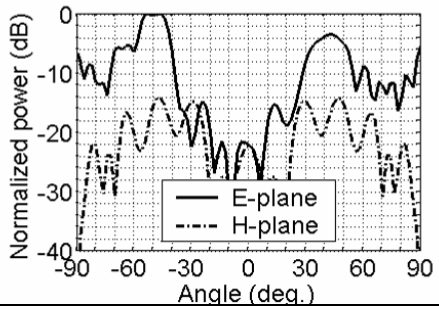	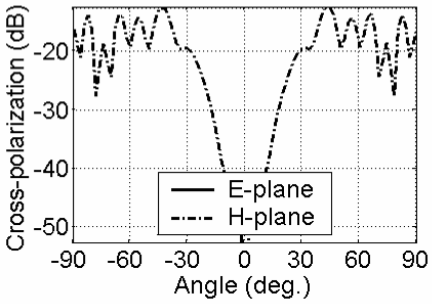
35000	14.5dB	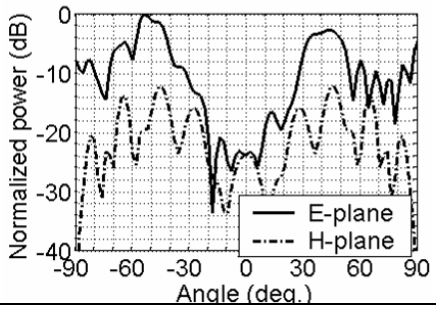	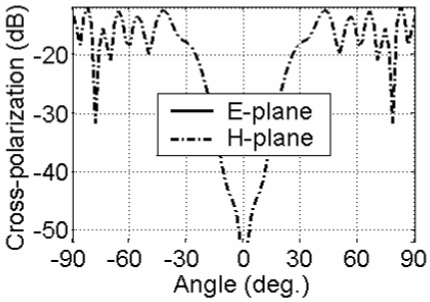
40000	14.4dB	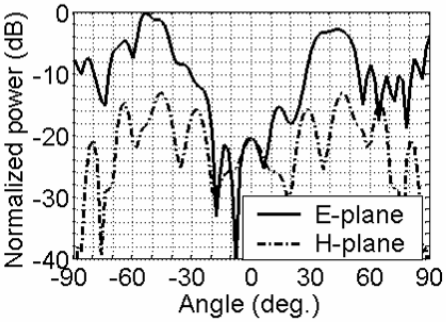	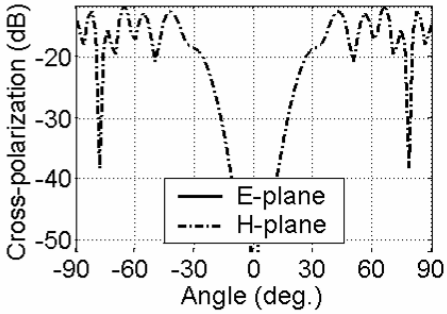

figure 6.3. Radiation Patterns and Directivity for different number of Iterations. Macor lens, D=5·λ, with patch source decentred X/R=0.64. Small Meshing

Watching the results, we can check that there are few changes when we increase the number of iterations. However these changes exist, the directivity varies some dBs between the lower numbers of iterations, so there are still reflections of a high order we have to consider to get an accurate result. To avoid unnecessary errors, we will make the simulations with the highest number of iterations, that is, 20000 for the big meshing and 40000 for the small meshing.

6.3 Meshing

Now we are going to work with the small and big meshing. If we can use a big cell size instead of the thin one, we will save a lot of time and computer resources to make the next studies. However, when we increase the cell size, the design of the lens will have a worse resolution, the approximation to the curve of the hemisphere will be less accurate, which will have influence in the simulations. In order to check the differences, in the **figure 6,4** and **figure 6.5** we compare the results of the lenses with a diameter of $3 \cdot \lambda$ and $5 \cdot \lambda$, simulated at 26GHz:

We check that there are very important differences between the results obtained with small and big meshing. These differences aren't only related with the side radiation, but the main lobe shape also suffers considerable variations, especially when the centre deviation is bigger. This means that the big meshing approximation is not suitable for studying these lenses.

So, from now we will only study the performance of the lens with a small meshing.

Diameter=3λ	Big meshing	Small Meshing
Original	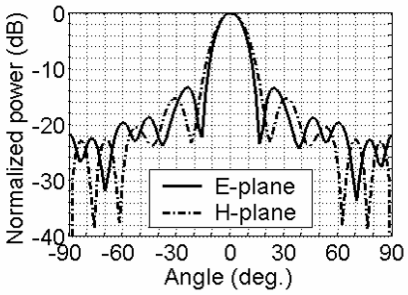	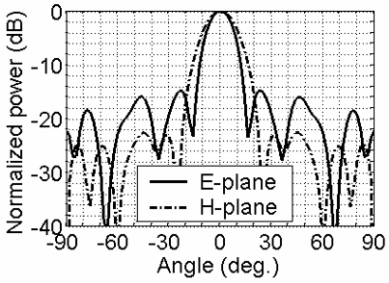
X/R=0.32	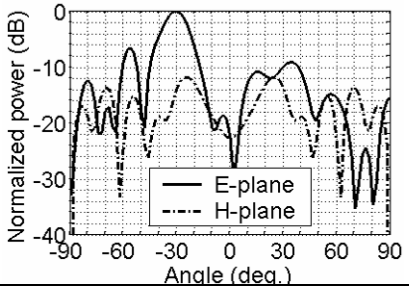	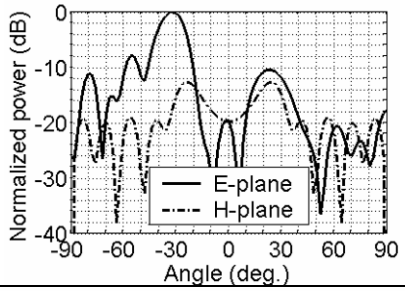
Y/R=0.32	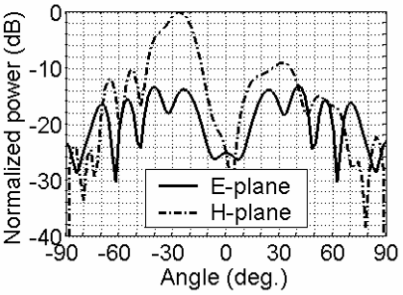	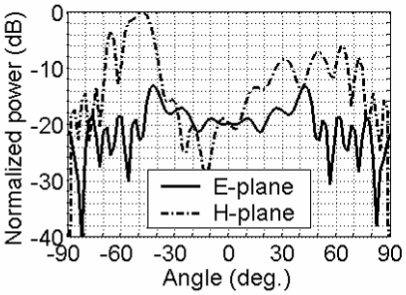
X/R=0.64	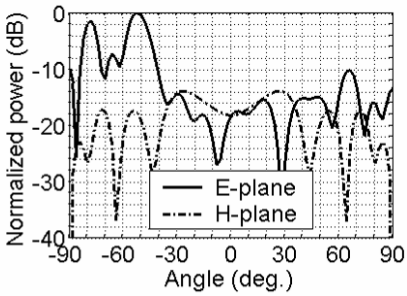	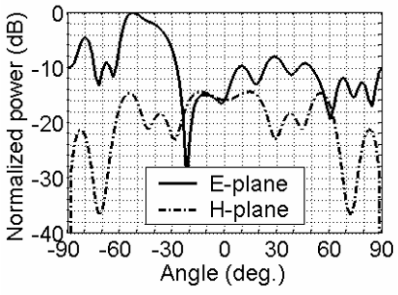
Y/R=0.64	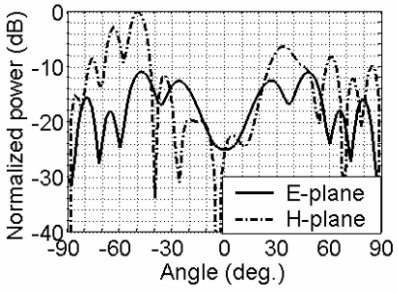	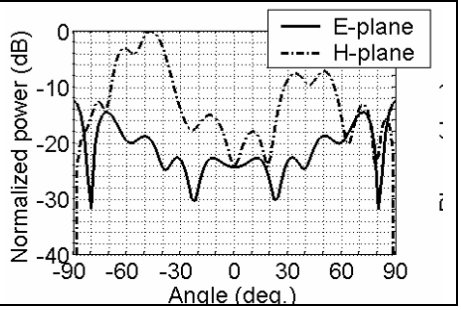

figure 6.4. Big and Small Meshing comparison for D=3·λ with Radiation Patterns for different decentrings. Macor lens.

Diameter=5λ	Big meshing	Small Meshing
Original	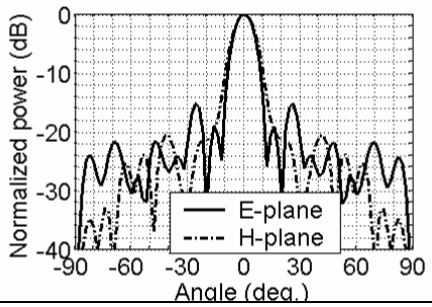	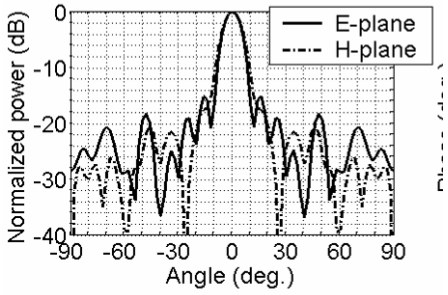
X/R=0.32	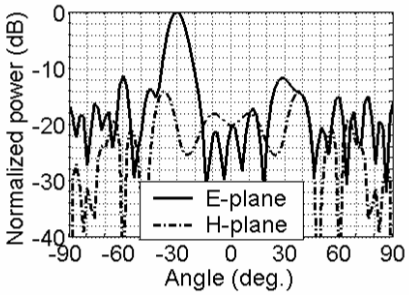	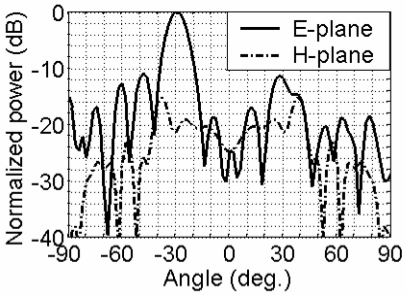
Y/R=0.32	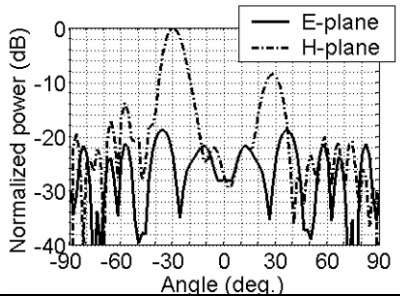	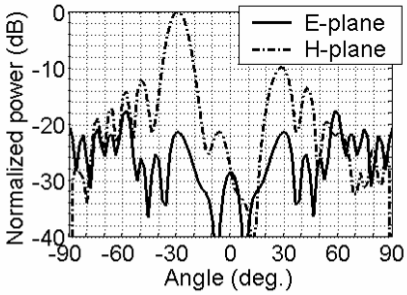
X/R=0.64	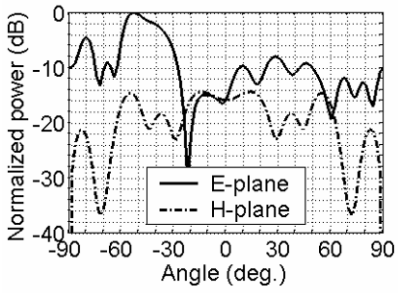	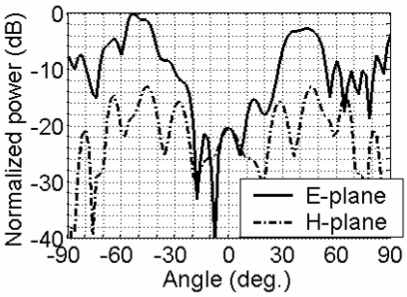
Y/R=0.64	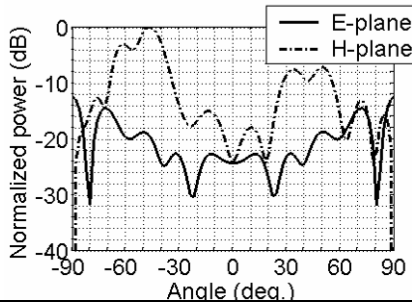	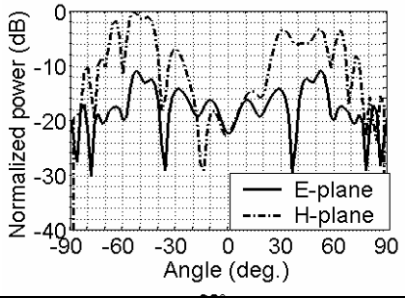

figure 6.5. Big and Small Meshing comparison for D=5·λ with Radiation Patterns for different decentrings. Macor lens.

6.4 Decentred patches performance

These are the variation of the performance parameters with the decentring, first for the lens of diameter of $3 \cdot \lambda_0$, for small meshing:

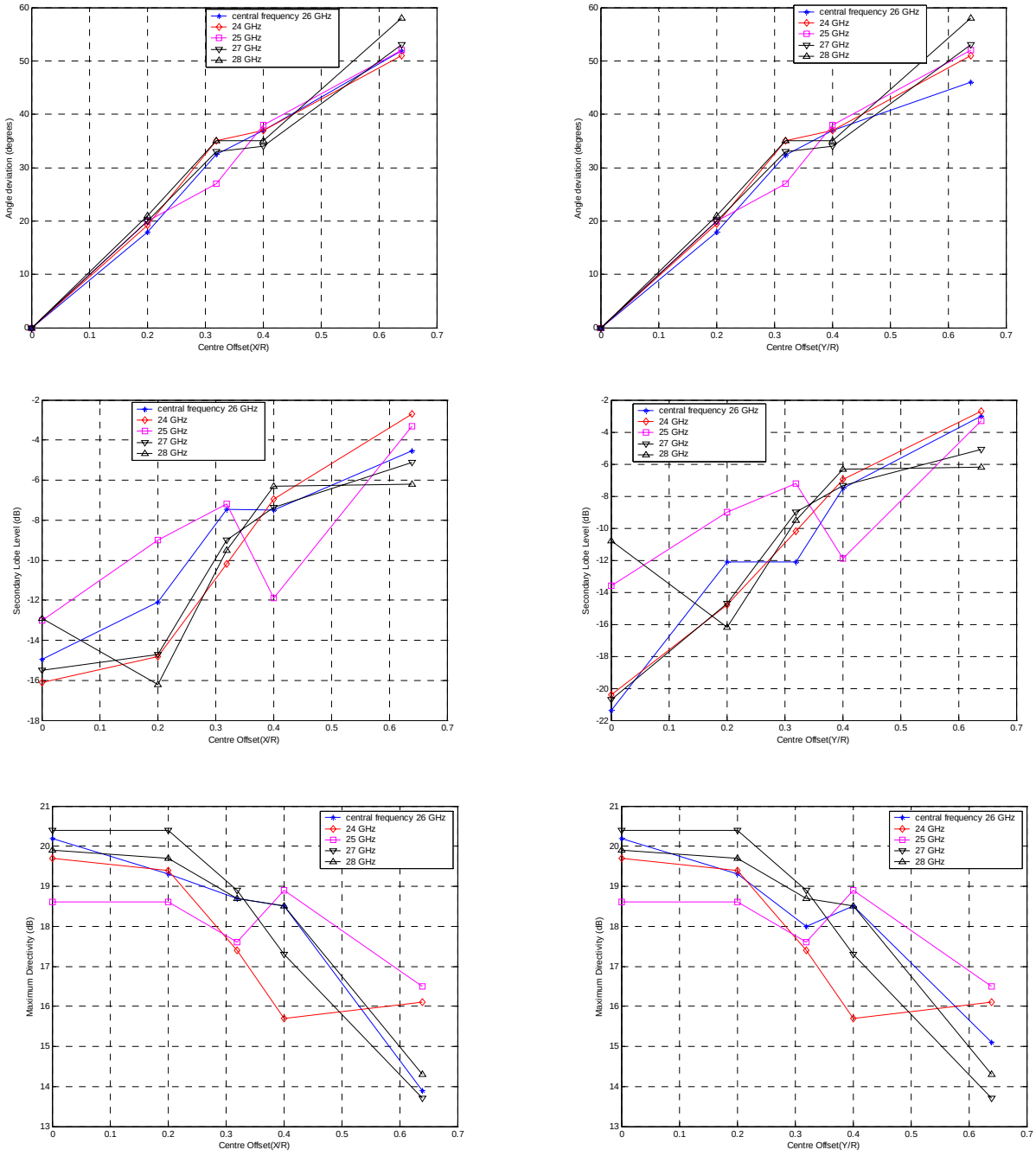

figure 6.6. Performance comparison between decentrings. Macor lens, D=3·λ,.Small meshing.

And these for the lens of diameter of $5 \cdot \lambda_0$:

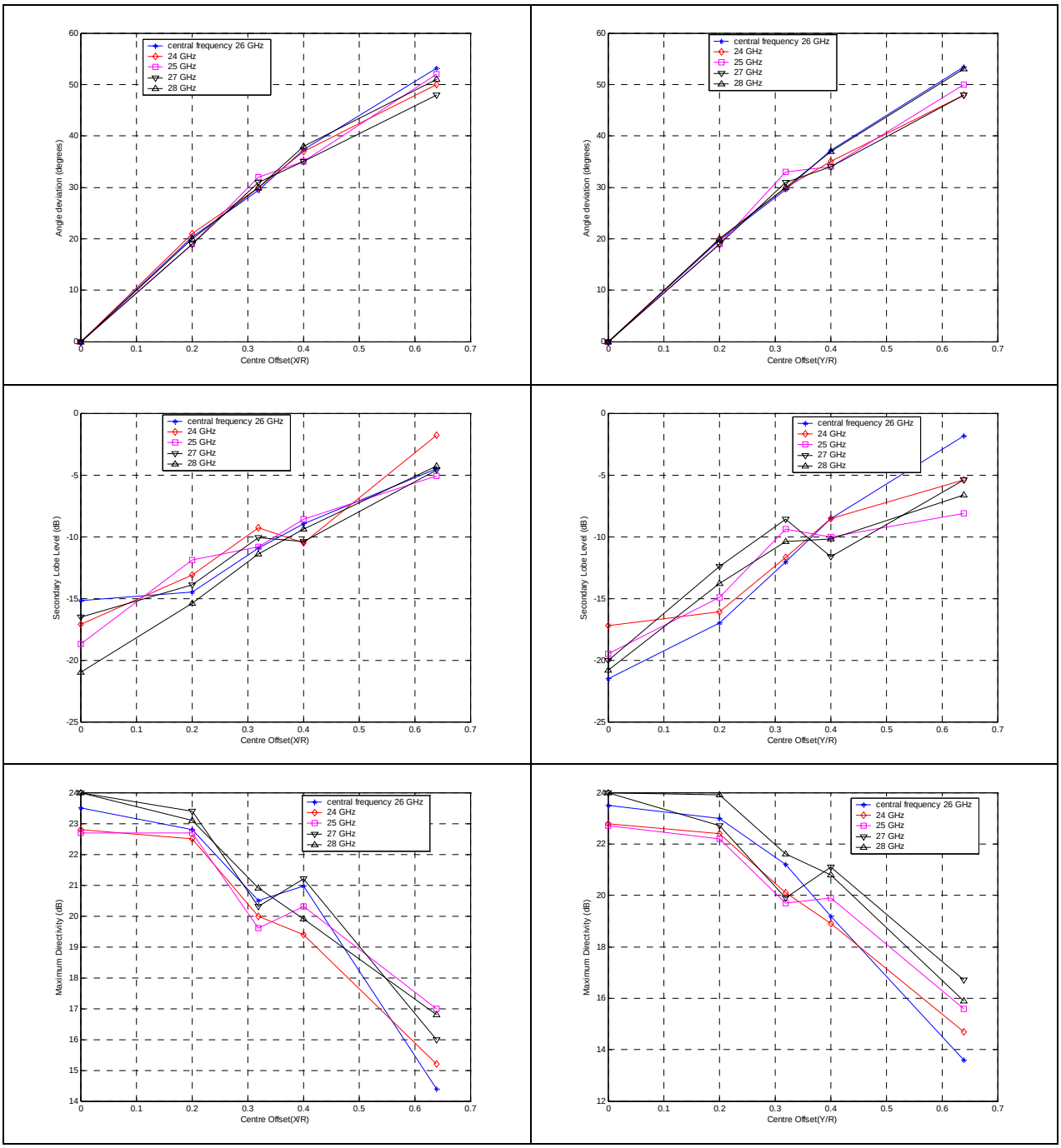

figure 6.7. Performance comparison between decentrings. Macor lens, D=5·λ,.Small meshing.

We check that the maximum radiation angle varies almost linearly with the centre offset in both directions. The behaviour of the scan angle is almost the same for both diameters, though there are some minor differences, both can be approximated to a strict line with the same slope. This is interesting, since it makes easy the design of applications where we have to "move" the centre of the patch to point in different directions. With the range of decentring we have simulated we can point from 0º to around 50º depending on the frequency. It's important to check that the aiming direction of the configuration depends on the ratio dencentring/radius of the lens, so for any considered lens with a

diameter big enough to focus the waves properly (see **section 4.6**) we can fix the aiming direction with this ratio.

The problem is that when we move apart the patch from the centre of the lens, its radiation characteristics get worse. The directivity keeps a high value until X/R=0.2, then it falls quite exponentially. The secondary lobe level rises exponentially (linear in dB) and the cross polarization shows an important rise; also, the aiming direction suffers more variations with the frequency when we increase the decentring. This is logical, because the lens is not designed for this kind of configuration. Anyway, depending on the specifications, it may be useful to seize this property for some applications.

The $5\cdot\lambda_0$ lens has a more predictable behaviour (we can check that the graphs are more linear for all the frequencies) and, in general, its secondary lobe level and directivity are better than the $3\cdot\lambda_0$ one.

6.5 Reflections Influence

We have checked that there are some problems with the models depending on the cell size. One of the possible causes is the internal reflections in the lenses. There is a big difference of permittivity between the Macor and the air, and moving the patch from the centre of the lens causes more reflections, because the lens is not designed for a decentred radiation.

Let's check the differences in the lenses with **centred patch** at the central frequency (26GHz):

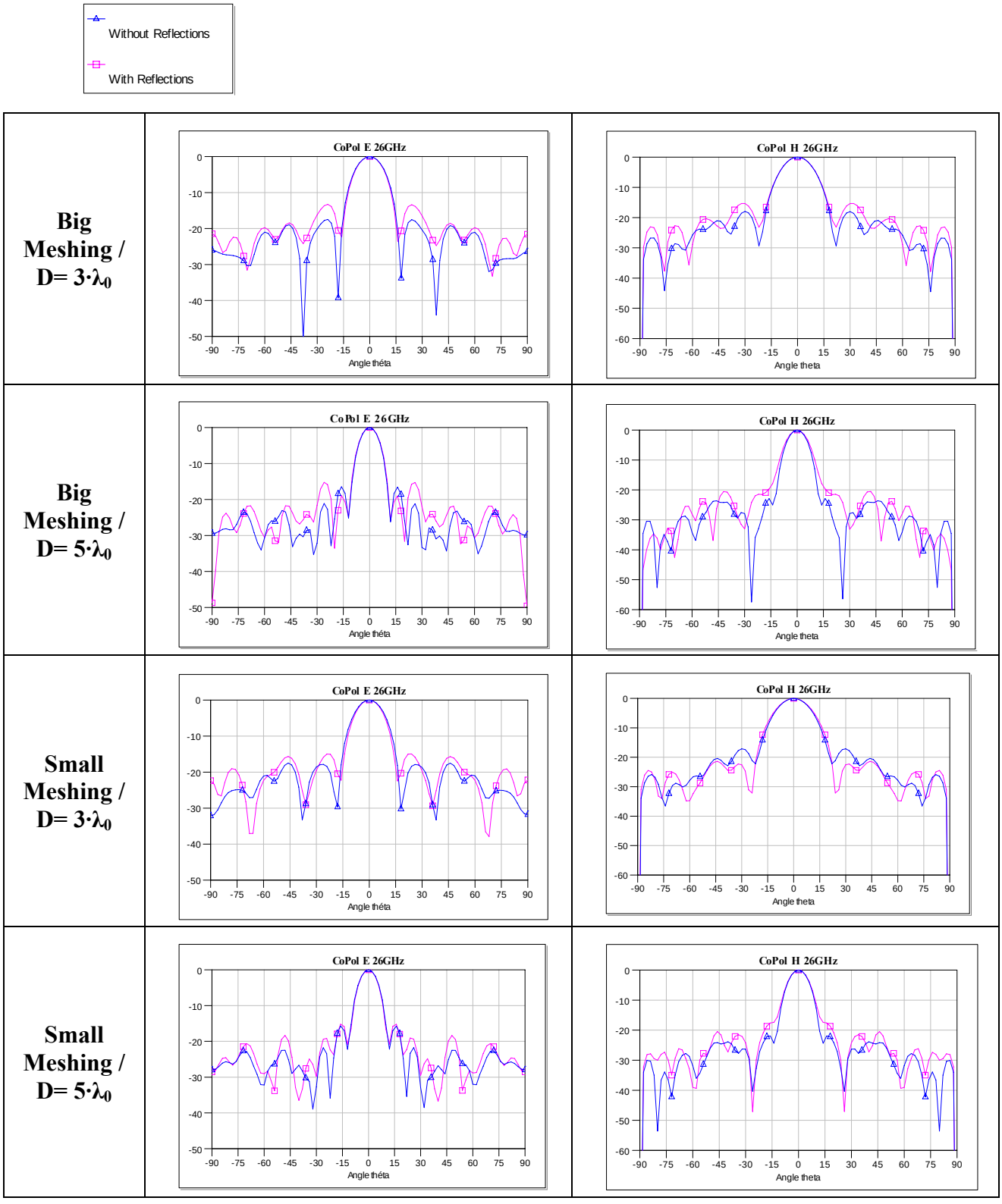

figure 6.8. Radiation Patterns with and without reflections for different sizes and meshings, and centred patch.

In these configurations the reflections are not so important. The side radiation raises a bit, and we get a higher secondary lobe level, but not in a critical way, and the main lobe

hardly suffers changes. Also, these reflections have quite the same influence with both meshings.

To check properly the influence of the reflections on the meshings accuracy we can compare the radiation patterns of the decentred lenses with both meshings without reflections:

Without Reflections	X/R=0.64	Y/R=0.64
$D= 3\cdot\lambda_0$	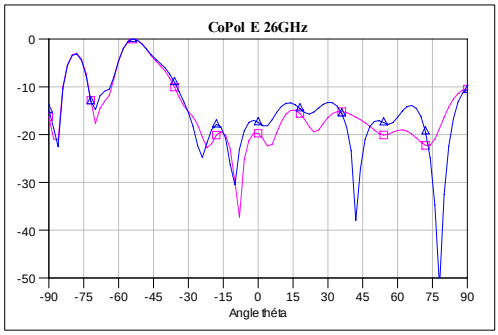	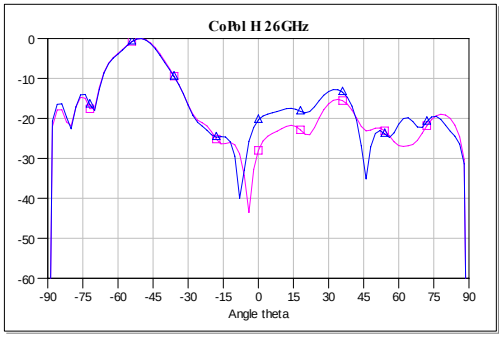
$D= 5\cdot\lambda_0$	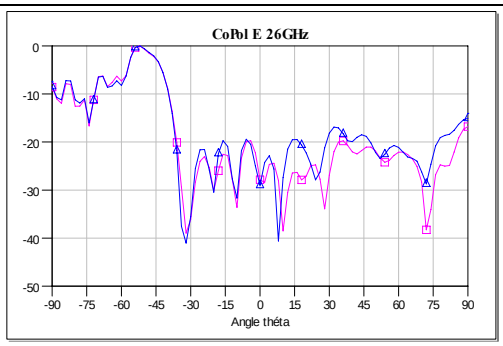	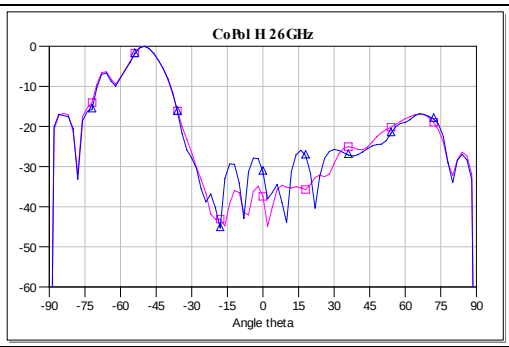

figure 6.9. Radiation Patterns without reflections for different sizes and meshings. decentring X,Y/R=0.64

We check that the radiation patterns in the simulations without reflections are very similar with a small and a big meshing, especially in the main lobe.

This means that the big meshing configuration has problems to model the internal reflection of the lenses, so in the same design, the reflections have a very different influence depending on the meshing we are using.

In conclusion, we have to be careful when we use a model with a big meshing, especially when reflections are important, as in the designs with big differences in the electrical permittivity of the dielectrics.

Now we will draw the synthesis graphs of the simulations **without reflections** and with **small meshing** with the behaviour parameters, as in the previous part. First for a diameter of $\mathbf{3\cdot\lambda_0}$:

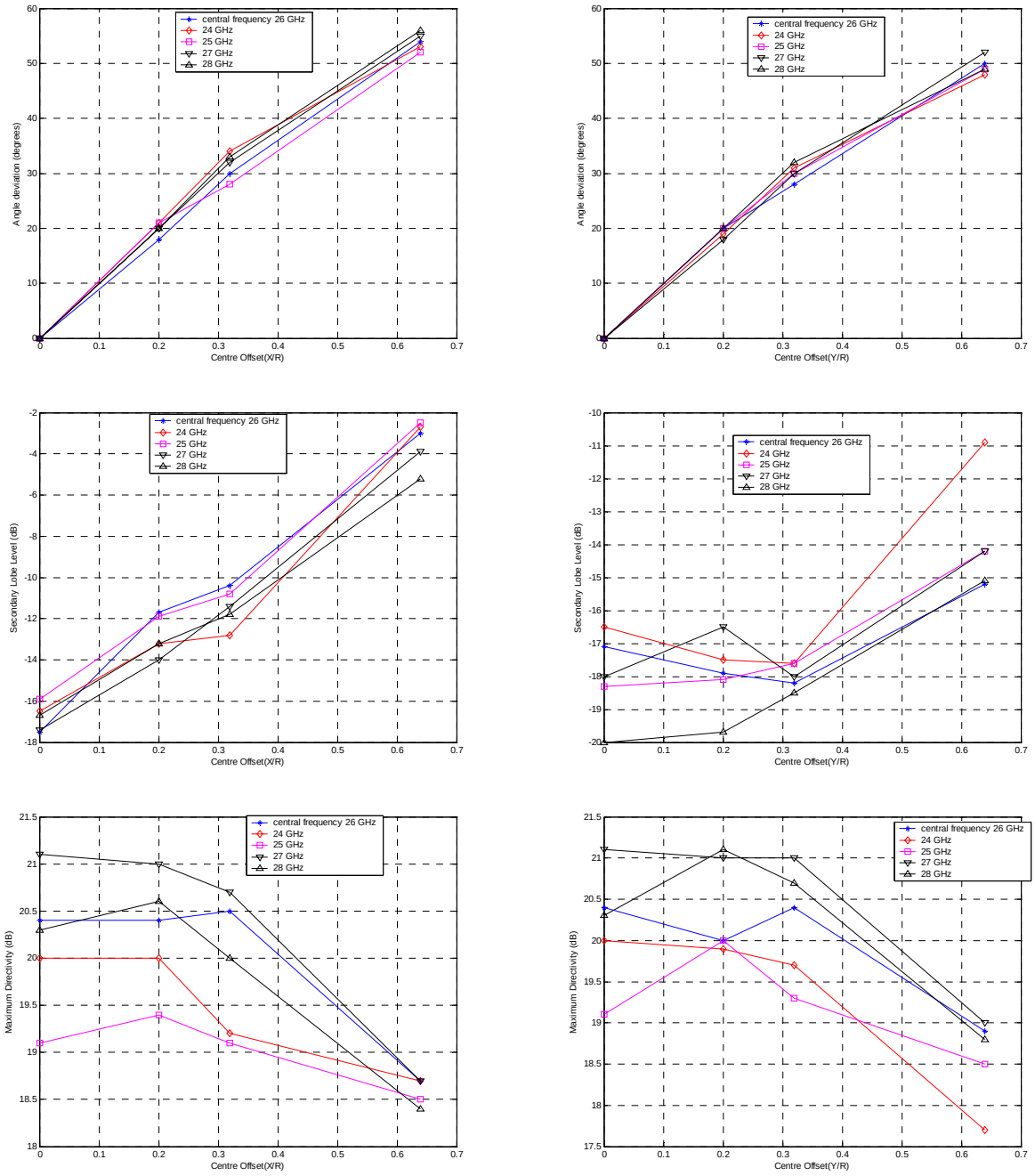

figure 6.10. Performance comparison between decentrings. Macor lens, D=3·λ,.Small meshing.

And also for a diameter of $\mathbf{5 \cdot \lambda_0}$:

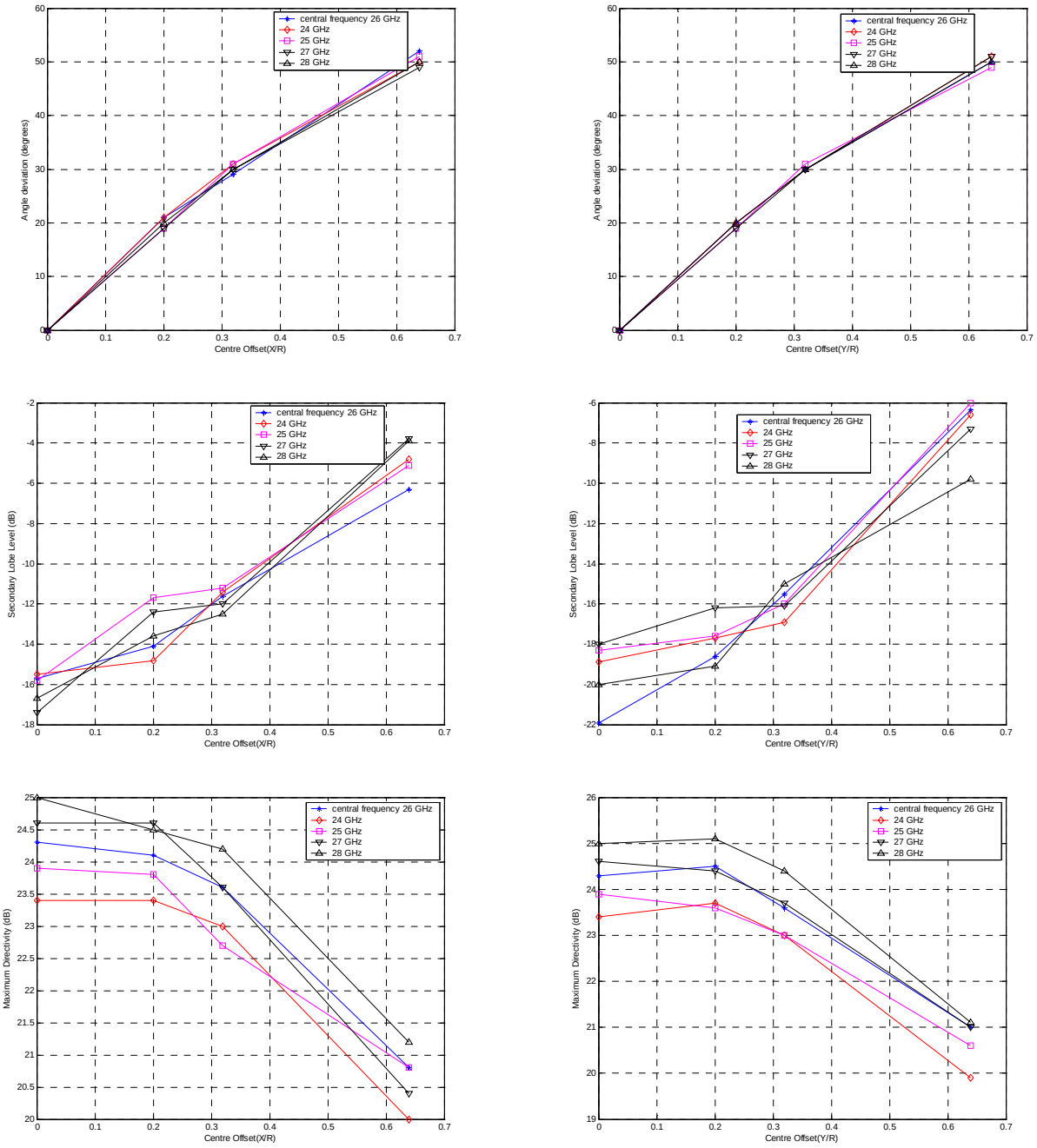

figure 6.11. Performance comparison between decentrings. Macor lens, D=5·λ,.Small meshing.

The behaviour is quite the same we noticed in the complete measures, but it has fewer deviations than when we consider the reflections. The scan angle is almost linear with the decentring, with less variability with the frequency, the secondary lobe level rises exponentially and the directivity starts falling also exponentially from X/R=0.2. The most important difference is in the directivity that does not fall as much as with reflections. Here, with the maximum offset the directivity obtained is about 18 and 20dB, while with reflections it felt under 15dB.

6.6 Anti-Reflections Layer

We have checked that in these configurations the reflections have a big influence on the radiation pattern. We want to reduce this influence in order to get a better performance of these lenses. We are going to add an internal antireflection layer of λ/4 matched at 26GHz (λ_0=11.53mm) to the lenses. The designs would be as follows:

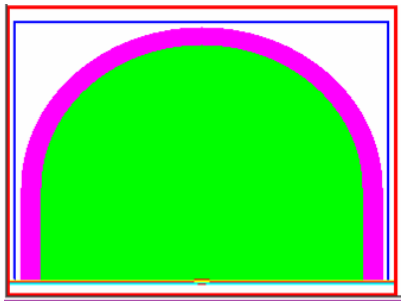

figure 6.12. Substrate lens with anti-reflection layer

The green dielectric is the Maccor. The purple one belongs to the matching layer, which has the following parameters:

$$\varepsilon_{\substack{adaptation\\layer}} = \sqrt{\varepsilon_{Maccor}} = \sqrt{5.67} = 2.3812 \tag{11}$$

$$Thickness = \frac{\lambda_o}{4 \cdot \sqrt{\varepsilon_{\substack{adaptation\\layer}}}} = 1.9mm \tag{12}$$

$$\text{Number of Cells (X and Y direction)} = \frac{Thickness}{\Delta x} = \frac{1.9mm}{0.113mm} = 16.81 \approx 17cells \tag{13}$$

$$\text{Number of Cells (Z direction)} = \frac{Thickness}{\Delta z} = \frac{1.9mm}{0.127mm} = 14.96 \approx 15cells \tag{14}$$

The total diameter of the lens kept constant (that's why we call it an internal layer). Also the parameters of the layer will remain the same for all our configurations, since we are only changing the size and the position of the patch.

We are not going to keep studying the big meshing configurations; we will make the comparisons with the small meshing ones only.

First we will watch the centred configurations:

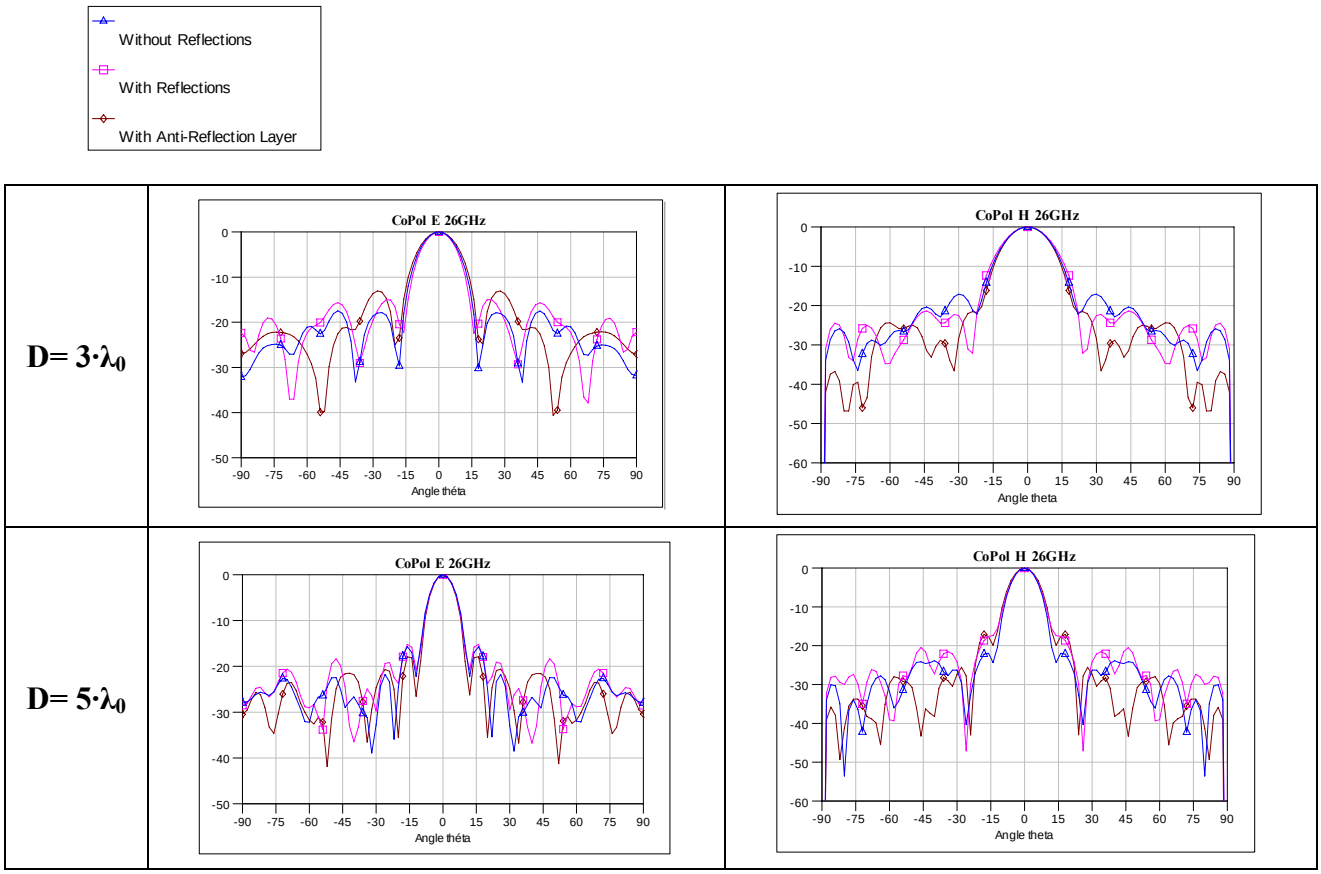

figure 6.13. Radiation Patterns for different sizes and reflections treatment. Centred Patch, 26 GHz.

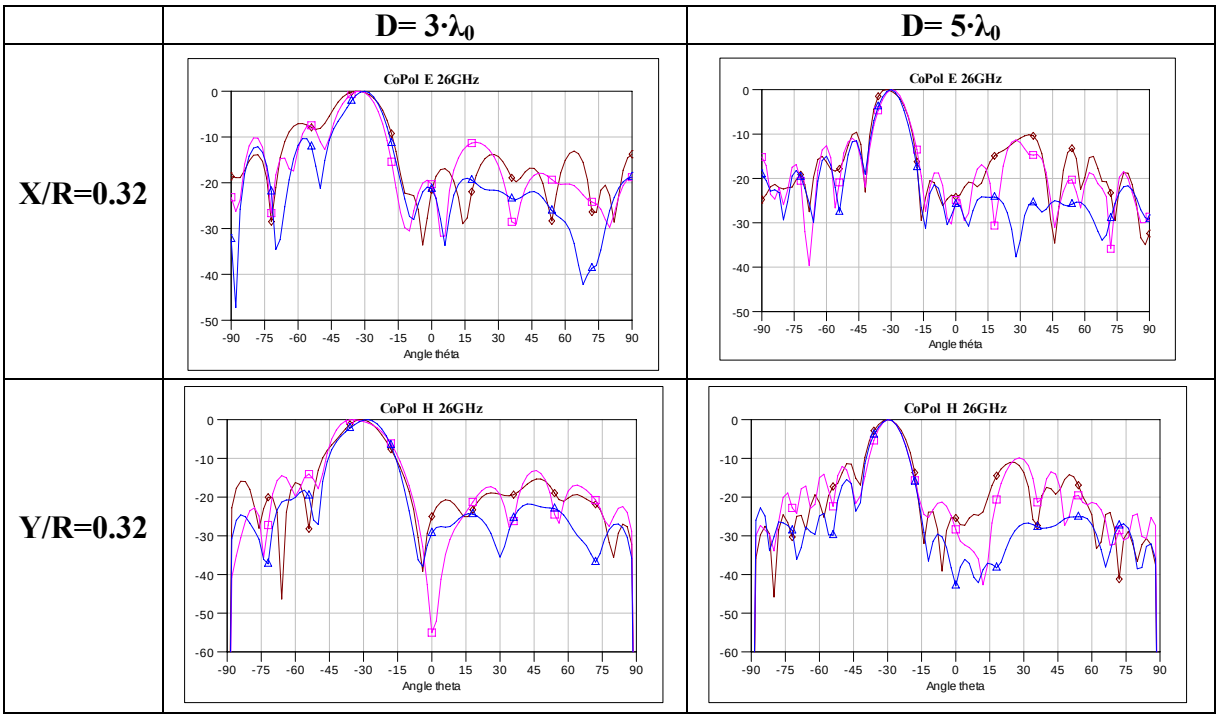

figure 6.14. Radiation Patterns for different sizes and reflections treatment. X,Y/R=0.32,, 26 GHz

	D= 3·λ_0	D= 5·λ_0
X/R=0.64	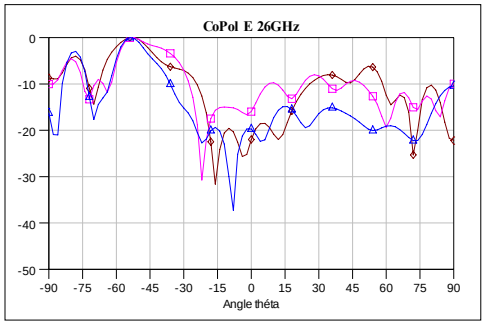	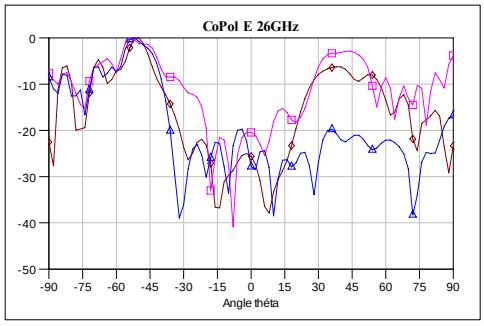
Y/R=0.64	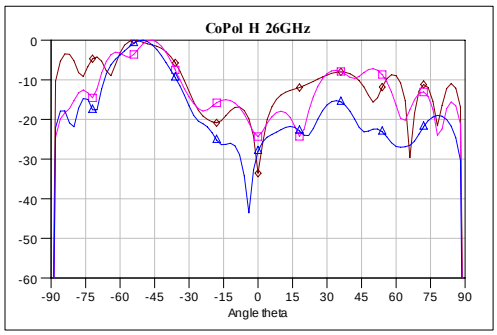	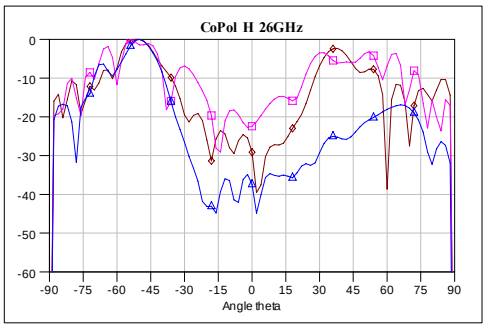

figure 6.15. Radiation Patterns for different sizes and reflections treatment. X,Y/R=0.64, 26 GHz

We don't find important differences in the radiation patterns of the lens with anti-reflections layer and the one without it. The main lobes are still very different from the ones without reflections, and the side lobes are still much higher. In the following graph we will compare the performance figures in order to have an easier way to compare the results:

D= 3·λ_0

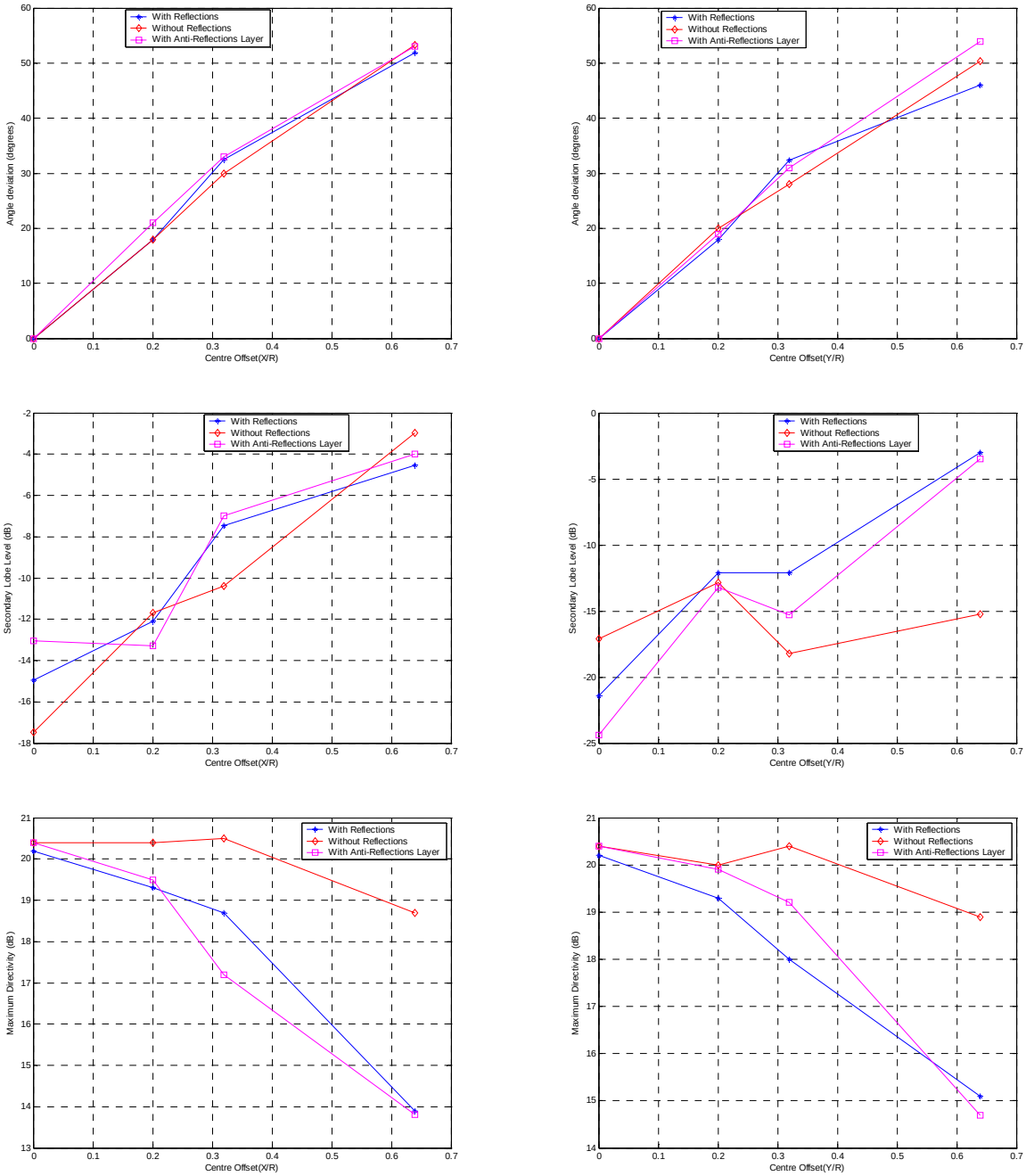

figure 6.16. Performance comparison between decentrings. Macor lens with and without reflections and antireflection layer, D=3·λ_0.Small meshing

D= 5·λ_0

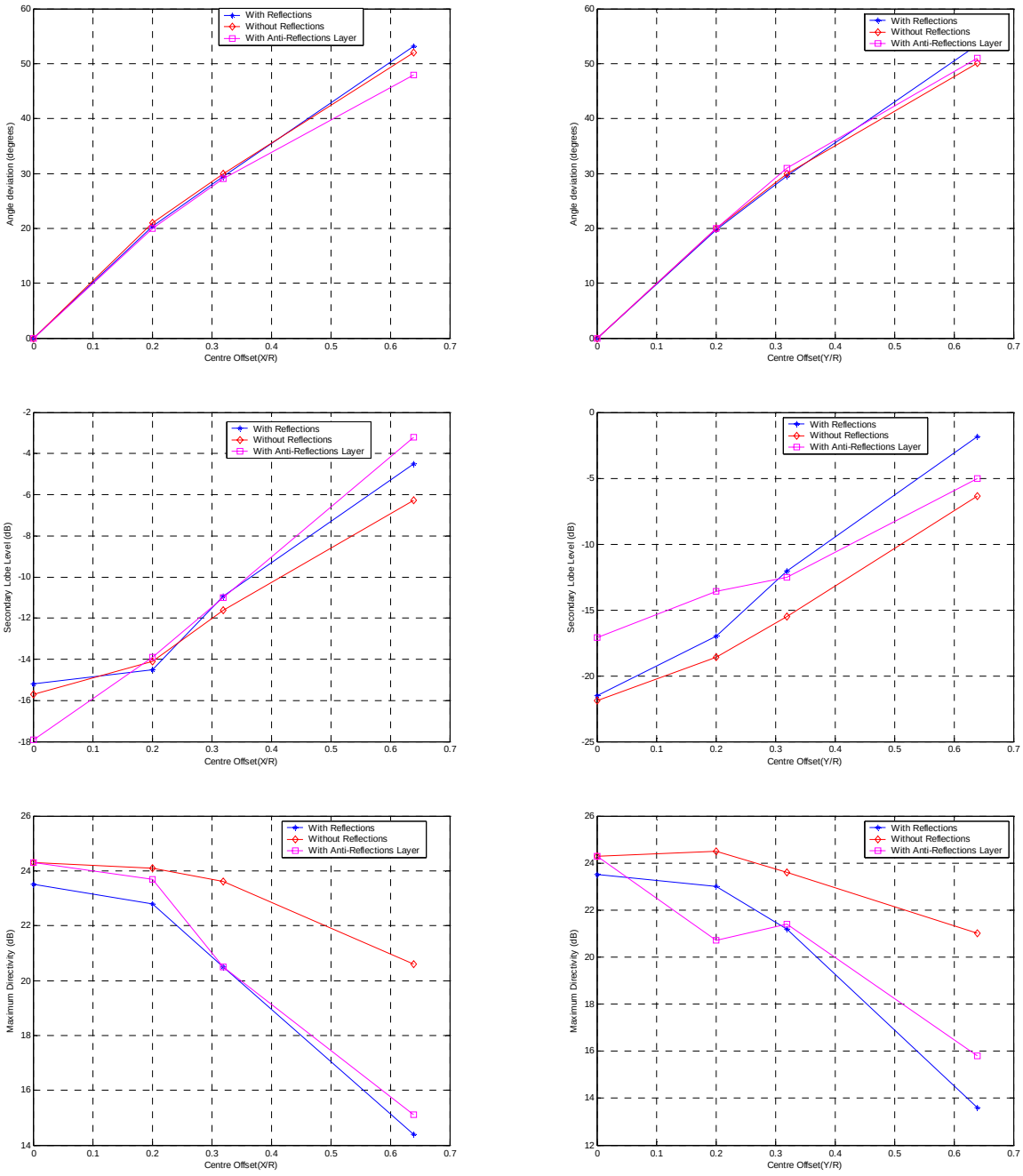

figure 6.17. Performance comparison between decentrings. Macor lens with and without reflections and antireflection layer, D=5·λ_0.Small meshing

It seems that reflections doesn't have a big influence on the pointing direction, in the three cases is quite similar.

Save some punctual exceptions, the secondary lobe level and the directivity are always better when we don't have reflections; even the directivity falls much slower. The anti-reflection layer doesn't make any improvement in the performance; the results are still

more similar to the original configuration than to the simulations without reflections. It seems that it's not worth using it in these configurations.

6.7 Diagonal Decentring

We are going to move the feed patch in the design along a diagonal axis placed at 45º. We will measure the radiation of the lens also in a plane that contains that axis. We will only make simulations with **small meshing.**

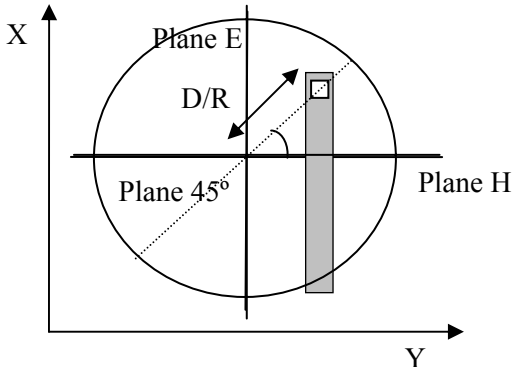

figure 6.18. Patch decentring directions

We are going to make the same simulations as in the other directions, so we will not stop in explanations. Here they are the graphs of synthesis, first for the lens of **$3\cdot\lambda_0$**:

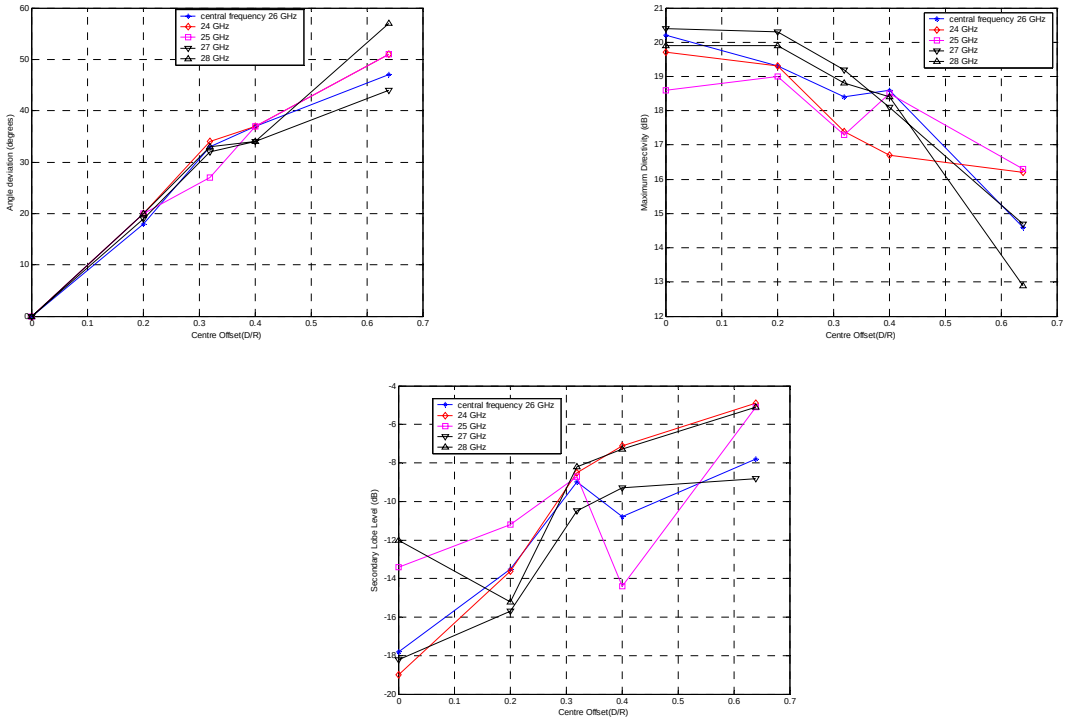

figure 6.19. Performance comparison between diagonal decentrings. Macor lens, D=3·λ,.Small meshing.

For **$5\cdot\lambda_0$:**

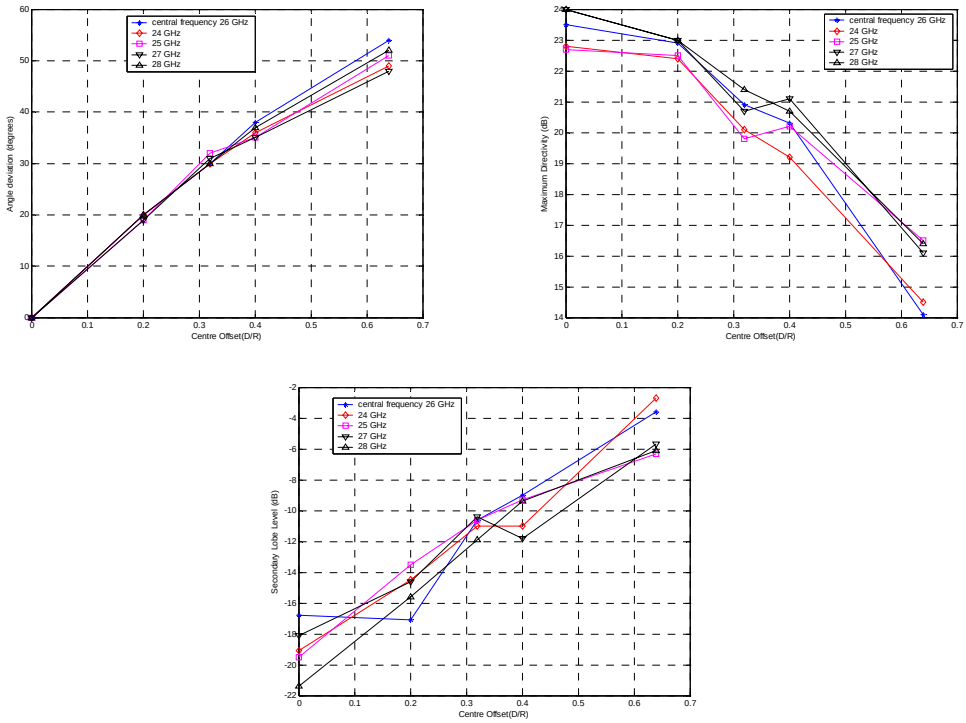

figure 6.20. Performance comparison between diagonal decentrings. Macor lens, D=5·λ,.Small meshing.

The behaviour of the lens with diagonal decentring is exactly the same that in the other directions. In conclusion, the behaviour is very similar in any direction we move the patch, so we presume that the relative position of the patch with the feed line isn't decisive, save for the distance to the lens centre, in the radiation patterns.

6.8 Radiated Power and Losses

Finally, we want to study the radiated power in these configurations, in order to know the influence of the patch position on it. We will introduce some losses in the dielectrics also, first only on the source, and then in the source and in the lens, and we will measure the difference of power. We can see more easily in this table the configurations we are going to simulate:

Configuration	Losses tangent in the Source	Losses tangent in the Lens
1	0	0
2	10^{-3}	0
3	10^{-3}	10^{-4}
4	10^{-3}	10^{-3}
5	10^{-3}	$5\cdot10^{-3}$

figure 6.21. Different configurations for the measure of the radiated power in Macor lens with decentrings.

To obtain the radiated power we will use the same method as in the chapter "Extended Hemispherical Lenses (Eccostock) fed by waveguides", that is, five surfaces that contain the lens where we will make a frequencial cartography in order to obtain the power that goes through them. To make a frequencial cartography we can only run the simulations with one processor, that's why we will only simulate the lens of a $3 \cdot \lambda_0$ diameter, with a bigger design the simulations would take very long.

The following graphs represent the power radiated by the lens without losses for different positions of the patch:

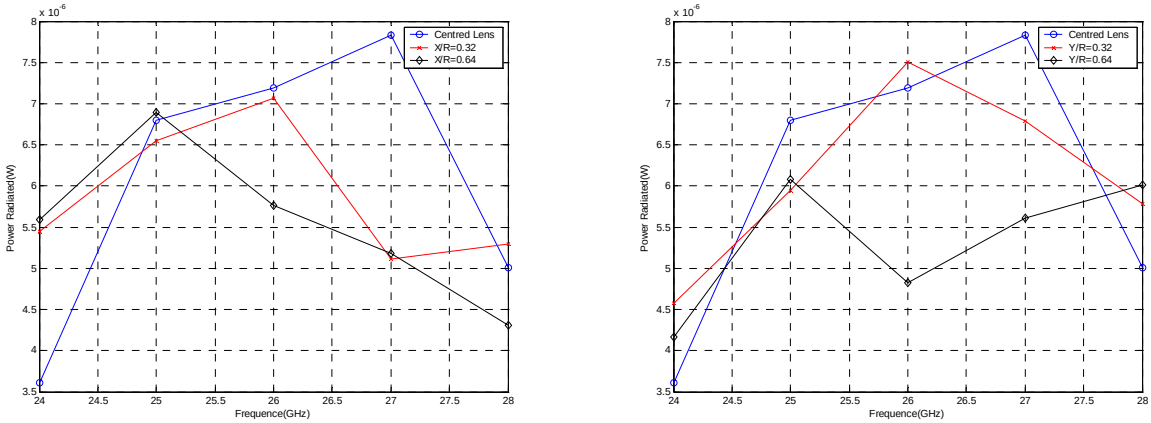

figure 6.22. Radiated power for different decentrings, across E-plane (left), and across H-plane (right), in Macor lens without losses.

We notice a big loss of power with the decentring, the more we move apart the patch form the centre, the smaller the radiated power is. While with the centred patch we have quite plane behaviour for the frequencies between 25 and 27 GHz, the decentred configurations make a shape change that mismatches the power to these frequencies. For example, with an X/R=0.32 and 0.64 the radiated power is higher for frequencies under 26GHz. Also this change is more violent with bigger decentring.

The reflections are the main reason of these changes, we can add the anti-reflection layer we designed before and check the radiated power:

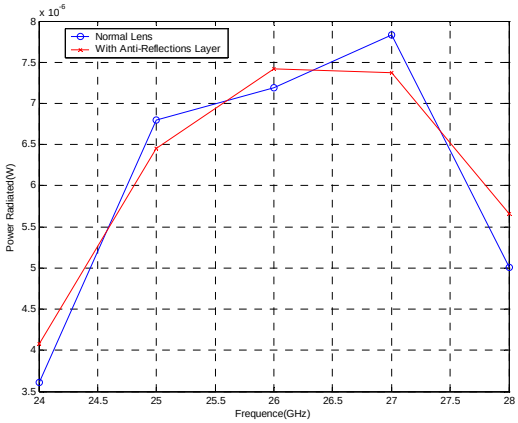

figure 6.23. Radiated power for centred patch, with and without anti-reflections layer.

We will not obtain more power with the anti-reflection layer, just a bit in 26GHz (the layer is matched with that frequency) and a softer shape with the frequency.

Now we will measure the influence of the losses in the dielectric in the radiated power. As in the previous power studies, the logarithmic difference will be the parameter used to check this influence. In the following graph we compare the logarithmic difference between the radiated power of each decentred configuration (for E and H plane) and the configuration with the centred patch, at the central frequency. We have considered the source with losses (tgδ=10^{-3}) to simplify the graph. According to this formula:

$$LD(dB) = 10 \cdot Log\left(\frac{Rad.Power_{XorY\,/\,R\neq 0}}{Rad.Power_{XorY\,/\,R=0}}\right) \tag{15}$$

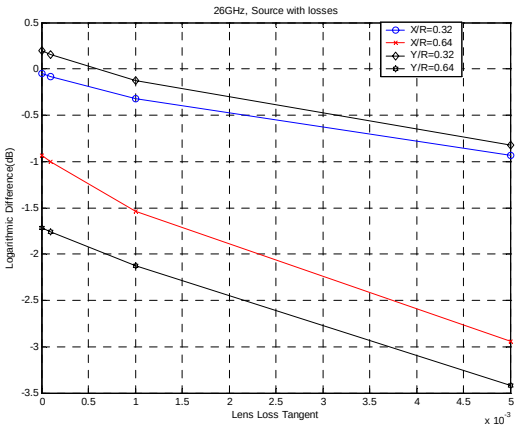

figure 6.24. Logarithmic Difference between the radiated power of some decentred configuration, across E and H plane, and the configuration with the centred patch.

Without losses there is a power loss with the decentring. As expected, the bigger the decentring is, the higher the losses are. There may be considerable differences in these losses with the direction of decentring, though we can see in the graph that for each separation there is a different direction with bigger losses (for 0.32 is the E-plane, and for 0.64 is H-plane).

When we consider the losses in the lens dielectric, the radiated power difference is exponential with the loss tangent, and its rate is bigger with the decentring, that is, with dielectric with losses we have a much bigger power loss with an extreme decentring. In this case, this difference doesn't depend on the direction of the decentring.

We can also calculate the logarithmic difference between the configuration without losses and the ones with losses, though we always consider the source with losses. For the centred configuration, at 26GHz:

$$LD(dB) = 10 \cdot Log\left(\frac{Rad.Power_{tg\delta\neq 0}}{Rad.Power_{tg\delta=0}}\right) \tag{16}$$

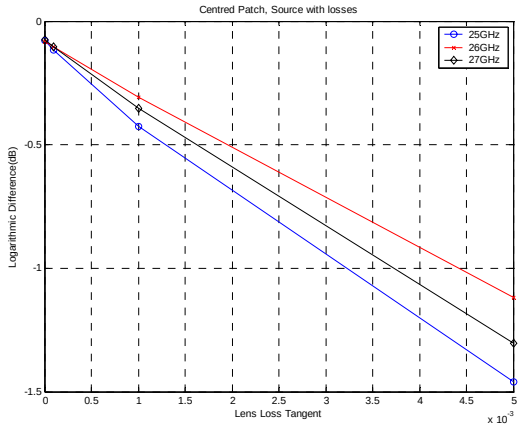

figure 6.25. Logarithmic difference for centred patch lens. Macor with losses in the source.

As we have seen in other studies, the difference is exponential with the losses tangent, that is, the logarithmic difference is linear. The slope in this graph is smaller at the central frequency, while in the other frequencies we have bigger losses for the same tangent.

6.9 Conclusions

- When the patch that feed the lens is decentred, the maximum radiation angle is moved. For two identical lenses but with a different radius, the angle variation is the same when we decentre the same proportion distance/radius.

- The performance of the system gets worse when the patch is decentred. The directivity keeps its value until X/R=0.2 and then it falls sharply. The secondary lobe level rises exponentially with the decentring.

- A lens with a bigger diameter is more stable in frequency, and has a thicker main lobe. So, in pointing applications, it can be considered more accurate.

- The reflections do not have a big influence in the maximum radiation angle nor in the secondary lobe level. However, the directivity falls way faster with the decentring when the reflections are considered.

- Adding an anti-reflections layer does not improve the radiation performance.

Chapter 7: Patches Networks

7.1 Introduction

We want to make a design with a dielectric lens able to aim in several directions instead of only one. In order to achieve that, we are going to feed the lens with several patches, but only one of them will radiate at the same time, so depending on the position of the active one the lens will aim in a certain direction. We want to cover completely a revolution cone. This is important, because we know that the superposition of the radiation with different fed patches will not be plane, as we can check in the following graph taken from the Elefthteriades report [99]:

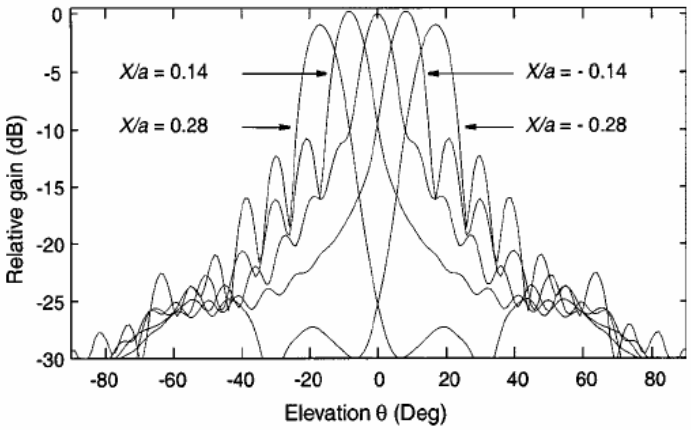

figure 7.1. Superposition of the radiation patterns in a lens fed by patches with different decentrings

So in our design we must consider that there will be a certain fall; this can be varied changing the separation of the patches. We will call overlap to the distance between the crossing point of two consecutive lobes and the maximum of both lobes. This overlap represents the fall of radiated field in dB between two maximums, so we have to try to keep it low if we want our structure to cover properly the area.

We have checked in the previous chapter that the main lobe is wider with lenses diameter of $3\cdot\lambda_0$, than with $5\cdot\lambda_0$, and the maximum scan angle we can get is the same if we use the same ratio decentring/radius of the lens. This means that to cover without radiation falls a range of directions we will need more patches with a diameter of $5\cdot\lambda_0$ than with the smaller one, so in spite of having a worse performance in terms of secondary lobe level and directivity, we have chosen a Macor lens with a $3\cdot\lambda_0$ diameter to design the patches network. Using a $5\cdot\lambda_0$ diameter would mean a more directive and accurate aiming, this is something that could be considered in further studies.

For this study we are going to use a Macor lens and a patch source (see specifications in the appendix B) which will radiate at 26GHz. We will only feed one of the patches in each configuration, so the others will be passive patches, connected by a coaxial line of 50Ω to the ground plane of the source. It's important to notice that, in order to match the passive patches at 26GHz frequency, it has been necessary to increase its area, so in the

designs, the passive patches will be bigger than the active one. We can recognise in the graphs of the design the active and the passive patch with this consideration.

The lens parameters are the following:

Source: Macor patch antenna, matched at 26GHz
Lens:
Dielectric: Macor (ε_r=5.67), without losses
Diameter=3·λ_0=34.6mm
Extension=100%=9.8mm
Simulation:
Cell size:
Δx=0.113mm
Δy=0.113mm
Δz=0.127mm
Simulation Dimensions (cells):
Nx=323
Ny=323
Nz=238

Nº Iterations: 30000
Centre of the patch: X =162; Y=162; Z=11
Centre of the Lens: X =162; Y=162.

Simulation on Idris:

Number of Processors: 1X and 8Y
CPU Time: 25552 seconds
Simulation Class: upp23

In the **Appendix B** is described the design of the printed sources in Imelsi for both the active and the passive patch, and its radiation patterns. For measuring the S11 of the passive patch we have excited the coaxial that links the patch with the ground plane with little tension.

These designs don't intend to be close approximations to the final implementation. We are not considering important problems as the commutation mechanism; in fact we are using slightly different designs for the active and the passive patches, something that is out of question because we have to commutate the sources in real time. This study is more a description of the ideal behaviour that should have this structure; the next part of the work should be trying to find a real implementation for these ideas.

7.2 Two Patches

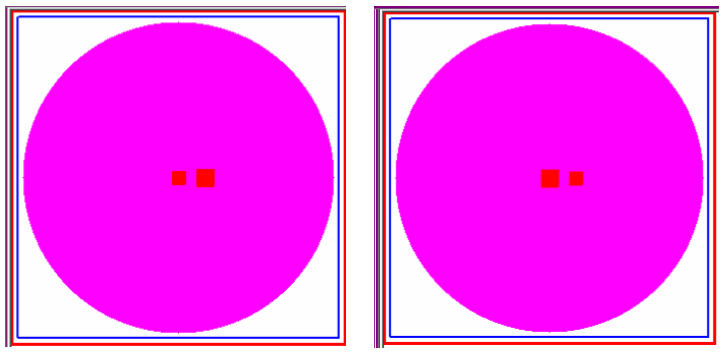

figure 7.2. Two Patches design. The active one is in the centre, the one on its side is passive (left) or the active one is on the side, the one in the centre is passive (right)

First, we want to find a distance between two patches to be used afterwards in our designs. To simplify the fabrication we want as less patches as possible, but in the other side we have to consider the overlap. We will try to have an **overlap around -3dB.**

We don't know the influence that will have the passive patches on the radiation of the lens. The reflected waves inside the lens will eventually reach the passive patches, which are matched at the central frequency, and will be either absorbed or reflected by them. We will study this causality in the following sections.

To measure the overlap, we will take the design showed in **figure 7.2**, a lens with two patches, one in the centre and other at its side, separated a certain distance. We will run two simulations, one with the central patch fed and the other with the side one fed. With this we will obtain two radiation patterns with the main lobe pointing at different directions. We will move the second patch across the H-plane, so the patterns that will be affected are the H-plane ones. We just have to superpose both diagrams and measure the intersection point.

The chosen separation had an overlap of -3.2dB, and a distance between centres of 27 cells (with the cell size, it means 3.051mm). The superposed diagrams remain as follows:

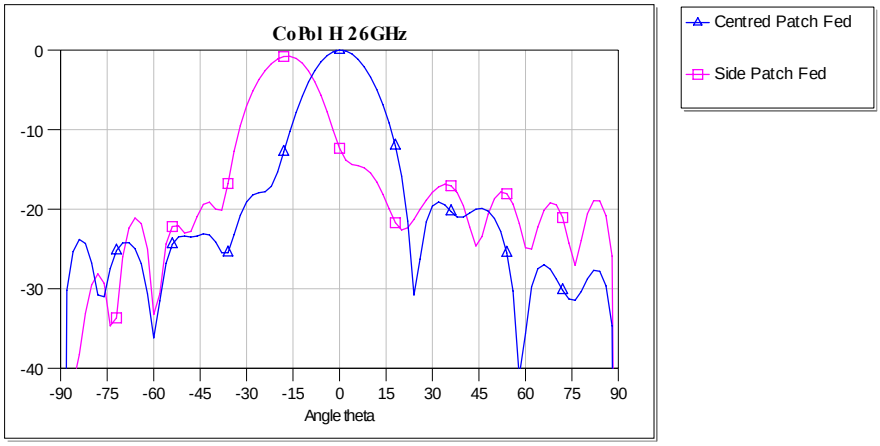

figure 7.3. Radiation patterns of lens fed by centred and side patch, with a distance of 3.051mm

Note: The diagrams are normalized to the maximum of both radiation patterns (the **central** fed patch one in this case)

We notice that the diagrams with central patch fed are not symmetrical; this happens because the design is not symmetrical itself, since there is only a side patch. This means that the passive patch has its influence in the radiation pattern. It would be interesting to compare the patterns in both cases and check if the diagram would be symmetric if we add a second passive patch on the other side, like in the following figure:

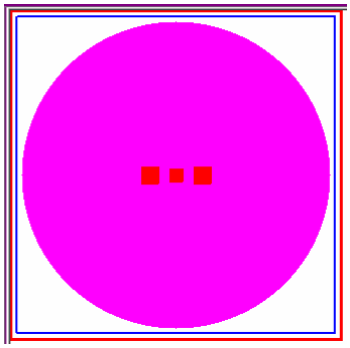

figure 7.4. Three Patches design. Symmetric Design with active patch in the centre and two passive patches at the same distance on its side.

So we are going to simulate the lens fed by the central patch with one, two or no side patch:

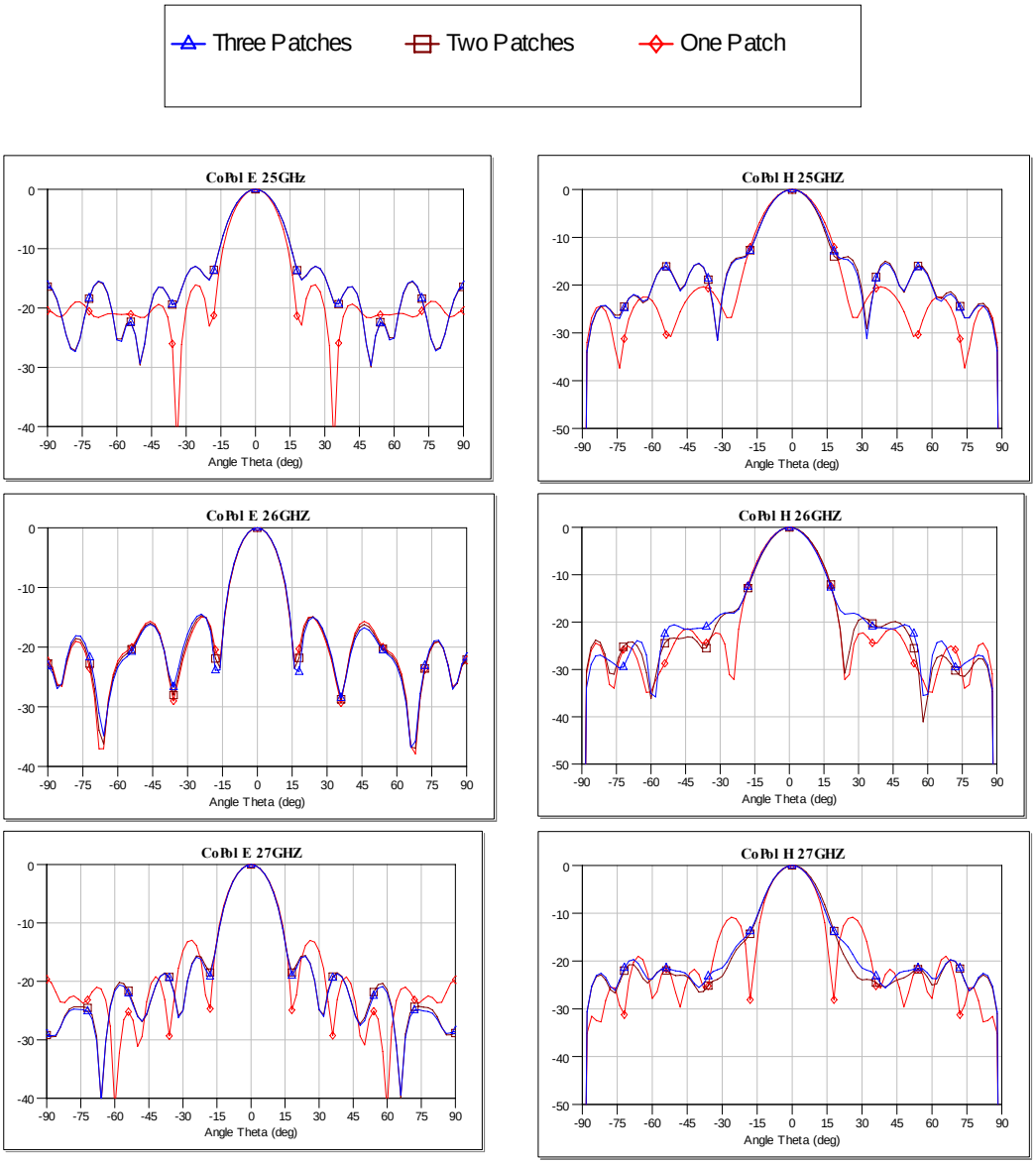

figure 7.5. Macor lens fed by centred patch with one, two or no side passive patch. Simulateds at 25, 26 and 27 GHz.

In the E plane there is no dissymmetry in the diagrams, which was expected, since the design is symmetric in that direction. The effect on the diagram has a strong dependence on the frequency, while with 25 GHz the performance falls when we add the side patches because of the increase of the side lobe level; in 26 GHz it doesn't make an important difference, and with 27 GHz diagram has a lower side lobe level when we add the passive patches.

In the H plane, there is a dissymmetry in the configuration with two patches, as we knew, this issue is bigger with 26GHz, with the other frequencies is difficult to notice. This happens because the passive patch is matched at 26GHz, so the power reflected by its surface has mainly this frequency.

7.3 Linear Array

Now we are going to design arrays of patches to feed the lens, using all the information we have gathered in this and the previous chapters. We have just chosen a distance between patches, and we have an accurate idea of how the behaviour of the lens with the offset of the patch centre for this lens (section **6.4).**

The first array we are studying is the linear one, we will set a line of patches across the E and H-planes, with a distance of 3.051mm. The array will be symmetrical and will have a patch in the centre. We will place two patches on each side of the central patch to make the array, so that the ones of the extremes will have a distance to the centre about 0.35 times the lens radius. A third one would be at 0.53 times the radius, if we watch the graphs we obtained in the study of decentred patches (**figure 6.12**), that separation would mean a bad performance of the patch. The design would be as follows:

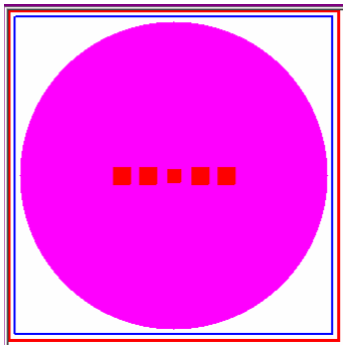

figure 7.6. Linear Array of patches with the central one active. Macor lens with diameter of $3\cdot \lambda_0$.

We can check in the following graphs how the radiation parameters change in each configuration:

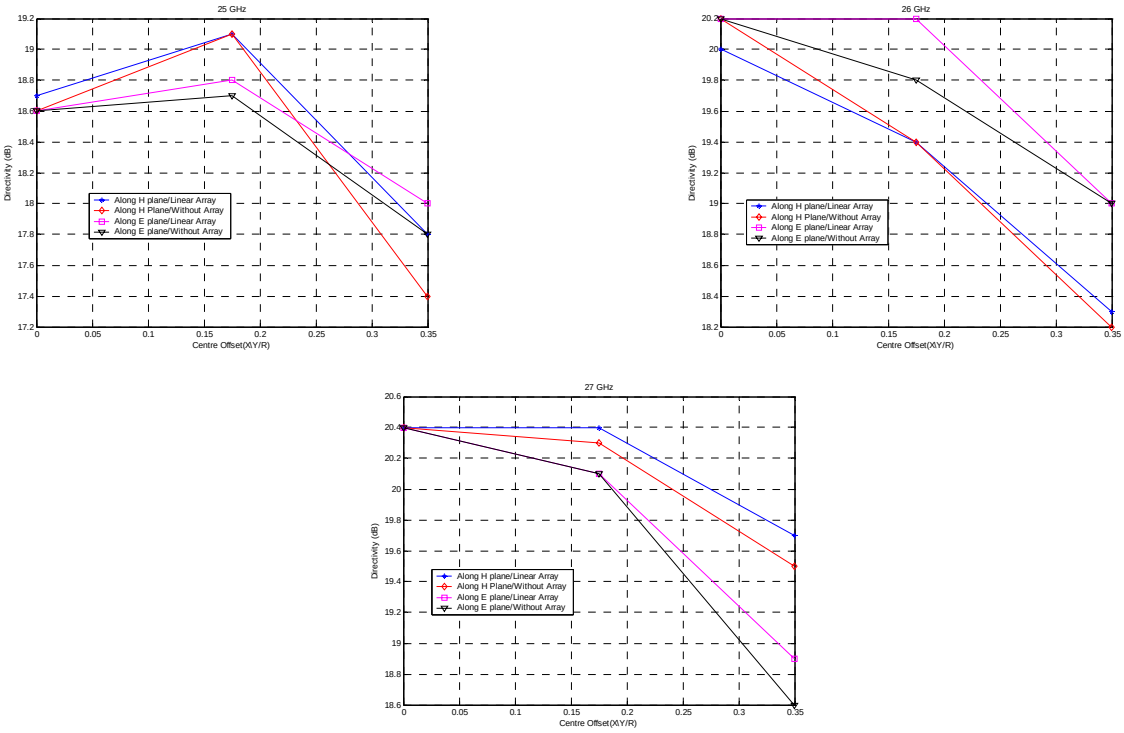

figure 7.7. Directivity variation in Linear Array along E and H plane for decentrings of the fed patches. Compared with fed patches without array.

In all the frequencies simulated, adding the array of patches doesn't mean an important variation of the directivity (tenths of dB), nor the direction is important; the difference for both parameters is always bellow a dB, and it doesn't follow a clear pattern since it has dependence with the frequency.

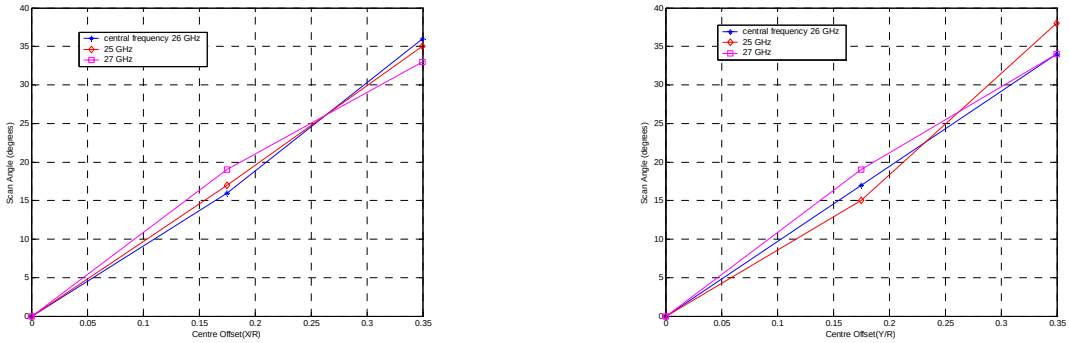

figure 7.8. Scan angle in Linear Array along E and H plane for decentrings of the fed patches.

The scan angle is linear with the decentring, as in the configurations without array that we have already seen in the previous chapters. We can see that in both directions the angle of the maximum is around 35º. This means that working with a frequency of 26GHz the allowed linear sweep is approximately ±35º for this configuration.

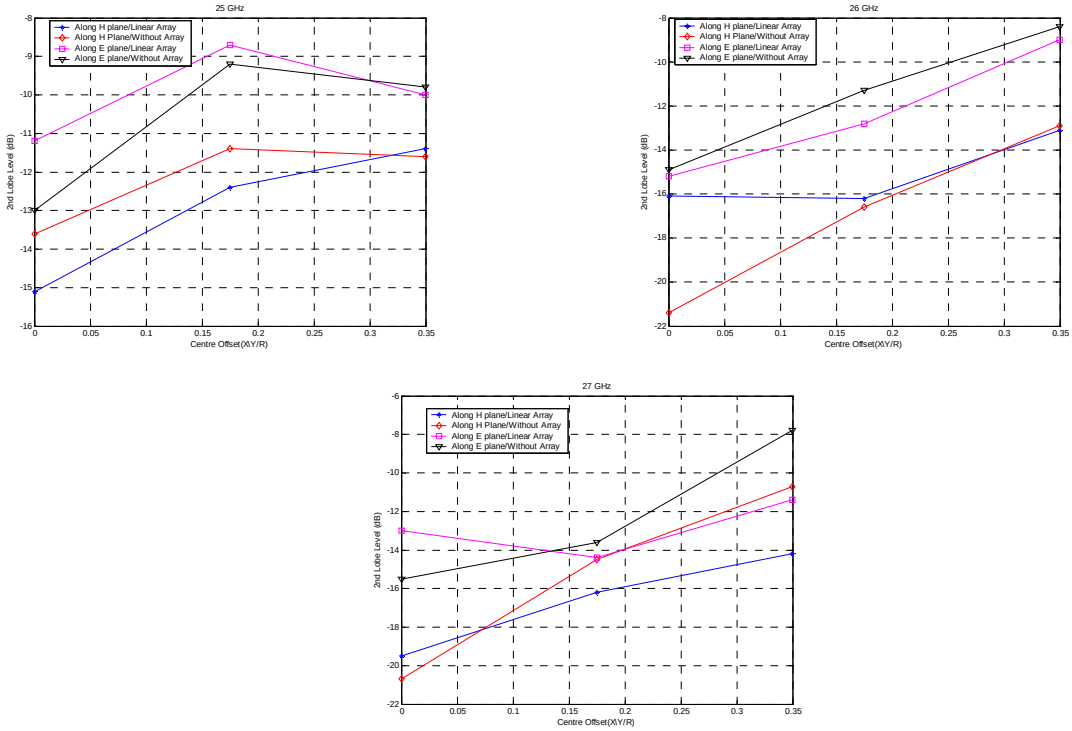

figure 7.9. Side lobe level variation in Linear Array along E and H plane for decentrings of the fed patches. Compared with fed patches without array.

The 2nd lobe level also has similar values with or without array. In conclusion, the radiation of a patch in a linear array is not degraded compared to the active patch only.

7.4 Hexagonal Array

The next array of patches we are going to analyse is the honeycomb hexagonal array, this design has been taken from the Elefthteriades report [99]. It's a bidirectional array composed by several interconnected hexagons, like in the following graph:

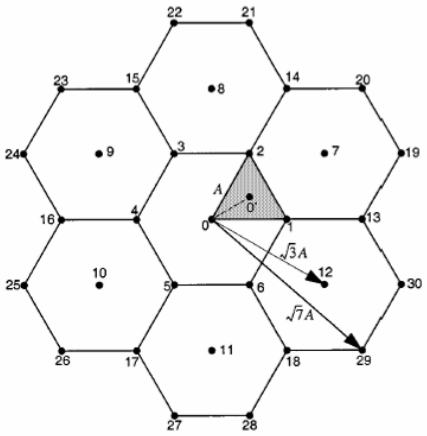

figure 7.10. Honeycomb Patch Array

Each point is a patch, being **0** the central one. The radius of the hexagons is the same as the distance for the linear array; so, if we consider only the patches **16**, **4**, **0**, **1** and **13**, we would have exactly the linear patch of the previous section.

With this configuration we can cover a bigger volume with the same device, in two dimensions, so it's more interesting in order to design aiming applications.

We can make a comparison similar to the one made with the linear array. We have a linear array across the H plane (the above specified), and an approximate one across the E plane (**2** and **6** are not over the axis, but they are close) let's check the graphs with their parameters:

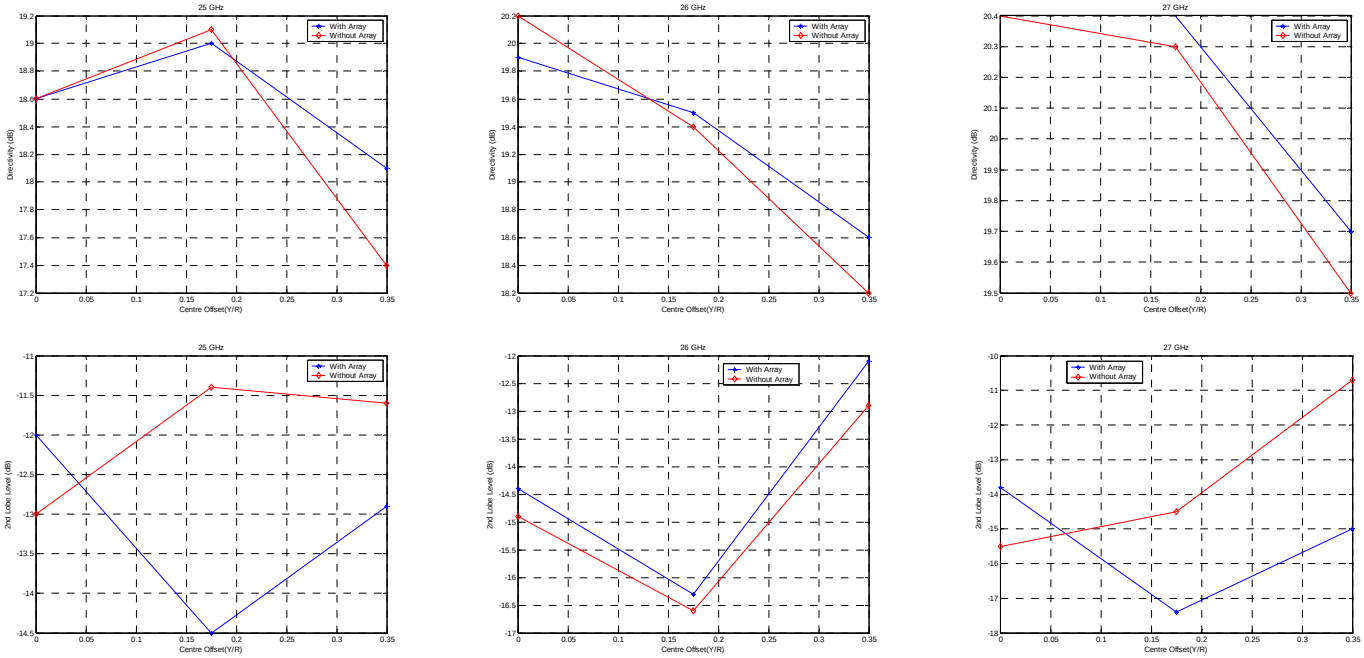

figure 7.11. Directivity, Scan Angle and Side lobe level variation in Linear Array along H plane inside Honeycomb array, for decentrings of the fed patches. Compared with fed patches without array.

We find that the configurations with the patches array don't show degradation in the performance, indeed, the side lobe level has a better behaviour for side frequencies when we have the array. So finally, and also considering the results obtained with a linear array, adding passive patches to the design doesn't degrade the design.

We have simulated all the possible configurations, which involves only one of the squares, because the other three can be deduced by symmetry. We find that the patches on the border don't have good radiation patterns; its directivity is far lower than with the others, except the configuration with **13** as centred patch, which is the extreme patch across the H Plane, since is not so far from the centre. We can check this in the following table, where we have referenced the fed patch with its number in **figure 7.10**:

Freq(GHz)	0	1	13	2	7	19	8	14	20	21
25	18.6	19.0	18.1	18.8	18.5	15	18.8	18.3	16.2	15.8
26	19.9	19.5	18.6	19.9	19.5	16.6	19.6	18.6	17.3	18.3
27	20.4	20.4	19.7	20.1	20.1	16.1	20.0	19.6	16.6	16.4

table 7.1: Table of Directivities (in dB) for all the configurations, (considering active patch plus all the passive ones). The underlined configurations are the ones in the extremes.

These patches, **19, 20 and 21** doesn't need to be implemented because its radiation performance may not be suitable for general specifications.

7.5 Conclusions

- In a patches network, it is possible to have a concrete overlap value between the different lobes of the radiation by setting a distance between the patches. Then, there will not be any blind point in the volume covered by the radiating system.

- A linear array has been designed. Considering an overlap of -3.2dB, five patches have been placed across the E or H plane. An angle sweep of ±35º can be obtained with an acceptable loss of performance.

- A bi-dimensional array can be designed from the previous linear array, adding patches in the other directions, shaping a honeycomb array with little patches hexagons with the fixed distance previously calculated as the radius. The system can cover a revolution cone.

- The passive patches in the arrays do not degrade the radiation of the system. The performance is almost the same as if it were an only patch radiating in the desired direction.

8. Conclusions

In this project, several radiating configurations with dielectric lenses have been studied. The first objective was to obtain the general behavior of these lenses depending on its parameters: size, extension and permittivity. Several simulations were made sweeping these parameters, the following conclusions could be obtained watching the results:

- In the design of the lens, the upper extension is the most decisive pattern, since is the one that has the biggest influence in the focalisation of the radiated wave. The synthesized ellipse is the configuration that focalise the wave to the infinite, and it is the one with whom we obtain the best results in terms of directivity and secondary lobe level. However, the lower extension, which actually may be more a fabrication necessity than a parameter of design, has proven to have no importance.

- The size of the lens also has influence on the focalisation. With bigger diameters, better directivities can be obtained, despite of the increase in the size and the weight. If we want to reduce its size to permit its use in very exigent application, we have to be careful because with small diameters the lens may not focalise properly. From a diameter of $3 \cdot \lambda_0$ we have always obtained suitable results.

- The permittivity does not have a big influence on the radiation performance compared with the other parameters.

- The S11 keeps its level bellow -10dB with the $3 \cdot \lambda_0$ and $5 \cdot \lambda_0$ diameters. Permittivity and lower extension does not have an important influence on this parameter.

Then, a further research was made with a specific dielectric, the Eccostock. Here, the study would stress the importance of the frequency, the reflections and the radiated power. A ground plane was also added. The previous results would help to reduce the number of simulations needed, because the most important configurations are already known:

- Adding a ground plane to the lens is only suitable when we work with a synthesized ellipse one, otherwise the side lobe level increases a lot. However, it does not have an important influence on the directivity.

- The directivity of the waveguide without lenses has an exponential increase with the frequency. The only configuration that respects this relationship is the synthesized ellipse lens, others have a chaotic behavior.

- The configurations that radiates more power, that is, they have fewer reflections, are the ones with its extension between 50% and 100%. The ground plane does not have an important influence on the radiated power.

- When the lens dielectric has losses, the difference of radiated power increases exponentially with the losses tangent. The rate of the exponential is minimal at the central frequency, while with a different one it has a little increase.

- A big amount of the radiated power is in the reflections. The first incident wave conforms a radiation pattern with a clean main lobe and its maximum directivity, while the next ones increase the secondary lobe level.

The synthesized ellipse lens has been chosen for the next part of the project. The objective is to design a configuration that points in a direction different than 0º of elevation. In order to do this, it is necessary to move the feed from the centre of the lens (here, printed antennas will be used). The next study intends to obtain the behavior of the lens with different feed decentrings:

- When the patch that feed the lens is decentred, the maximum radiation angle is moved. For two identical lenses but with a different radius, the angle variation is the same when we decentre the same proportion distance/radius.

- The performance of the system gets worse when the patch is decentred. The directivity keeps its value until X/R=0.2 and then it falls violently. The secondary lobe level rises exponentially with the decentring.

- A lens with a bigger diameter is more stable in frequency, and has a thicker main lobe. So, in pointing applications, it can be considered more accurate.

- The reflections do not have a big influence in the maximum radiation angle nor in the secondary lobe level. However, the directivity falls way faster with the decentring when the reflections are considered.

- Adding an anti-reflections layer does not improve the radiation performance.

Finally, several patches placed in different positions in the base of the lens are used to radiate. This is called patches network, only one of the patches will be fed each time, and the rest will be passive. Here, several distributions of the patches will be studied:

- In a patches network, it is possible to have a concrete overlap value between the different lobes of the radiation by setting a distance between the patches. Then, there will not be any blind point in the volume covered by the radiating system.

- A linear array has been designed. Considering an overlap of -3.2dB, five patches have been placed across the E or H plane. An angle sweep of ±35º can be obtained with an acceptable loss of performance.

- A bi-dimensional array can be designed from the previous linear array, adding patches in the other directions, shaping a honeycomb array with little patches hexagons with the fixed distance previously calculated as the radius. The system can cover a revolution cone.

- The passive patches in the arrays do not degrade the radiation of the system. The performance is almost the same as if it were an only patch radiating in the desired direction.

After this study and watching our results we can highlight some important ideas. The lens subtract has proven to be a very useful element for focalising antennas of a small size, we just have to watch the measured performance. We can obtain a directivity about 15 dB higher than without the lens, the antenna has a better adaptation to the medium, and we can handle the parameters to get different performances.

Decentring the feed of the lens permit us to aim in a different direction that the perpendicular one. This aim direction is linear with the decentring of the lens, and depends only on the ratio of decentring with the radius of the lens. So, even using lenses with different diameters, we obtain the same aiming directions. This is very useful for pointing applications, using a commutation system for the feed we can design a structure that radiates selectively in several directions. In order to do this, we have designed some patches network that could work for these applications.

The test of these designs has accomplished our expectatives, we can make sweeps of the pointing directions across one or two dimensions, and the presence of more metallic patches in the source than usually doesn't degrade the performance of the system.

In further studies it would be interesting to study decentred configurations with lenses with a different extension, since we have not made sure if the synthesized ellipse is the optimum lens for our objectives. We also could increase the size of the lenses used, in order to have a more accurate aiming system and better radiation patterns.

It's also necessary to consider a real implementation of the patches networks design, specially regarding to the problem of the commutation, which would imply several changes in the source fabrication.

It could also be interesting to study the use of the circular polarization in the excitation, since it has properties that make it more suitable for applications nowadays.

APPENDIX

A. Lenses and Simulation Dimensions

Chapter 4

Table 1: Diameters of the lenses

ø	**λ_0**	**$3\lambda_0$**	**$6\lambda_0$**
ø(mm)	5	15	30
Nº Cells	50	150	300

Table 2: Extension in mm {$L_{100\%}$(mm)}:

ø(mm)\\ε_r	**2.2**	**3.8**	**11.7**
5	3.16	1.90	0.87
15	9.5	5.72	2.63
30	19.0	11.44	5.27

Table 3: Number of upper extension cells in each configuration {Lup(Nº Cells)}:

%\\ε_r		**2.2**			**3.8**			**11.7**	
ø(mm)	**5**	**15**	**30**	**5**	**15**	**30**	**5**	**15**	**30**
25	8	24	48	5	14	29	2	7	13
50	16	48	95	10	29	57	4	13	26
75	24	71	143	14	44	86	7	20	40
100	32	95	190	19	57	114	9	26	53
125	40	119	238	24	72	143	11	33	66
150	47	143	285	29	86	172	13	39	79

Table 4: Number of FDTD cells we have to add for each lower extension {Ldown(Nº Cells)}:

%\\ε_r	**2.2**	**3.8**	**11.7**
ø(mm)*	**30**	**15**	**15**
25	0	-	-
50	50	0	0
75	95	-	-
100	150	30	0

*These diameters are the ones with whom we have made the study of *Ldown* for each material

Table 5: Number of Cells of the FDTD Simulation with Lup=Ldown=0%

ø(mm)	**5**	**15**	**30**
Nx	64	164	314
Ny	64	164	314
Nz*	82	151	226

*: To calculate the number of cells of the FDTD simulation with other extension, we only have to add to Nz the number of cells of both the Lup and Ldown extension, which can be obtained looking up respectively in the Table 3 and 4. There are some configurations with lower extension where we don't have to add cells to the FDTD design, that's because its length doesn't overpass the length of the waveguide.

Chapter 5.

We are using a lens diameter of $6\lambda_0$ in all the simulations, so the number of cells of the simulations will always be the same in the *x* and *y* directions. Using a central frequency of 60GHz, the diameter of the lenses are of 30mm. The cell size in our simulations in IMELSI is 0.1mm.

To simulate a lens with all the extensions equal to 0% we just need these cells:

Nº x cells	**Nº y cells**	**Nº z cells**
314	**314**	**226**

We don't use 300 cells because we need more space to place the Huygens surface with a minimum distance from the PML border and the lens. In the *z* direction we have to consider the length of the waveguide (7mm) and the Radius of the Lens (15mm), plus the free space we told before about.

When we want to simulate a lens with a higher upper extension we just have to add the cells that this extension requires. For the lower extension, we don't need to add more cells:

Lup	**Extension Length (mm)**	**Nº of Cells**
0%	0	0
50%	3.151	32
75%	4.725	47
100%	6.303	63
125%	7.879	79
150%	9.455	95

Notice that we have to make a little trim to adjust the extension length to the cell resolution. Though the size will not be exact, this difference is negligible.

Chapter 6

Big Meshing, Diameter=3·λ_0

Source: Macor patch antenna, 26GHz

Lens:
Dielectric: Macor (ε_r=5.67)
Diameter=3·λ_0=34.6mm
Extension=100%=9.8mm
Simulation:

Cell size:	Simulation Dimensions:
Δx=0.280mm	Nx=140
Δy=0.280mm	Ny=140
Δz=0.254mm	Nz=123

Nº Iterations: 15000
Centre of the patch: X =71; Y=71; Z=9
Centre of the Lens: X =71; Y=71.
Number of Processors: 1X and 8Y
Simulation Class: upp23

Big Meshing, Diameter=5·λ_0

Source: Macor patch antenna, 26GHz

Lens:
Dielectric: Macor (ε_r=5.67)
Diameter=5·λ_0=57.7mm
Extension=100%=16.3mm

Simulation:

Cell size:	Simulation Dimensions:
Δx=0.280mm	Nx=222
Δy=0.280mm	Ny=222
Δz=0.254mm	Nz=193

Nº Iterations: 20000
Centre of the patch: X =112; Y=112; Z=9
Centre of the Lens: X =112; Y=112.
Number of Processors: 1X and 8Y
Simulation Class: upp23

Small Meshing, Diameter=3·λ_0

Source: Macor patch antenna, 26GHz

Lens:
Dielectric: Macor (ε_r=5.67)
Diameter=3·λ_0=34.6mm
Extension=100%=9.8mm

Simulation:

Cell size:	Simulation Dimensions:
Δx=0.113mm	Nx=323
Δy=0.113mm	Ny=323
Δz=0.127mm	Nz=238

Nº Iterations: 40000
Centre of the patch: X =162; Y=162; Z=11
Centre of the Lens: X =162; Y=162.
Number of Processors: 1X and 8Y
Simulation Class: upp23

Small Meshing, Diameter=5·λ_0

Source: Macor patch antenna, 26GHz

Lens:
Dielectric: Macor (ε_r=5.67)
Diameter=5·λ_0=57.7mm
Extension=100%=16.3mm

Simulation:

Cell size:	Simulation Dimensions:
Δx=0.113mm	Nx=527
Δy=0.113mm	Ny=727
Δz=0.127mm	Nz=373

Nº Iterations: 40000
Centre of the patch: X =264; Y=264; Z=11
Centre of the Lens: X =264; Y=264.
Number of Processors: 1X and 8Y
Simulation Class: upp23

B. Printed Sources dimensions and radiation

Macor Source (Active)

Big Meshing

Z-X

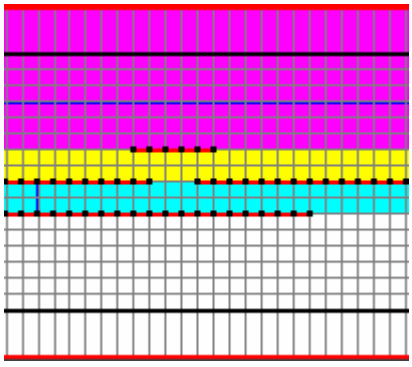

Z-Y

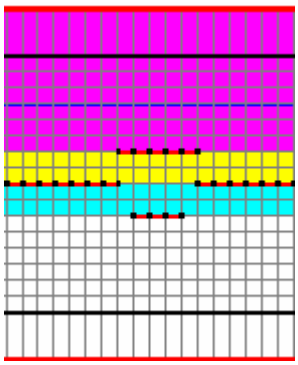

Dielectrics Permittivity (ε_r):
Blue: 2.20
Yellow: 6.15
Purple: 5.67
Blue Line (inside the Macor): Huygens Surface

All of them with no losses.

Dimensions(μm):

Δx=280	Line Width: 3 cells=840
Δy=280	Patch side: 5 cell=1400
Δz=254	Nx=Ny=100 cells=28,000
	Nz=14 cells=3556

Radiation Pattern, simulated at 26 GHz:

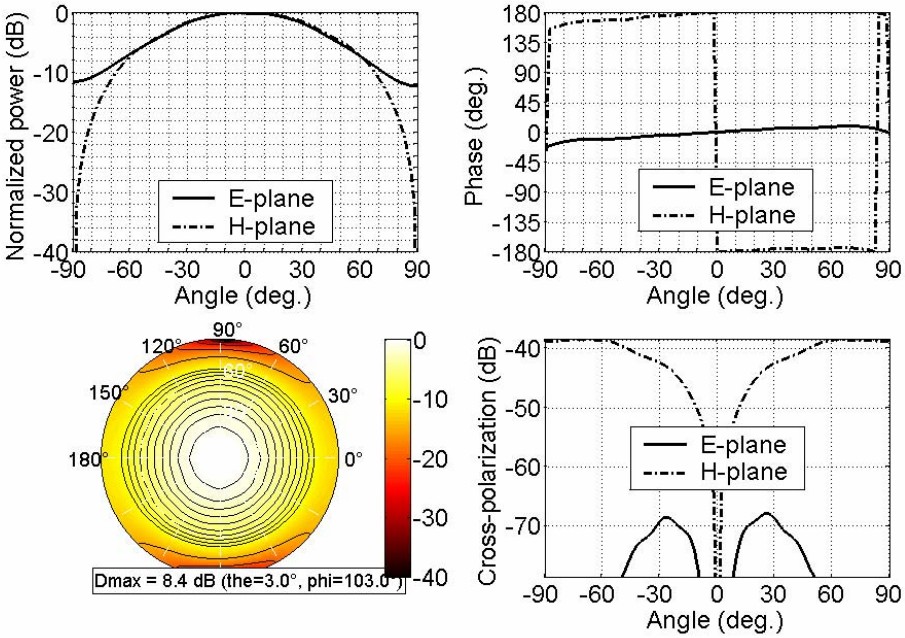

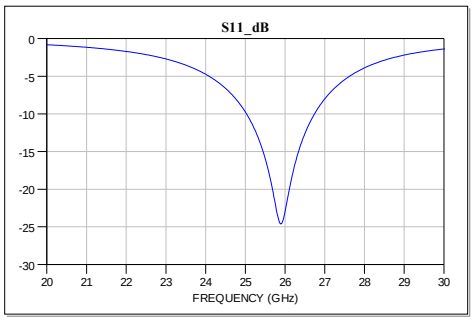

Matched at 26 GHZ

Small Meshing:

Z-X

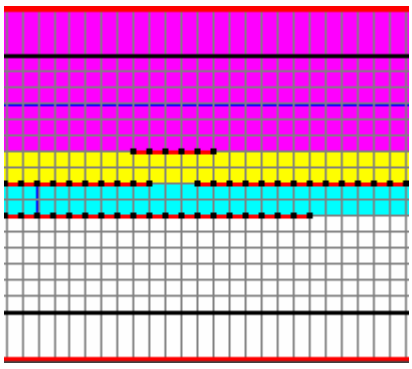

Z-Y

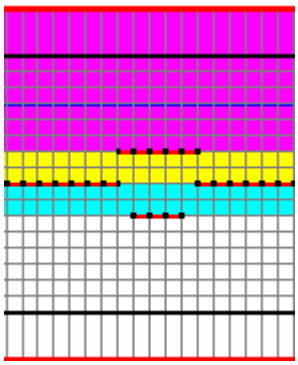

Dielectrics Permittivity (ε_r):
Blue: 2.20
Yellow: 6.15
Purple: 5.67
Blue Line (inside the Macor): Huygens Surface

All of them with no losses.
The field measures will be all taken in 26GHz.
5000 Iterations

Dimensions(μm):

Δx=113	Line Width: 7 cells=791
Δy=113	Patch side: 13 cell=1469
Δz=127	Nx=Ny=301 cells=34,013
	Nz=17 cells= 1968

Radiation Pattern, simulated at 26 GHz:

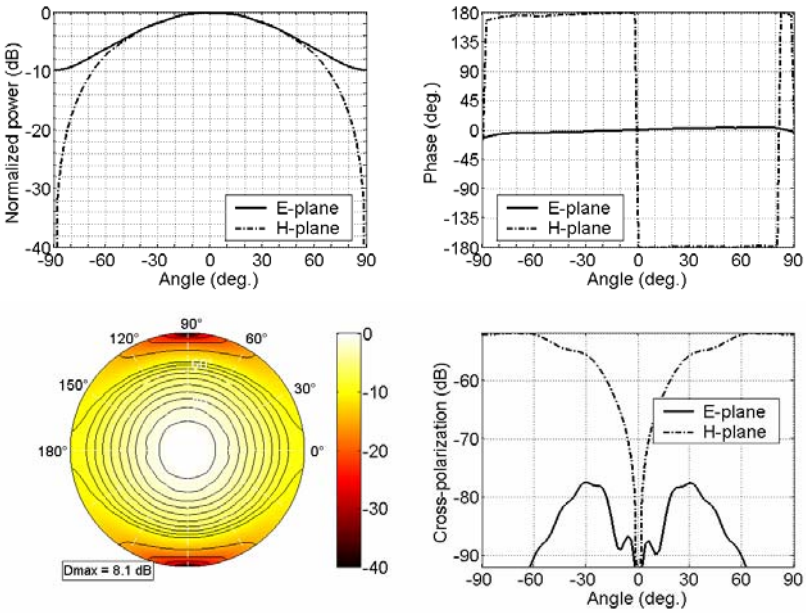

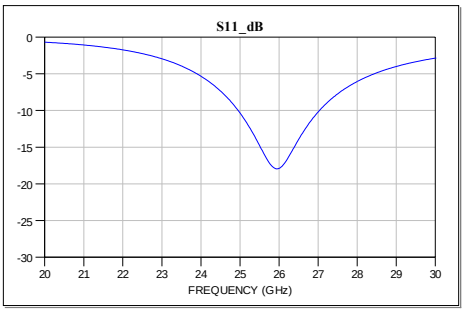

Matched at 26 GHZ

Macor Source (Passive)

Z-X

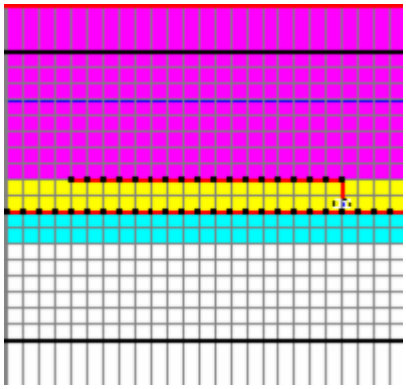

Z-Y

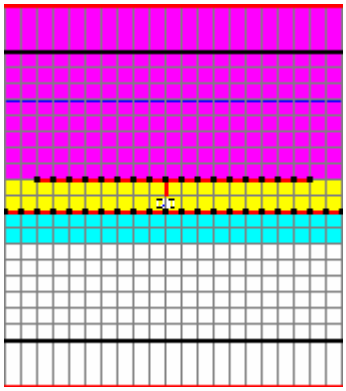

Dielectrics Permittivity (ε_r):
Blue: 2.20
Yellow: 6.15
Purple: 5.67
Blue Line (inside the Macor): Huygens Surface

All of them with no losses.
5000 Iterations

Dimensions(μm):

Δx=113	Patch side: 17 cell=1921
Δy=113	Nx=Ny=123 cells=13,899
Δz=127	Nz=18 cells= 2286

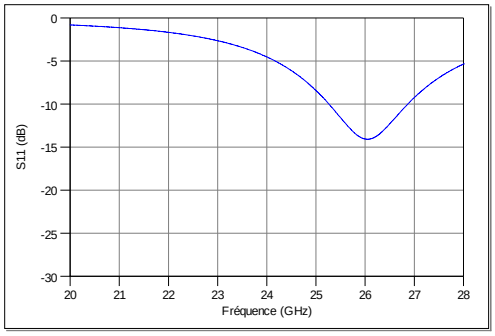

Matched at 26 GHZ

C. Resumen en Español

1. Introducción

Al aumentar la demanda de sistemas de comunicación *wireless* de banda ancha, el espectro de microondas empieza a congestionarse o simplemente no puede satisfacer los crecientes requerimientos de velocidad. Es por esto que la frecuencia de operación está desplazándose cada vez más hacia las ondas milimétricas. Esto ha ocasionado que en los últimos años haya aumentado el interés por el desarrollo de antenas milimétricas integradas para comunicaciones *wireless* tanto interiores como exteriores.

Por otra parte, algunas aplicaciones en hiper-frecuencias, como comunicaciones locales de alta velocidad, seguridad en automóviles o comunicaciones por satélite, necesitan estructuras radiantes con una ganancia entre 40~50 dB. Las antenas con reflectores y las redes de antenas impresas cubren parcialmente estos valores. Sin embargo, los refectores clásicos son voluminosos (especialmente en las configuraciones empotradas), y con la tecnología impresa tenemos redes de antenas con baja eficiencia, debida a las pérdidas de arborescencia en la alimentación, y las causadas por las ondas de superficie. Existe una tercera solución, la asociación de una fuente de excitación principal (impresa o guiada) con un sistema de focalización, como una lente.

Con una lente dieléctrica podríamos implementar un subsistema de ondas milimétricas, integrándolas con antenas planares. Las principales ventajas de esta técnica son diagramas de radiación con alta directividad, compatibilidad con técnicas de circuitos integrados, rigidez mecánica y estabilidad térmica, al igual que la posibilidad de implementar configuraciones multi-rayo de forma sencilla. Además, esta aproximación puede suprimir las pérdidas por ondas de superficie, lo cual es bastante importante para ondas milimétricas.

2. Antenas de lente

Los principios de las antenas de lente se basan en la óptica geométrica (Leyes de Snell-Descartes, conservación de la energía dentro de un tubo de rayos, longitud del camino óptico). Las antenas de lente están pensadas para múltiples aplicaciones:

- Sistemas de comunicación *wireless* de banda ancha.
- Radares de asistencia a la conducción de automóviles.
- Seguimiento de satélites de órbita baja.
- Sistemas de comunicación en plataformas elevadas.

Lentes dieléctricas

Al trabajar con dimensiones milimétricas, los sustratos empiezan a guiar las ondas. Las ondas de superficie generadas provocan una reducción de rendimiento y un mayor acoplamiento de los elementos. Para amortiguar este fenómeno se utilizan las lentes dieléctricas.

Los modos del sustrato no se excitan si las fuentes están impresas en un sustrato de espesor infinito. Para simular este espesor podemos fabricar las antenas sobre la cara plana de una semiesfera dieléctrica. De ahí el nombre de lente dieléctrica. Como todos los rayos

inciden normalmente sobre el lado esférico de la lente, no pueden ser atrapados por el medio, evitando así la aparición de ondas de superficie.

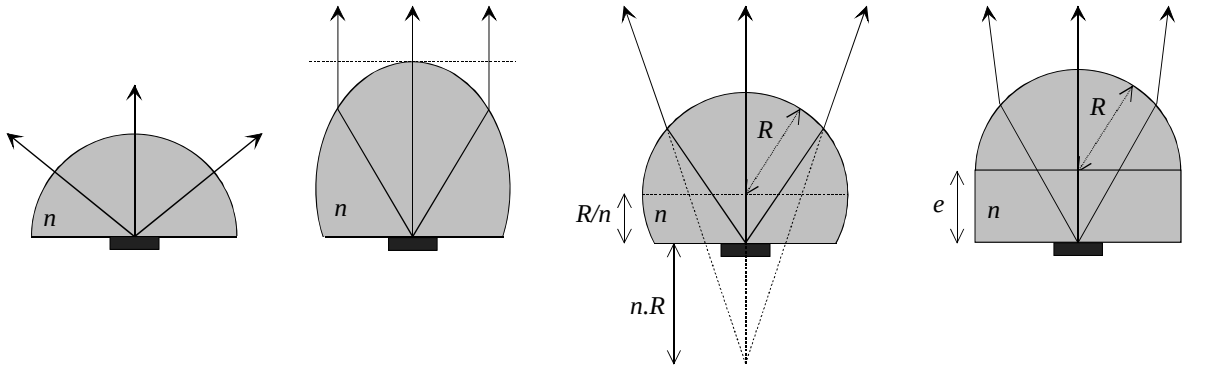

***(a)** - Semiesfera* ***(b)** - Elipse* ***(c)** – Hiper-semiesfera* ***(d)** – Semiesfera Extendida*

figura 2.17: Configuraciones típicas de lentes de substrato (índice $n = \sqrt{\varepsilon_r}$).

En la práctica es preferible utilizar otras configuraciones para mejorar la directividad de la antena:

- Lentes Elípticas (***figura b)***: La fuente principal se coloca en el segundo foco de la elipse: Los rayos emitidos conforman un haz de rayos paralelos a la salida. El sistema trabaja en el límite de difracción. Su gausicidad es del 80%.
- Lentes hiper-semiesféricas (***figura c***): Una esfera dieléctrica de radio *R* e índice *n* cortada por un plano a una distancia del centro *e = R/n*. Esta lente satisface la condición de seno de Abbe, con lo que anula las aberraciones coma. Tiene menos directividad que la lente ellíptica, aunque mayor gausicidad (90%).
- Lentes semiesféricas extendidas: Están formadas por una semiesfera dieléctrica (de Radio *R* e índice *n*) conectada con una sección cilíndrica del mismo índice y altura *e*. La. Es la configuración más habitual, ya que permiten controlar la directividad y la gausicidad fácilmente modificando la extensión *e*, y su fabricación y ensamblaje son mucho más sencillos. Cuando la lente tiene un valor de *e* tal que el frente de ondas de salida es plano, la llamamos lente elíptica sintetizada.

3. Metodología

La estructura estudiada en este proyecto es la lente semiesférica extendida, descrita en el apartado anterior. A continuación se describe la implementación y nomenclatura utilizadas. La siguiente figura representa una susodicha lente alimentada por una guía de onda:

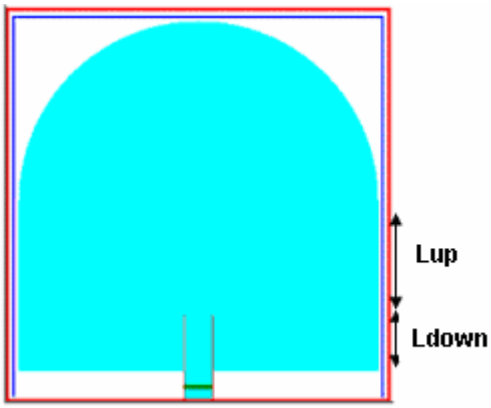

Figura 3.1: Lente semiesférica extendida alimentada por guía de onda.

El radio y el diámetro de la lente vienen referidos normalmente a la longitud de onda (por ejemplo, $D=6\cdot\lambda_0$). La extensión viene representada por dos variables, *Lup* y *Ldown*, es decir, extensión superior e inferior respectivamente, ambas presentes en la figura anterior. La extensión superior es la que va desde la boca de la guía de onda hasta la base de la semiesfera, en teoría es la extensión real de la lente, ya que comienza por donde surge la radiación. La inferior es la que se encuentra por debajo de la boca de la guía de onda. En principio no es un parámetro de diseño sino una necesidad para el correcto montaje físico, pero su influencia debe ser estudiada.

Al trabajar con fuentes impresas o planos de masa en general la extensión inferior no existirá.

A la hora de referirse a la extensión de la lente, no se hará en unidades métricas, sino en relación porcentual con la extensión de la lente elíptica sintetizada. La longitud de la lente sintetizada coincide con la longitud de la lente elíptica del mismo radio (entendiendo radio como semieje menor). En la siguiente figura se pueden apreciar las medidas de la lente elíptica:

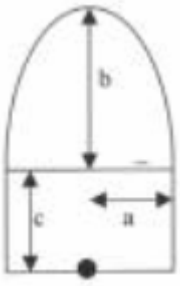

Figura 3.2: Lente Elíptica

El valor de las variables sería:

$$b = \frac{a}{\sqrt{1-\frac{1}{\varepsilon_r}}} \tag{1}$$

$$c = \frac{b}{\sqrt{\varepsilon_r}} \tag{2}$$

Por lo tanto, obtener la extensión de la lentilla elíptica sintetizada es sencillo. La altura total es $c+b$, formada por el cilindro de extensión e y la semiesfera de radio a. La extensión sería entonces esa altura menos el radio:

$$L_{100\%} = b + c - a \tag{3}$$

El método de análisis de campos electromagnéticos utilizado en el análisis de las estructuras estudiadas es el FDTD (Diferencias Finitas en el Dominio del Tiempo), presentado por Kane Yee en 1966. Yee eligió una relación geométrica para el muestreo de las componentes vectoriales de los campos eléctricos y magnéticos, representados en la forma integral y diferencial de las ecuaciones de Maxwell.

Este método tiene varias ventajas:

- Es preciso, ya que describe correctamente el mundo físico.

- Es versátil y sencillo, pues permite modelar antenas de geometría y alimentación complejas, aparte de poder trabajar con el software SPICE.

- Es robusto. Puede modelar cualquier tipo de material para tecnología electromagnética: conductores, dieléctricos, medios anisótropos y materiales no-lineares y dispersivos.

- Calcula detalles del campo cercano alrededor de la antena.

- Es de banda ancha. Excitando con un impulso en el dominio del tiempo permite obtener la respuesta en frecuencia, al aplicar la tranformada de Fourier, en un amplio espectro de frecuencias (con una sóla ejecución de FDTD).

Kane Yee escribió las ecuaciones curvas de Maxwell como ecuaciones diferenciales en el dominio del tiempo. El medio donde se encuentran los campos se descompone en celdas elementales (***figura 3.3***) con una dimensión diferente para cada eje: Δx, Δy y Δz.

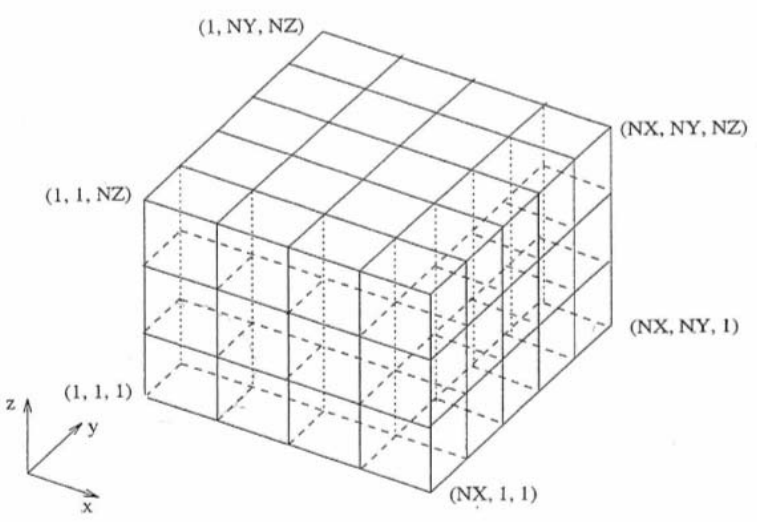

figura 3.3: Descomposición en celdas elementales

Cada célula viene referenciada siguiendo los tres ejes (de 1 a NX siguiendo el eje *x*, de 1 a NY siguiendo el eje *y*, y de 1 a NZ siguiendo el eje *z*). Por lo tanto, el volumen total de cálculo consta de NX x NY x NZ celdas.

La componente E_x del campo eléctrico dentro de una célula (i,j,k) en el instante t_n (es decir, $t_n=n\cdot\Delta t$) viene expresada como:

$$E_x(i\Delta x, j\Delta y, k\Delta z, n\Delta t) = E_x^n(i, j, k) \tag{4}$$

Como se puede ver en la **figura 3.4**, el algoritmo de Yee centra los componentes de los campos E y H en el espacio tridimensional de manera que cada componente de E esté rodeada por cuatro componentes de H, y viceversa.

- El algoritmo calcula simultáneamente la forma diferencial e integral de las ecuaciones de Maxwell. Es muy útil al especificar las condiciones en los límites del campo y en las singularidades.

- Las expresiones diferenciales para las derivadas espaciales de los operadores curvos están centradas por defecto y tiene una precisión de segundo orden.

- La continuidad de las componentes tangenciales de los campos a través de la interfaz es resuelta fácilmente al ser dicho interfaz paralelo a uno de los ejes.

- La posición de las componentes de los campos en las celdas de Yee y las operaciones de diferencias centradas hacen que las leyes de Gauss se verifiquen siempre e imponen la ausencia de cargas magnéticas y eléctricas.

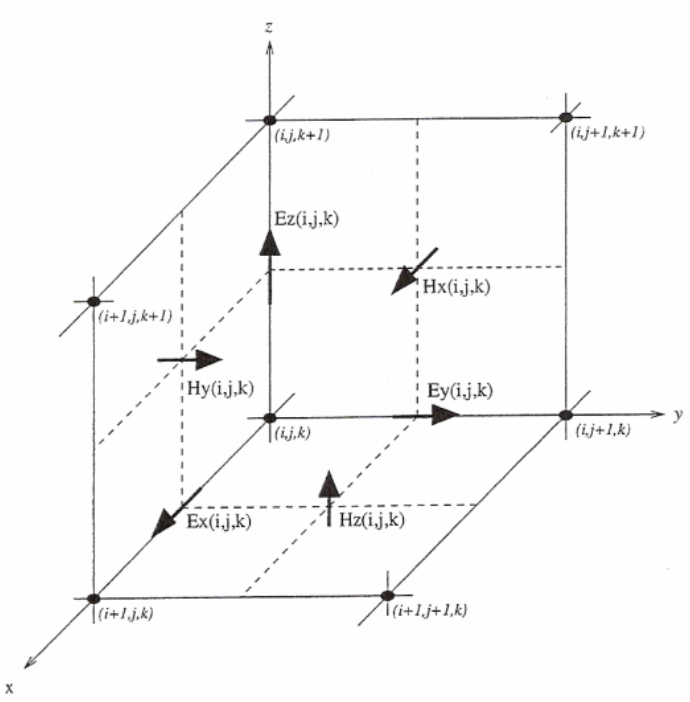

figura 3.4: Celda de Yee

El algoritmo de Yee también centra las componentes de los campos en el dominio del tiempo: Las componentes de E se calculan en el instante $t_n = n\Delta t$, y las de H en el instante $t_{n+\frac{1}{2}} = \left(n + \frac{1}{2}\right)\cdot\Delta t$.

El software utilizado para realizar los modelos es Imelsi (simulador de impulsos electromagnéticos), un simulador electromagnético FDTD que permite analizar estructuras finitas e infinitas, teniendo en cuenta (de ser necesario) pérdidas y dispersión en los dieléctricos y metales. También contiene formalismos para tratar elementos concretos como aberturas e hilos finos. Permite también elegir las condiciones en los límites del diseño. Es un simulador muy versátil, pues se pueden obtener tanto las características de radiación, cartografías de los campos en el dominio del tiempo y la frecuencia, y parámetros de adaptación.

Con este software se han optimizado las fuentes de alimentación y se han simulado las asociaciones fuente – lente. Para diseños medianamente grandes el programa requiere muchos recursos informáticos. No es posible realizar las simulaciones en un PC o una estación de trabajo. Para realizar los análisis se ha tenido que recurrir al centro de cálculo IDRIS, que presta procesadores con grandes capacidades de cálculo y discos duros y memorias del mismo nivel.

Para calcular el campo lejano se ha utilizado la aproximación frecuencial, que es eficiente en tiempo y computación a la hora de obtener los diagramas de radiación trabajando con un número de frecuencias limitadas (hasta 10 o 20).

A la hora calcular el campo lejano, es necesario definir unas superficies que rodeen completamente la estructura radiante, llamadas superficies de Huygens, al igual que el tipo de diagrama que se desea calcular.

4. Estudio paramétrico de lentes dieléctricas

Utilizando como dieléctrico el Teflón (ε_r=2.2) y el cuarzo (ε_r=3.8) sin pérdidas ambos, se han realizado simulaciones de lentes semiesféricas extendidas alimentadas con una guía de ondas, con diferentes diámetros y variando la extensión, tanto superior como inferior, estudiando la influencia de dichos parámetros sobre la radiación.

En las siguientes gráficas observamos la influencia de ambas extensiones sobre la directividad, para cada dieléctrico (nótese que los diámetros son distintos):

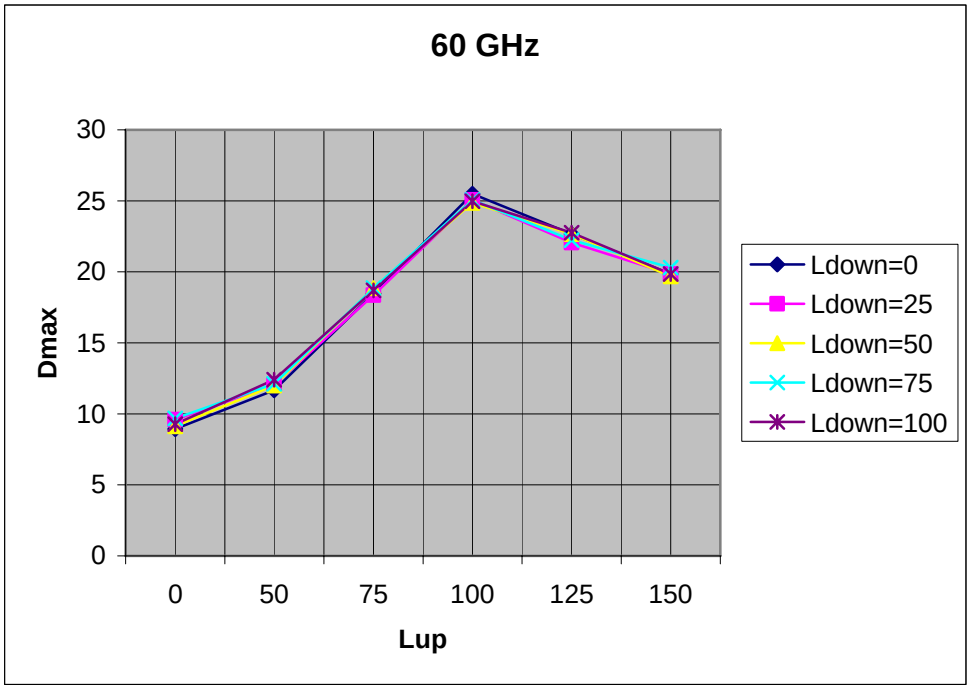

figura 4.6: Directividad máxima en dB..Lente de Teflón, diámetro $6\lambda_0$, Teflón, 60GHz

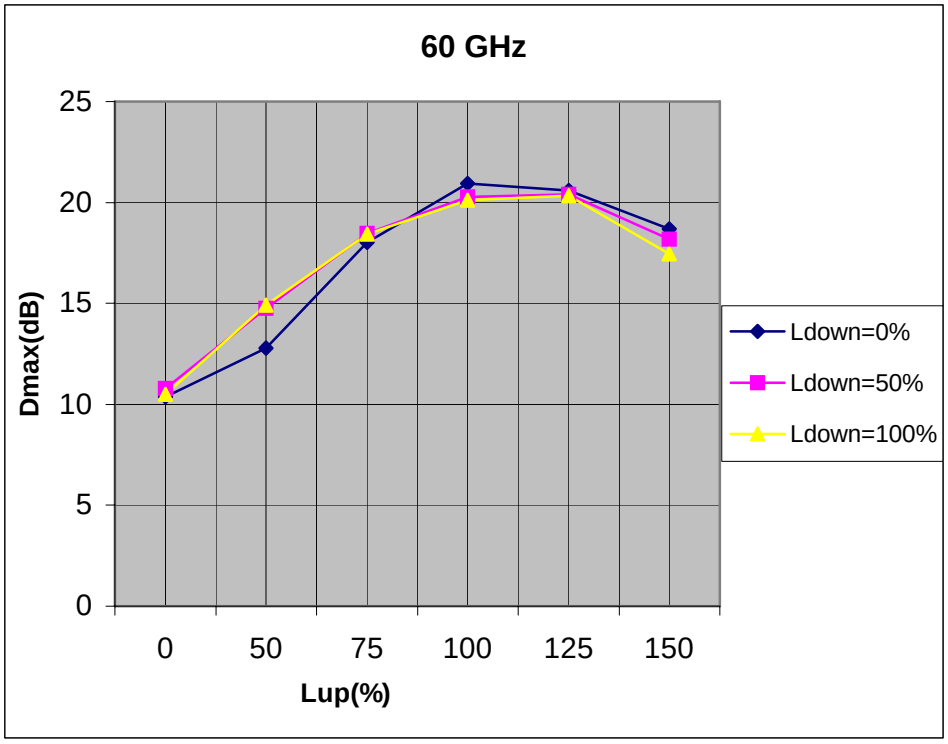

figura 4.13: Directividad máxima en dB. Lente de cuarzo, diámetro $3\lambda_0$, Teflón, 60GHz

La configuración de extensión *Lup*=100%, que corresponde a la elipse sintetizada, es la que posee en ambos casos una mayor directividad, como podía esperarse por sus características teóricas. La directividad aumenta de una forma ligeramente lineal desde la semiesfera (*Lup*=0%) hasta la elipse sintetizada, y después desciende, abruptamente en el caso del Teflón, y más suavemente en la lente de cuarzo. Observando los diagramas de radiación se puede obtener más información:

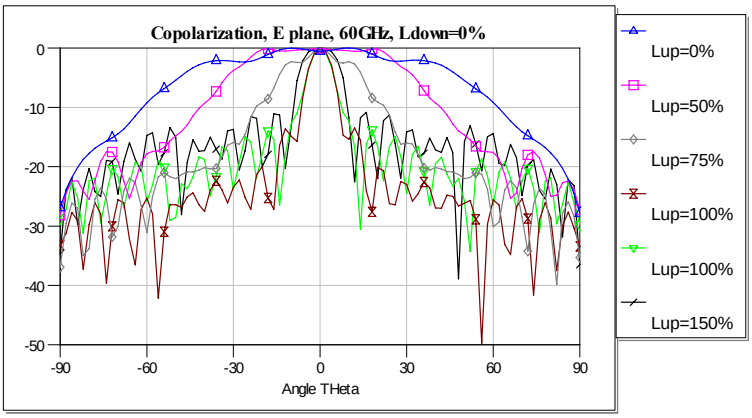

figura 4.8: Copolarización, plano E, Ldown=0%, diametro $6\lambda_0$,,Teflón, 60 GHz

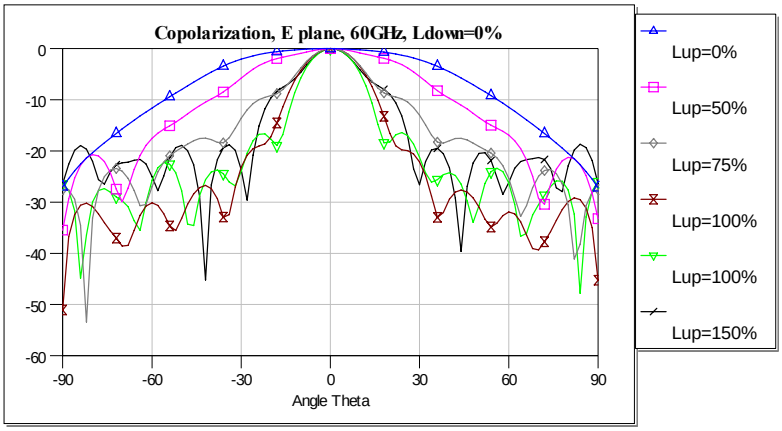

figura 4.15: Copolarización, plano E, Ldown=0%, diametro $3\lambda_{0,}$,cuarzo,, 60 GHz

En general, la elipse sintetizada es la configuración con mejor rendimiento, ya que tiene un lóbulo principal muy directivo y mantiene el nivel de lóbulo secundario más bajo. La extensión inferior no tiene una influencia muy notable, como se ve en las gráficas de la directividad, los diagramas de radiación resultan demasiado similares para poder extraer conclusiones significativas:

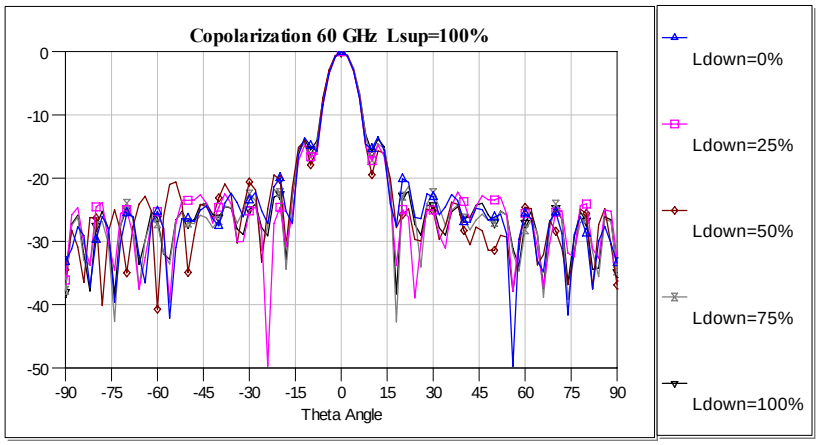

figura 4.10: Copolarización, plano E, Lup=100%, diametro $6\lambda_{0,}$,Teflón,, 60 GHz

Los siguientes diagramas de radiación ilustran la influencia del diámetro y la permitividad del dieléctrico:

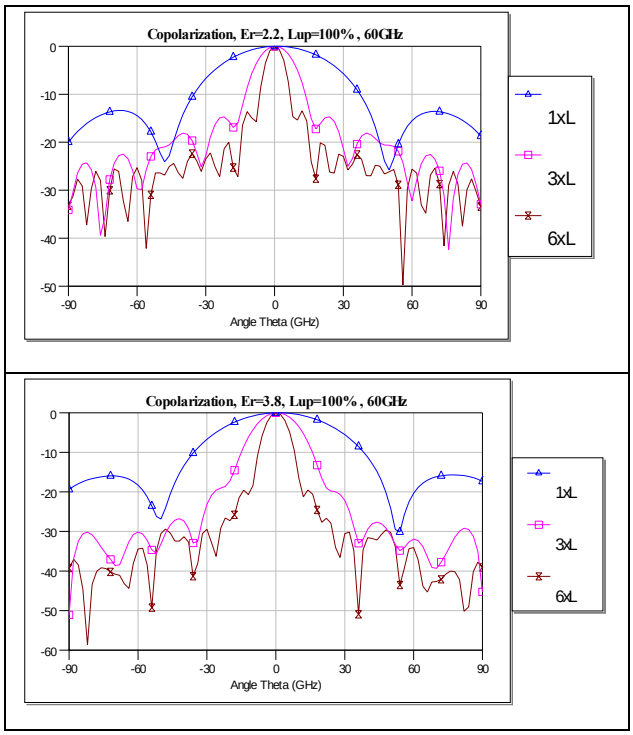

figura 4.24: Copolarización Campo E, comparativa, Lup=100%, 60GHz

Se aprecia claramente que, como cabía esperar, la lente de mayor radio resulta ser la más directiva. La lente de menor diámetro tiene sin embargo una directividad muy inferior, el lóbulo principal es apenas directivo (en torno a 12dB), tan sólo 5dB más que la directividad de la guía de onda sola, y muy inferior a la de las otras configuraciones (20-25 dB), de lo que se puede inferir que una lente requiere de un tamaño mínimo para poder focalizar correctamente la radiación de la antena.

Al tener los dos dieléctricos una permitividad similar, no se aprecian diferencias excesivas en los diagramas de radiación. El comportamiento es ligeramente mejor para el cuarzo, ya que tiene una directividad algo superior, y un mejor nivel de lóbulo secundario.

5. Lentes semiesféricas extendidas de Eccostock alimentadas por guía de onda

A partir del diseño usado por el instituto IST [98], y considerando las conclusiones del capítulo anterior, se realiza un estudio más profundo de un diseño concreto. Se utilizará una lente de Eccostock (ε_r=8.8) sin pérdidas, de diámetro $6\cdot\lambda_0$, y se medirá un mayor número de frecuencias.

Se ha simulado también la estructura añadiéndole un plano de masa infinito, que suele usarse para evitar la radiación trasera, para comprobar si degrada el rendimiento.

Al igual que en el anterior capítulo, la directividad es máxima para la configuración de elipse sintetizada, en esta gráfica se ve la evolución de este parámetro con la frecuencia en dos configuraciones, con y sin plano de masa:

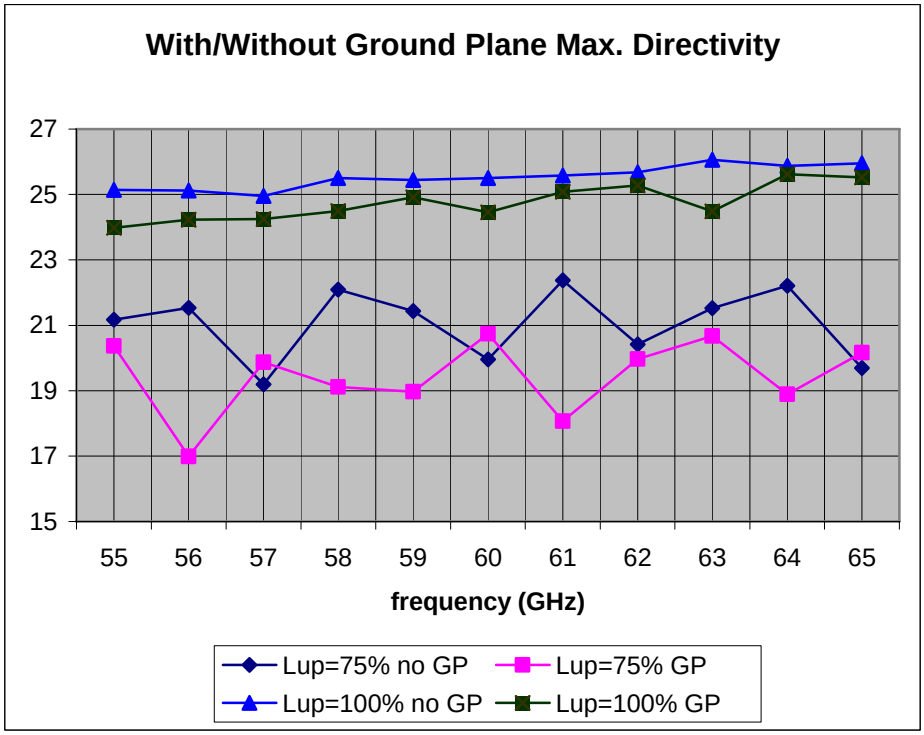

figura 5.22: Comparativa de directividades máximas, lentes con o sin plano metálico. *Ldown*=0%, Diámetro=6λ_0, Eccostock

Sin plano de masa se obtiene una directividad ligeramente superior, añadir un plano de masa supone para la elipse sintetizada una pérdida de poco más de 1 dB, algo asumible en principio. La directividad para esta configuración asciende de forma bastante lineal en dB, es decir, exponencialmente en unidades lineales, aunque con una pendiente muy ligera, comportamiento que coincide con el de la guía de onda sola (aunque evidentemente esta última es mucho menos directiva). Para otras extensiones la dependencia con la frecuencia resulta más caótica, como ejemplifican las curvas de extensión del 75%.

La observación de los diagramas de radiación ayudará a sacar más conclusiones:

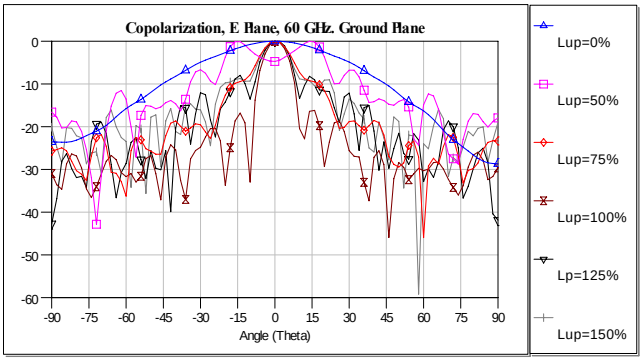

figura 5.15: Copolarización campo E, 60 GHz, diametro 6λ_0, Eccostock, con plano de masa

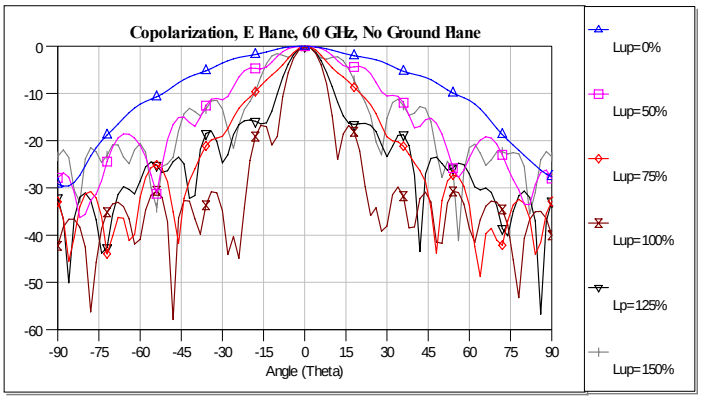

figura 5.23: Copolarización, campo E, 60GHz, Ldown =0%, diametro $6\lambda_0$, Eccostock, sin plano de masa.

Al parecer el plano de masa introduce un mayor nivel en la radiación lateral. Esto no afecta demasiado al nivel de lóbulo secundario de la elipse sintetizada, que queda en unos -17dB, pero si al del resto de configuraciones ya que aumenta bastante. Esto significa que el plano de masa sólo es adecuado para la elipse sintetizada, ya que sino se pierden muchas prestaciones.

Se ha realizado también un análisis de la potencia radiada por las lentes, comparada con la potencia inyectada por la guía. La medida de la reflexión en la entrada, el S11, puede servir de ayuda para la interpretación de los resultados.

Se entiende que las configuraciones con menos reflexiones son las que más potencia van a radiar. Las configuraciones con mayor potencia en ambos casos son las que tienen extensiones del 50% al 100%, que mantienen un S11 inferior a los -15dB. La configuración hemisférica tiene un altísimo S11 debido a que la dirección de los rayos reflejados es la misma que la de los incidentes. El utilizar plano de masa no parece implicar cambios demasiado importantes en la radiación, al menos para la configuración de elipse sintetizada (ver gráficas **5.17-18 y 5.25-26**).

Se ha simulado la lente con extensión superior (Lup) del 100% considerando pérdidas en los dieléctricos, y se ha medido la potencia emitida. Los resultados son idénticos con o sin plano de masa, la **figura 5.32** ilustra el comportamiento de las pérdidas en general.

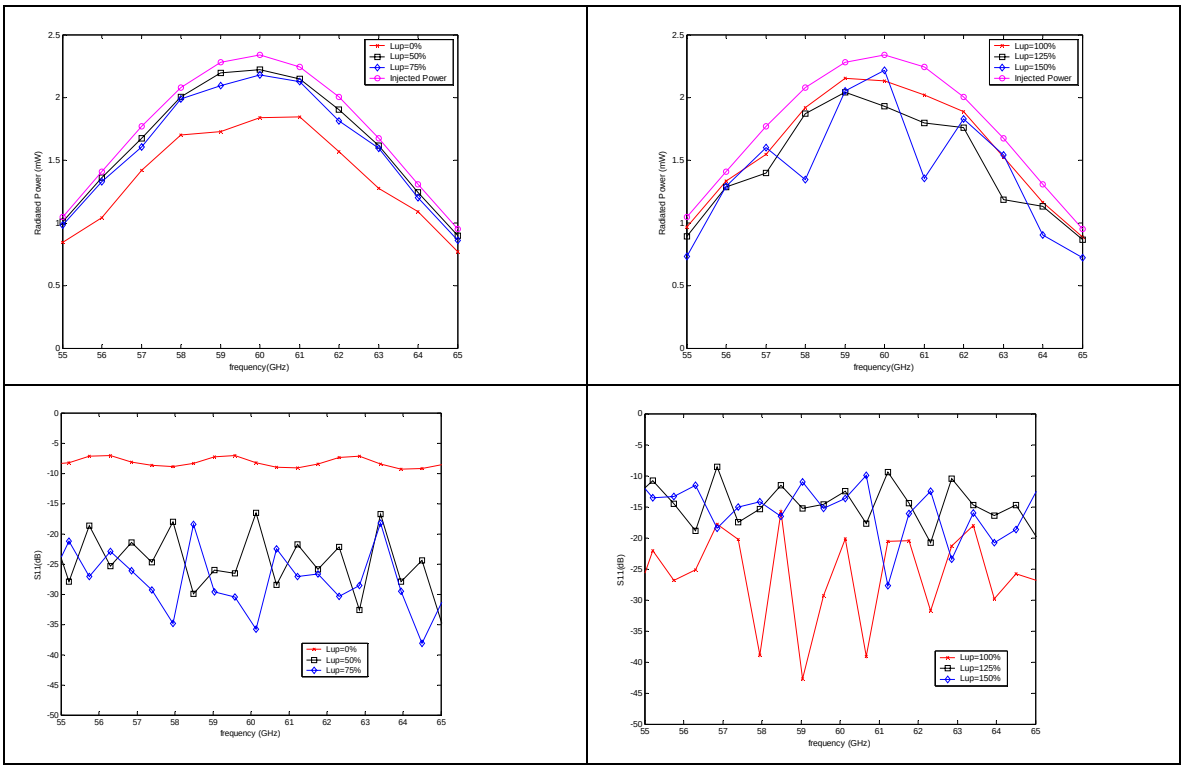

figuras 5.17 y 5.18: Comparativa de potencia radiada y S11. Diámetro $6\lambda_0$, Eccostock, con plano de masa.

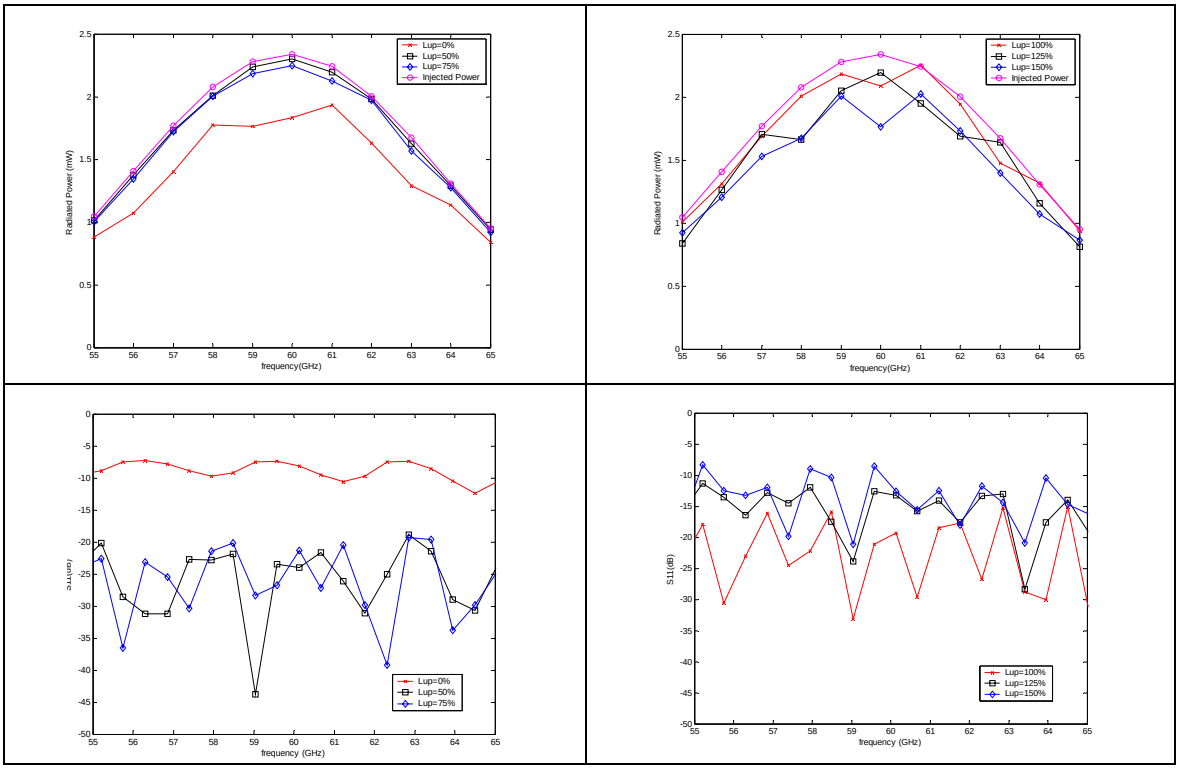

figura 5.25 y 5.26: Comparativa de potencia radiada y S11. Diámetro $6\lambda_0$, Eccostock, sin plano de masa.

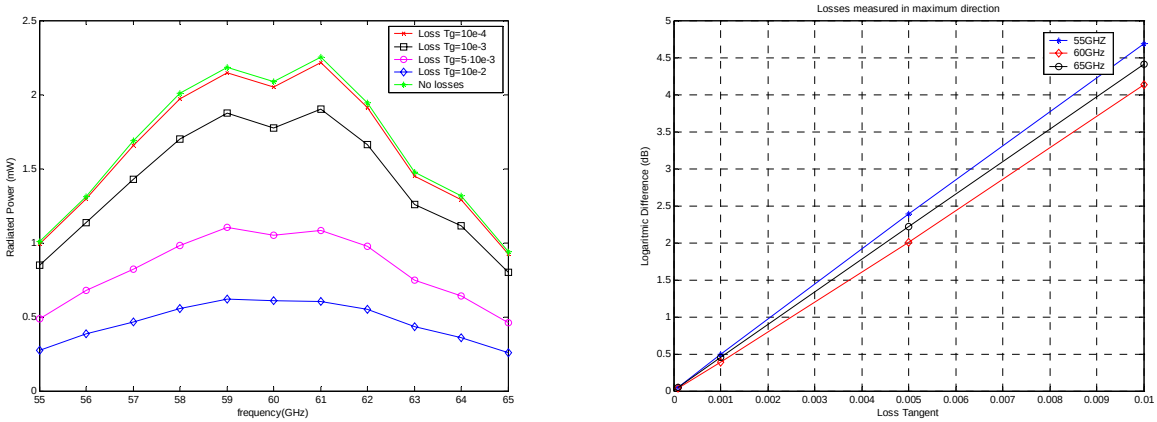

Figure 5.32: Comparativa de pérdidas: Potencia radiada y Diferencia logarítmica. Eccostock, Lup=100%, Ldown=0%, sin plano de masa.

Considerando la diferencia logarítmica como:

$$LD(dB) = 10 \cdot \log_{10}\left(\frac{\left|E_{\max}{}^{2}{}_{tg\delta=0}\right|}{\left|E_{\max}{}^{2}{}_{tg\delta\neq 0}\right|}\right) \tag{5}$$

A medida que aumenta la tangente de pérdidas del dieléctrico de la lente, la diferencia de potencia radiada aumenta exponencialmente (linealmente en dB). La frecuencia también influye, como se puede ver en la gráfica de las diferencias logarítmicas, la pendiente de dicha diferencia es menor a la frecuencia central, mientras que en las laterales es más pronunciada.

La influencia de las reflexiones en la potencia radiada y los diagramas de radiación puede apreciarse en la **figura 5.38**, donde hemos tomado medidas en una lente de elipse sintetizada, con y sin reflexiones.

La onda incidente como tal conforma el lóbulo principal, todo lo directivo que puede llegar a ser. Al considerar las posteriores reflexiones aumenta la radiación lateral, no mejorando la directividad sino aumentando el nivel de lóbulo secundario. Gran parte de la potencia radiada viene de las reflexiones, se puede ver que la onda incidente tiene una forma gausiana, como la potencia inyectada, mientras que las reflexiones alteran sensiblemente esta forma.

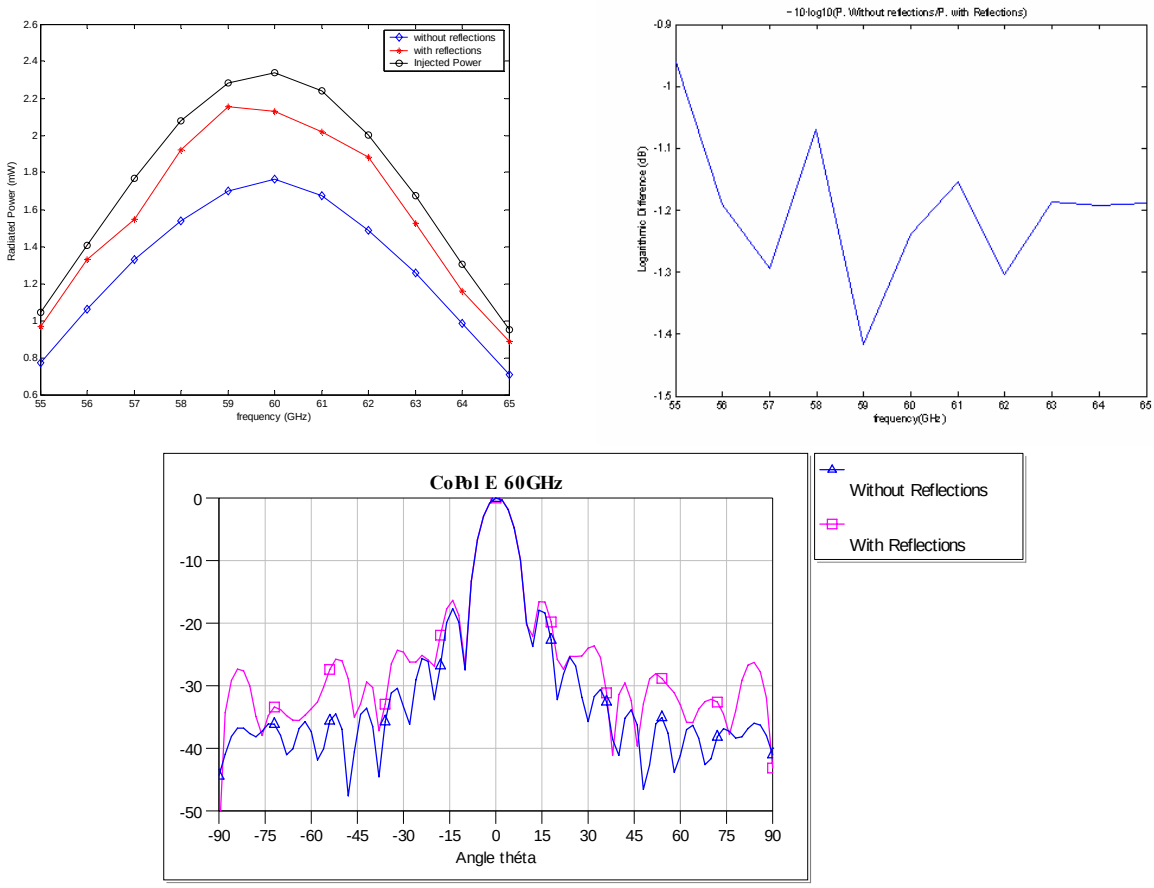

figura 5.38: Comparativa de potencia radiada y diagramas de radiación. Eccostcock, con y sin reflexiones, Lup=100%, con plano de masa.

6. Lentes de elipse sintetizada con alimentación descentrada

Después de hacer un estudio completo de las antenas de lente en los anteriores capítulos, va a efectuarse una aproximación en los últimos apartados a las aplicaciones de apuntamiento. Para estas aplicaciones se usarán fuentes impresas, para variar la dirección de radiación se moverá el centro de la fuente en posiciones diferentes al centro de la lente. La siguiente figura ilustra las direcciones en las que moveremos el centro de la fuente impresa, al que llamaremos *patch*, correspondientes a los ejes X e Y, que se corresponden a su vez con el plano E y H respectivamente (ver **figura 6.1**)

Las distancia al centro la mediremos en fracciones de radio (X/R o Y/R), los valores típicos utilizados serán 0.2, 0.32, 0.4 y 0.64. En el apéndice B (**Appendix B**) se pueden ver los diseños de las fuentes impresas y sus características. La lente utilizada será de Macor (ε_r=5.67) sin pérdidas, con la configuración de elipse sintetizada, que es la que mejores prestaciones ha dado en anteriores estudios, se ha simulado para dos diámetros, $3\cdot\lambda_0$ y $5\cdot\lambda_0$. La fuente impresa diseñada lleva un plano de masa infinito, con lo que la lente no tiene extensión inferior.

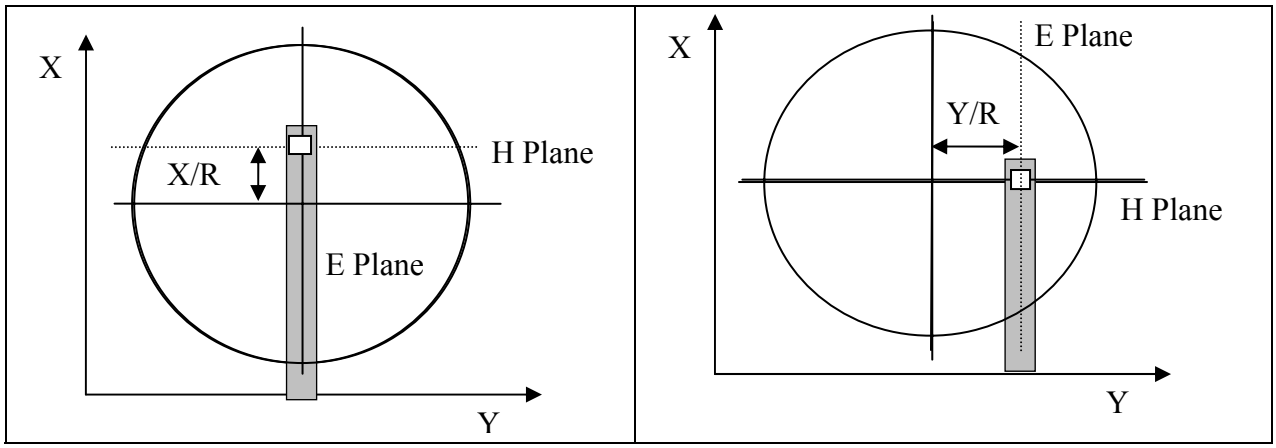

figura 6.1: Direcciones de movimiento del patch

A la hora de modelar la asociación fuente impresa – lente, se ha tenido que utilizar un tamaño de celda que permitiera una radiación adaptada a 26 GHz (la frecuencia de trabajo con Macor). En trabajos anteriores se había utilizado un tamaño de celda cercano a la décima de milímetro, durante este proyecto se obtuvo un modelo adaptado a la frecuencia de trabajo con un tamaño de celda del doble de tamaño para así requerir menos procesamiento su análisis. Sin embargo, los resultados con estas celdas no correspondían con los obtenidos con el otro tamaño de celda debido a la falta de precisión al dibujar la curva de la lente. Por lo tanto se optó por continuar trabajando con el tamaño de celda habitual.

En las siguientes gráficas se puede observar la dirección de máxima radiación, la directividad y el nivel de lóbulo secundario con respecto a la distancia que se mueve el *patch* del centro, en ambas direcciones, primero para un diámetro de $\mathbf{3\cdot\lambda_0}$ (ver **figura 6.6**) y también para $\mathbf{5\cdot\lambda_0}$ (ver **figura 6.7**).

Se observa que el ángulo de máxima radiación (lo que vendría a ser el ángulo en el que apunta la antena) varía siempre de forma prácticamente lineal con la distancia al centro del *patch*. Además, si se normaliza esta distancia al radio de la lente (como en las gráficas) se verifica que la recta ideal a la que podemos aproximar esta variación es idéntica independientemente del radio de la lente y de la dirección en la que movamos el centro. Esto supone que, salvo ligeras variaciones, para un mismo ratio distancia al centro - radio de la lente (X/R) se obtiene el mismo ángulo de apuntamiento.

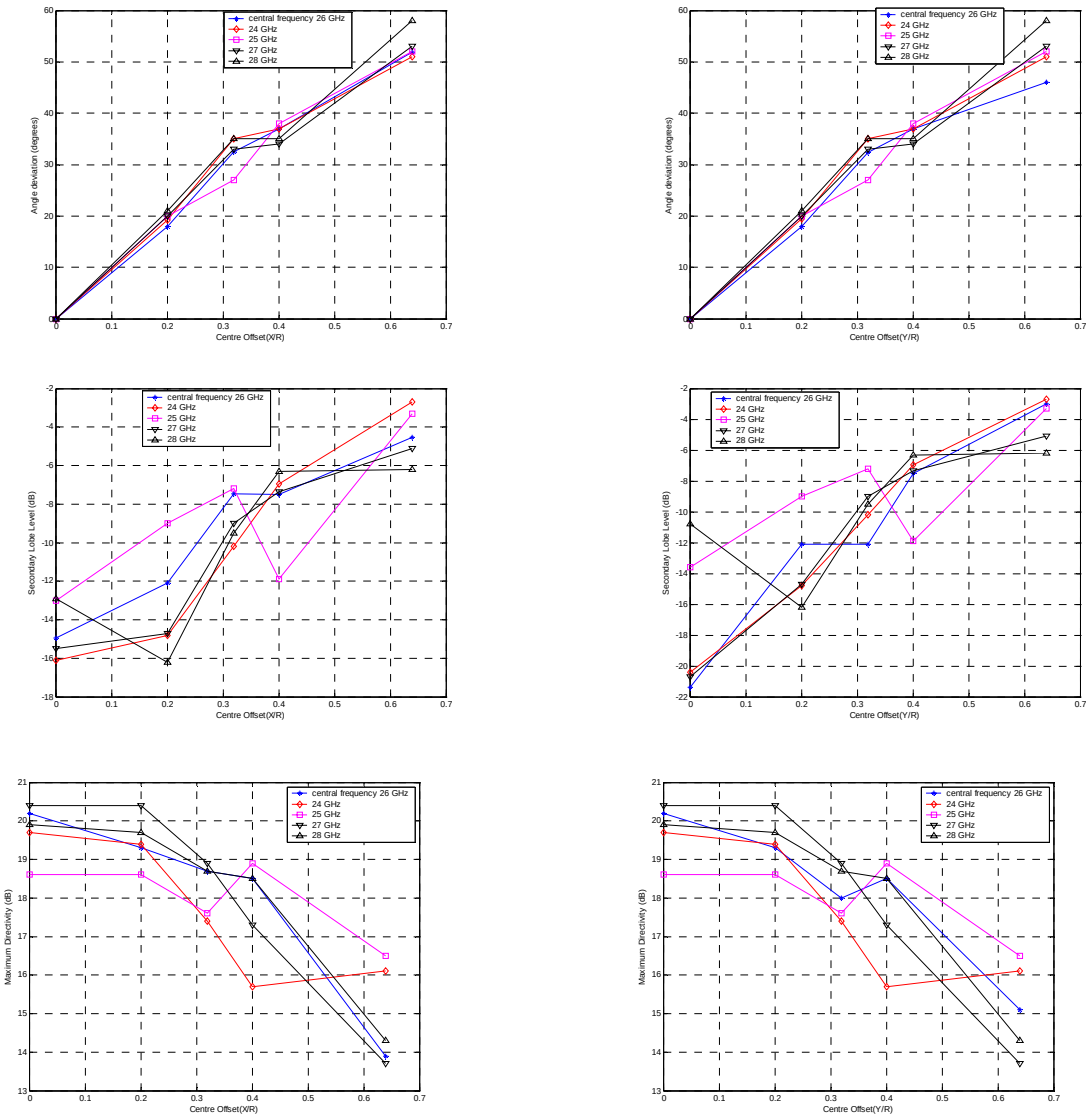

figura 6.6: Comparativa de rendimiento con respecto a la distancia (relativa al radio) de la fuente al centro de la lente(a la izquierda en el eje X y a la derecha en el Y). Lente de Macor de diámetro $3 \cdot \lambda_0$

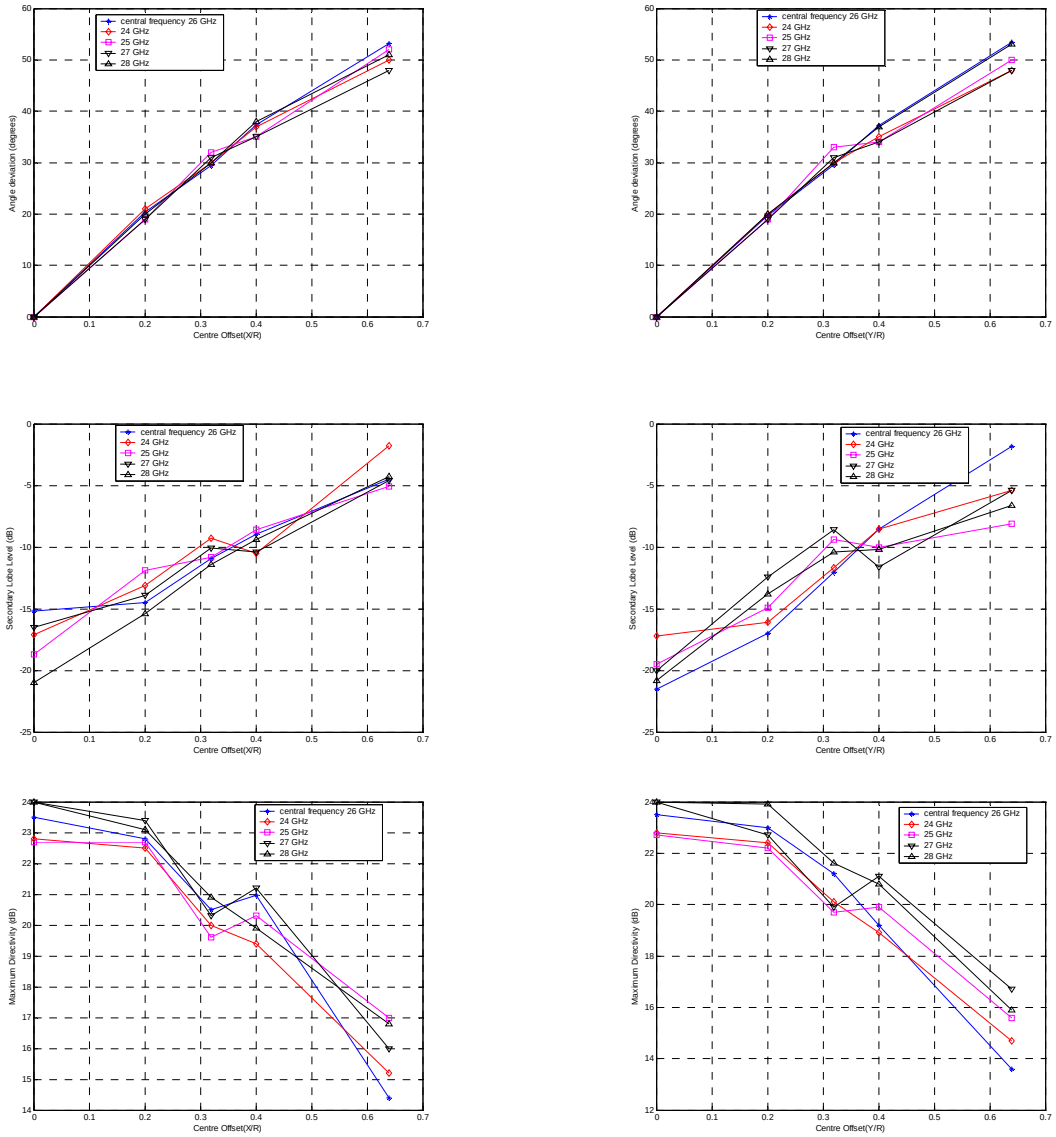

figura 6.7: Comparativa de rendimiento con respecto a la distancia (relativa al radio) de la fuente al centro de la lente (a la izquierda en el eje X y a la derecha en el Y). Lente de Macor de diámetro $5 \cdot \lambda_0$

Como era de esperar, al mover la fuente del centro de la lente el rendimiento disminuye. La directividad se mantiene hasta un X/R de 0.2, y después empieza a caer bruscamente, y el nivel de lóbulo secundario aumenta exponencialmente con el *offset*. Aún así, dependiendo de las especificaciones técnicas, se puede considerar esta degradación aceptable hasta un X/R de 0.4 o 0.32, lo que permite apuntar la lente hasta unos 30 o 40º (ver gráficas) dando un cono de barrido de algo menos de 80º.

La lente con diámetro de $3 \cdot \lambda_0$ sufre mayores variaciones de sus parámetros con la frecuencia, mientras que la lente más grande es más estable, y por lo tanto más precisa. Otra diferencia interesante a la hora de diseñar aplicaciones, y que ya había observado en los anteriores capítulos, es que la anchura del lóbulo principal es mayor cuanto más

reducido es el diámetro de la lente. A la hora de apuntar hay que tener en cuenta tanto la dirección del lóbulo principal como la anchura de este lóbulo, luego si la aplicación a diseñar requiere una precisión a la hora de apuntar muy grande, habrá que tener en cuenta este ancho, y habrá que escoger una lente con un diámetro grande.

Se ha estudiado también la influencia de las reflexiones, de forma similar a como se hizo en los anteriores capítulos. El evitar las reflexiones no varía de forma sensible la dirección de máxima radiación, ni mejora de forma significativa el nivel de lóbulo secundario, sin embargo sí afecta bastante a la directividad, que cae mucho más lentamente cuando no consideramos reflexiones, quedando con el máximo *offset* a un nivel en torno a 18-20dB, mientras que con reflexiones suele aparecer por debajo de los 15dB.

Se ha añadido también una capa anti-reflexiones adaptada a 26GHz con la que se pretendía amortiguar la degradación en el rendimiento que producen las reflexiones, sin embargo no se consiguieron mejoras sensibles. Esto queda bastante bien ilustrado en la siguiente comparativa de directividad para los tres casos, con reflexiones, sin reflexiones y con capa anti-reflexiones:

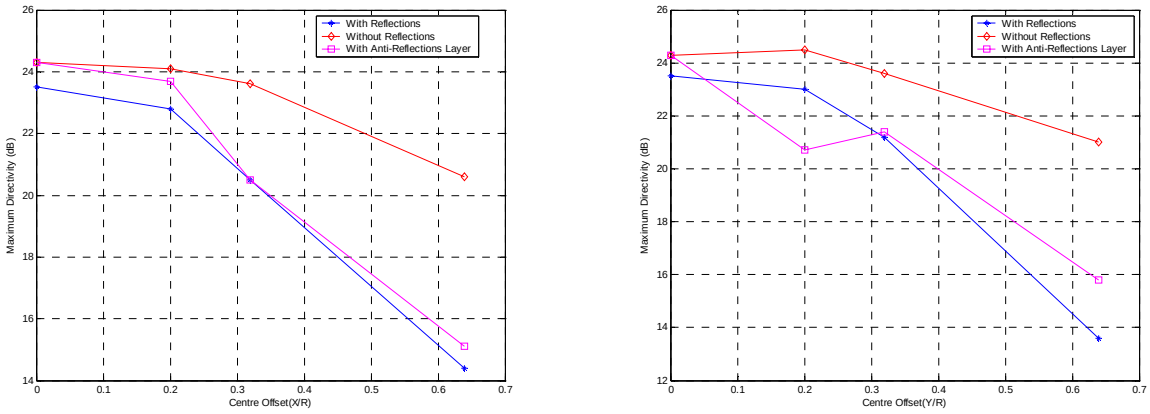

figura 6.17: *Comparativa de directividades para lente de Macor con diámetro* $5 \cdot \lambda_0$

7. Redes de *Patches*

Por último, una vez estudiados los efectos de descentrar la alimentación de la lente, se pretende diseñar una serie de configuraciones en las que aparezcan varios *patches* en el sustrato, de forma que se pueda conmutar la alimentación entre ellos. Se han estudiado diversas distribuciones de *patches* sobre el sustrato en *arrays*, bien lineares, bien bidimensionales. El objetivo es que la superposición de las posibles radiaciones emitidas por cada *patch* barra una línea o un área determinada, de forma que se pueda emitir con una cierta calidad de señal en dicha superficie de barrido. En la siguiente figura se puede observar la superposición lineal de varios *patches* activos:

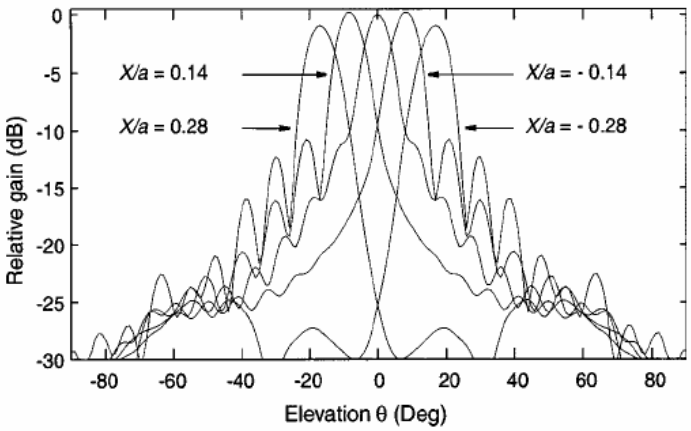

figura 7.1: Superposición de los diagramas de radiación en una lente alimentada por patches descentrados distancias diferentes

Se ha utilizado la misma lente de Macor del capítulo anterior, en su configuración de elipse sintetizada, con un diámetro de $3 \cdot \lambda_0$, pues a pesar de tener peores prestaciones y precisión que las lentes de tamaño mayor, su diseño resulta más sencillo.

Nótese que no se pretende hacer un diseño real, y por lo tanto no se consideran los mecanismos de conmutación necesarios para mover la alimentación de un *patch* a otro. Se puede considerar como un diseño "ideal". Los *patches* no alimentados estarán conectados a masa mediante un coaxial de 50 ohmios, estos *patches* pasivos han sido diseñados para tener una radiación adaptada a 26GHz, como se puede observar en el apartado B de los apéndices.

Como se puede comprobar en la figura, la superposición de los lóbulos principales hace que la ganancia no sea constante para todos los valores de elevación. Para el valor donde se cruzan dos lóbulos, el diagrama alcanza un mínimo. Si se quiere que el sistema radie con intensidad suficiente en todo el rango de direcciones para el que está diseñado es necesario impedir que dicho mínimo tenga un valor demasiado pequeño (la diferencia entre el máximo del lóbulo y el valor mínimo se denomina *overlap).* Para ello se forzará una distancia entre *patches* con el que se obtenga un *overlap* concreto, que podría ser una especificación del sistema.

Para los diseños de este apartado se ha utilizado una distancia entre los centros de los *patches* de 3.051mm (dividiendo entre el radio, quedaría un cociente de 0.175), con la que se obtiene un *overlap* aproximado de -3.2dB. Se puede observar como se superpondrían los diagramas de radiación de dos patches separados por tal distancia en la lente estudiada:

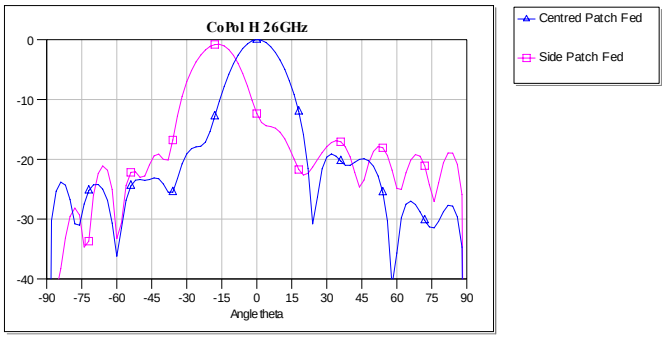

figura 7.3: Diagramas de radiación de una lente alimentada por un patch centrado y otro descentrado una distancia de 3.051mm

Primero se diseñó una red de *patches* lineal con la separación anteriormente establecida. A partir de un primer *patch* centrado se colocan otros a ambos lados, en una dirección concreta (bien la del plano E, bien la del H), separándolos la distancia antes especificada. Se puede observar la colocación de los *patches* en el siguiente dibujo:

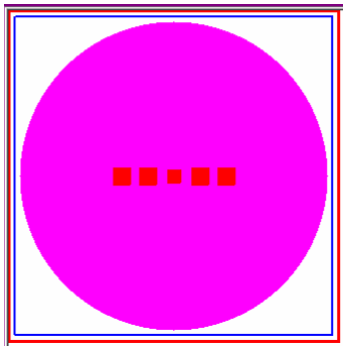

figura 7.6: Red linear de patches, donde el central es el activo y los laterales son pasivos. Lente de Macor de diámetro $3\cdot \lambda_0$.

Es interesante comprobar la influencia de los *patches* pasivos en el diagrama de radiación, así que se simulará cada posición de la alimentación con y sin los *patches* pasivos de la red. Los parámetros de radiación de cada *patch* pueden verse en las siguientes gráficas:

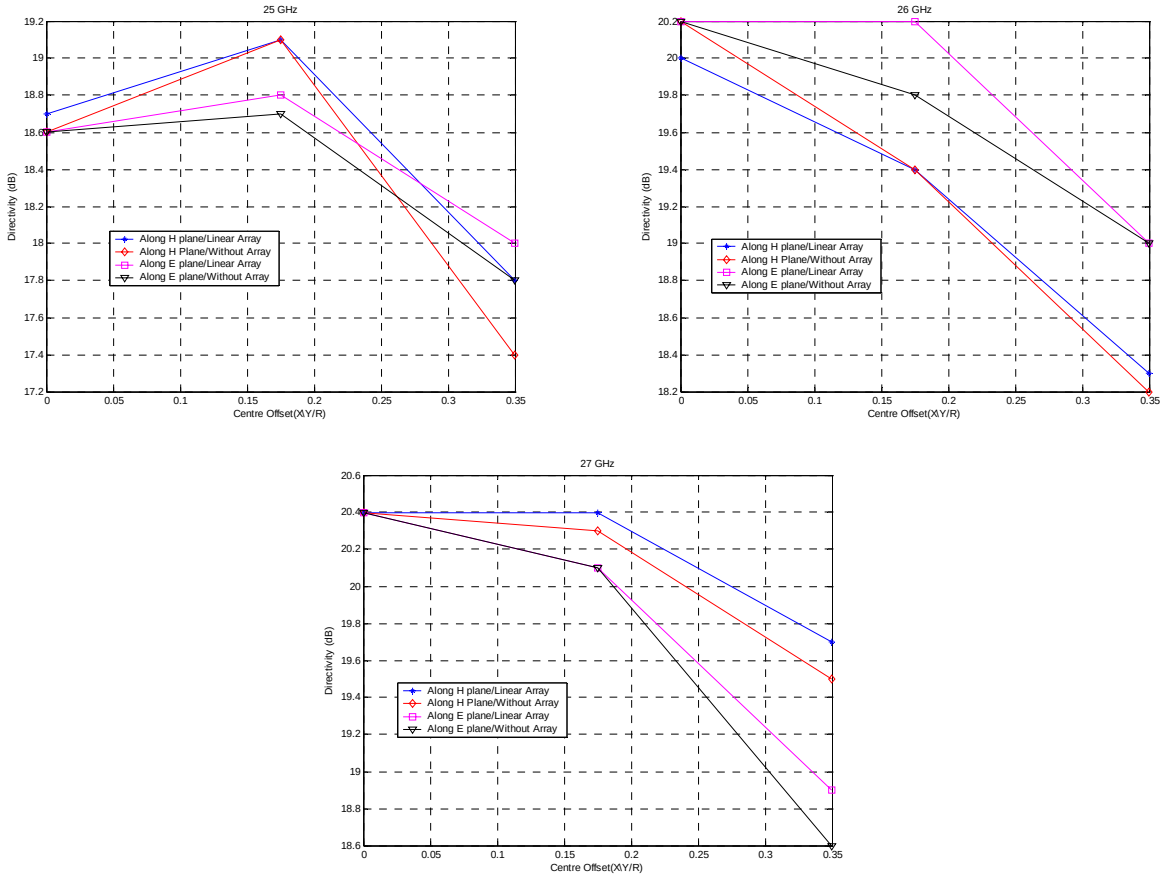

figura 7.7: *Variación de directividad en redes lineares según el plano E y el plano H para diferentes patches descentrados, y en patches descentrados sin red.*

El comportamiento de la directividad con la distancia al centro de la alimentación es similar al visto en el anterior apartado. El primer *patch* mantiene el nivel del central, mientras que el segundo sufre una mayor caída, en torno a 2 dB, que tampoco es demasiado violenta. La dirección de la red y los *patches* pasivos no resultan factores determinantes a la hora de considerar la directividad, ya que apenas producen diferencias de décimas de decibelio, y ni siquiera siguen un patrón claro, sino que varían en un sentido o en otro según la frecuencia.

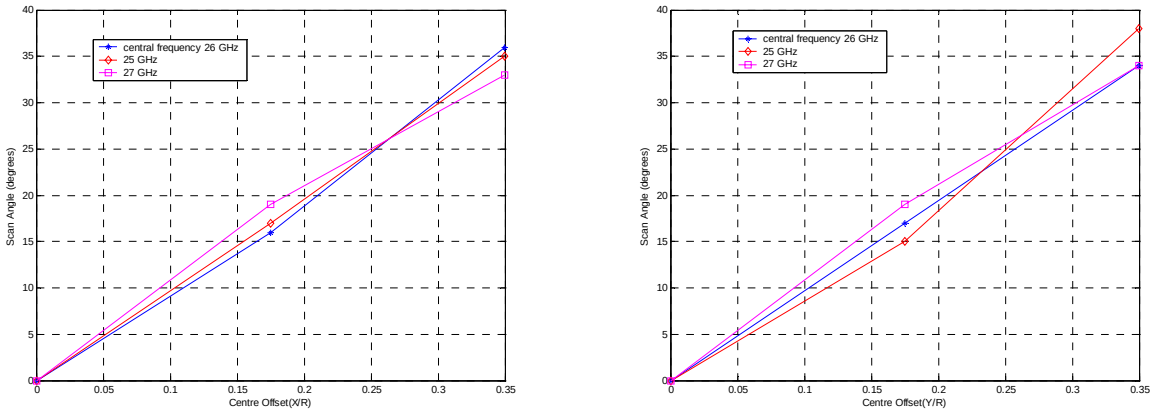

figura 7.8: *Ángulo de máxima radiación en Red linear según los planos E y H para diferentes distancias al centro de los patches.*

El ángulo de máxima radiación varía linealmente con la distancia al centro, como ya se pudo comprobar en el anterior apartado con los *patches* sin red. En ambas direcciones, el máximo ángulo en el que apunta el sistema se encuentra alrededor de los 35º, lo que quiere decir que esta configuración permite un barrido aproximado de ±35º.

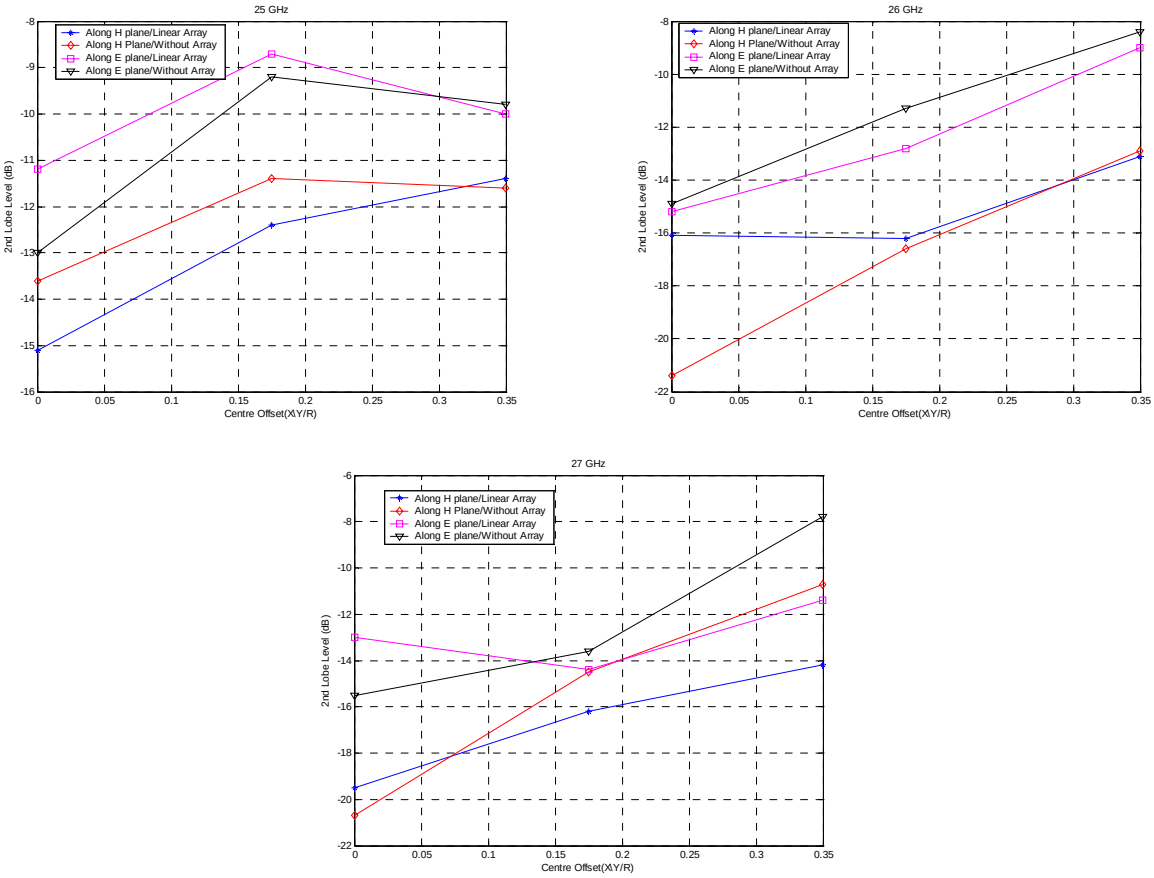

figura 7.9: Nivel de lóbulo secundario para diferentes distancias al centro sobre los planos E y H, tanto con Red como con el patch activo sólo.

El nivel de lóbulo secundario sigue el comportamiento previamente estudiado. No se aprecia una influencia importante de los *patches* pasivos en este parámetro.

Podemos, pues, concluir que la presencia de los *patches* pasivos de la red no degrada la radiación del sistema, ergo se pueden utilizar redes de *patches* lineares obteniendo un rendimiento de radiación similar al obtenido con un solo *patch*.

Se pueden diseñar también redes bidimensionales, de forma que se pueda apuntar en más direcciones en un mismo sistema, barriendo un cono de revolución. La configuración que se va a estudiar a continuación fue propuesta por Elefthteriades [99], y sigue una distribución poli-hexagonal, como un panal:

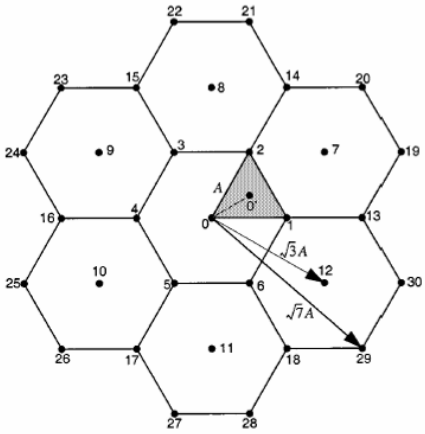

figura 7.10: Array de patches en panal.

En esta figura, cada punto representa un patch, siendo 0 el central. El radio de los hexágonos coincide con la distancia entre patches de la red linear. La lente y el resto de parámetros es el mismo que para la red lineal. Se puede hacer comparativa similar a la realizada con la anterior configuración, ya que los patches 16-4-0-1-13 formarían una red lineal en el plano H:

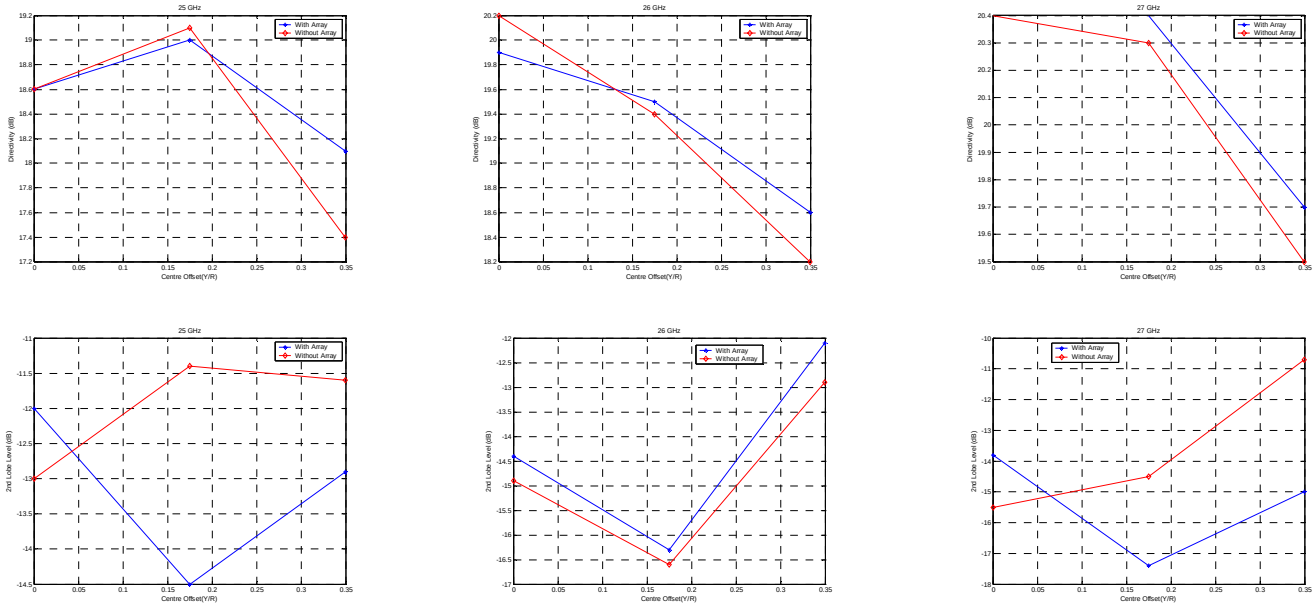

figura 7.11: Directividad, ángulo de máxima radiación y nivel de lóbulo secundario con la distancia al centro, Red linear según plano H dentro de red en panal. Con y sin patches pasivos.

Se puede comprobar que, a pesar de aumentar sensiblemente el número de *patches,* siguen sin tener una influencia relevante en la radiación, luego no supone una degradación de esta.

Para obtener el comportamiento de todos los *patches* activos posibles dentro de la red, sólo es necesario simular un cuadrante del diseño, ya que el resto se puede deducir por simetría. Mirando la directividad, se puede comprobar que el diseño es posee quizá demasiados

patches, ya que los más extremos tienen este parámetro excesivamente bajo. En esta tabla podemos observar este hecho:

Freq(GHz)	0	1	13	2	7	19	8	14	20	21
25	18.6	19.0	18.1	18.8	18.5	15	18.8	18.3	16.2	15.8
26	19.9	19.5	18.6	19.9	19.5	16.6	19.6	18.6	17.3	18.3
27	20.4	20.4	19.7	20.1	20.1	16.1	20.0	19.6	16.6	16.4

Tabla 7.1*:* Directividades en decibelios de todas las configuraciones, considerando la red completa de patches activos y pasivos. Los números indican la posición del patch activo en la figura 7.10. Las configuraciones subrayadas son las de los extremos.

Los *patches 19, 20 y 21* pueden no ser implementados, ya que la radiación desde esas posiciones está muy degradada.

D. Figures and Tables Index

figures:

Tables:

References

[1] D. N. Black, J. C. Wiltse, "Millimeter wave characteristics of phase correcting Fresnel zone plates", *IEEE trans. on Microwave Theory and Techniques*, vol. 35, n°12, pp. 1122-1129, Déc. 1987

[2] H. D. Hristov, M. H. A. J. Herben, "Millimeter wave Fresnel zone plate lens and antenna", *IEEE trans. on Microwave Theory and Techniques*, vol. 43, n°12, pp. 2779-2785, Déc. 1995

[3] H. D. Hristov, "Fresnel Zones in Wireless Links, Zone Plate Lenses and Antennas", London, Artech House, 2000

[4] D. M. Pozar, S. D. Targonski, H. D. Syrigos, "Design of millimeter wave microstrip reflectarrays ", *IEEE trans. on Antennas and Propagation*, vol. 45, n°2, pp. 287-295, Fév. 1997

[5] E. Girard, "Conception et simulation de cellules rayonnantes déphaseuses pour réseau réflecteur à polarisation circulaire", Thèse de l'INSA de Rennes, Novembre 2003

[6] R. Sauleau, "Etude de résonateurs de Pérot-Fabry et d'antennes imprimées en ondes millimétriques. Conception d'antennes à faisceau gaussien", Thèse de l'Université de Rennes 1, 9 décembre 1999

[7] R. Sauleau, Ph. Coquet, D. Thouroude, J.-P. Daniel, T. Matsui, "Radiation characteristics and performances of millimeter wave horn-fed gaussian beam antennas, *IEEE trans. on Antennas and Propagation*, vol. 51, n°3, pp. 378-387, Mars 2003

[8] R. Sauleau, Ph. Coquet, T. Matsui, J.-P. Daniel, "A new concept of focusing antennas using plane-parallel Fabry-Perot cavities with non-uniform mirrors", *IEEE trans. on Antennas and Propagation*, vol. 51, n°11, pp. 3171-3175, Nov. 2003

[9] F. Gallée, G. Landrac, M. Ney, "Artificial lens for third generation automotive radar antenna at millimeter-wave frequencies", *IEE Proc. Microwaves, Antennas, Propagation*, vol. 150, n°6, pp. 470-476, Déc. 2003

[10] P. F. Goldsmith, "Perforated plate lens for millimeter quasi-optical systems", *IEEE transactions on Antennas and Propagation*, vol. 51, n°11, pp. 3171-3175, Nov. 2003

[11] A. R. Dion, "An investigation of a 110-wavelength EHF waveguide lens", *IEEE trans. on Antennas and Propagation*, pp. 493-496, Juillet 1972

[12] C. M. Rappaport, A. I. Zaghloul, "Optimized three-dimensional lenses for wide-angle scanning", *IEEE trans. on Antennas and Propagation*, vol. 33, n°11, pp. 1227-1236, Nov. 1985

[13] H. H. Fuchs, D. Nüssler, "Design of a Rotman lens for beamsteering of 94 GHz antenna array", *Elec. Letters*, vol. 36, n°6, pp. 834-838, Juin 1991

[14] T. H. Chio, K. K. Chan, "A Rotman lens fed ridge-element multibeam array demonstrator", *IEEE AP-S International Symposium,* Monterey, CA, vol. 1, pp. 655-658, 20-25 Juin 2004

[15] A. F. Peterson, E. O. Rausch, "Scattering matrix integral equation analysis for the design of a waveguide Rotman lens", *IEEE trans. on Antennas and Propagation*, vol. 47, n°5, pp. 870-878, Mai 1999

[16] J. B. L. Rao, D. P. Patel, V. Krichevsky, J. C. Sureau, "Low-cost phased arrays using bulk phase shifting", *Proc. of the 2000 International Symposium on Antennas and Propagation*, Fukuoka, Japon, vol. 3, pp. 1163-1166, 21-25 Août 2000

[17] J. B. L. Rao, D. P. Patel, V. Krichevsky, "Voltage-controlled ferroelectric lens phased arrays",

IEEE trans. on Antennas and Propagation, vol. 47, n°31, pp. 458-468, Mars 1999

[18] J. R. Sanford, "Scattering by spherically stratified microwave lens antennas", *IEEE trans. on Antennas and Propagation*, vol. 42, n°5, pp. 690-698, Mai 1994

[19] H. Mosallaei, Y. Rahmat-Samii, "Nonuniform Luneburg and two-shell lens antennas: radiation characteristics and design optimization", *IEEE trans. on Antennas and Propagation*, vol. 49, n°1, pp. 60-69, Janv. 2001

[20] S. Rondineau, "Modélisation de lentilles sphériques à gradient d'indice et sources conformes associées", Thèse de l'Université de Rennes 1, 13 décembre 2002

[21] C. Abella, M. Marin, J. Vazquez, J. Peces, J. A. Romera, R. Graham, G. Crone, R. Garcia, "Artificial dielectric lens antennas : assessment of their potential for space applications", *23rd European Microwave Conference*, pp. 896-898, Madrid, Espagne, Sept. 1993

[22] K. F. Sabet, T. Ozdemir, P. Frantzis, K. Sarabandi, L. P. B. Katehi, "Compact wireless antennas using an artificial dielectric lens", *2002 IEEE Aerospace Conference Proc.*, Montana (US), vol. 2, pp. 931-938, 9-12 Mars 2002

[23] M. G. M. V. Silveirinha, C. A. Fernandes, "Design of a non-homogeneous wire media lens using genetic algorithm", *IEEE AP-S International Symposium,* San Antonio, Texas, vol. 1, pp. 730-733, 16-21 Juin 2002

[24] J. R. Risser, "*Dielectric and metal-plate lenses*", Chapitre 11, *Microwave Antenna Theory and Design*, S. Silver, Ed. MIT Radiation Laboratory Series, vol. 12, New York: McGraw-Hill, 1949

[25] H. Jasik, "*Antenna engineering handbook*", Mc-Graw Hill, chap. 14 et 15, 1961

[26] R. E. Collin, F. J. Zucker, "*Antenna theory*", Mc-Graw Hill, chap. 18, 1969

[27] D. L. Sengupta, R. E. Hiatt, "*Reflectors and lenses*", Chapitre 10, *Radar Handbook*, M. I. Skolnik, Ed. New York: McGraw-Hill, 1970

[28] E. M. T. Jones, "Paraboloid reflector and hyperboloid lens antennas", *IRE trans. on Antennas and Propagation*, pp. 119-127, Juillet 1954

[29] K. Chang, "*Handbook of microwave and optical components*", vol. 1 "*Microwave passive and antenna components*", Wiley, New York, chap. 11 (J. J. Lee), 1989

[30] G. G. Cloutier, G. Bekefi, "Scanning characteristics of microwave aplanatic lenses", *IRE trans. on Antennas and Propagation*, pp. 391-396, Oct. 1957

[31] F. S. Holt, A. Mayer, "A design procedure for dielectric microwave lenses of large aperture ratio and large scanning angle", *IRE trans. on Antennas and Propagation*, pp. 25-30, Janv. 1957

[31bis] P. F. Goldsmith, "*Quasioptical systems: Gaussian beam, Quasioptical propagation and Applications*", IEEE press, 1998

[32] J. J. Lee, "Dielectric Lens Shaping and Coma-Correction Zoning, Part I: Analysis", *IEEE Trans. Antennas Propagat.*, vol. 31, n° 1, pp. 211-216, Janv. 1983

[33] J. J. Lee and R. L. Carlise, "A Coma-Corrected Multibeam Shaped Lens Antenna, Part II: Experiments", *IEEE Trans. Antennas Propagat.*, vol. 31, n° 1, pp. 216-220, Janv. 1983

[34] B. S. Westcott, F. Brickell, "General dielectric-lens shaping using complex co-ordinates", *IEE Proc. Microwaves, Antennas and Propagation*, vol. 133, n°2, pp. 122-126, Avril 1986

[35] W. Rotman, "Analysis of an EHF Aplanatic Zoned Dielectric Lens Antenna", *IEEE Trans. Antennas Propagat.*, vol. 32, n° 6, pp. 611-617, Juin 1984

[36] A. L. Peebles, “A Dielectric Bifocal Lens for Multibeam Antenna Applications”, *IEEE Trans. Antennas Propagat.*, vol. 36, n° 5, pp. 599-606, Mai 1988

[37] G. F. Delgado, "Scanning properties of teflon lenses", *Microwave and Optical Technology Letters*, vol. 11, n°5, pp. 271-273, Avril 1996

[37bis] P.-S. Kildal, K. R. Jakobsen, “Scalar horn with shaped lens improves Cassegrain efficiency”, *IEEE trans. on Antennas and Propagation*, vol. 32 n° 10, pp. 1094-1100, Oct. 1984

[37ter] O. Pascal, F. Lemaître, G. Soum, "Dimensionnement d'une lentille diélectrique pour antenne GOLA", *Journées Internationales de Nice sur les Antennes*, pp. 524-527, 1996

[38] A. Yamada, T. Matsui, “CPW-fed lens antenna for 25 GHz-band wireless communication system”, *29th European Microwave Conference,* Munich, Allemagne, pp. 5-8, 1999

[39] X. Wu, G. V. Eleftheriades, “Two-lens and lens-fed reflector antenna systems for mm-wave wireless communications”, *IEEE Antennas and Propagation Symposium*, Salt Lake City, UT, vol. 1, pp. 660-663, 16-21 Juillet 2000

[40] L. de Haro, A. G. Pino, J. L. Besada, A. M. Arias, J. O. Rubinos, “Antennas feasibility study for LMDS communication system”, *IEEE Antennas and Propagation Symposium*, Orlando, FL, vol. 3, pp. 2162-2165, 11-16 Juillet 1999

[41] H.-O. Ruoss, P. M. Maier, F. M. Landstorfer, G. Villino, “Lens antennas for mobile broadband systems in the millimeter-wave range”, *Elec. Letters*, vol. 33, n°18, pp. 1510-1512, Août 1997

[42] C. A. Fernandes, “*Shaped-beam antennas*”, Chap. 15, *Handbook of antennas in wireless communications*, Ed. L. C. Gogara, CRC Press, Août 2001

[43] C. A. Fernandes, “Shaped Dielectric Lenses for Wireless Millimeter-Wave Communications”, *IEEE Antennas and Propagation Magazine*, vol. 41, n°5, pp. 141-150, Octobre 1999

[44] M. Rodrigo, C. A. Fernandes, “Shaped dielectric lens fed by a printed element for WLANs at 40 GHz”, *Proc. of Millennium Conf. on Antennas and Propagat.*, Davos, Suisse, Avril 2000

[45] C. A. Fernandes, J. G. Fernandes, “Performance of Lens Antennas in Wireless Indoor Millimeter-Wave Applications”, *IEEE Trans. Microwave Theory Tech.*, vol. 47, n° 6, pp. 732-737, Juin 1999

[46] C. A. Fernandes, L. M. Anunciada, “Constant flux illumination of square cells for millimetre-wave wireless communications”, *IEEE Trans. Microwave Theory Tech.*, vol. 49, n°11, pp. 2137-2141, Nov. 2001

[47] M. G. M. V. Silveirinha, C. A. Fernandes, “Shaped Double-Shell Dielectric Lenses for Wireless Millimeter-Wave Communications”, *IEEE International Symposium on Antennas and Propagation*, Salt-Lake City, UT, vol. 3, pp. 1674-1677, 16-21 Juillet 2000

[48] X. Wu, G. V. Eleftheriades, T. E. van Deventer-Perkins, “Design and Characterization of Single- and Multiple-Beam mm-Wave Circularly Polarized Substrate Lens Antennas for Wireless Communications”, *IEEE Trans. Microwave Theory Tech.*, vol. 49, n° 3, pp. 431-441, Mars 2001

[49] D. Lemaire, C. A. Fernandes, P. Sobieski, A. Barbosa, “A method to overcome the limitations of G.O. in axis-symmetric dielectric lens shaping*”, International Journal of Infrared and Millimeter Waves*, vol.17, n°8, pp.1377-1390, 1996

[50] C. A. Fernandes, V. Brankovic, S. Zimmermman, M. Filipe, L. M. Anunciada, “Dielectric lens antenna for wireless broadband communications”, *Wireless Personnal Communications Journal*, vol. 10, n°1, pp. 19-32, Juin 1999

[51] C. A. Fernandes, “Research work from Instituto Superior Técnico”, *Antenna Center of*

Excellence, WP 2.1, Mai 2004

[52] F. Gallée, “Conception d’antennes pour radar automobile détecteur d’obstacles à 76 GHz. Réalisations à base de réflecteurs et de lentilles artificielles sur substrat faible coût”, Thèse de l’Université de Bretagne Occidentale, 2001

[53] I. Gresham, N. Jain, T. Budka, A. Alexanian, N. Kinayman, B. Ziegner, S. Brown, P. Staecker, “A compact manufacturable 76-77 GHz radar module for commercial ACC applications”, *IEEE Trans. Microwave Theory Tech.*, vol. 49, n°1, pp. 44-58, Janv. 2001

[54] B. G. Porter, L. L. Rauth, J. R. Mura, S. S. Gearhart, “Dual-Polarized slot-coupled patch antennas on Duroïd with Teflon lenses for 76.5 GHz automotive radar systems”, *IEEE trans. on Antennas and Propagation*, vol. 47, n°12, pp. 1836-1842, Déc. 1999

[55] B. Schoenlinner, X. Wu, J. P. Ebling, G. V. Eleftheriades, G. M. Rebeiz, “Wide-Scan Spherical-Lens Antennas for Automotive Radars”, *IEEE Trans. Microwave Theory Tech.*, vol. 50, n° 9, pp. 2166-2175, Sept. 2002

[56] B. Schoenlinner, G. M. Rebeiz, “Compact multibeam imaging antenna for automotive radars”, *IEEE Microwave Theory Tech. Symposium*, Seattle, WA, pp. 1373-1376, 2-7 Juin 2002

[57] N. Kitamori, F. Nakamura, T. Hiratsuka, K. Sakamoto, Y. Ishikawa, “High-ε ceramic lens antenna with novel beam scanning mechanism”, *Proc. of the 2000 International Symposium on Antennas and Propagation*, Fukuoka, Japon, vol. 3, pp. 983-986, 21-25 Août 2000

[58] H. Mosallaei, Y. Rahmat-Samii, “Nonuniform Luneburg and two-shell lens antennas: radiation characteristics and design optimization”, *IEEE trans. on Antennas and Propagation*, vol. 49, n°1, pp. 60-69, Janv. 2001

[59] F. Averty, “Antenne source pour lentille homogène en technologie mousse”, Thèse de l’Université de Bretagne Occidentale, 10 mars 2004

[60] F. Averty, A. Louzir, J.-F. Pintos, Ph. Chambelin, Ch. Person, G. Landrac, J.-P. Coupez, “Cost effective antenna for LEO satellites communication system using a homogeneous lens”, *IEEE AP-S International Symposium,* Monterey, CA, vol. 1, pp. 671-674, 20-26 Juin 2004

[61] J. Thornton, “A low sidelobe asymmetric beam antenna for high altitude platform communications”, *IEEE Microwave and Wireless Components Letters*, vol. 14, n°2, pp. 59-61, Fév. 2004

[62] D. M. Pozar, "Considerations for millimeter wave printed antennas", *IEEE trans. on Antennas and Propagation*, vol. 31, n°5, pp. 740-747, Sept. 1983

[63] D. B. Rutledge, D. P. Neikirk, D. P. Kasilingam, "*Integrated circuit antennas*", Infrared and Millimeter Waves, vol. 10, chap. 1, pp. 1-89, 1983

[64] N. G. Alexopoulos, D. R. Jackson, P. B. Katehi, "Criteria for nearly omnidirectional radiation patterns for printed antennas", *IEEE trans. on Antennas and Propagation*, vol. 33, n°2, pp. 195-205, Fév. 1985

[65] I. Papapolymerou, R. F. Drayton, L. P. B. Katehi, "Micromachined patch antennas", *IEEE trans. on Antennas and Propagation*, vol. 46, n°2, pp. 275-283, Fév. 1998

[66] R. Gonzalo, P. de Maagt, M. Sorolla, "Enhanced Patch-Antenna Performance by Suppressing Surface Waves Using Photonic-Bandgap Substrates", *IEEE Trans. Microwave Theory Tech.*, vol. 47, n°11, pp. 2131-2138 , Nov. 1999

[66b] D. Sievenpiper, E. Yablonovitch, "High-impedance electromagnetic surfaces with forbidden frequency band", *IEEE Trans. Microwave Theory Tech*, vol. 47, n°11, pp. 2059-2074, Nov. 1999

[67] C. R. Brewitt-Taylor, D. J. Gunton, H. D. Rees, "Planar antennas on a dielectric surface", *Elec. Letters*, vol. 17, n°20, pp. 729-731, Oct. 1981

[68] D. B. Rutledge, M. S. Muha, "Imaging antenna arrays", *IEEE trans. on Antennas and Propagation*, vol. 30, n°4, pp. 535-540, Juillet 1982

[69] H. van de Stadt, Th. de Graauw, A. Skalare, R. A. Panhuyzen, R. Zwiggelaar, "Millimeter and submillimeter studies of planar antennas", *First Int. Symp. on Space THz Techn.*, Ann Arbor, MI, pp. 235-255, Mars 1990

[70] C. J. Adler, C. R. Brewitt-Taylor, M. Dixon, R. D. Hodges, L. D. Irving, H. D. Rees, "Microwave and millimeter-wave receivers with integral antennas", *IEE Proc.*, Pt H, vol. 138, n°3, pp. 253-257, Juin 1991

[71] A. Skalare, Th. de Graauw, H. van de Stadt, "A planar dipole array antenna with an elliptical lens", *Microwave and Optical Technology Letters*, vol. 4, n°1, pp. 9-12, Janv. 1991

[72] D. F. Filipovic, S. S. Gearhart, G. M. Rebeiz, "Double-slot antennas on extended hemispherical and elliptical silicon dielectric lenses", *IEEE trans. on Microwave Theory and Techniques*, vol. 41, n°10, pp. 1738-1749, Oct. 1993

[73] J. Zmuidzinas, H. G. LeDuc, "Quasi optical slot antenna SIS mixers", *IEEE trans. on Microwave Theory and Techniques*, vol. 40, n°9, pp. 1797-1804, Sept. 1992

[74] M. J. Wengler, D. P. Woody, R. E. Miller, T. G. Phillips, "A low noise receiver for millimeter and submillimeter wavelengths", *Int. Journ. of Infrared and Millimeter Waves*, vol. 6, n°8, pp. 697-706, Août 1985

[75] X. Wu, G. V. Eleftheriades, "Two-lens and lens-fed reflector antenna systems for mm-wave wireless communications", *IEEE Antennas and Propagation Symposium*, Salt Lake City, UT, vol. 1, pp. 660-663, 16-21 Juillet 2000

[76] D. F. Filipovic, G. M. Rebeiz, "Double-slot antennas on extended hemispherical and elliptical quartz dielectric lenses", *Int. Journ. of Infrared and Millimeter Waves*, vol. 14, n°10, pp. 1905-1924, Oct. 1993

[77] G. Godi, R. Sauleau, "FDTD analysis of reduced size substrate lens antennas", *IEEE AP-S International Symposium,* Monterey, Californie, vol. 1, pp. 667-670, 20-26 Juin 2004

[77-gael] G. Godi, R. Sauleau, D. Thouroude, "Performance of electrically small substrate lens antennas for millimetre-wave communications", *IEEE transactions on Antennas and Propagation*, révisions mineures, Juillet 2004

[77a] T. Ozdemir, P. Frantzis, K. F. Sabet, L. P. B. Katehi, K. Sarabandi, J. F. Harvey, "Compact wireless antennas using a superstrate dielectric lens", *IEEE AP-S International Symposium,* Salt Lake City, UT, vol. 3, pp. 1678-1681, 16-21 Juillet 2000

[77b] L. Mall, R. B. Waterhouse, "Simple, small antenna terminal for maritime satellite communications", *Elec. Letters,* vol. 40, n°11, pp. 646-648, Mai 2004

[77c] X. Wu, G. V. Eleftheriades, T. E. van Deventer-Perkins, "Design and Characterization of Single- and Multiple-Beam mm-Wave Circularly Polarized Substrate Lens Antennas for Wireless Communications", *IEEE Trans. Microwave Theory Tech.*, vol. 49, n° 3, pp. 431-441, Mars 2001

[77d] L. Mall, R. B. Waterhouse, "Millimeter-wave proximity-coupled microstrip antenna on an extended hemispherical dielectric lens", *IEEE trans. on Antennas and Propagation*, vol. 49, n°12, pp. 1769-1772, Déc. 2001

[77d-bis] Ch. Chatenet, "Etude de dispositifs rayonnants millimétriques à lentilles diélectriques alimentées par des antennes imprimées. Application à la réalisation de systèmes de télécommunication haut débit", Thèse de l'Université de Limoges, 10 Décembre 1999

[77e] R. Alkhatib, M. Drissi, “Broadband lens antenna for wireless communications”, *IEEE AP-S International Symposium*, Monterey, Californie, vol. 1, pp. 663-666, 20-26 Juin, 2004

[77f] R. B. Waterhouse, D. Novak, A. Nirmalathas, C. Lim, “Broadband printed antennas for point-to-point and point-to-multipoint wireless millimetre-wave applications”, *IEEE AP-S International Symposium,* Salt Lake City, UT, vol. 3, pp. 1406-1409, 16-21 Juillet 2000

[77g] S. Raman, N. Scott Barker, G. Rebeiz, “A W-band dielectric-lens-based integrated monopulse radar receiver”, *IEEE trans. Microwave Theory Tech.*, vol. 46, n°12, pp. 2308-2316, Déc. 1998

[77h] M. Tonouchi, M. Tani, Z. Wang, K. Sakai, “Enhanced THz radiation from YBCO thin film bow-tie antennas with hyper-hemispherical MgO lens”, *IEEE trans. on Applied Superconductivity*, vol. 7, n°2, pp. 2913-2916, Juin 1997

[77i] J. Van Rudd, D. M. Mittleman, “Influence of substrate-lens design in terahertz time-domain spectroscopy”, *Journal of the Opt. Soc. of Am. B*, vol. 19, n°2, pp. 319-328, Fév. 2002

[77j] V. Popescu, “Modélisation et conception de matrices de mélangeurs en structure ouverte destinées à l’imagerie focale millimétrique et submillimétrique”, Thèse de l’Université de Marne-la-Vallée, 16 Octobre 1996

[77k] V. Popescu, F. Baudrand, Ch. Letrou, D. Bajon, H. Baudrand, G. Beaudin, "Conception d'antennes de type lentille substrat avec fente annulaire destinées aux domaines millimétrique et submillimétrique", *Journées Internationales de Nice sur les Antennes*, pp. 486-489, 1996

[77l] T. H. Büttgenbach, "An improved solution for integrated arrays optics in quasi optical mm and submm receivers : the hybrid antenna", *IEEE trans. on Microwave Theory and Techniques*, vol. 41, n°10, pp. 1750-1761, Oct. 1993

[77m] A. Gaugue, D. Robbes, A. Sentz, Ch. Letrou, A. Kreisler, "Antenne planaire log-périodique pour détecteur bolométrique à supraconducteur en ondes submillimétriques", *Journées Internationales de Nice sur les Antennes*, pp. 710-713, 1996

[77n] Y. Huo, G. W. Taylor, R. Bansal, "Planar log-periodic antennas on extended hemispherical silicon lenses for millimeter / submillimeter wave detection applications", *Int. Journ. of Infrared and Millimeter Waves*, vol. 23, n°6, pp. 819-839, Juin 2002

[78] B. K. Kormanyos, G. M. Rebeiz, "20-GHz power combining slot-oscillator array", *IEEE Microwave and Guided Wave Letters*, vol. 4, n°7, pp. 226-228, Juillet 1994

[79] H. Kobayashi, Y. Yasuoka, "Receiving properties of extended hemispherical lens coupled slot antennas for 94 GHz millimeter wave radiation", *Electronics and Communications in Japan*, Part 1, vol. 84, n°6, pp. 32-40, 2001

[80] G. Gauthier, T. P. Budka, W. Y. Ali-Ahmad, D. F. Filipovic, G. M. Rebeiz, "A low-noise 86-90 GHz uniplanar Schottky receiver", *IEEE MTT-S Int. Symp. Dig.*, Atlanta, pp. 325-328, 14-18 Juin 1993

[81] P. Otero, G. V. Eleftheriades, J. R. Mosig, "Integrated modified rectangular-loop slot antenna on substrate lenses for millimeter and submillimeter-wave frequencies mixer applications", *IEEE trans. on Antennas and Propagation*, vol. 46, n°10, pp. 1489-1497, Oct. 1998

[82] S. Raman, G. M. Rebeiz, "Single and dual polarized millimeter wave slot ring antennas", *IEEE trans. on Antennas and Propagation*, vol. 44, n°11, pp.1438-1444, Nov. 1996

[83] Barbara : IEEE trans. AP

[83] Barbara : IEEE AP’s 2003

[85] G. V. Eleftheriades, Y. Brand, J.-F. Zürcher, J. R. Mosig, "ALPSS: a millimeter-wave aperture-coupled patch antenna on a substrate lens", *Elec. Letters*, vol. 33, n°3, pp. 169-170, Janv. 1997

[86] B. Chantraine-Barès, R. Sauleau, G. Godi, “Design of a Compact Millimeter-Wave Lens Antenna for Satellite Communications in Q-Band”, *26th ESA Antenna Technology Workshop on Satellite Antenna Modelling and Design Tools*, ESTEC, Noordwijk, The Netherlands, pp. 229-236, 12-14 Nov. 2003

[87] M. Rodrigo, C. A. Fernandes, “Shaped dielectric lens fed by a printed element for WLANs at 40 GHz”, *Proc. of Millennium Conf. on Antennas and Propagat*., Davos, Suisse, 9-14 Avril 2000

[88] M. van der Vorst, P. de Maagt, M. Herben, "Influence of internal reflections on the far-field pattern of integrated lens antennas", *Proc. of ISAP'96*, Chiba, Japon, vol. 4, pp. 1225-1228, 24-27 Sept. 1996

[89] M. J. M. van der Vorst, P. J. I. de Maagt, M. H. A. J. Herben, “Effect of internal reflections on the radiation properties and input admittance of integrated lens antennas”, *IEEE trans. Microwave Theory Tech.*, vol. 47, n°9, pp. 1696-1704, Sept. 1999

[90] M. J. M. van der Vorst, P. J. I. de Maagt, A. Neto, A. L. Reynolds, R. M. Heeres, W. Luingue, M. H. A. J. Herben, “Effect of Internal Reflections on the Radiation Properties and Input Impedance of Integrated Lens Antennas – Comparison Between Theory and Measurements”, *IEEE Trans. Microwave Theory Tech.*, vol. 49, n° 6, pp. 1118-1125, Juin 2001

[91] A. Neto, D. Pasqualini, A. Toccafondi, “Mutual Coupling Between Slots Printed at the Back of Elliptical Dielectric Lenses”, *IEEE Trans. Antennas Propagat.*, vol. 47, n° 10, pp. 1504-1507, October 1999

[92] M. van der Vorst, P. de Maagt, M. Herben, "Matching layers for integrated lens antennas", *Journées Internationales de Nice sur les Antennes*, pp. 511-515, 1996

[93] K. Uehara, K. Miyashita, K. I. Natsume, K. Hatakeyama, K. Mizuno, "Lens-coupled imaging arrays for the millimeter and submillimeter wave regions", *IEEE trans. on Microwave Theory and Techniques*, vol. 40, n°5, pp. 806-811, Mai 1992

[94] D. F. Filipovic, G. P. Gauthier, S. Raman, G. M. Rebeiz, “Off-Axis Properties of Silicon and Quartz Dielectric Lens Antennas”, *IEEE Trans. Antennas Propagat.*, vol. 45, n° 5, pp. 760-766, Mai 1997

[95] J. R. Bray and L. Roy, “Physical Optics Simulation of Electrically Small Substrate Lens Antennas”, *IEEE Canadian Conference on Electrical and Computer Engineering*, vol. 2, pp. 814-817, Mai 1998

[96] A. F. Fray, I. D. King, I. Anderson, “Radiation from small hemispherical lenses”, *6th Int. Conf. on Antennas and Propagation*, *ICAP’89*, pp. 390-393, 4-7 Avril 1989

[97] D. Kasilingam and D. Rutledge, “Focusing Properties of Small Lenses”, *International Journal of Infrared and Millimeter Waves*, vol. 7, n° 10, pp. 1631-1647, 1986

[98] Design and Analysis of double-shell axial-symmetric integrated lens antennas for space applications (2002), Jorge R. Costa, Mario Silveirinha, Carlos A Fernandes.

[99] Design and characterization of single- and multiple-beam mm-wave circularly polarized substrate lens antennas for wireless communications (2001), George V. Eleftheriades.